Advances in Electrochemical Science and Engineering

Alkire, Kolb, Lipkowski, Ross (Eds.)

WILEY-VCH

Chemically Modified Electrodes

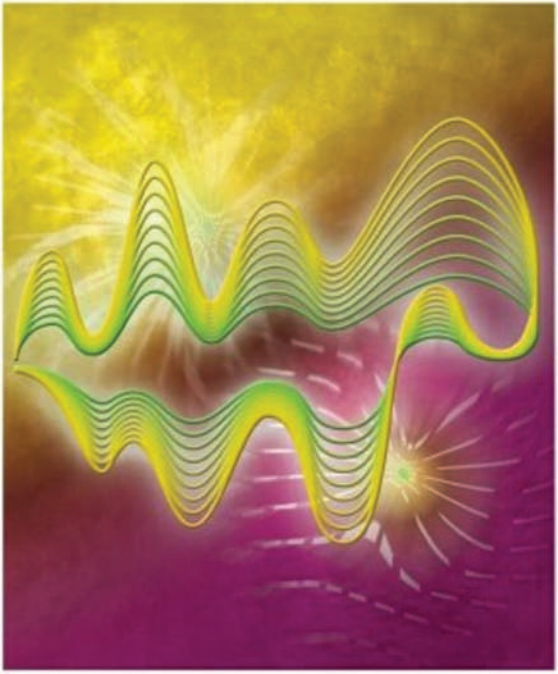

Volume 11

Advances
in Electrochemical
Science and Engineering

Volume 11
Chemically Modified
Electrodes

Advances in Electrochemical Science and Engineering

In collaboration with the International
Society of Electrochemistry

Advances in Electrochemical Science and Engineering

Volume 11
Chemically Modified Electrodes

Edited by
Richard C. Alkire, Dieter M. Kolb, Jacek Lipkowski,
and Philip N. Ross

WILEY-VCH Verlag GmbH & Co. KGaA

The Editors

Prof. Richard C. Alkire
University of Illinois
600 South Mathews Avenue
Urbana, IL 61801
USA

Prof. Dieter M. Kolb
University of Ulm
Institute of Electrochemistry
Albert-Einstein-Allee 47
89081 Ulm
Germany

Prof. Jacek Lipkowski
University of Guelph
Department of Chemistry
N1G 2W1 Guelph, Ontario
Canada

Prof. Philip N. Ross
Lawrence Berkeley National Laboratory
Materials Science Department
1 Cyclotron Road MS 2-100
Berkeley, CA 94720-0001
USA

Library of Congress Card No.: applied for

British Library Cataloguing-in-Publication Data
A catalogue record for this book is available from the British Library.

Bibliographic information published by the Deutsche Nationalbibliothek
The Deutsche Nationalbibliothek lists this publication in the Deutsche Nationalbibliografie; detailed bibliographic data are available on the Internet at http://dnb.d-nb.de.

Typesetting Thomson Digital, Noida, India
Printing betz-druck GmbH, Darmstadt
Binding Litges & Dopf GmbH, Heppenheim
Cover Design Grafik-Design Schulz, Fußgöheim

Printed in the Federal Republic of Germany
Printed on acid-free paper

ISBN: 978-3-527-31420-1
ISSN: 0938-5193

Contents

Preface

The steady expansion of interest in electrochemical science and technology creates the need for a monograph series of the highest standards for the experienced reader. The purpose of the *Advances in Electrochemical Science and Engineering* series is to provide high-quality advanced reviews of topics of both fundamental and practical importance.

The current volume addresses issues of chemically modified electrodes. Whenever bare surfaces do not fulfill the needs required, their chemical modification is a most promising way out of the dilemma. Purposeful attachment of atoms, molecules or even whole (nano)particles to the surface allows one to tailor the electronic and structural properties of a surface and hence, its functionality over a wide range. In the five chapters of this volume, internationally renowned scientists describe, how to modify a surface and what to do with it.

M. Buck reviews in great depth the literature on self-assembled monolayers (SAMs) of thiols on gold, a classic means of surface modification. The wide variety of functional groups that is provided by synthetic chemists makes thiol-SAMs an exciting playground for applications where the gap between two worlds, the inorganic and the organic, needs to be closed. Examples are molecular electronics and biochemistry.

M. Tagliazucchi and E.J. Calvo present another important and exciting means of modification: by electrochemically active polyelectrolytes. Polyelectrolytes modify surfaces by their inherent electric charges, which can be used, e.g., for constructing multilayer films of opposite charge, or simply by changing the electrochemical potential of reaction partners. Their role in many areas of chemistry, particularly of electroanalysis and biochemistry, cannot be overemphasized.

Carbon nanotubes are increasingly recognized as a promising tool for surface functionalization. M.J. Esplandiu presents a state-of-the-art overview of their applications in electrochemistry. As with SAMs of organic molecules the great potential of carbon nanotubes lies, among others, in biochemical applications and in molecular electronics.

Gold nanoparticles (NP) are just one of a variety of ways to modify the chemical behavior of surfaces by entities that can be described by their solid-state rather than atomic or molecular properties. From D.A. Buttry's chapter it becomes evident that their potential is mainly in electrocatalysis, an area of vast practical importance.

J.J. Gooding *et al.* touch upon many of the above-described systems on their exciting tour through the field of nanostructured electrodes with unique properties, particularly for biochemical and sensor applications. Again, it is the intelligent design of a bridge between measuring devices and the living world, which is highlighted in this review.

The reader may notice many cross-references between the five contributions, which support the view that chemical modification of surfaces, particularly the nanostructuring, is not only interesting for its own sake, but also relevant to a wide range of practice applications. Their seminal role in bioelectrochemistry, biosensing, electrocatalysis and electroanalysis among others is clearly evident in this volume.

Ulm, April 2009 *Dieter M. Kolb*

List of Contributors

Manfred Buck
EaStChem School of Chemistry
University of St Andrews
North Haugh, St Andrews
KY16 9ST
United Kingdom

Daniel A. Buttry
Department of Chemistry and Biochemistry
Arizona State University
PO Box 871604
Tempe, AZ 85287-1604
USA

Ernesto J. Calvo
INQUIMAE. DQIAyQF. Facultad de Ciencias Exactas y Naturales
Universidad de Buenos Aires
Pabetlón 2-liudad universitate CP 1428
Buenos Aires
Argentina

María José Esplandiu
Departamento de Quimica
Universidad Autónoma de Barcelona
08193 Bellaterra
Spain

Ian Y. Goon
School of Chemistry
The University of New South Wales
Sydney NSW 2052
Australia

J. Justin Gooding
School of Chemistry
The University of New South Wales
Sydney NSW 2052
Australia

Leo M.H. Lai
School of Chemistry
The University of New South Wales
Sydney NSW 2052
Australia

Mario Tagliazucchi
INQUIMAE. DQIAyQF. Facultad de Ciencias Exactas y Naturales
Universidad de Buenos Aires
Pabetlón 2-liudad universitate CP 1428
Buenos Aires
Argentina

1

Nanostructured Electrodes with Unique Properties for Biological and Other Applications

J. Justin Gooding, Leo M.H. Lai, and Ian Y. Goon

1.1

Introduction

Modifying the surface of electrodes to provide some control over how the electrode interacts with its environment has been one of the most active areas of research interest in electrochemistry within the last 30 years [1]. Whereas once the performance of an electrode was limited to the solution it was placed into, the material from which the electrode was made and the potential applied to the surface, the ability to chemically modify electrodes has provided a powerful route to tuning their performance. This has been particularly important to electroanalytical chemistry [2, 3], where modification has provided routes to providing selectivity, resisting fouling, concentrating species, improving electrocatalytic properties [4] and limiting access of interferences in a complex sample [5], such as a biological fluid, but has also had major impact for research into energy conversion [6, 7] and storage, corrosion protection [8], molecular electronics [9–11], electrochromic devices [12] and fundamental research into phenomena that influence electrochemical processes [9]. In recent years this revolution into tailoring electrode surfaces, such that the electrode has unique properties, has continued at an even greater rate with unprecedented control over the modification process via advances in nanofabrication. Taken in its broadest context, nanostructuring electrodes can be regarded as controlling the architecture of an electrode at the nanoscale; whether it be using nanomaterials, templating methods, organic monolayer modification of electrode surfaces or hybrid modification layers involving organic monolayers and nanomaterials. These different strategies for modifying electrodes provide opportunities to confer a unique range of properties to electrode surfaces from ultrahigh surface areas achieved with templated electrodes, to electrocatalytic properties with nanoparticles, strategies to achieve electrochemistry in locations too small for conventional electrodes, such as inside enzymes, and give electrodes with switchable properties.

Many of the unique properties that can be achieved with nanostructuring at the nanoscale are due to the ability of the unique properties of the nanomaterials employed, the ability to control the architecture of the electrode interface at the nanoscale or both. This nanoscale design of electrode interfaces potentially provides spatial control vertically from the surface and/or laterally across the electrode surface. In many ways self-assembled monolayers (SAMs) and templated methods offer the greatest possible control over how an electrode interface is modified as the electrode design and properties are tailored at something akin to the molecular level [13–15]. This spatial control is coupled with chemical control via the ability to incorporate multiple chemical components into a single interface to provide the interface with a range of properties. An example of such control is in the ion-channel biosensor where up to 10 or more molecular components are incorporated into a lipid bilayer for modifying electrodes where both lateral and vertical control are required to give one of the most versatile and sensitive biosensing concepts ever developed [16]. It is this molecular-level control with monolayer technologies that also forms the basis of many unique nanostructured electrode concepts involving nanoparticles, nanotubes and other nanomaterials where self-assembled monolayers form the linker between a macroscopic electrode and the nanomaterial [14].

It is the unique properties that can be conferred to an electrode by nanostructuring using nanomaterials, self-assembled monolayers and templating methods, particularly with regards to a biological context, that are the subject of this chapter. The chapter is not intended to be a comprehensive review of all the work done on nanostructuring electrodes but rather to cover some of the recent advances in nanostructuring electrodes, which are important for using electrodes for biological applications. Firstly, strategies to produce electrodes with high surface areas and their applications in enhancing electrode sensitivity will be discussed. The discussion of surface area will be followed by the structuring of electrodes with nanoscale features that provide catalytic properties to the electrode. The third section will cover the small size of features providing the opportunity to intimately interface electrodes with proteins. This section will include using molecular wires to give blocked electrodes where electrochemical communication is maintained through molecular wires. The final section of the chapter will explore switchable surfaces where spatial modulation of the electrode modification layer is exploited to radically alter the properties of the electrodes. In all cases our emphasis will be on methods of electrode modification that are highly controlled.

1.2
High Surface Area Electrodes

Incorporation of nanostructures onto the surface of electrodes began in the early 1990s. These structures were initially used to enhance electrochemical signals due to their high surface-to-volume ratio. Gradually, work progressed to their application into bioconjugated systems. The increase in electroactive surface area allows for lower detection limits and higher sensitivity to analytes. This is demonstrated in the detection of H_2O_2 using films of nanoparticles in a three-dimensional structure [17, 18]. In these studies, multilayers of nanoparticles were built up with bridging molecules between the layers. The bridging molecules have redox-active centers, which are sensitive to H_2O_2. By having large areas of nanoparticle film, the number of redox-active centers increases, providing a more sensitive sensor compared with electrodes of the same material that do not comprise the nanoparticle films. The main challenge in achieving a high surface area electrode is the control over the size and distribution of the structures produced on the electrode surface. To accomplish this, the four main strategies in producing high surface area electrodes that have been employed are (1) the direct attachment of nanoparticles onto an electrode, (2) templating with membranes such as polycarbonates or alumina, (3) the use of lyotropic liquid crystals as templates and (4) colloidal templating. We will discuss each of these in this section.

1.2.1
Attachment of Nanoparticles onto Electrodes

Increasing the electroactive surface area has been successfully achieved by the attachment of nanoparticles onto an electrode. Natan and coworkers [19] pioneered this approach, where the initial idea was to attach nanoparticles onto a platinum surface to enhance electrode performance. In this first study the surface of a platinum foil was coated with a polymer, (3-mercaptopropyl) methyldimethoxysilane (MPMDMS). Subsequently, the modified electrode was placed into a solution of 15-nm diameter Au nanoparticles. The MPMDMS and Au nanoparticle-modified layer was electrochemically active to the redox-active species, methyl viologen. An important observation made by Natan and coworkers [19] in this work is the electrochemistry was blocked when the Pt foil electrode was modified with the MPMDMS in the absence of Au nanoparticles but was 'switched on' when the nanoparticles were present. This demonstrates that the Au nanoparticles act as electrodes. However, when the oxidation and reduction peaks in the cyclic voltammogram (CV) were compared to a bare platinum electrode, the peaks in the CV of the nanoparticle-modified electrode had a slight broadening. The broadening was attributed to a closely spaced array of nanoelectrodes. Although this paper did not explore the effect of multilayers of nanoparticle films, nor the enhancement of the electrochemical signal provided by the increased surface area, this work paved the way for further investigation into nanoparticle-modified electrodes in general and for sensing in particular.

Following the lead of Natan and coworkers, further studies have demonstrated the ability of nanoparticles to enhance sensitivity by constructing multilayer structures composed of nanoparticles. Multilayers of nanoparticles linked together with conductive species create large internal surface area, which can be accessible to redox probes. The multilayered systems effectively create a porous network providing much higher surface area than a monolayer. For example, Blonder *et al.* [20] have modified indium tin oxide (ITO) electrodes with multilayers of Au nanoparticles. In this example the ITO surface was first modified with triethoxy aminopropylsilane in toluene, followed by the attachment of 12-nm nanoparticles (Figure 1.1). This nanoparticle-modified layer was then further functionalized with *N,N′*-bis(2-aminoethyl)-4,4′ bipyridinium, a redox-active bridging molecule. Four layers of

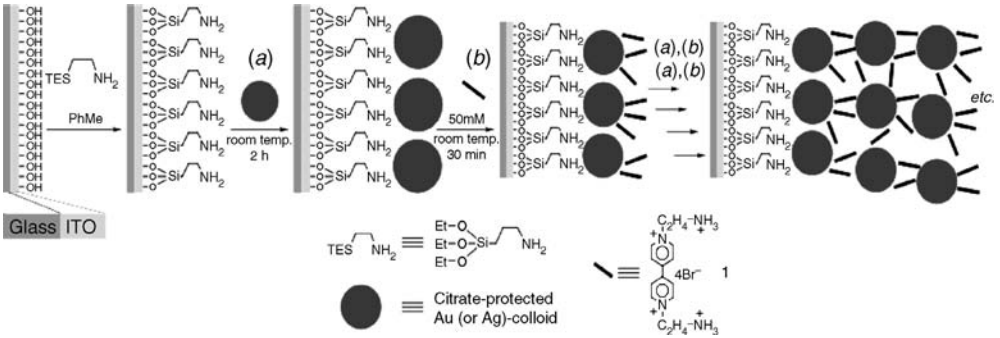

Figure 1.1 Stepwise production of metal-particle multilayer arrays. The attachment of the Au or Ag nanoparticles onto ITO-modified glass was achieved by using silanes that have an amine terminus group. This modification step allows for further modification with nanoparticles onto the surface of the ITO. After the nanoparticle attachment a redox-active bridging molecule was assembled onto the Au or Ag nanoparticle monolayer. This step was repeated a number of times to produce a three-dimensional array of nanoparticles that has large internal surface area and increased redox-active species concentration. (Reproduced by permission of The Royal Society of Chemistry from [20].)

nanoparticle films were constructed by repeating the exposure to Au nanoparticles and the redox bridge. This study demonstrated that, as more nanoparticles were placed on the electrode, an increase in peak current was observed for the oxidation and reduction, when a cyclic voltammogram was taken in phosphate buffer at pH 7. The increase in signal was attributed to two related factors. The first was the increase in the number of redox molecules in the layer and the second was the increase in electroactive surface area.

The main idea demonstrated by Willner and coworkers [20] is the ability to construct multilayered nanoparticle electrodes, which are porous. In a related study Patolsky *et al.* extended this idea further using biocatalysts to detect H_2O_2 [18]. In this example, the construction of the electrode is similar to the one described above but the redox-active bridging molecule was replaced with microperoxidase-11 (MP-11).

MP-11 is an 11 amino acid long chain, with the heme center of cytochrome *c* (Figure 1.2), which is produced by proteolytic digestion. It is an electrocatalyst and biocatalytic unit for H_2O_2. By keeping the concentration of H_2O_2 constant at 0.5 mM and changing the number of layers of nanoparticles and MP-11, Willner and coworkers [18] observed the enhancement of peak current as the number of layers of nanoparticles and MP-11 deposited on the electrode was increased. Therefore, Willner and coworkers concluded that the three-dimensional structure can provide a tunable and sensitive sensing interface for H_2O_2 by adjusting the amount of nanoparticle layers present in the three-dimensional structure.

Electrodeposition is an alternative way to produce nanostructures on an electrode surface from solution onto a surface. Using electrodeposition to construct nanostructures allows for greater control over the amount of material deposited on the surface due to the ability to precisely control the charge that is passed into the system. Some control over the morphology is also afforded. For example, Liu *et al.*

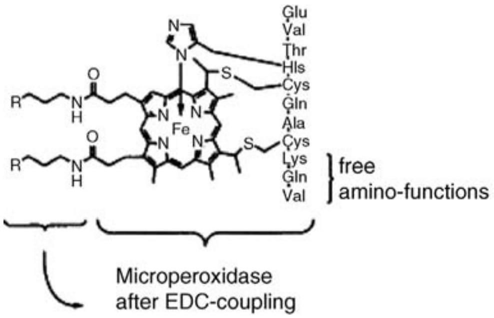

Figure 1.2 Stepwise assembly of MP-11, Au nanoparticle superstructure on ITO. (Reprinted with permission from Ref. [18]. ©1999 Elsevier.)

demonstrated the production of pyramidal, rod-like and spherical Au structures on Au foil [21]. The production of these nanostructures was simply achieved by electrodeposition of gold from an aqueous solution of 0.1 M $HClO_4$ and different concentrations of $HAuCl_4$. For example, to produce pyramidal structures 40 mM $HAuCl_4$ was used and deposited at -0.08 V vs. Ag|AgCl, to produce rod-like structures 4 mM $HAuCl_4$ and -0.08 V vs. Ag|AgCl was used and finally spherical structures were produced with 40 mM $HAuCl_4$ at -0.2 V vs. Ag|AgCl. After the formation of the nanostructures the surface was modified with Cu, Zn-superoxide dismutase (Cu, Zn-SOD). The enzyme immobilization was achieved simply by adsorption. The resulting electrodes were exposed to superoxide (O_2^-) and exhibited an improvement in the direct electron transfer between the SOD and the gold nanostructures compared with an electrode without nanostructuring. In particular the spherical nanostructured electrode showed excellent analytical performance, such as a wider linear range (0.2–200 μM), a lower detection limit (0.1 μM), a shorter response time (4.1 s) and a higher stability compared with the pyramidal and rod-like nanostructures.

The observation made by Natan and coworkers [19] that electrochemistry at a Pt foil electrode modified with the MPMDMS was dramatically altered when nanoparticles were present was also the first example where nanoparticles were used to alter the resistance of polymer films. At a similar time, Murray and coworkers [22] used nanoparticle films to explore the resistance properties of films relative to the length of the species that were used to bind the nanoparticles together into films. In this first study the modifiers were octanethiol, dodecanethiol and hexadecanethiols. The modified nanoparticles were produce by the reduction of $HAuCl_4$ in toluene followed by extraction into toluene where a molar equivalent amount of the thiol was added. The gold nanoparticles were flocculated to give a nanoparticle film. Conductivity of the films was measured and Murray and coworkers [22] reported a significant decrease in conductivity (150 times when compared between octanethiol and hexadodecanethiol) as the length of the monolayer coating the gold nanoparticle increase. This unique ability of the dependence on length of monolayers on nanoparticle surface on resistance has been used to detect gaseous analytes.

Following the concept of Murray and coworkers, Evans *et al.* [23] applied the system to the detection of gaseous methanol, ethanol, propanol, hexane, pentane, toluene, chloroform and acetic acid samples. In this study the nanoparticles were produced by the reduction of $HAuCl_4$ with $NaBH_4$. The synthesized modified nanoparticles were deposited onto an interdigitated electrode by the evaporation of the nanoparticle solution directly onto the electrode surface. The particles were tested at room temperature with no exposure to solvent vapors. Evans and coworkers observed a change in conductivity upon the change in functional groups (in decreasing order: $CH_3 > COOH > OH$) and size (larger-sized nanoparticle exhibited higher conductivity). The nanoparticle films were then exposed to different solvents, both polar and nonpolar solvents. The change in conductivity with the exposure to different solvents varied depending on the functional groups. Polar groups (OH, NH_2 and COOH) responded well to polar solvents and the nonpolar (CH_3) group responded well to nonpolar solvents. This preliminary study demonstrated the sensitivity of different functionalized nanoparticles to different analytes, in vapor phase.

Apart from using simple molecules, alkanethiols or mercaptophenyl's more complex molecules, dendrimers have been used to modify and improve the sensing capabilities of gold nanoparticle films to vapors (Figure 1.3). In a study by Krasteva *et al.* [24] the application of dendrimers was used to functionalize, as well as linking the modified nanoparticles together to produce a conducting film of gold nanoparticles and dendrimers. The study involved three types of dendrimers, one was hydrophobic (polyphenylene: PPh), and two hydrophilic (poly-amidoamine: PAMAM and poly-propyleneimine: PPI). All the dendrimer-modified nanoparticle films were made from gold nanoparticles with an average size of 4 nm that were suspended in toluene. To construct the nanoparticle/dendrimer film a glass substrate was used, which was functionalized with aminopropyldimethylethoxysilane and then placed into the gold nanoparticle solution. Then, the nanoparticle-modified glass film was placed into a solution of either PAMAM (third-generation Starburst*) in methanol, PPI (fourth-generation DAB-Am-32-poly(propylenimine-dotriacontaamine) in methanol or PPh (second-generation dithiolane-functionlized polyphenylene) in toluene and dichloromethane. This deposition of gold nanoparticles and dendrimers was repeated ten times to ensure a full coverage on the glass surface. The dendrimer-modified nanoparticle film was then exposed to three solvents, water, 1-propanol and toluene. Depending on the dendrimer used to functionalize the nanoparticles, a change in the resistance response to different solvents was observed. The Au/PPh was the most responsive to toluene due to the nonpolar nature of both the dendrimer and solvent. Au/PPI was the most responsive to 1-propanol and Au/PAMAM was the most responsive to water. Krasteva *et al.* [24] suggested that the chemical selectivity is related to the solubility of the dendrimers to the solvent exposed. This unique ability to detect vapors of solvents by nanoparticle films modified with dendrimers, by tailoring the functionality of the molecules allows for the use in sensors.

Other materials have also been used to produce modified nanoparticle films to detect organic vapors. Murray and coworkers [26] showed that the modification of nanoparticles with a carboxylate ligand, which can complex with a metal ion, Cu^{2+},

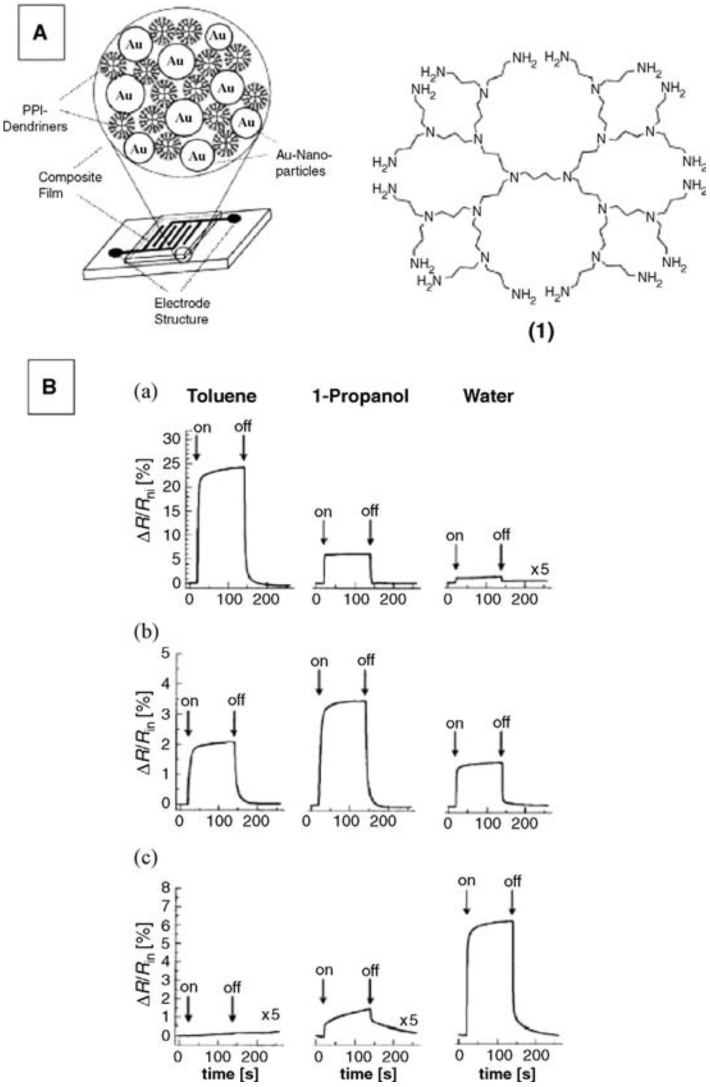

Figure 1.3 (A) Chemresistor containing gold nanoparticles and PPI. (Reprinted with permission ©2002 American Chemical Society.) (B) Response of the Au nanoparticle film to toluene, 1-propanol and water: (a) Au/PPh; (b) Au/PPI; (c) Au/PAMAM. (Reprinted with permission ©2003 Elsevier.) (Reproduced with permission from Ref. [25] © 2004 Wiley-VCH Verlag GmbH & Co. KGaA.)

to produce a flexible network polymer film (Figure 1.4). To produce the flexible polymer film, the nanoparticles were first synthesized with a protective layer of butanethiol, hexanethiol, octanethiol, decanethiol or dodecanethiol. This initial layer acted as a capping layer rather then a linker layer. To allow the nanoparticle film to

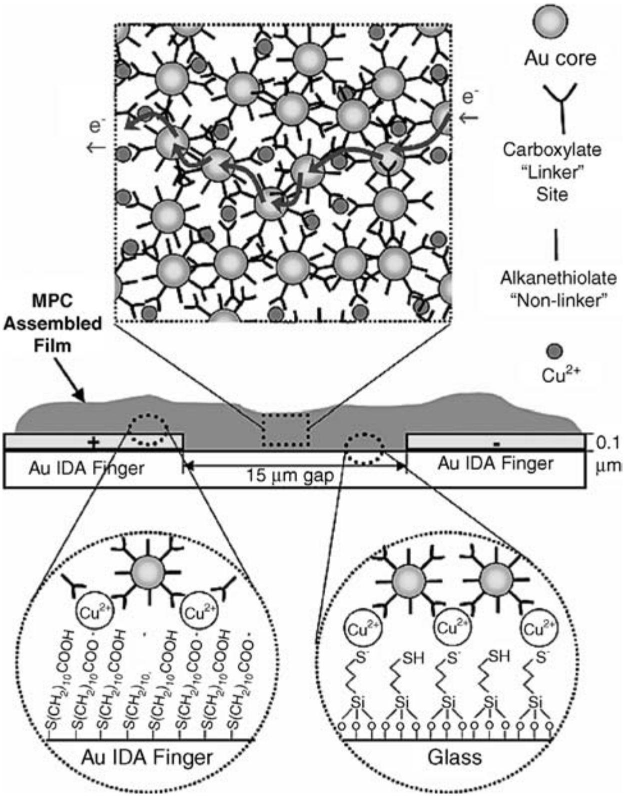

Figure 1.4 Schematic of the flexible nanoparticle film and construction. (Reprinted with permission from Ref. [26]. ©2002 American Chemical Society.)

form, some of the capping thiols were replaced with linker molecules such as 6-mercaptohexanoic acid, 11-mercaptoundecanoic acid or 16-mercaptohexadecanoic acid, using the place-exchange reaction. To construct the nanoparticle film, firstly two gold interdigitated electrodes were modified with a layer of 11-mercaptoundecanoic acid and the glass substrate with 3-mercaptopropyltrimethoxy silane. This functionalized electrode was then exposed to Cu^{2+} ions in ethanol, which complexed with the carboxylic acid, followed by the linker-modified gold nanoparticle. After this, the nanoparticle-deposited electrodes were rinsed with ethanol and the process of exposure to Cu^{2+} and nanoparticles was repeated numerous times to construct the film over the two electrodes, which connected the two gold fingers. This film was then exposed to ethanol vapor of various concentrations (0.1–1 saturated ethanol vapor). The conductivity results were compared to quartz crystal microgravimetry (QCM) data and showed highly comparable results, where the decrease in conductivity is related to the increase in mass by the QCM data. Zamborini *et al.* [26] have also reported the rapid switching between the exposure of ethanol vapor and N_2 gas. It was also reported that particles that were functionalized with 6-hexanethiol and

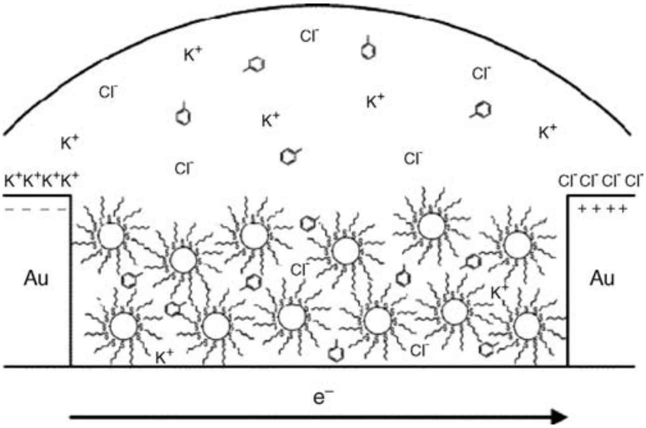

Figure 1.5 Schematic representation of hexanethiol-modified Au nanoparticles deposited between gold electrodes, in the presence of dissolved toluene in KCl solution. (Reprinted with permission from Ref. [27] ©2007 American Chemical Society.)

11-mercaptoundecanoic acid performed the best with a fast response rate (8 s) and the highest absorption of ethanol onto the structure (68 nmol).

Many of the applications of modified nanoparticle films have been used in the detection of gaseous chemicals but have not been applied in an aqueous environment. This inability to be applied to the detection of analytes in aqueous media is due to the high conductivity of the electrolyte solution. For nanoparticle film electrodes to be able to sense in aqueous solutions, the device must be miniaturized so the impedance of the solution is higher than the resistance of the nanoparticle film. In a study by Wieczorek and coworkers [27], the detection of analytes in water was demonstrated (Figure 1.5). On an interdigitated electrode where there was a separation between electrodes, 6-nm gold nanoparticles were deposited. Once deposited, the nanoparticles were modified with 1-hexanethiol by exposing the surface to 1-hexanethiol vapors. The nanoparticle-modified surfaces were then exposed to an aqueous solution containing varying amounts of chloroform. The impedance signal was shown to vary with the concentration of chloroform. As for the switching time, this was demonstrated by exposing the nanoparticle modified film to an aqueous solution containing toluene and showed a 10-s switching from the detection to the absence of toluene in the film. Reproducibility was also demonstrated by exposing the nanoparticle film to a series of aqueous solutions containing toluene, which showed repeatable signals upon each consecutive exposure. Wieczorek and coworkers [27] demonstrated that the device had a fast response time, good repeatability and sensitivity down to 0.1 ppm.

Changing the resistance between two electrodes using nanoparticles has also been applied to the detection of large biomolecules. In a study by Velev and Kaler [28] latex nanoparticles modified with protein A, a receptor for the immunoglobulin molecule, were aggregated onto the gap between two electrodes (Figure 1.6). The surface was then exposed to immunoglobulin G (IgG). After the binding of the IgG molecules to

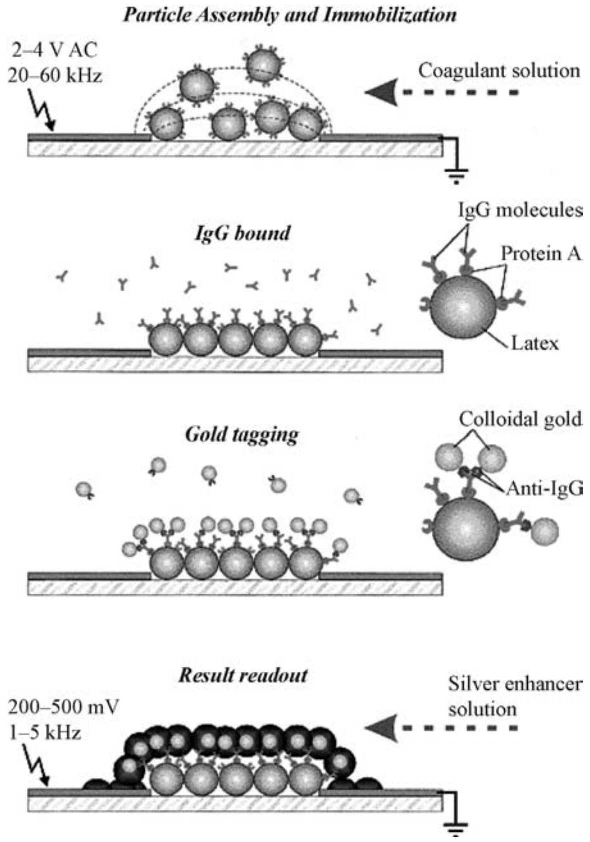

Figure 1.6 Schematic of the main stages of sensor assembly and functioning, demonstrated by an immunoglobulin test. (Reprinted with permission from Ref. [28]. ©1999 American Chemical Society.)

the nanoparticles, the surface was exposed to anti-IgG-modified gold nanoparticles. The gold nanoparticles acted as seeds for the deposition of silver, which linked the two electrodes with a concomitant increase in conductivity between the two electrodes. When a current was passed through this layer the resistance ranged from 50–70 Ω in the wet state and 40–50 Ω in the dry state. The electrodes that had negative controls, meaning no formation of the antibody–antigen bond, had resistances of 10^3 Ω. The experiment was also repeated with biotin-streptavidin biological molecules, which showed similar results to the above. Velev and Kaler concluded that the method developed in this study is as sensitive to those of clinical assays. Also, the detection limit of a few tens or hundreds of molecules is possible due to the low number of gold nanoparticles required to create the link between the two electrodes.

The use of nanoparticles to form bridges between two electrodes was also utilized to detect DNA hybridization, including single base-pair mismatches, by Mirkin and coworkers [29]. In this case DNA-modified gold nanoparticles were used to seed the silver deposition. The setup for the device is to firstly modify the glass substrate in the gap between the two gold electrodes with succinimidyl 4-(malemidophenyl)-butyrate, then the capture DNA was immobilized onto the activated glass surface. The target DNA formed a bridge between the surface-bound capture DNA and the DNA on the gold nanoparticles. Thus, in the presence of target DNA a network of gold nanoparticles will form between the two electrodes. Finally, a deposition of silver completed the setup, linking the two gold electrodes and resulted in a reduction in the resistance. The study demonstrated the ability to detect a single base pair mismatched by a less significant reduction of resistance compared with a fully complementary DNA strand. Another feature that this concept demonstrated was the exquisitely low detection limit for DNA (500 fM of DNA). With the reduction of the gap between the electrodes and a narrower conducting channel between the two electrodes it is possible that even higher sensitivities, as demonstrated by Lieber *et al.* with nanowires, may be possible [30, 31].

Narrower conducting channels can be fabricated by dip-pen nano lithography (DPN) [32]. Basnar *et al.* [33] have shown the possibility of the use of DPN to deposit gold nanoparticles modified with glucose oxidase enzymes and the subsequent growth of these gold nanoparticle by the enzymatic reaction with glucose (Figure 1.7). In this study, the enzyme glucose oxidase was modified with *N*-hydroxysuccinimide functionalized gold nanoparticles. This solution of glucose oxidase gold nanoparticle aggregate was used as an ink to deposit the aggregate at a specific location using DPN. Once deposited, a solution of glucose and $AuCl_4^-$ was exposed to the enzyme layer. The reaction of glucose to gluconolactone resulted in the reduction of O_2 to H_2O_2. The H_2O_2 then reacted with the $AuCl_4^-$ to deposit gold onto the glucose oxidase conjugated gold seed nanoparticles (a concept previously demonstrated by Willner and coworkers [34]). The process resulted in the growth of the gold nanoparticles such that they merged and formed a conducting wire. Willner and coworkers [33] have also concluded that with the application of other biocatalytic inks it is possible to extend the concept into production of semiconducting polymers, magnetic nanowires, semiconductor nanowires and insulating polymers.

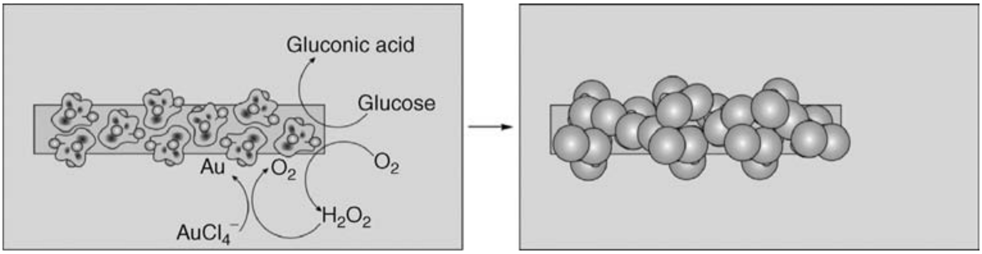

Figure 1.7 General scheme for the formation of Au nanowires created by DPN, using flavoenzymes. (Reprinted with permission from Ref. [33] ©2006 Wiley-VCH Verlag GmbH & Co. KGaA.)

1.2.2
Templating using Membranes

Although nanoparticles can increase the surface area of an electrode, the positioning of these nanostructures is difficult to control. An alternative way that allows for greater control of positioning of nanostructures is templating. Templating not only provides greater control over the locality of nanostructures but provides opportunities for a different range of shapes to be produced, such as tubes [35–37], rods [35, 36, 38, 39] and wells [21, 38–41]. The first example of producing nanostructures using templates was by Martin and coworkers [35], where polypyrrole was templated in a track-etched polycarbonate membrane or porous alumina membrane. Both types of membranes are commercially available, but each has different advantages with regards to producing nanostructures. Track-etched templates are produced by an initial bombardment of the membrane material with nuclear fission particles followed by further chemically etching. These membranes have uniform pores of sizes down to 10 nm in diameter and with pore densities as high as 10^9 pores per square centimeter. However, one drawback of these membranes is the pores are randomly distributed. Alumina membranes, on the other hand, have pore sizes that are uniform and distributed in a hexagonal pattern (Figure 1.8). These templates are produced electrochemically using aluminum metal and have pore densities up to 10^{10} pores per square centimeter [42]. This high pore density has the advantage that it allows for higher surface area nanostructures to be templated. The pore sizes that are commercially available, however, are limited to a minimum of 20 nm diameter. As a consequence, Martin and coworkers [43] have developed electrochemical strategies for the production of a range of pore sizes with the smallest being 5 nm.

The deposition of a conductive polymer (polypyrrole) into either a track-etched polycarbonate or alumina membrane was either achieved by electrochemical reduc-

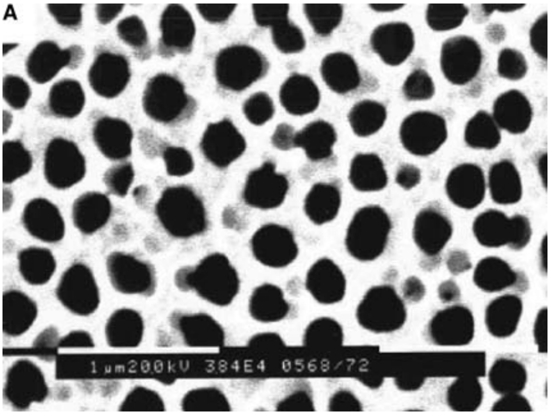

Figure 1.8 SEM image of porous alumina membrane, used in templating. (Reproduced by permission of The Royal Society of Chemistry from [36].)

tion [44] or chemical deposition [45, 46]. For example, the electrochemical synthesis of polypyrrole [44] can be achieved by the reduction of the pyrrole monomers in the presence of the membrane and a metal anode. Martin and coworkers [44] used an alumina template upon which they sputter coated one side with a thick layer of Au that covered the entrance to the pores. Following this process, the Au membrane film was placed in epoxy with only the area to be templated exposed. This template was then placed into a pyrrole solution to electrodeposit polypyrrole. Depending on the length of the desired tubes the time of current application is varied. The diameter of the tube is determined by the size of the membrane structure. Once the reduction of polymer is complete the membrane is then dissolved to expose the nanotubes. The produced nanofibrillar electrode demonstrated slightly higher current density (3–7%) when compared to unstructured electrodes. The magnitude of the increase in current density is greater as the nanofibers become narrower. The largest increase in current density recorded was one order of magnitude [45].

An alternate method to produce templated electrodes is the use of chemical reduction of the monomer in the presence of a track-etched or alumina membrane. Parthasarathy *et al.* [46] have produced enzyme-loaded nanotubules by a combination of both electrochemical and chemical deposition. Initially, the alumina membrane was sealed at one end with a thick Au film (Figure 1.9a), after which the membrane was placed into a mixture of pyrrole and Et_4NBF_4. The pyrrole was then electropolymerized to form a small plug of polypyrrole at the closed end of the alumina membrane (Figure 1.9b). Subsequently, the membrane was placed into a

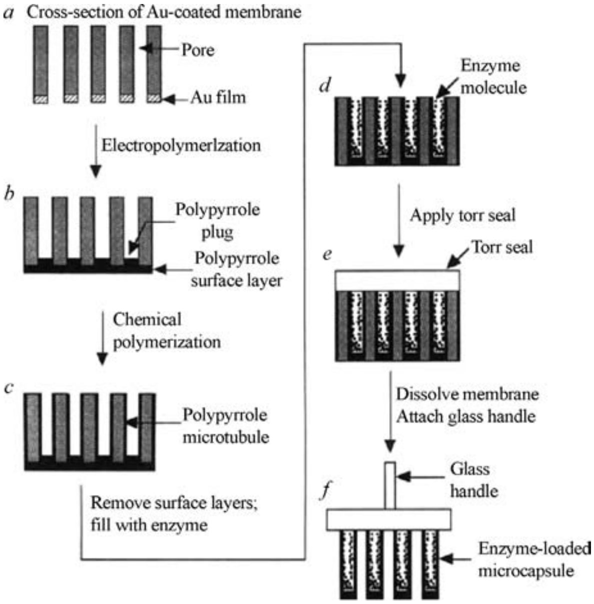

Figure 1.9 Schematic diagram for the method used to produce and enzyme load microcapsule arrays. (Reprinted with permission from Ref. [46]. ©1994 Nature Publishing Group.)

mixture of pyrrole and chemically polymerized. The resultant structure conformed to the shape of the membrane (Figure 1.9c). The enzyme was then loaded (Figure 1.9d) and finally the open end was sealed off with a Torr seal (Figure 1.9e). Once the Torr seal is dried, the membrane was removed to reveal an array of polypyrrole plugged tubes that contained the immobilized enzyme in their interior (Figure 1.9f). Placement of this electrode into a solution of H_2O_2 showed decomposition of the H_2O_2 to O_2 and H_2O, suggesting the polymer is porous to the biological analyte, H_2O_2.

In a related study by Contractor and coworkers [47] similar structures were produced but without the chemical polymerization step. The production of the structure used a polycarbonate membrane, where first a thin layer of Au was deposited over the top and bottom surfaces of the membrane (Figure 1.10a). Upon

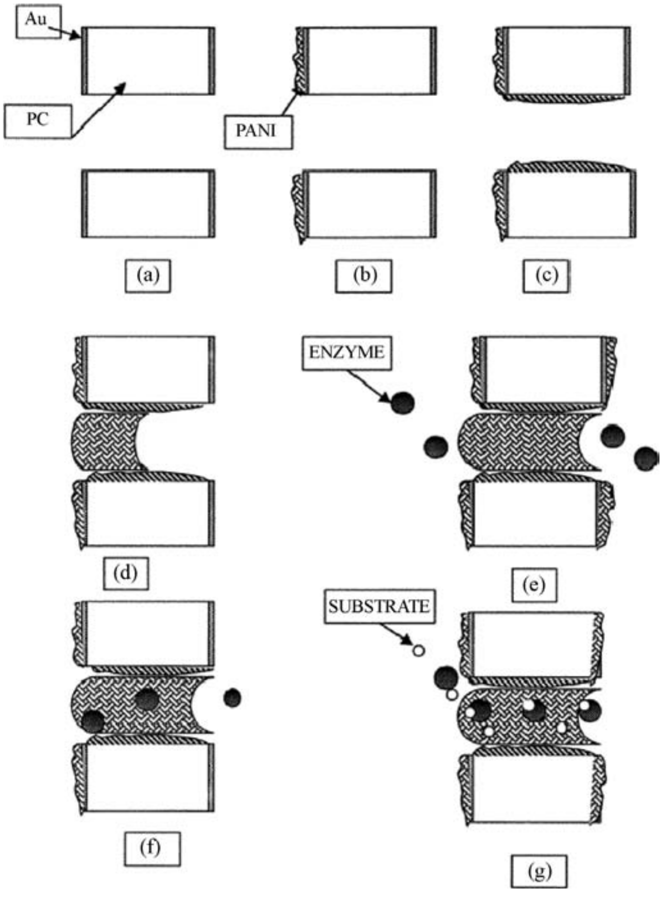

Figure 1.10 Production scheme for polyaniline nanotubules, loading of enzymes into the tubes and finally exposure to an analyte. (Reprinted with permission from Ref. [47]. ©1999 American Chemical Society.)

transferring the membrane to a 0.1 M aniline solution the Au-coated membrane was cycled between −0.2 and +0.8 V vs. SCE to produce polyaniline tubes (Figures 1.10b–d). Once this was completed the tubes were exposed to the enzyme and immobilized in a solution containing 0.1 M aniline (Figures 1.10e–g). The completed nanostructured electrode could be connected on the front and back (source and drain), creating a potential drop across the polymer film. This potential drop allowed for the controlled oxidation of the polyaniline, as a result amplifying the reduction of the polyaniline by the enzymatic reaction when reacting with H_2O_2. The produced nanostructured electrode showed excellent performance capabilities, sensitivity and response rate. These capabilities are a combination of three factors (1) small source and drain separation improving the transduction ability, (2) disorder in the polyaniline microstructure, resulting in large changes in conductivity on switching of the polyaniline and (3) a large loading of the enzyme, resulting in faster diffusion of substrate to the enzyme.

The differently produced conductive polymer structures described above all have enhanced conductivity, which can be employed in microelectronics [44] and as sensors using immobilized enzymes [46, 47]. Martin and coworkers used polarized infrared absorption spectroscopy to access the alignment of the polymer fibers on the outer surface of the nanotubes [48]. The study showed that the enhancement of the conductivity is due to the alignment of the polymer fibers on the outer surface of the tubes.

Production of nanostructured electrodes by templating is restricted not only to conducting polymers but also to a range of other materials including metals [35, 38, 41, 49], metal oxides [39], and semiconductors [40]. Although conductive polymers are easily templated, the electrical and optical properties exhibited by the nanostructuring are limited. This is in contrast to nanostructured metals, which have demonstrated unique optical and electronic properties [35, 50, 51]. This was demonstrated by Martin and coworkers using an alumina template to nanostructure gold tubules, by three techniques, electrochemical deposition [35], chemical reduction from solutions [51] and direct sputtering into the alumina membrane [41, 52].

The electrochemical technique entails the use of an alumina template, which has been surface modified with (2-cyanoethyl)triethoxysilane [50]. Before the electrodeposition of Au onto the surface, a 50-nm layer of Au was sputtered onto one end of the membrane (Figure 1.11a:A). This sputtering did not close the pores but converted the alumina template into an electrode. Following the sputter treatment the membrane was placed into a commercially available gold-electroplating solution (Orotemp 24, Technics) and a current density of 0.5–2.0 mA cm^{-2} was passed through the membrane (Figure 1.11a:B and C). After the growth of the tubes was completed the alumina membrane was dissolved to reveal the gold tubules (Figure 1.11a:D). Due to the modified membrane surface the growth of the gold that was being deposited does not favor the formation of fibers but tubes. Martin and coworkers have reported tube lengths as long as 2 μm can be produced by this method. The gold nanostructure within the alumina films showed very interesting optical properties. Due to the alumina membrane being transparent the color of the film produced is a direct result of the gold nanofibers produced within the

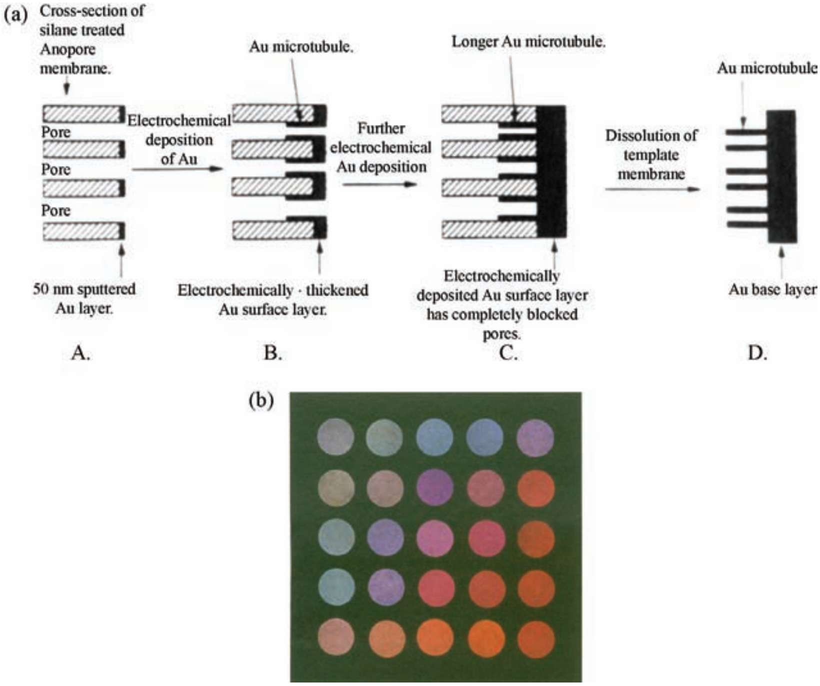

Figure 1.11 (a) Stepwise production of metallic nanotubules, where the internal surface area was modified with (2-cyanoethyl)triethoxysilane, followed by electrochemical deposition and removal of the alumina template. (Reprinted with permission from Ref. [50]. ©1991 American Chemical Society.) (b) Optical properties of gold nanotubes in alumina membranes at various sizes and lengths. (From [35] C.R. Martin, Science, 266, (1994), 1961–1966. Reprinted with permission from AAAS.)

membrane. Similar to free-standing gold nanoparticles where the color is size dependent (smaller-sized nanoparticles give a blue shift, larger size a red shift) the same can be said for the nanotubes within alumina membranes. Martin and coworkers have synthesized a range (20–150 nm diameter and various lengths) of gold nanotubes within alumina membranes (Figure 1.11b). This study demonstrated the color dependence on size, where the wider nanotubes showed a blue shift, but as the nanotubes became longer there is a red shift in the observed color.

In a related study, silver microtubules were produced by chemical deposition [38]. Similar to electrochemical deposition, the surface of the membrane must first be modified, not with a silane but with a catalyst such as Sn^{2+} ions. Initially, one side of the membrane is protected by tape (Figure 1.12b) and then the surface is activated with $SnCl_2$ (Figure 1.12c). The activated membrane was then placed into a solution of silver-plating solution (Figure 1.12d). This resulted in the deposition of silver over the activated surface; finally the alumina membrane was dissolved away.

Direct sputtering of the desired metal into an alumina membrane to give arrays of nanotubules has also been achieved. This was demonstrated by Guo *et al.* [41] where by controlling the sputter rate and pressure of the chamber it was possible to

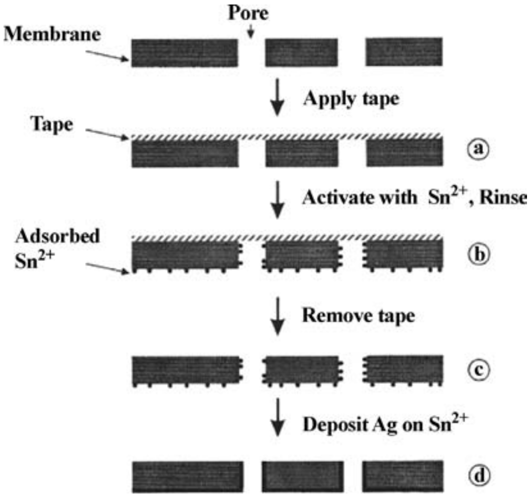

Figure 1.12 Stepwise synthesis scheme for chemical deposition of silver into an alumina membrane. (With kind permission from Springer Science + Business Media: [38]. A. Huczko, Applied Physic A, 70, (2000), 365–376 Figure 1.7 Reprinted with permission from The Materials Research Society.)

directly deposit metals into the porous structure of an alumina membrane. In this study the alumina membrane was placed at an angle, which was normal to the sputtering beam. Initially, the membrane was coated with a layer of gold, which was ~100 nm in thickness at a sputtering rate of 0.05 nm/s and a pressure of 8.7×10^{-5} Pa. Following this slow deposition the rate was increased to 0.2 nm/s at a pressure of 4.4×10^{-4} Pa (Figure 1.13a). This deposition closed the pores and deposited a further 200 nm of gold on top of the film (Figure 1.13b). The membrane was then dissolved away with sodium hydroxide leaving behind an array of nanotubules on a surface of Au (Figures 1.13c and d). This array of nanotubules exhibited an electroactive surface area of 2.4 times that of the geometric area. With an increase in the electroactive area, it becomes possible to apply these arrays to the area of sensors, electrochemical analysis and catalysis.

Other structures have been produced apart from metallic nanotubules. Nanorods have also been produced employing electrochemical deposition. Hong and coworkers [52] have used alumina membranes to produce gold nanorods, which have been shown to have high catalytic responses to biologically important analytes. In this study the nanostructured surface was produced by first etching a glass surface with argon plasma followed by an initial 50-nm sputtered layer of platinum and a further 100-nm layer of gold. The gold surface was then modified with the alkanethiol cysteamine. An alumina membrane was placed onto this cysteamine-modified surface and gold was then electrodeposited. Upon the removal of the alumina membrane in sodium hydroxide, a nanostructured electrode of gold nanotubes was produced. The nanostructured electrode was demonstrated to have a 4.6 times higher electroactive surface area than that of the unmodified, flat gold electrode. Apart from

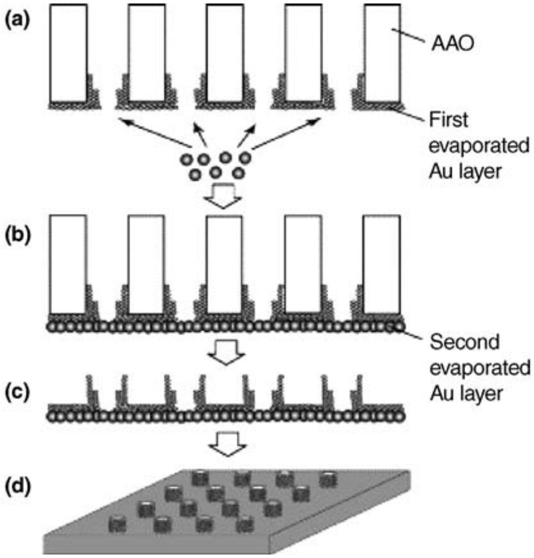

Figure 1.13 Stepwise synthesis of direct gold sputtering onto alumina membrane to produce nanostructures. (Reprinted with permission from Ref. [41]. ©2005 Elsevier.)

the increased surface area, the nanostructured electrode also exhibited catalytic characteristics, allowing for the electrode to be used as an enzyme-free sensor for glucose (oxidation begins at 0.1 V vs. Ag|AgCl for bare electrodes and −0.25 V vs. Ag|AgCl for nanostructured electrodes), H_2O_2 (reduction commences at −0.26 V vs. Ag|AgCl on nanostructured electrodes and −0.61 V vs. Ag|AgCl for flat electrodes) or O_2 (−0.06 V vs. Ag|AgCl on a nanostructured electrode). The porous structure, in combination with the catalytic response demonstrated by the electrodes, allows for the discrimination of glucose from other interferring agents, ascorbic acid, uric acid and acetamidophenol.

Membrane templates have been used extensively to create other high surface area structures. In recent years the application of polycarbonates and alumina membranes has been used to template electrodes for batteries [39] and capacitor devices [40]. For example, Sides and Martin have used membranes to produce V_2O_5 nanofibers for enhanced performance of Li-ion batteries in low temperatures. The production of the nanostructured film entails the use of a polycarbonate membrane. This polycarbonate membrane was placed over the top of a metal electrode, and then a solution of the V_2O_5 precursor tri-isopropoxyvanadium (TIVO) filled the pores. The TIVO was hydrolyzed to V_2O_5, excess V_2O_5 was removed simply by wiping with a cotton swab and finally the nanostructured electrode was place in an O_2 plasma for 2 h to remove the polycarbonate template. The nanostructured V_2O_5 electrode surface showed much better low-temperature performance, which was most evident at −20 °C. Martin and coworkers [39] suggest that the enhanced performance at low temperatures is due to a decrease in diffusion coefficient within the electrode nanostructure.

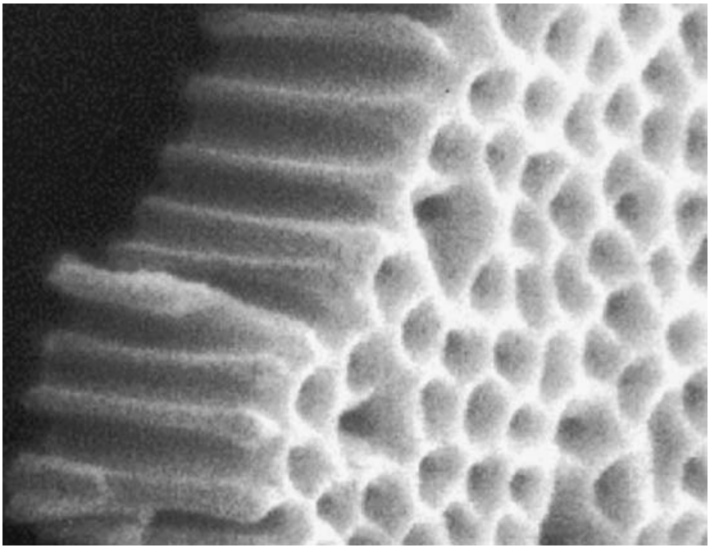

Figure 1.14 SEM image of honeycomb-structured alumina onto a carbon electrode before O_2 plasma exposure. (Reprinted with permission from Ref. [40]. ©2003 The Electrochemical Society.)

Martin and coworkers [40] have also employed alumina membranes in the production of high surface area carbon electrodes in the shape of honeycomb structures for capacitors. In this study the electrode was produced by the use of alumina membranes. First, the pores of the membrane were widened with an Ar plasma. After this etching, the alumina membrane was placed over the top of a carbon electrode (Figure 1.14). This assembly was then placed into a plasma mixture of O_2 and Ar and was exposed for 2 min. During this time the O_2 plasma propagated through the alumina membrane to the carbon film located at the bottom. This plasma etching produced a structure on the carbon electrode that mimicked the alumina membrane used. This electrode was tested in terms of discharge rate and capacity. Martin and coworkers [40] observed a low-rate discharge capacity of 325 mAh g^{-1}. However, at high rates, delivery of 50 times the capacity of an unmodified electrode was observed. This high rate of discharge is due to the increased surface area and is required for the application of high discharge devices, as is the case in electric car acceleration.

1.2.3
Templating using Lyotropic Liquid Crystals

Membrane templating is capable of producing a range of structures in various sizes. However, the degree of control is not at the molecular scale. An alternative templating method that has molecular-level control over the pore size and the ability to produce ordered arrays of pores is lyotropic liquid crystal templates [53]. Lyotropic liquid crystals are surfactant phases produced at high percentages of surfactant to solvent.

If the solvent is polar, the surfactant forms self-assembled structures with the headgroups remaining in contact with the polar solvent and the hydrophobic tails maintain their contact with each other and away from the solvent. Depending on the ratio of surfactant to solvent different periodic surfactant nanostructures are possible. For example, structures produced with a normal topology hexagonal (H_1) phase contain cylindrical self-assembled surfactant rods arranged in a close-packed hexagonal fashion. However, if the cubic phase (la3d) was used, interconnected cylindrical rods that form a gyroid lattice are produced [53]. Attard and coworkers [54] have demonstrated the ability to produce nanostructured metals such as Pt films using lyotropic liquid crystals as a templating technique. In this initial study lyotropic liquid crystals were used to template the production of nanostructured platinum films. The surfactant octaethyleneglycol monohexadecyl ether was first used to form a hexagonal mesophase, which was stable at room temperature. In the continuous water phase hexachloroplatinic acid was dissolved. A large piece (>3 mm) of a less-noble metal (Fe, Zn Mg) was placed into the liquid crystal, which reduced the platinum precursor. The mixture turned black when the reaction was left to stand at room temperature for 24 h. These particles were imaged using a TEM (Figure 1.15), which revealed that the particles have a close-packed hexagonal nanostructure consisting of pores, which have a diameter of 3 nm in size and a surface area of up to 23 $m^2 g^{-1}$, which is much greater in comparison with flat platinum films where the surface areas is 4.5 $m^2 g^{-1}$.

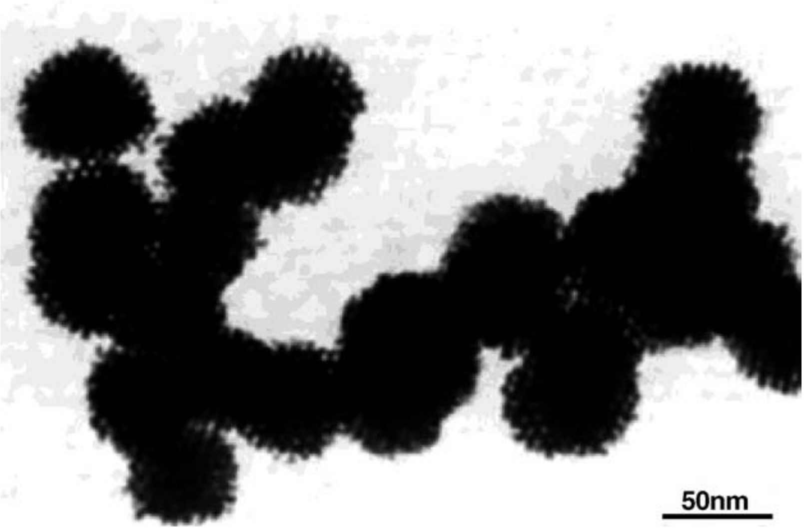

Figure 1.15 TEM image of Pt nanoparticles that have been produced by lyotropic liquid crystal templating. Porous structures can be seen and are spaced in an hexagonal array. (Reprinted with permission from Ref. [54]. ©1997 Wiley-VCH Verlag GmbH & Co. KGaA.)

Utilizing the ability of lyotropic liquid crystal as templates to produce high surface area and arrayed structures, Attard and coworkers [53] applied the concept to the production of nanostructured electrodes by electrodeposition. In this study the use of a nonionic surfactant octaethyleneglycol monohexadecyl ether was employed with hexachloroplatinic acid to produce a H_1-templated platinum structure on the surface of a flat gold electrode. The resulting electrodeposited structure had pore sizes of $\sim$2.5 nm, but using the same strategy and placing nonpolar solvents caused a swelling of the surfactant rods, thus increasing the pore size to 3.5 nm. This platinum film had a higher surface area of $20\,m^2\,g^{-1}$ compared to flat platinum films, which have a surface area of $4.5\,m^2\,g^{-1}$. As for electrochemical properties, due to the higher surface area a much higher capacitance of $5.2 \times 10^{-2}\,F\,cm^{-2}$ was also observed in comparison to flat platinum electrodes, which have a capacitance of $1.2 \times 10^{-2}\,F\,cm^{-2}$. Attard *et al.* [53] concluded that the production of metallic films by lyotropic liquid crystals showed enhanced electrochemical properties. Also, the ability to tune the size and spacing of the pores was demonstrated.

There has been a range of materials that have been templated by lyotropic liquid crystals other than platinum including polymers [55], Pd [56], Zn [57], Cd [57], Ni [58], Sn [59] and Co [60]. Apart from the range of materials that can be templated with lyotropic liquid crystal, the electrodes have also been proposed to find applications in fuel cells [53], batteries, hydrogen storage [56] and sensors [61]. These applications typically exploit the high surface area and or electrocatalytic properties of these electrodes. An example is templated palladium electrodes for hydrogen storage. Denuault and coworkers [56] demonstrated the use of a nanostructured palladium electrode for use in hydrogen adsorption. The synthesis of the electrode was once again achieved using electrodeposition of $(NH_4)_2PdCl_4$ from a H_1 phase liquid crystal where the surfactant was either octaethyleneglycol monohexadecyl ether or Brij 56 (46 weight %). The highly pure octaethyleneglycol monohexadecyl ether gave more ordered structures compared with the Brij 56 where the surfactant possessed a broader range of molecular weights. However, the majority of the structures produced in this study were made by using Brij 56 due to the cost being $\sim$88 times less than the ether and yet the same average properties were achieved. Once the lyotropic liquid crystal structure was in equilibrium, the palladium was electrodeposited onto a flat platinum electrode. This nanostructured electrode demonstrated a much larger electroactive surface area of 300 times, when compared to the unmodified electrodes. This study showed the adsorption of hydrogen gas was rapid due to the catalytic properties and large surface area. The electrode also showed an excellent potentiometric response over a pH range of 2–12.

The high surface areas of these electrodes make them ideal for electroanalytical applications where the high surface area is exploited to improve detection limits and/or detection range. Evans *et al.* [61] have demonstrated the production of platinum mesoporous electrodes and their application into the detection of H_2O_2. The produced electrode had an internal surface area that was $\sim$100 times higher than the original electrode. The study demonstrated a larger detection range of 0.02–100 mM H_2O_2 compared to the unstructured electrode, which had a range of 0.02–40 mM. This broader range can be ascribed to the larger surface area giving a larger number of surface sites for the hydrogen peroxide to adsorb and undergo oxidation. Apart from the enhanced surface area Evans *et al.* [61] also observed an improvement in the surface catalytic property.

1.2.4
Colloidal Templates

Nanoparticles have also been used as template nanostructured surfaces. The main advantage that nanoparticle templating has over membranes or lyotropic liquid crystals is simply the huge range of materials and sizes that can act as templates. The challenge, however, is to form ordered arrays of colloids on surfaces. This approach will not be discussed in detail here but to demonstrate the benefits of the strategy one example will be illustrated. In a study by Sun *et al.* [62] the production of a porous SnO_2 film by templating with a polystyrene (PS) nanoparticle monolayer was demonstrated. The production of the porous film from a nanoparticle template entailed firstly the spin coating of the polystyrene nanoparticles onto a flat glass substrate. Following the spin coating the monolayer film of PS nanoparticles were floated off the glass slide onto the top of a $SnCl_4$ solution. The film was then lifted off the surface of the $SnCl_4$ solution by a glass rod and heat treated. This deposition process was repeated 4 times to form the final electrode to detect ethanol vapors. Characterization under TEM of the surface revealed a network of pores arranged in a close-packed hexagonal array (Figure 1.16).

In normal air, the SnO_2 can adsorb oxygen species of O_2^-, O^- and O^{2-} on the surface, which increased the resistance of the SnO_2 nanostructured film [63]. Sensing of ethanol vapors was completed in a 300 °C environment. At this temperature the ethanol vapor reacts with the oxygen species on the surface of the SnO_2 and removes

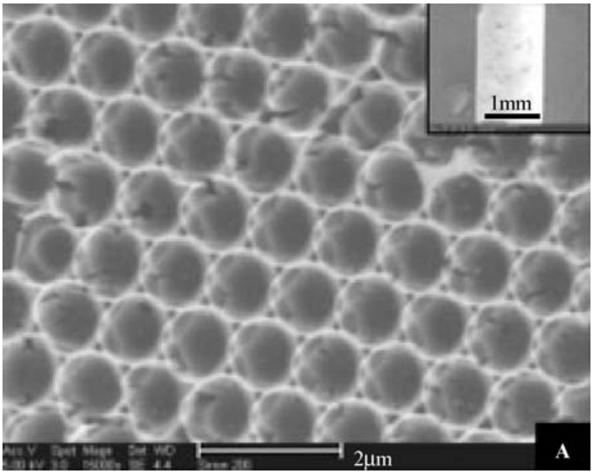

Figure 1.16 TEM images of SnO_2 ordered porous films on the external surface of a glass tube. (Reprinted with permission from Ref. [62]. © 2005 Wiley-VCH Verlag GmbH & Co. KGaA.)

the oxygen from the surface, and as a result decreases the resistance in the film. The production of porous films with smaller (200 nm) PS nanoparticles showed a 7-fold increase in sensitivity and additionally led to a response rate that was 5 times faster response when compared to a similar film produced by larger particles (1000 nm). This significant increase in sensing is attributed to the increased surface area.

1.3
Catalytic Properties

Recent rapid developments in nanoparticle preparation, surface modification and assembly have led to the widespread use of nanostructures immobilized on electrodes to catalyze electrochemical reactions [64]. While a diverse range of reactions have been shown to be electrocatalytically enhanced by nanostructured electrodes, this section will focus on reactions that involve the direct electron transfer between electrodes and redox-active molecules of biological relevance. Such enhancement of electron transfer has facilitated the development of biosensors for direct quantification of the redox-active biomolecule, with greater sensitivity, wider detection limits and decreased response times. The effective quantification of biological molecules using nanostructured electrodes requires that nanostructures attached to electrodes are able to electrochemically catalyze redox reactions of the biological molecules. Electrodes functionalized for this purpose can be broadly categorized into metallic-nanoparticle and carbon-nanotube structures. This section will highlight the key advances in the synthesis and performance of metallic-nanoparticle nanostructured electrodes for biological reactions.

The use of metallic nanostructures to enhance direct electrocatalysis of a biological molecule has developed in parallel to carbon nanotubes. Gold nanoparticles were the first example of this application owing to their ease of fabrication and well-known electrocatalytic and conductive properties. This was demonstrated by Jin and coworkers [65] who immobilized ~14-nm gold nanoparticles on cysteine-modified platinum electrodes coated with a thin film of Nafion. The electrode displayed excellent catalytic activity towards nitric oxide (NO), a physiological messenger and cytotoxic agent. Differential pulse voltammetry (DPV) showed large increases in current response for gold nanoparticle-modified electrodes along with cathodic shifts of oxidation peaks in comparison to bare platinum electrodes due to the catalytic oxidation of NO. The enhanced electrocatalytic ability of the nanostructured electrode was attributed to the gold nanoparticles acting as 'electron antennae', which efficiently funnel electrons between the electrode and electrolyte. The Au nanostructured electrodes also showed linear current response with increasing NO concentrations, selectivity to NO and detection limits of 5.0×10^{-8} mol/L NO, making the use of such electrodes for NO quantification very attractive.

A different example of gold-nanoparticle-modified electrodes for NO detection was shown by Caruso and coworkers [66]. In this work, the layer-by-layer technique was utilized as a means to immobilize oppositely charged layers of gold-nanoparticle-loaded poly(sodium 4-styrene-sulfonate) (PSS) and poly(allylamine hydrochloride)

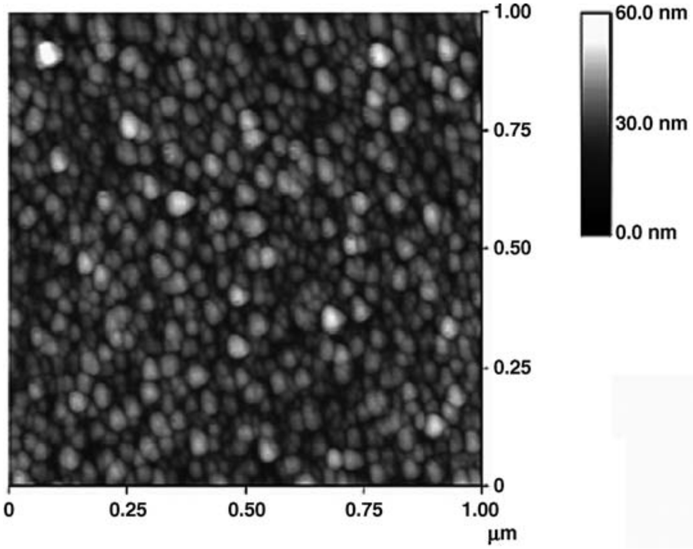

Figure 1.17 AFM image of a gold-nanoparticle-loaded polyelectrolytes film. (Reprinted with permission from Ref. [66]. ©2003 American Chemical Society.)

(PAH) (Figure 1.17) onto indium tin oxide (ITO) electrodes. This approach allowed for fine control of the amount of Au nanoparticles bound on the electrode surface. The system was again applied to the detection of NO using sodium nitrite ($NaNO_2$) as the precursor of NO and it was shown that the sensitivity of the electrode could be improved by increasing the gold nanoparticle content through the deposition of more polyelectrolyte layers.

The use of organic molecules or polymers to assist in binding nanoparticles to electrodes was highlighted as possibly having adverse effects on electrode catalytic reactivity and conductivity [67]. The influence of the organic binding molecules on the conductivity of nanoparticle-modified electrodes is clearly demonstrated for nanoparticle resistance sensors discussed in Section 1.2.1 above. With this in mind, Oyama and coworkers [68] attempted to reduce the interference of organic binders on electrode performance by using a two-step approach. This approach involved the initial immobilization of gold seed nanoparticles onto an ITO electrode followed by reductive growth of the seeded particles. Electrochemical impedance spectroscopy used in this study demonstrated convincingly that there was a significant enhancement of charge transfer for a gold nanoparticle/ITO electrode compared to a gold nanoparticle/ITO electrode with a 3-mercaptopropyltrimethoxysilane (MPTMS) linker. To show the biological applicability of this new approach, Oyama and coworkers [69] tested the electrocatalytic performance of a gold nanoparticle/ITO electrode for the direct electrochemical detection of a wide range of biological molecules including, paracetamol, uric acid, ascorbic acid, guanosine and the catecholamines epinephrine, norepinephrine and dopamine. In all the cases, comparison of cyclic voltammograms between gold nanoparticle/ITO electrodes and bare electrodes show a cathodic shift in the oxidation peaks for these biomolecules as well as an enhancement of peak current, both of which provide evidence of the electrocatalytic properties of gold nanostructures on electrodes. Selectivity of the electrode in the presence of interfering molecules, however, was sometimes found to be an issue for these gold nanoparticle/ITO electrodes [69].

Further development of the use of gold nanostructures to enhance biological electrocatalysis involved the use of different polymer binders on the surface to enhance selectivity of the electrodes. One such study by Lin and coworkers [70] used overoxidized polypyrrole (PPyox) to immobilize gold nanoclusters onto a glassy-carbon electrode (GCE), for the simultaneous quantification of epinephrine and uric acid in the presence of ascorbic acid. The PPyox in this case acted as a molecular sieve and allowed for the resolution of three distinct peaks for each of the analytes, which was not previously possible. In another study, poly(3,4-ethylenedioxythiophene)–poly(styrene sulfonic acid), (PEDOT–PSS) was spin coated onto an ITO electrode followed by the electrochemical deposition of gold nanoparticles into the polymer matrix for NADH oxidation [71]. The use of PEDOT-PSS is attractive because it easily forms thin films through many conventional techniques. In this study, Lee and coworkers show that the gold nanoparticle/PEDOT-PSS-modified ITO electrodes displayed high selectivity and sensitivity for NADH, making these nanostructured electrodes particularly attractive for NADH-sensing applications as well as in those that use NADH as a cofactor for enzymatic reaction.

A novel extension of utilizing gold nanostructures for electrocatalysis was the demonstration by Yu and coworkers [72] of electrocatalytic gold nanowires (Figure 1.18). The carbon-nanotube-inspired gold nanowires were synthesized through templated electrodeposition. The gold nanowires were then dispersed in a chitosan matrix and deposited onto a GCE (Figure 1.18). The gold nanowire electrode was found to provide excellent electrochemical response and also was found

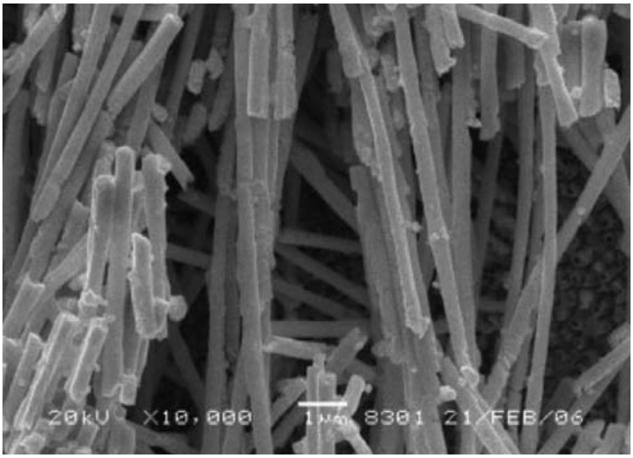

Figure 1.18 SEM image of the electrodeposited gold nanowires in a chitosan matrix. (Reprinted with permission from Ref. [72]. ©2007 Elsevier.)

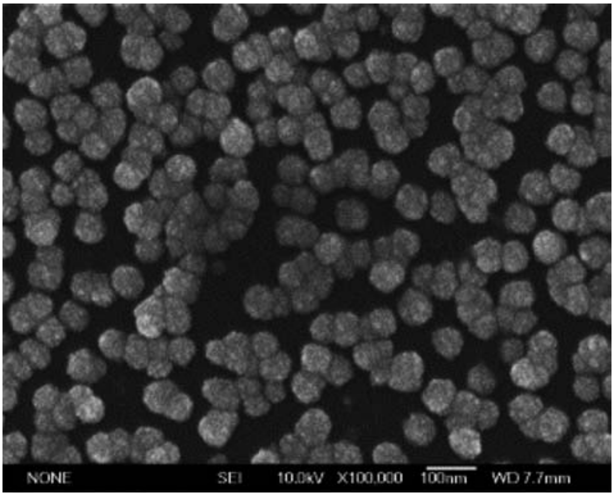

Figure 1.19 SEM image of the Pt/Fe(III) cooperative composites immobilized on a Nafion-coated GCE. (Reprinted with permission from Ref. [74]. ©2004 Elsevier.)

to be 30 times more sensitive to H_2O_2 than a conventional gold electrode. These enhancements were attributed to the higher effective surface area resulting from the immobilization of the gold nanowire structures on the electrode as well as their unique electrical properties and high conductivity.

Other metallic materials that have been used to produce nanostructured electrodes for biological electrocatalysis include platinum, platinum/iron composites and copper [73–75]. The nanostructured electrodes in these studies were produced either by electrodeposition of nanoparticles onto Nafion-modified electrode surfaces, [73, 74] or by covalent binding using MPTMS as a linker molecule [75]. Lin and coworkers showed that the use of platinum/Fe(III) nanoparticles on a Nafion-coated GCE could be used for the selective detection of NO (Figure 1.19), while Selvaraju and Ramaraj immobilized platinum nanoparticles on a Nafion-coated GCE for the detection of dopamine and serotonin. As in the case of gold nanostructured electrodes, the platinum nanostructures enhanced the catalytic and conductive properties of the electrodes by acting as ‘electron antennae’, while the Nafion coating acts as an ion-selective membrane, giving rise to the enhanced selectivity. It should be noted, however, that the polymeric coatings result in a reduced electrocatalytic response when compared to nanostructured electrodes without these coatings. This makes the decision to use such coatings a tradeoff between electrocatalytic ability and selectivity of the electrode. The electrocatalytic performance of copper nanoparticles immobilized on ITO electrodes was also studied for NO detection by Wang and coworkers [75]. They found that copper nanoparticles showed an enhanced electrocatalytic response to NO and displayed a wider linear detection range when compared to the gold nanoparticle/polyelectrolyte films synthesized by Caruso and coworkers [66]. The selectivity of the nanostructured electrode was not explored, however, and this remains an issue for electrodes that do not have chemoselective polymer coatings.

1.4
Exploiting Nanoscale Control to Interface Electrodes with Biomolecules

As discussed above nanomaterials can provide electrocatalytic properties. However, one unique property that can be achieved by nanostructuring electrodes with conducting elements that are of the order of just a few nanometers or less is the opportunity to perform electrochemistry in confined spaces. Such a possibility is particularly attractive for interfacing electrodes with biomolecules. Interfacing electrodes with biomolecules is important for biosensing, biofuel cells and other bioelectronic devices [13, 76–78]. In the case of both biosensing with redox enzymes and the employment of redox enzymes in biofuel cells one of the main challenges is electronic communication with the biomolecules. It is this process that is the limiting factor in the performance of both types of devices. This is perhaps most ably demonstrated with the glucose biosensor where the enzyme glucose oxidase is interfaced with an electrode. To allow transduction in such enzyme electrodes, electrons are shuttled between the enzyme and the electrode by freely diffusing redox molecules. The need for this freely diffusing molecule is not only the rate-limiting step but is also the source of many of the problems these devices face with regards to reproducibility and interferences [79]. As a consequence, there is a considerable research effort motivated towards achieving direct electron transfer to proteins [80–83]. The main challenge in achieving direct electron transfer to proteins is that in most proteins the redox-active center is located deep within the redox protein [84]. For example, in the case of glucose oxidase the redox-active center, flavin adenine dinucleotide, is located about 20 Å from the surface of the glycoprotein [85]. Such distances are too far for appreciable electron transfer to occur. Two possible strategies for 'wiring' redox proteins to overcome this distance problem are to either (1) nanostructure electrodes with nanomaterials that are sufficiently small that they can penetrate the proteins and reduce the distance electrons must tunnel to the electrode or (2) nanostructure electrodes with organic molecules that can plug into the proteins and serve as conduits for electron transfer [86]. We will discuss these two strategies in turn.

1.4.1
Plugging Nanomaterials into Proteins – Nanoparticles

The modification of electrodes with nanoparticles followed by the attachment of redox enzymes is one approach to nanostructuring electrodes that has been successful at achieving direct electron transfer to enzymes. Perhaps the most stunning example of this approach is to use nanoparticles to wire into glucose oxidase, as has been achieved by Willner and coworkers [87]. In this work, a gold electrode was modified with a dithiol self-assembled monolayer such that one thiol attached to the gold electrode and the other to gold nanoparticles, which were 1.4 nm in diameter. Active glucose-oxidase-modified gold nanoparticles were produced in one of two ways (Figure 1.20). In the first the redox-active center of glucose oxidase, flavin adenine dinucleotide (FAD), was immobilized onto a SAM-modified

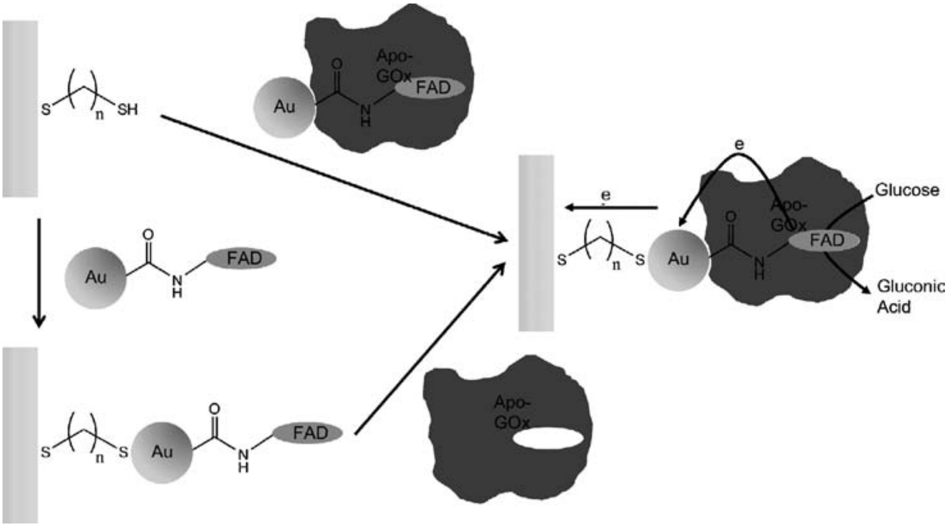

Figure 1.20 Assembly of Au-nanoparticle-reconstituted GOx electrode by adsorption of Au-nanoparticle-reconstituted GOx onto a dithiol monolayer and a stepwise build-up of the electrode by deposition of the Au-nanoparticle FAD onto the dithiol surface followed by the reconstruction of the apo-GOx.

nanoparticle that was subsequently attached to the electrode. The active enzyme was produced by reconstitution of the apo-enzyme around the FAD-modified nanoparticle attached to the electrode surface. In the second approach, the enzyme was reconstituted onto the FAD-modified nanoparticles in solution prior to attaching the nanoparticle to the electrode surface. Both strategies produced active enzyme and enzyme electrodes where direct electron transfer to glucose oxidase could be achieved with almost identical performance. The electrode performance itself was outstanding. The enzyme electrode responded to glucose in the absence of oxygen at a rate seven times the maximum rate observed in nature when oxygen recycles the enzyme. Furthermore, the rapid rate was also regarded as an explanation for the fact that there was no apparent influence of either oxygen (the natural cosubstrate for the enzyme) or ascorbic acid in the sample on the performance of the enzyme electrode. The mechanism by which direct electron transfer to the enzyme's redox-active center is not yet explained, although it is logical to assume the size of the nanoparticles are important. Within this paper the impact of nanoparticle size was not explored although it was stated in the paper that the nanoparticles must be of appropriate dimensions. The particles used in this paper were only 1.4 nm in diameter, which is significantly smaller than the dimensions of glucose oxidase of $5.5 \times 6 \times 8$ nm [85]. Thus, it seems possible that the nanoparticles allow the refolding of the enzyme into its native configuration and the covalent link between the nanoparticle and the active center allows appreciable electron transfer to occur [88].

What the Willner study highlights is the enormous possibilities of connecting electronic elements to proteins using nanoparticles. In particular, the absence of interferences from oxygen and ascorbic acid with this enzyme electrode provides strong support for the notion that efficient direct electron transfer to enzymes such as glucose oxidase could solve many of the problems associated with diffusing redox species shuttling electrons between the enzyme and the electrode. Other workers have also demonstrated fast electron transfer to enzymes using nanoparticle assemblies but typically these electrodes have employed enzymes with redox-active centers close to the exterior of the protein. As far back as 1996, Natan and colleagues [89] modified tin oxide electrodes with gold colloids and showed direct electron transfer to cytochrome *c*. The tin oxide electrodes were modified with a self-assembled monolayer of (3-aminopropyl) trimethoxysilane, whereupon the colloids were exposed to the electrode and adsorbed via bonding between the amine and the particles. The electrochemistry of cytochrome *c* was explored at these electrodes with the most significant result being the demonstration of a size dependence of the electrochemistry; a phenomenon alluded to in the Willner work [87]. In a similar example, Liu *et al.* [90] have modified graphite electrodes with silver nanoparticles to enable rapid electron transfer to cytochrome *c*. In this example the pyrolytic graphite electrode was oxidized in permanganate. Cysteamine was then attached to the carboxylic acid functionalized surface via its amine. Silver nanoparticles of 11 nm in diameter were then attached to the thiol end of the electrode and cytochrome *c* absorbed onto this surface. The ability of nanoparticles to facilitate electron transfer over very long distances was shown by Ulstrup and coworkers [91] when they used 3 to 4-nm diameter gold-nanoparticle-modified gold electrodes to electrochemically interface with cytochrome *c*. They showed that enhanced rates of electron transfer were achieved but more significantly that electron transfer could proceed at an appreciable rate over distances of greater than 50 Å.

1.4.2
Plugging Nanomaterials into Proteins – Carbon Nanotubes

Carbon nanotubes have also been used to facilitate wiring of enzymes, again exploiting the small size of these nanomaterials as electrodes that can penetrate close to the active site of the enzymes. The first example of this strategy was by Guiseppi-Elie and coworkers [92] where carbon nanotubes were randomly dispersed onto a glassy-carbon electrode, whereupon glucose oxidase was adsorbed onto the electrode. With this very simple electrode construct direct electron transfer to the enzyme was achieved with a rate of electron transfer of $1.7\ s^{-1}$, which is significantly faster than that reported when immobilizing glucose oxidase onto a self-assembled monolayer modified gold electrode where a rate of $0.026\ s^{-1}$ has been reported [93]. The fast rate constant for electron transfer was attributed to the small size of the single-walled carbon nanotubes employed (typically only 1 nm in diameter [94]). It is noteworthy that an almost identical rate constant was reported by Zhao *et al.* [95] using nanotube-modified electrodes prepared in a very similar way.

Work on the nanostructuring of electrodes with carbon nanotubes by Gooding and coworkers [96, 97] has demonstrated that superior electrochemical performance can be achieved with carbon nanotubes that are vertically aligned compared with being randomly dispersed. Aligning carbon nanotubes can be achieved in one of two ways. The first method is by growing the nanotubes vertically off a surface [98–103]. This strategy, however, usually produces multiwalled carbon nanotubes that are possibly too large to penetrate enzymes, however, it is possible as single-walled carbon nanotubes (SWNTs) have been grown off a surface [104]. The other method is via self-assembly using strategies developed by Liu and coworkers [105–107] and extended by others [96, 108–112]. In this strategy, SWNTs are purified in concentrated acids that open the closed ends such that the they are terminated with carboxylic acid moieties [106]. The surface chemistry of the electrode surface is then tailored to allow the carboxylic acid moieties to bind to give aligned nanotubes. These aligned carbon nanotube arrays were first interfaced with enzymes by Gooding *et al.* [108]. In this case an array of perpendicularly oriented SWCNTs on a gold electrode was fabricated by covalently attaching carboxylic acid functionalized SWCNTs, generated by the oxidative scission of the carbon nanotubes, to a cysteamine monolayer-functionalized gold electrode. The enzyme microperoxidase MP-11 was attached to the distal ends of the SWCNTs. The efficiency of the nanotubes acting as molecular wires was determined by calculating the rate constant of heterogeneous electron transfer between the electrode and microperoxidase MP-11 attached to the ends of the SWCNTs. A variety of different length distributions were assembled onto the electrode to explore the distance dependence of electron transfer through these nanotube arrays. What the paper showed was that the length distribution of nanotubes assembled on the electrodes had very little impact on the apparent rate of electron transfer compared with transferring the electrons from the redox-active center to the nanotube; thus highlighting the efficiency of electron transfer through the nanotubes and hence that nanotubes can serve as nanoscale electrodes as described in Chapter 3. At the same time, using a similar strategy of CNTs aligned by self-assembly, Yu *et al.* [109] reported that quasireversible Fe^{3+}/Fe^{2+} voltammetry was observed for the iron heme enzymes, myoglobin and horseradish peroxidase.

An exciting extension of this idea of assembling enzymes onto the ends of carbon nanotube electrodes was to plug the electrodes inside proteins. This has been achieved by both Willner and coworkers [110] and by Liu *et al.* [113] with surprisingly similar results considering the complexity of the systems. In both cases plugging the nanotubes inside glucose oxidase was achieved by first covalently attaching the FAD cofactor carboxylic groups at the free ends of the aligned SWCNTs. Apo-glucose oxidase was then reconstituted around the FAD units linked to the ends of the standing SWCNTs, in a similar manner to that for interfacing nanoparticles with glucose oxidase, to give the active enzyme [110, 113]. Willner and coworkers measured the interfacial electron-transfer rate constants to be $83\,s^{-1}$, $42\,s^{-1}$, $19\,s^{-1}$, and $12\,s^{-1}$, for assemblies that include standing SWCNTs of mean length 25 nm, 50 nm, 100 nm, and 150 nm average length, respectively. Thus, the nanotube length did influence the electron-transfer rate between the FAD units and the electrode in this case.

The rate constants for electron transfer achieved by plugging the nanotubes into the proteins as described above are an order of magnitude or more greater than those reported by Guiseppi-Elie *et al.* [92] and Zhao *et al.* [95] when interfacing wild-type glucose oxidase with the randomly dispersed carbon nanotubes. Similarly, they are significantly faster than that reported by Liu *et al.* [113] where wild-type glucose oxidase was adsorbed onto aligned carbon-nanotube-modified electrodes. These studies therefore highlight the importance of plugging the nanotubes into the enzyme and forming a direct covalent link with the redox-active center of the protein. They also highlight the importance of the size of the nanoscale features on an electrode such that they can connect to the redox center of the protein without disrupting the ability of the protein to refold into an active form.

1.4.3
Plugging Nanomaterials into Proteins – Molecular Wires

The importance of forming a direct link between the redox center and the underlying electrode has been shown numerous times with organic monolayers by Willner and coworkers [114–117] where redox relays form a connection between a macroscopic electrode and FAD whereupon apo-glucose oxidase is assembled over the surface-bound redox-active center. The nanotube approach, however, makes the connection by using the nanotube essentially as a molecular wire. Gray and coworkers [118–120] have demonstrated excellent connectivity to the redox-active centers of enzymes using conjugated organic molecular wires. In the first example of this approach electrodes were modified with a self-assembled monolayer of rigid oligo(phenyl-ethynyl)-thiol molecular wires that contained diethylaniline at the distal end (Figure 1.21) [120]. Oligo (phenyl ethynyl) and related conjugated molecular wires have been shown to allow very rapid electron transport due to the extended conjugation of π-electron and the rigidity of the molecules [9, 121, 122]. The enzyme amino acid oxidase, another enzyme with flavin adenine dinucleotide (FAD) as the redox-active center, was adsorbed onto this interface and the electrochemistry of FAD in its natural position buried deep within the wild-type enzyme was investigated. Remarkably, a lower limit of the rate constant of electron transfer was $1000\,s^{-1}$, which is consistent with other electron-transfer studies through these types of molecules [121, 122] but unprecedented for electron transfer to redox enzymes. This incredibly rapid rate confirms that there is excellent electronic coupling between the FAD and the electrode despite the molecular wire being 22 Å long. This excellent electronic coupling is because the molecular wire is designed to bind directly to the redox-active center of the enzyme. The diethylaniline at the distal end of the molecular wire was chosen as it is a known inhibitor of amine oxidase. Thus, the binding of the diethylaniline terminus in the active site serves to direct the molecular wire close to the active site; hence enabling efficient electron transfer through the molecular wire between the electrode and FAD.

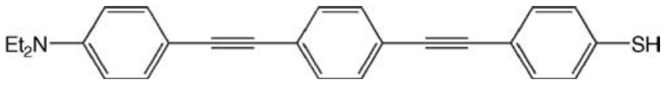

Figure 1.21 Molecular wire: rigid oligo(phenyl-ethynyl)-thiol molecular wires that contained diethylaniline at the distal end.

The interfacial design used in the study of Hess *et al.* [118] is not only important for interfacing electrodes with redox proteins but because it demonstrates three important recent advances for nanostructuring electrodes that offer unique properties. These three concepts are (1) using binding moieties on a monolayer surface to ensure intimate connectivity with biomolecules, (2) using rigid molecules that extends the capability of nanofabrication on surfaces by allowing coupling to the interior of nanoscale features and (3) the use of molecular wires in electrochemistry such that long-distance electron transfer can be exploited for a variety of applications. We will discuss each of these three features in turn.

1.4.3.1 **Nanostructuring Electrodes to Achieve Intimate Connectivity with Biomolecules**

Waldeck and coworkers [123, 124] had previously explored this concept using alkanethiol SAMs terminated with different moieties at the omega position and determined the best connectivity to cytochrome *c* was achieved with pyridine-terminated SAMs [125]. Armstrong and coworkers have also recently employed a similar strategy for interfacing graphite electrodes with blue copper oxidase (laccase) enzymes, where graphite electrodes are modified with an anthracene diazonium salt where the diazo group was on the 2 position. The reductive adsorption of aryl diazonium salts has been shown to produce very stable layers on carbon electrodes [126–128] and here will give anthracene-modified electrodes (Figure 1.22). The anthracene molecules were shown to bind the laccase enzymes tightly via the hydrophobic, π-electron-rich, binding pocket. The resultant laccase-modified electrode showed excellent performance, with the current density for the electrocatalytic reduction of oxygen at least twice as large as for laccase adsorbed onto unmodified graphite electrodes. Electroactivity was retained with repeated cycling, indicating the laccase was strongly attached to the electrode and the electrode demonstrated long-term stability (catalytic activity being 57% of the original current density after 8 weeks). An important aspect of this electrode modification was the orientation of the anthracene on the electrode. If the diazo moiety was on the 1 position, such that the anthracene was less able to protrude from the electrode surface, no catalytic enhancement was observed.

1.4.3.2 **Nanostructuring Electrodes using Rigid Molecules**

The correct orientation and rigidity of the anthracene is also related to the second important idea in the nanostructuring of the electrode interface used by

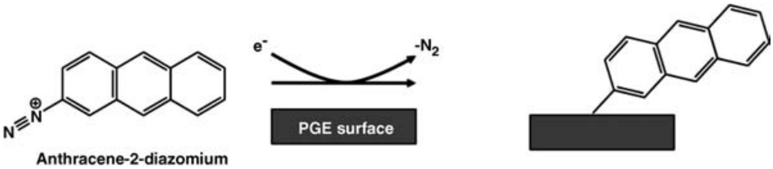

Figure 1.22 Anthracene-2-diazonium deposition by an electrochemical means. (Reproduced by permission of The Royal Society of Chemistry from [129].)

Hess *et al.* [118]; that is the use of rigid molecules to allow surface assembly onto electrodes that would not be possible with flexible molecules. When using SAMs for nanofabrication of a surface in a stepwise manner (that is sequentially adding additional components to the surface one after another rather than forming the entire molecular system and then assembling it) the common strategy is to use either a single component or a mixed SAM of multiple components. Mixed SAMs are used to allow lateral spacing of the coupling points such that their surface density can be controlled, which can be particularly important if the material to be assembled onto the surface has a larger footprint than the individual SAM forming molecules. The distance of the assembled species from the underlying electrode surface is defined by the thickness of the SAM. Because of the flexibility of the individual molecules in the SAM, close packing of molecules is required to define the distance. Hence, if one of the components is longer than the other species in the SAM then the distance from the surface is defined by the major component (Figure 1.23). That is, if the shorter component is the minor component then it will be buried within the SAM [130]. Alternatively, if the longer component is the minor component, its flexibility means that the distance from the surface is still defined by the shorter component and connectivity of the SAM to a nanoscale feature is still limited to the exterior of the material being coupled. Rigid molecules on the other hand can protrude from the interface as if they are molecular posts (Figure 1.23). Using such molecules the opportunity exists for connections to be made to the interior of nanomaterials (Figure 1.23).

In connecting the diethylaniline into the redox-active center of the amine oxidase in the study by Hess *et al.* [118] the connection is made possible for the connection to be made to the interior of the enzymes because the molecules were rigid. However, for this to occur requires sufficient spacing between the molecular wires on the

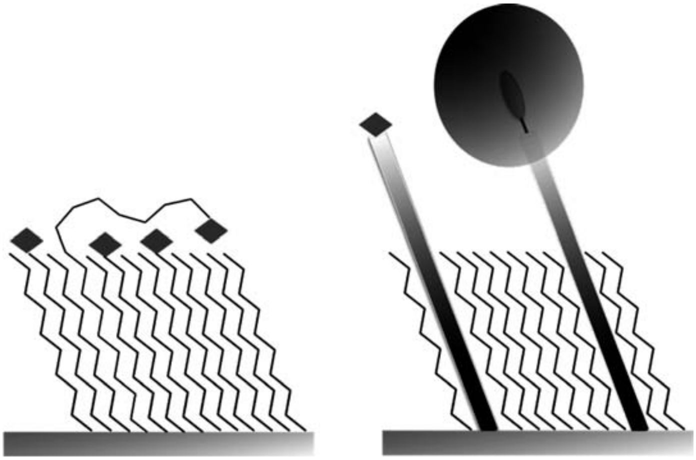

Figure 1.23 Scheme of long aliphatic molecules to project redox molecules above the environment (left) and the utilization of rigid molecules to probe into proteins and project redox molecules above the SAM surface (right).

electrode surface to ensure that the enzymes fit over the molecular wires. In the interfacial design by Hess *et al.* [118] the molecular wires have not been separated by a diluent but only 75% of the surface was reported to be covered by the molecular wires. The coverage of the enzyme was determined voltammetrically to be only 25% of a monolayer. This low coverage may in fact reflect the locations on the surface where there is sufficient space for the enzyme molecules to slide over the rigid molecular wires or alternatively the surface may be covered by a monolayer of enzyme but connectivity is not made to all enzymes.

The Gooding group has extended this concept of using rigid 'molecular posts' in the formation of hybrid enzyme–electrode constructs using both oligo (phenyl ethynyl) molecular wires [131, 132] and norbornylogous (NB) bridges [133, 134] as minor components in a mixed self-assembled monolayer where the major component was significantly shorter than the molecular post. In this way, the molecular posts stand proud above the plane of the SAM with sufficient space between the posts such that individual posts can connect to sites in the interior of large biomolecules. This strategy is illustrated in Figure 1.24 for achieving direct electron transfer to glucose oxidase [132] using a mixed layer of an oligo (phenyl ethynyl) molecular wire and a benzoic acid diluent, where both molecules on the surface were derived from aryl diazonium salts. The enzyme is allowed to adsorb onto the interface, whereupon it is anchored to the electrode using standard carbodiimide coupling. If this coupling procedure is performed then stable peaks in the cyclic voltammograms attributed to flavin adenine dinucleotide within the protein are observed with a half-wave potential of −443 mV versus Ag|AgCl. Without the

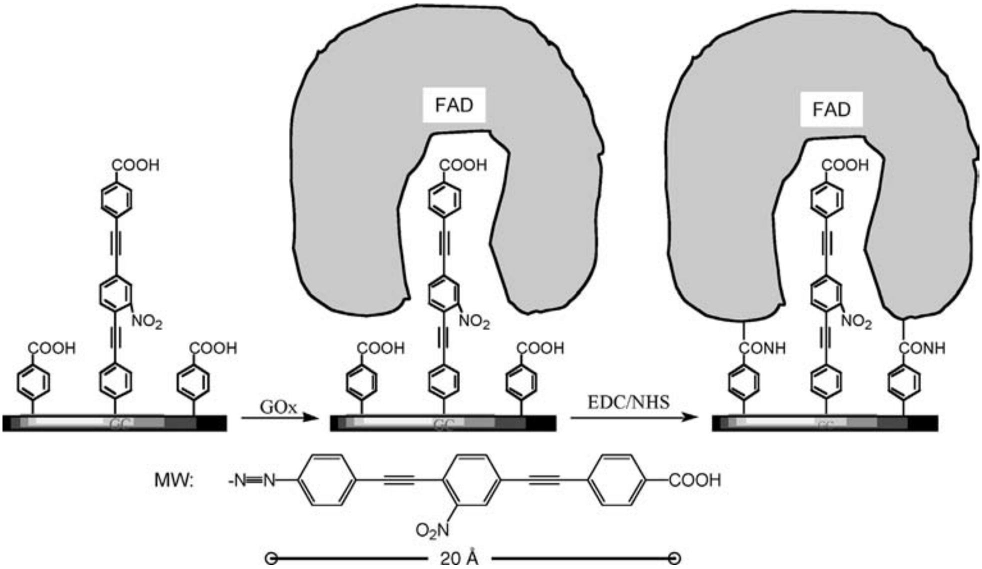

Figure 1.24 Scheme for the use of rigid molecular wires to plug into enzymes. (Reprinted with permission from Ref. [132]. ©2007 Elsevier.)

anchoring step the electrochemistry was observed to be unstable. The rate constant for electron transfer was calculated to be 78 s^{-1}, which is a massive enhancement in rate compared with the 1.6 s^{-1} reported in other studies on direct electron transfer to wild-type glucose oxidase using graphite electrodes [135] and carbon-nanotube-modified electrodes [92, 95]. This high rate is because the molecular wire is thought to penetrate close to the active site via the channel through which the glucose gets to the active site. The entrance of the active site is approximately 10 Å in diameter [85], which is sufficient to allow the molecular wire to at least partially penetrate the protein towards the active site without denaturing the enzyme. The important aspects of this study were firstly the enzyme was shown to be able to turn over glucose in the absence of oxygen or any other freely diffusing mediating species, which indicates the enzyme is being turned over by direct electron transfer, and secondly that enzyme turnover was occurring at −400 mV versus Ag|AgCl. This turnover potential is the most negative yet recorded for direct electron transfer to glucose oxidase, which has important consequences for fuel cells where the more cathodic the potential of the anode the greater the power output.

With regards to interfacial design, the molecular wires on the surface are diluted using a short carboxy phenyl derivative, which as mentioned above also serves to anchor the protein to the surface. Changing the ratio of the two components in solution was shown to be able to influence the amount of glucose oxidase interrogated electrochemically at the electrode surface. The optimal ratio in the assembly solution was 1 : 30 molecular wire:carboxy phenyl derivative. At this ratio there was a surface coverage of glucose oxidase, as determined from the voltammetric peaks, of 2.4 pmol cm^{-2}. This surface coverage is consistent with the coverage of GOx (2.6 pmol cm^{-2}) on 3-mm diameter GC electrodes determined by radioactive ^{125}I labeling [136] and this value is only just below the theoretical maximum coverage of a monolayer of GOx of between 2.6 and 3.8 pmol cm^{-2} [137] that was calculated from the crystallographic size of GOx of 5.5 × 7.0 × 8.0 nm [85]. Increasing the ratio of molecular wires results in a decrease in surface coverage that is attributed to the surface density of molecular wires crowding the interface such that there is insufficient spacing between wires to allow all the enzymes attached to the surface to fit over a wire and at lower ratios of molecular wires there are insufficient number of wires to get a complete monolayer of enzyme immobilized.

As a final aside in this section, it is important to note that carbon-nanotube-modified electrodes where the carbon nanotubes are vertically aligned, the nanotubes can essentially be exploited in the same basic way as molecular posts. That is, in essence, what was demonstrated in the examples by the Willner group and the Gooding group into plugging carbon nanotubes into glucose oxidase. In these cases the small size and the rigidity of the carbon nanotubes were crucial for the success of these enzyme-wiring strategies.

1.4.3.3 **The use of Molecular Wires in Electrochemistry such that Long-Distance Electron Transfer can be Exploited for a Variety of Applications**

The final aspect of the electrode design in the work by Hess *et al.* [118] is the use of molecular wires for modified electrodes for applications other than molecular

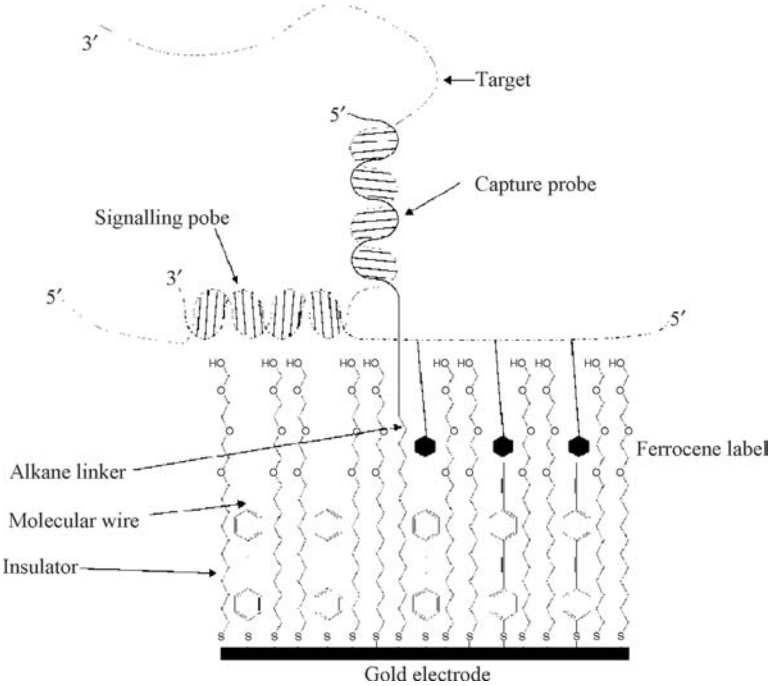

Figure 1.25 Scheme for the use of molecular wires to sense DNA hybridization where a capture DNA is used to attract the target DNA and then a signal DNA with ferrocene labels is hybridized to signal the hybridization event. (Reprinted from [138] J. Mol. Diagn. 2001 3: 74–84 with permission from the American Society for Investigative Pathology and the Association for Molecular Pathology.)

electronics. This was not the first use of molecular wires in such a way that the concept has been previously demonstrated in the Clinical Microsensors (CMS) DNA biosensor [138] (Figure 1.25). The self-assembled monolayer used to modify the electrode to give it selectivity for DNA comprised three components. These were (1) thiolated DNA molecules to selectively detect complementary strands of DNA in the sample, (2) a oligoethylene glycol (OEG) -terminated alkanethiol as an antifouling layer that resists nonspecific binding of DNA and proteins and (3) oligo (phenylethynyl) thiols as the molecular wires to allow electrochemical communications to the underlying electrode.

Liu and Gooding have adapted this type of interface for protein electrochemistry and to allow electrochemistry to be performed in biological media without electrode fouling [131]. As with the interface for probing direct electron transfer to glucose oxidase by the same workers the self-assembled monolayers were derived from aryl diazonium salts reductively desorbed onto a glassy-carbon electrode rather than alkanethiols on gold. The reason for using aryl diazonium salts [128, 139] is that they form much more stable layers on carbon and metal surfaces than the alkanethiol system [128, 140]. As with the CMS system the molecular wire allows electrochemical communication with the electrode and the OEG molecules resist nonspecific adsorption of proteins to the surface. The ability of the interface to ensure proteins are selectively attached to the molecular wires was shown using horseradish peroxidase (HRP), a protein to which direct electron transfer can easily be achieved. The electrochemistry of the heme center shows a close to ideal full width half-maximum (E_{FWHM}) for the oxidation peak. The close to ideal E_{FWHM} is good evidence that all the proteins being interrogated electrochemically are in the same environment, which essentially means the only enzymes that are wired to the electrode are those covalently attached to the molecular wires.

The crucial aspect of this interface is that the oligoethylene-glycol-terminated molecules passivate the electrode such that species in solution cannot access the underlying electrode. Hence, the oligophenylethynyl molecules are absolutely necessary for any electrochemical response. What the antifouling layer and molecular wire in combination does, however, is to bring the design of electrode interfaces into the realms of interfaces in optical detection [141] where interactions of proteins with the surface can be precisely controlled. This has not been previously possible because in most electrode constructs the electrode interface must be open and accessible to freely diffusing species such that electrochemical signals can be achieved. The drawback of allowing electroactive species to diffuse to the electrode surface is that if any other species in solution are electroactive at the same potential then they will become interferences. As this interface does not require access of diffusing species to the electrode surface the interface also serves the function of preventing these electroactive interferences reaching the electrode and solving this long-standing problem.

The monolayer construct in Figure 1.24 has already been shown to have advantages for DNA biosensors [138], protein electrochemistry [131] and immunosensing [142] but its potential has yet to be touched for performing electrochemistry in complex biological media such as found in cell-culture media. The important features of this system for performing electrochemistry in complex media are the highly stable aryl diazonium salt SAMs, the protein resistance and restriction of electroactive interferences from accessing the electrode surface. The challenge is to configure the interface with a biorecognition molecule that can be attached to the molecular wire that will allow detection of an analyte of interest. This is the challenge we are now pursuing.

Liu *et al.* [140] have also used this interface for an electrochemical immunosensor for small molecules (Figure 1.26). In this sensor, one end of the molecular wire is attached to ferrocene dimethylamine with a covalent link formed between one of the amine groups on the ferrocene and the carboxyl group on the wire. To the other amine is attached the antibody-binding epitope for the antibody, in this proof-of-concept study the epitope is biotin. Electron transfer can be readily achieved to the ferrocene molecule but upon antibody binding to this interface, the electrochemical signal is dramatically reduced.

The immunosensor based on the modulation of electrochemical signals by protein binding can be used in two modes. The first is to detect the presence of antibodies in a

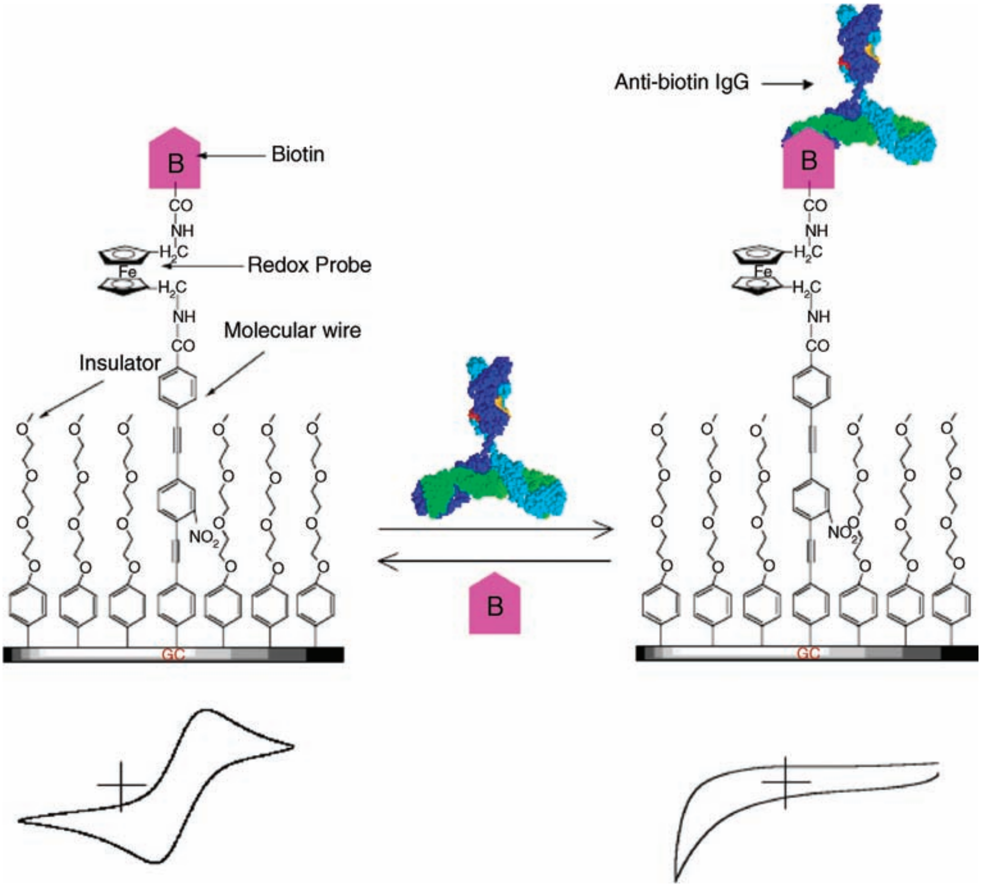

Figure 1.26 Scheme of immuno-biosensor developed by Liu and Gooding, exploiting the size of proteins and the space that a protein takes up to block ion access to the redox probe. (Reproduced by permission of The Royal Society of Chemistry from [142].)

sample. In this mode the biosensing reaction is going from left to right in Figure 1.26. In this case the sensing interface is comprised of the OEG component and the molecular wire with the ferrocene attached and an epitope for the target antibody. If the antibody is present in the sample it will selectively bind to the interface with a concomitant decrease in ferrocene current. In the second mode for detecting small molecules the antibody is actually bound to the epitope attached to the end of the molecular wire such that the attenuation of the electrochemistry has occurred. In the presence of the small molecular analyte in solution, a competition for the antibody is created and some of the surface-bound antibody will dissociate from the surface and an increase in current will be observed. Thus, this sensing system has the ability to detect both proteins and small molecules in a sample, using immunoreagents, without requiring the user to perform any tasks other than expose the sample to the sensor. The sensing concept is general for any small molecule so could be applied to analytes such as drugs or pollutants.

The interfacial design and the presence of the antifouling layer are absolutely vital for the success of this sensing concept. Evidence has been provided that the attenuation of the electrochemistry is due to restricting the access of ions to the ferrocene to balance the charge once the ferrocene is immersed in protein [134, 142]. As a consequence, any nonspecific adsorption of protein to the interface will also cause an attenuation in electrochemistry. Hence, the antifouling layer is required to ensure the attenuation of the electrochemistry associated with the presence of antibodies is due to a specific interaction with the binding epitope on the molecular wire rather than any nonspecific effects. The ability of this layer to resist nonspecific adsorption of proteins, as well as preventing electroactive species reaching the electrode, was demonstrated by Liu and Gooding [131] previously and is demonstrated in the current paper via controls that show there is little attenuation in the ferrocene electrochemistry if a different antibody is used or if the biotin epitope is absent from the interface.

1.5
Switchable Surfaces

1.5.1
Switching Properties of Monolayer Systems

SAMs containing two or more constituent molecules provide a practical experimental system with which to generate model systems to study fundamental aspects of the interactions of surfaces with biological systems. The primary advantage that SAMs (especially mixed SAMs) have over other methods of creating organic surfaces (polymer films, adsorbed proteins) is that the chemical composition of the surface can be modified in a deliberate manner. The other key advantage is the spatial control that SAMs afford. One of the most dramatic examples of this spatial control is a reversibly switching surface developed by Langer and coworkers [143, 144]. The basic idea is shown in Figure 1.27. A gold surface was modified with an alkanethiol SAM with a labile head group that had a footprint larger than the size of the alkyl chain such that the molecules could not close pack on the electrode surface. Removal of the labile headgroup left a hydrophilic mercaptohexadecanoic-acid-modified surface. The spacing between the molecules on the surface was such that each molecule occupied an area of about 0.67 nm^2, which was greater in comparison to a close-packed surface where each molecule occupies an area of 0.29 nm^2. The greater spacing between molecules was necessary to allow room for the mercaptohexadecanoic acid to bend towards the underlying gold surface. Application of an electrical potential was used to control the orientation of SAM molecules on a gold electrode surface, which can reversibly switch the surface between two conformations and hence two properties. A potential positive of the point of zero charge attracted the negatively charged

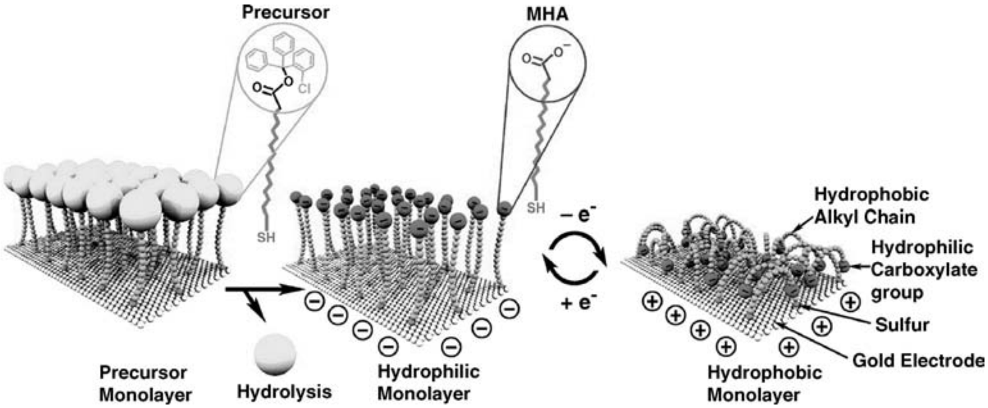

Figure 1.27 Scheme showing the use of charged head groups to 'switch' between hydrophilic and hydrophobic surfaces by changing the potential applied to the surface. (From [144] J. Lahann, S. Mitrogotri, T.N. Tran, H. Kaido, J. Sundaram, I.S. Choi, S. Hoffer, G.A. Somorjai and R. Langer, Science, 299, (2003), 371–374. Reprinted with permission from AAAS.)

carboxylic acid moieties at the distal end of the SAM to the electrode surface. The bending of the molecules towards the electrode resulted in the surface changing from presenting carboxylic acids to alkyl chains to the exterior, which caused a change in character of the electrode from hydrophilic to hydrophobic. This change in orientation altered the wettability of the surface almost instantaneously. A similar approach was explored by Willner and coworkers [145, 146] where the distal group on the SAM was a dipyridinium species. The essential difference was that the attraction and repulsion was not purely electrostatic as the distal moiety was also redox active. Hence, upon switching to a positive potential the distal species was also oxidized and when switching negatively the redox-active group was reduced. Thus, although still reversible switching, the Willner study is an example of redox as well as electrostatic switching.

Redox switching of surface properties has significant potential in cell biology as it affords the opportunity to conduct mechanistic studies of cell attachment and the dynamics of how changes to a surface influence cell structural organization and intracellular signaling. Such studies have important implications for biomaterial developments. A good example is the demonstration that switchable surfaces based on SAMs can be used in controlling cell migration [147]. This was achieved using SAMs, patterned by microcontact printing [148]. One set of locations in the SAM were terminated in methyl moieties ($HS(CH_2)_{17}CH_3$) forming hydrophobic patches to which cells adsorb. These hydrophobic patches were surrounded by SAM-forming molecules terminated in oligo(ethylene glycol) ($HS(CH_2)(OCH_2OCH_2)_3OH$) moieties that resist the adsorption of proteins and cells from solution. Having allowed the cells to attach on the hydrophobic regions, and spread to the limits of these regions, it is then possible to selectively remove the oligo(ethylene glycol) moieties instantly, so the cells can start to migrate across the surface. The switching is achieved by the

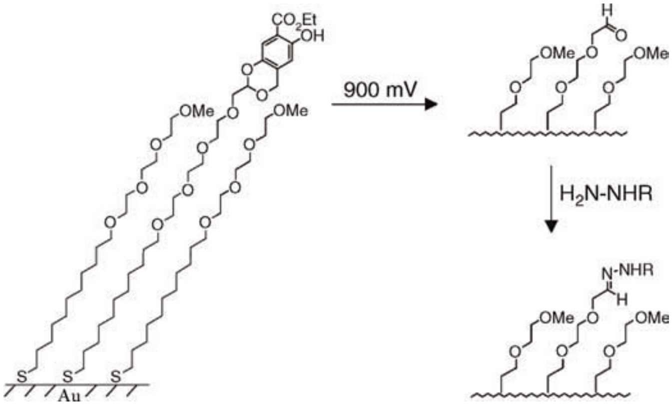

Figure 1.28 Scheme using potential cleavable molecules to switch the surface chemistry. (Reprinted with permission from Ref. [149]. © 2004 Wiley-VCH Verlag GmbH & Co. KGaA.)

application of a brief voltage pulse to the gold electrode at a potential that removes only the oligo(ethylene glycol) moieties. This is possible due to the inferior chain packing of the oligo(ethylene glycol) moieties relative to the $HS(CH_2)_{17}CH_3$. The inferior packing means that there are fewer van der Waals interactions between the alkyl chains. Consequently, the SAMs in these regions are less stable on the surface and can therefore be preferentially removed. As soon as the oligo(ethylene glycol) moieties are removed from the surface, proteins from the culture medium adsorb onto the gold surface, and generate a surface where cells can spread across. The ability to grow cells in patterns, and then to release them from these patterns with a simple electrochemical manipulation, provides the basis for new types of bioassays that make use of observations of cell motility.

More advanced electrochemical manipulation of cells on surfaces can be achieved with custom-synthesized switchable molecules. Mrksich and coworkers recently [149] demonstrated a SAM on gold with a 4-*H*-benzo[*d*][1,3] dioxinol terminal group (Figure 1.28). Subjecting the monolayer to a potential of 900 mV versus Ag|AgCl caused the oxidation of the aromatic ring of the 4-*H*-benzo[*d*][1,3]dioxinol with hydrolysis of the acetal to yield the aldehyde. The resulting aldehyde can be used for ligand immobilization, with corresponding protein capture or, alternatively, the surface can be used for studies of cell migration. The latter is demonstrated in the paper where surfaces were patterned with circular islands of hexadecanethiols to which fibronectin was adsorbed such that cells would adhere. The rest of the surface was modified with a mixed SAM as depicted in Figure 1.28 where the 4-*H*-benzo[d][1,3]dioxinal-terminated species was only 2%. The fibroblast cells used did not spread in these regions and hence circular patterns of cells were observed. After 4 h of culturing the cells, a potential of 900 mV versus Ag|AgCl was applied to the monolayer for 10 s. The cells began to migrate from these regions and after 10 h the circular patterns of cells were no longer evident.

Mrksich and coworkers [150] demonstrated even more sophisticated switchable surfaces where cells could be sequentially released and reattached. A SAM that

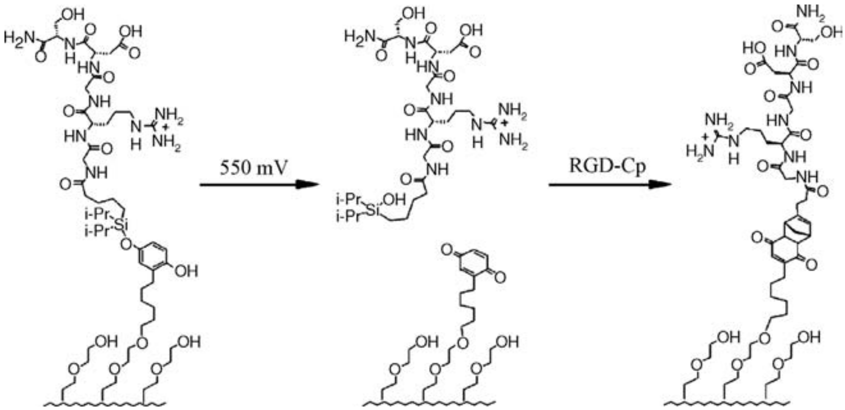

Figure 1.29 Scheme of sophisticated switchable surfaces where cells could be sequentially released and reattached. A self-assembled monolayer, using an O-silyl hydroquinone as the cleavable molecule, allows for the release and reattachment of cells onto a surface. (Reprinted with permission from Ref. [150]. ©2003 American Chemical Society.)

incorporated an O-silyl hydroquinone moiety was employed (Figure 1.29). To the distal end of the molecules a peptide ligand, Arg-Gly-Asp (known as RGD peptide) was attached. RGD is a ligand for integrin receptors, molecules on the cell surface that mediate cell adhesion. The O-silyl hydroquinone ether is electroactive and allows for the selective release of the peptide from the substrate. The release is triggered by applying a potential to the substrate of 550 mV versus Ag|AgCl, which oxidizes the hydroquinone to the corresponding benzoquinone with hydrolysis of the silyl ether. The resulting benzoquinone group undergoes a selective immobilization reaction with a diene-tagged peptide by way of a Diels–Alder reaction and therefore, provides the basis for a second dynamic event. The benzoquinone is redox active and can be reduced back to the hydroquinone, which prevents immobilization of the diene-tagged ligand. In this work, Yeo *et al.* demonstrated that surfaces could be switched from initially being adhesive to all cells, to release cells and then following addition of a new ligand to the surface, switching back to being adhesive to cells again.

These types of switchable electrode surfaces have been used to selectively pattern two different cell populations onto a surface [151] and additionally these surfaces can selectively release different cells at different applied potentials [152]. However, it is important to recognize that electrochemically switching a surface from inactive to conjugation and active to conjugation has been well explored with nitro-terminated aryl diazonium salts. In such studies, the application where very anodic potential resulted in a six-electron reduction to an amine [139], to which proteins could be attached [153–155]. The key difference is that the interaction of the biological medium with the surface is controlled by the presence of the antifouling layer. In many ways these electrode surfaces developed by Mrksich and coworkers [150–152, 156] are very similar to the antifouling surfaces with molecular wires discussed in Section 1.4.2 [131, 132, 138, 142]. In both cases the electrode is effectively passivated by the presence of an antifouling layer and electrochemical communication is achieved via electron transfer through the organic monolayer to a redox-active species attached to its surface. The next step in the development of these electrodes could in fact be the combination of these two concepts, where surfaces show electrochemically switchable properties, which control the response of cells and at the same time the surface could act as a sensing surface and monitor changes in the cells biochemically.

1.5.2
Control and Enhancement of Electrochemical Reactions using Magnetic Nanostructures on Electrodes

The electrochemically switchable surfaces discussed rely on either a change in conformation of molecules attached to an electrode surface, or a change in the actual attached moieties, to give switchable properties. Recent advances in magnetic nanoparticles, and the modification of these particle surfaces, offers a range of unique opportunities to switch the properties of electrochemical systems by using magnetic fields to achieve spatial control over the position of the functionalized magnetic structures. The aim of spatially manipulating these magnetic structures by altering the magnetic field location or orientation is to allow for the systematic control of reactions on electrode surfaces.

This concept in the form of ‘magneto-switching’ was pioneered by Willner and coworkers [132, 157], who demonstrated the ability to reversibly switch ‘ON’ and ‘OFF’ bioelectrocatalytic reactions by changing the position of an applied magnetic field to provide vertical spatial control over magnetic particles. In this work, a gold electrode modified with glucose oxidase was switched ‘ON’ by magnetically attracting 1-μm magnetite particles modified with N-(ferrocenylmethyl) aminohexanoic acid mediators to the electrode that enabled the mediation of the enzyme reaction. The application of a potential of $E^\circ = 0.31$ V vs. SCE caused the oxidation of the ferrocene to ferricinium ions, whereupon the ferricinium could oxidize the reduced glucose oxidase back to the catalytically active oxidized form [158]. (Figure 1.30a). The electrode was switched

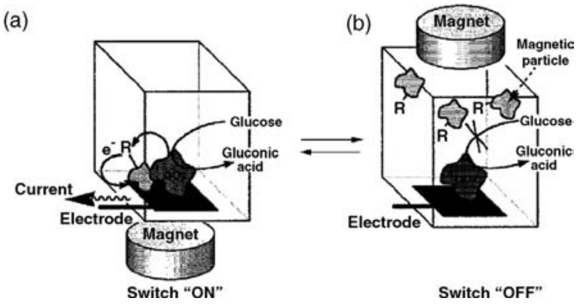

Figure 1.30 Magneto-switched bioelectrocatalyzed oxidation of glucose in the presence of relay-functionalized magnetic particles. (Reprinted with permission from Ref. [157]. ©2000 American Chemical Society.)

'OFF' by repositioning the magnet on top of the cell. This drew the ferrocene-modified magnetite particles away the electrode such that no ferricinium was produced and hence prevented the mediation of the enzyme reaction by the mediator-modified nanoparticles (Figure 1.30b). In the same paper, the concept of magneto-switching was also applied to the reduction of NO_3^- using N-methyl-N′-(dodecanoic acid)-4,4′-bipyridinium as the redox mediator in the presence of nitrate reductase.

Willner and colleagues [159] extended this idea further to demonstrate lateral spatial control of magnetic particles that enabled the magneto-switching of the electrochemical generation of light. In this work, aminonaphthoquinone-modified magnetite particles were introduced into an electrochemical cell that consisted of a glass slide, half of which was plated with gold, to give a working electrode with the other half being nonconducting glass. As before, the electrode reaction was switched 'ON' by positioning a magnet under the gold electrode, which attracted the magnetite particles onto the electrode. This initiated the electrochemical reduction of naphthoquinone under oxygen [160] at the applied potential region $E < -0.36$ V to produce electrogenerated H_2O_2. The H_2O_2 subsequently reacted with luminol in the presence of horseradish peroxidase to generate 3-amino-phthalate and light, ($\lambda_{em} = 425$ nm) (Figure 1.31a). The lateral repositioning of the magnetic particles onto the nonconducting glass plate was achieved by moving the magnet. This switched 'OFF' the electrochemical quinone reduction and hence the light emission (Figure 1.31B). This novel demonstration revealed the potential use of such systems as logic 'AND' gated elements where light emission occurs only in the presence of a magnetic field and with an appropriate potential step applied to the electrode.

Wang and coworkers [161] have extended the magneto-switching concept by demonstrating a number of switchable electrochemical reactions using biomolecules, metallic nanoparticles [162] or functionalized magnetic particles. In the case of biomolecule modification, Wang and Kawde [161] attached DNA oligonucleotides onto streptavidin-coated magnetic particles. They demonstrated that by magnetically attracting the DNA-modified particles onto a gold electrode and by applying a constant anodic current of $+5\,\mu A$ over a potential range of 0.6 to 1.2 V, a chronopotentiometric response corresponding to the oxidation of the guanine moiety ($E_p = 1.02$ V) was observed. The electrochemical reaction was

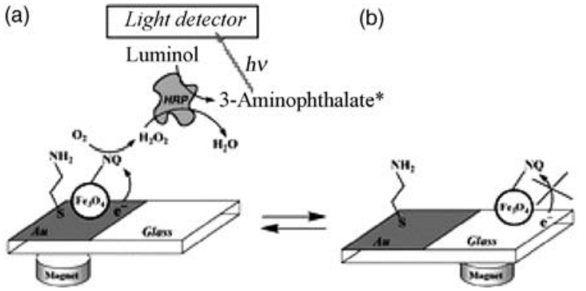

Figure 1.31 Magneto-triggered biochemiluminescence. (Reproduced by permission of The Royal Society of Chemistry from [159].)

switched 'OFF' by magnetically removing the DNA-modified particles. They also demonstrated lateral spatial control of the particles by moving particles between two electrodes placed side-by-side and showed the corresponding switching of chronopotentiometric signals. In this way it is possible to envisage applications where separate electrochemical reactions on the same particles are sequentially monitored at different electrodes. Wang and coworkers [162] also demonstrated the use of Pt/Ru-functionalized nickel particles for the magneto-triggered electrochemical oxidation of methanol and the reduction of oxygen. They showed the switchability of this system through the reversible appearance and disappearance of voltammetric peak currents on the cyclic voltammograms, corresponding to the placement and removal of modified nickel nanoparticles, with no apparent carry over. The switchable control was shown to facilitate the on-demand switching of direct-methanol fuel cells. Musameh and Wang [163] also extended the concept of magneto-switching to carbon nanotubes (CNTs) where they took advantage of the magnetic and catalytic properties of CNTs without the need for functionalized magnetic nanoparticles.

Willner and coworkers [164] further advanced the utility of magneto-switching by demonstrating the dual quantification of two substrates within a sample. In this work, a gold-coated glass electrode was modified with ferrocene, while magnetic particles were modified with the electron mediator pyrroloquinoline quinone (PQQ) and the cofactor aminoethyl-functionalized-NAD$^+$ (aNAD$^+$) as shown in Figure 1.32. Selective quantification of two substrates, glucose and lactate was reversibly accomplished by limiting the potential to a range that was appropriate to activate only one bioelectrocatalytic process. This idea exploits the difference in redox potentials of PQQ and ferrocene. In the case of lactate detection, this is switched on magnetically by bringing the nanoparticles with the cofactor for lactate (NAD$^+$) into contact with the electrode. A potential range of -0.36 V to $+0.15$ V was

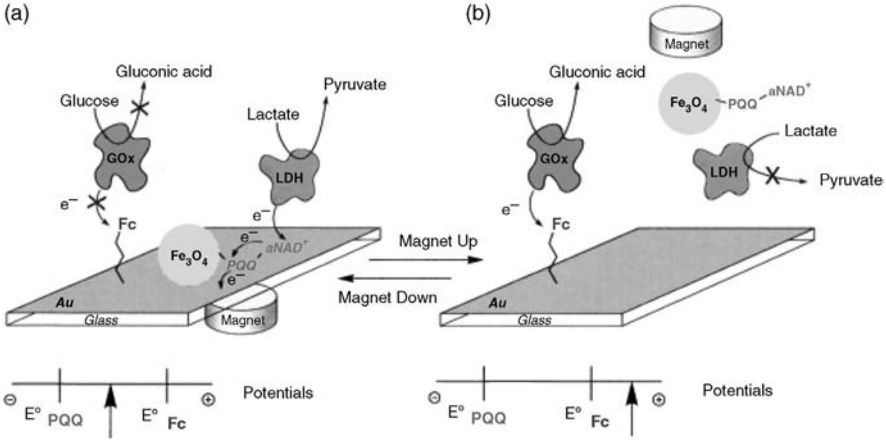

Figure 1.32 Magneto-switched dual biosensing of glucose and lactate. (Reprinted with permission from Ref. [164]. ©2002 Wiley-VCH Verlag GmbH & Co. KGaA.)

applied to oxidize PQQ that initiates electron hopping to the electrode when lactate reduces the NAD^+ cofactor to NADH in the presence of enzyme lactate dehydrogenase (LDH). The NADH is oxidized by PQQ, which results in the formation of $PQQH_2$ and the regeneration of NAD^+ (Figure 1.32a). The electrochemical oxidation of $PQQH_2$ results in the observation of an anodic current. Movement of the magnet to draw magnetic particles away from the electrode, lactate oxidation was blocked and the applied potential was set to allow for only the oxidation and resulting quantification of glucose in the system (Figure 1.32b). Similar to the first example, magneto-switching using ferrocene-modified magnetic nanoparticles are utilized to control the accessibility of mediators to the enzymes by movements of a magnet.

A further significant development in the field of magneto-switchable control over magnetic nanostructures on electrodes was the use of alkyl-chain-functionalized hydrophobic magnetic particles in a two-phase system to control and switch the hydrophobic or hydrophilic properties of the electrode surface [165]. This concept was unique because it allows for dual functions depending on how the concept is applied. The first function involves utilizing the hydrophobic magnetic nanoparticles for blocking of the electrode surface. The nanoparticles form a hydrophobic thin film on the surface that is not permeable for water-soluble components, thus blocking aqueous electrochemistry from occurring at the electrode. This was demonstrated by Willner and coworkers [165] who showed reversible magneto-switching of the electron transfer of ferrocene at gold electrodes corresponding to the attraction (off) and withdrawal (on) of hydrophobic nanoparticles to and from the electrode surface. The second function involves the altering of the electrochemical reaction occurring on the electrode surface from aqueous-type processes to an organic-phase-type electrochemistry enabling the electrochemical detection of substrates dissolved in organic solvents. Willner and coworkers [166] demonstrated this function by monitoring the cyclic voltammograms of the reduction of cumene hydroperoxide dissolved in toluene. In this work, cumene hydroperoxide together with hydrophobic undecanoate-capped magnetite particles were kept away from a microperoxidase-11 (MP) -modified gold electrode immersed in an aqueous environment (Figure 1.33a). Microperoxidase-11 had previously been found to act as an electrocatalyst for the reduction of organic peroxides in nonaqueous solutions [167]. Switching of the position of the applied magnetic field to below the electrode switched 'ON' the reaction by attracting the hydrophobic magnetic particles along with coadsorbed toluene to the electrode surface. In this way, cumene hydroperoxide dissolved in the toluene is also brought to the electrode surface, where it is reduced by microperoxidase-11 upon the application of a potential of $E^\circ = -0.7\,V$ (Figure 1.33b).

Willner and coworkers [168] demonstrated the applicability of this method for a range of applications including the magneto-switching of DNA hybridization and polymerization for programmed DNA chips, of photocatalytically activated reactions using CdS nanoparticles for optobioelectronic systems [169], and of quinone oxidation and reduction for 'write-read-erase' information storage systems [170].

An exciting advancement of the magneto-switching concept involved the demonstration by Wang and coworkers [171] of the ability to use magnetic fields to control electrochemical reactivity on electrodes in comparison to previous demonstrations

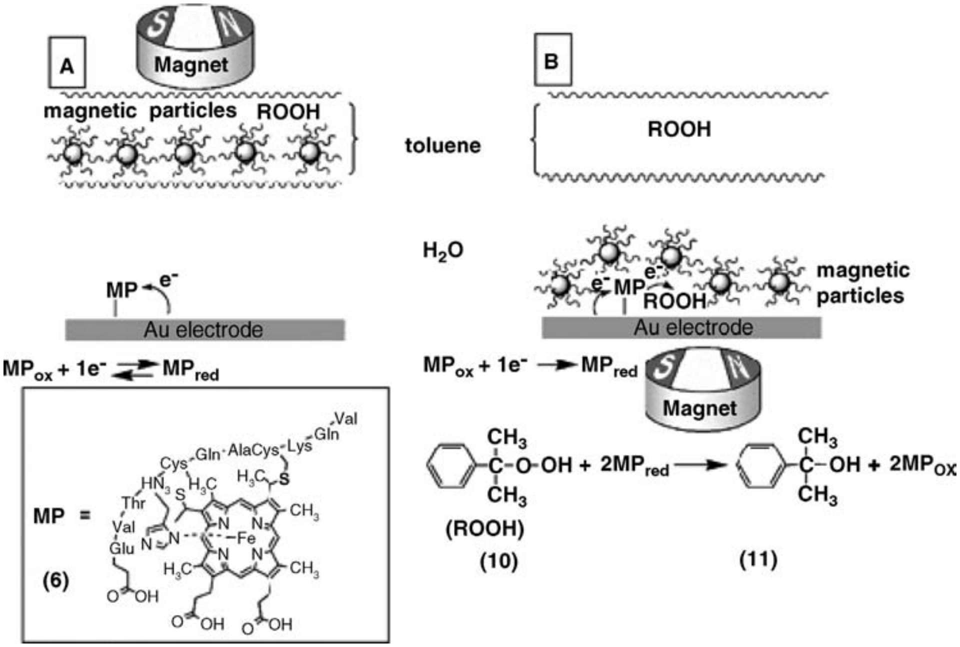

Figure 1.33 Magneto-controlled 'on"off' switching of microperoxidase-11-catalyzed reduction of cumene hydroperoxide in an organic environment. (Reprinted with permission from Ref. [166]. ©2000 American Chemical Society.)

that were limited to 'ON/OFF' switching. This breakthrough introduced the unique ability of modulating electrocatalytic activity by orienting catalytic nickel nanowires on electrodes at different angles. In this work, 6-μm nickel nanowires with diameters of 200 nm were synthesized via membrane template-directed electrodeposition for the oxidation of methanol and glucose. As nickel is known for its electrocatalytic action toward aliphatic alcohols, amino acids and carbohydrates [171], no further modification of the nanowires with mediators were required. Wang and coworkers demonstrated that electrochemical reactivity could be enhanced incrementally from a minimum when the nanowires were in the horizontal position on the carbon substrate (Figure 1.34a), to a maximum when the nanowires were in the vertical position (Figure 1.34b) by gradually changing the orientation of the applied magnetic field. This ability to tune electrode activity was attributed to changes in mass transport of glucose and methanol solutes due to tortuosity effects, as well as blocking effects that limit solute access to the portion of nickel surface facing the carbon electrodes.

The ability to selectively orientate nanowires on electrode surfaces was applied by Wang and coworkers [172] to provide on-demand protection for electrochemical sensors. In this study they showed that passivating the sensor electrode surfaces when measurements were not being taken could significantly increase the length of optimal performance of the sensor. Passivating the surface simply involved positioning of the magnetic field such that the alkanethiol-coated gold nanowires with a short

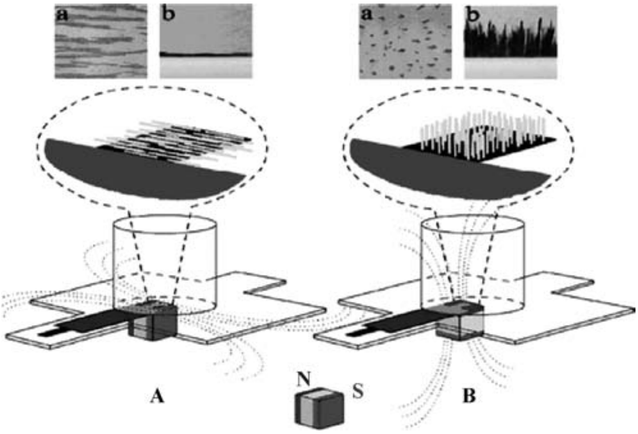

Figure 1.34 Experimental setup showing the nickel nanowires in a (A) horizontal and (B) vertical position depending on the magnetic field orientation. (Reprinted with permission from Ref. [171]. ©2006 American Chemical Society.)

magnetic nickel segment were oriented in the horizontal position (Figure 1.35). This protects the electrode surface from fouling by blocking the access of surface-active materials between measurements. The ability of the nanowires to reversibly change the operation of the sensor in response to an external stimulus led the authors to describe them as 'adaptive'. The same study also demonstrated that increasing both alkanethiol chain length and gold/nickel segment length ratio increased the

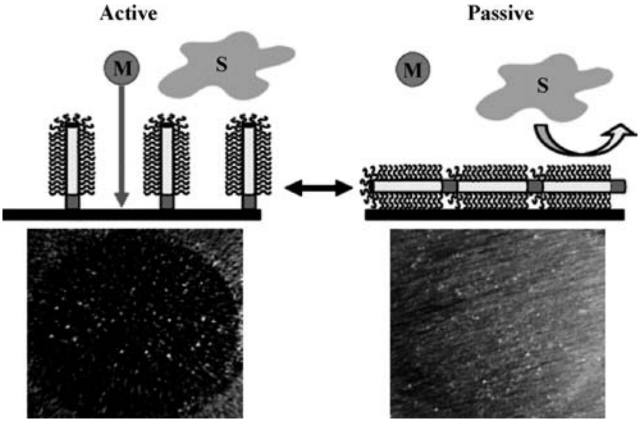

Figure 1.35 On-demand protection of an electrochemical sensor. Trace analysis of metal (M) analyte in the presence of surface active compounds (S) using the 'active' and 'passive' states. (Reprinted with permission from Ref. [172]. ©2006 American Chemical Society.)

electrode-fouling resistance. Attractive sensor behavior was also demonstrated with stripping voltammograms showing well-defined concentration dependence for the detection of cadmium and significantly enhanced the length of optimal performance when the electrode was in the ‘active’ state compared with an unmodified gold electrode.

Further development of adaptive nanowires was carried out by Wang and coworkers [173] to extend the use of these magnetic structures for control of biocatalytic processes. In this example, the previously reported two-segment gold/nickel nanowires were functionalized with glucose oxidase (GOx) to provide control of biocatalytic oxidation of glucose in combination with a ferrocene mediator bound onto a gold-coated glass electrode. In this case, magnetic-field-controlled horizontal orientation of the GOx-modified nanowires allows effective contact between the enzyme and mediator, resulting in activation of the biocatalytic reaction. Vertical reorientation of the nanowires leads to reduced contact between the enzyme and the mediator resulting in reduced glucose oxidation. Importantly, this study demonstrated for the first time, complete withdrawal of the nanowires from the electrode surface that blocked activation of GOx, hence switching ‘OFF’ the reaction.

The ability to modulate electrochemical reactivity and effectively switch ‘OFF’ the reaction was extended further by Wang and coworkers [174] to control, on-demand, the separation and detection processes in microfluidic devices. In this work, the catalytic nickel nanowires were placed, reoriented and removed on-demand at the exit of the separation channel of the microfluidic chip, offering unique possibilities for controlling externally, events inside and outside a microchannel.

Recent work in the area of using magnetic structures on electrodes to control electrochemical reactions has centered primarily on the search for more effective materials used for the applications mentioned in this section to improve performance. An example of such work includes that of Vasilyev *et al.* [175] who attempted to improve the work of Willner and coworkers on logic gates by using very small (17 ± 2 nm) and monodispered cobalt ferrite ($CoFe_2O_4$) nanoparticles that are important for achieving the aim of reducing the error read-out possibility of logic gates. Similarly, Zhai *et al.* [176] extend the ideas of Wang and coworkers by utilizing nanowires made from the assembly of magnetic iron-oxide particles to show tunability of the oxidation of glucose by glucose oxidase. Another example is the work of Jimenez *et al.* [175] who used magnetic fields to self-assemble conductive nanowires consisting of Au-shell/$CoFe_2O_4$ onto gold electrodes. In this work, these magnetic structures serve to increase the electrode surface area that results in up to a ~6.5 fold enhancement in electrochemical response for the ferrocene-mediated oxidation of glucose by glucose oxidase when compared to an unmodified bare gold electrode.

It is clear that there remain many possibilities for extending the concept of using magnetic nanostructures on electrodes to control and enhance electrochemical reactions. It can be envisaged that the coming years should see the improvement of existing applications along with the exciting emergence of new applications utilizing the concepts highlighted in this section.

1.6
Conclusions

Throughout this chapter we have described a range of different concepts from the literature where electrodes have been modified at the nanoscale to provide the electrode with unique capabilities. Throughout this chapter there has been emphasis on the properties relating to biological applications. In the simplest cases, this has been to increase the surface area for enhanced sensitivity or to provide electrocatalytic properties to the electrodes. However, nanostructuring electrodes have also enabled completely new concepts in electrochemistry to be explored, such as the interfacing of electrodes with proteins, having electrodes that are passivated from a sample solution such that electrochemical communication is only achieved through molecular wires, producing electrode surfaces with switchable properties or creating sensors where the spacing between conducting units is used to modulate the resistance of electrode layers.

Many of these unique properties are only possible because of the spatial control over the modification of the electrode and hence the emphasis throughout this chapter has been on control. However, our ability to structure electrodes at the nanoscale or even molecular level is really only in its infancy and so many new concepts will be revealed in the near future. To this point we have barely started considering vertically controlling the structure of electrodes at the molecular level and our ability to laterally structure electrodes with a high degree of control needs further development. With the latter in mind, a recent development by Buck and coworkers [177] is particularly important. In this work they showed, for the first time, strategies for patterning self-assembled monolayers using self-assembled supramolecular networks that are first assembled onto gold electrodes. What is unique about this work is that by placing electrodes modified with these networks into an alkanethiol solution for a short time enables the network to serve as a template for the alkanethiol deposition (that is the alkanethiol does not remove the network). In this way, patterns of alkanethiols can be produced, alternately copper patterning by this method was also demonstrated by the underpotential deposition of copper onto regions containing the alkanethiol but not the network. One cannot imagine what possibilities this new method of nanostructuring electrodes, nor many other new approaches, will bring, however, it is clear that developments will be rapid and exciting.

References

1 Martin, C.R. and Foss, C.A. Jr (1996) *Laboratory Techniques in Electroanalytical, Chemistry*.

2 Imisides, M.D., John, R., Riley, P.J. and Wallace, G.G. (1991) *Electroanalysis*, **3**, 879–889.

3 Wang, J. (1991) *Electroanalysis*, **3**, 255–259.

4 Malinauskas, A. (1999) *Synthetic Metals*, **107**, 75–83.

5 Situmorang, M., Gooding, J.J. and Hibbert, D.B. (1999) *Analytica Chimica Acta*, **394**, 211–223.

6 Markovic, N.M. and Ross, P.N. (2002) *Surface Science Reports*, **45**, 121–229.

7 Alexander, B.D., Kulesza, P.J., Rutkowska, L., Solarska, R. and Augustynski, J. (2008) *Journal of Materials Chemistry*, **18**, 2298–2303.

8 Mathiyarasu, J., Pathak, S.S. and Yegnaraman, V. (2006) *Corrosion Reviews*, **24**, 307–321.

9 Adams, D.M., Brus, L., Chidsey, C.E.D., Creager, S., Creutz, C., Kagan, C.R., Kamat, P.V., Lieberman, M., Lindsay, S., Marcus, R.A., Metzger, R.M., Michel-Beyerle, M.E., Miller, J.R., Newton, M.D., Rolison, D.R., Sankey, O., Schanze, K.S., Yardley, J. and Zhu, X.Y. (2003) *The Journal of Physical Chemistry B*, **107**, 6668–6697.

10 Ybarra, G., Moina, C., Florit, M.I. and Posadas, D. (2008) *Electrochimica Acta*, **53**, 3955–3959.

11 Haick, H. and Cahen, D. (2008) *Progress in Surface Science*, **83**, 217–261.

12 Mortimer, R.J. (1997) *Chemical Society Reviews*, **26**, 147–156.

13 Gooding, J.J., Mearns, F., Yang, W. and Liu, J. (2003) *Electroanalysis*, **15**, 81–96.

14 Love, J.C., Estroff, L.A., Kriebel, J.K., Nuzzo, R.G. and Whitesides, G.M. (2005) *Chemical Reviews*, **105**, 1103–1169.

15 Chen, D. and Li, J.H. (2006) *Surface Science Reports*, **61**, 445–463.

16 Cornell, B.A., Braach-Maksvytis, V.L.B., King, L.G., Osman, P.D.J., Raguse, B., Wieczorek, L. and Pace, R.J. (1997) *Nature*, **387**, 580–583.

17 Musick, M.D., Pena, D.J., Botsko, S.L., McEvoy, T.M., Richardson, J.N. and Natan, M.J. (1999) *Langmuir*, **15**, 844–850.

18 Patolsky, F., Gabriel, T. and Willner, I. (1999) *Journal of Electroanalytical Chemistry*, **479**, 69–73.

19 Freeman, R.G., Grabar, K.C., Allison, K.J., Bright, R.M., Davis, J.A., Guthrie, A.P., Hommer, M.B., Jackson, M.A., Smith, P.C., Walter, D.G. and Natan, M.J. (1995) *Science*, **267**, 1629–1632.

20 Blonder, R., Sheeney, L. and Willner, I. (1998) *Chemical Communications*, 1393–1394.

21 Liu, H., Tian, Y. and Xia, P. (2008) *Langmuir*, **24**, 6359–6366.

22 Terrill, R.H., Postlethwaite, T.A., Chen, C.-h., Poon, C.-D., Terzis, A., Chen, A., Hutchison, J.E., Clark, M.R., Wignall, G. *et al.* (1995) *Journal of the American Chemical Society*, **117**, 12537–12548.

23 Evans, S.D., Johnson, S.R., Cheng, Y.L. and Shen, T. (2000) *Journal of Materials Chemistry*, **10**, 183–188.

24 Krasteva, N., Besnard, I., Guse, B., Bauer, R.E., Muellen, K., Yasuda, A. and Vossmeyer, T. (2002) *Nano Letters*, **2**, 551–555.

25 Katz, E., Willner, I. and Wang, J. (2004) *Electroanalysis*, **16**, 19–44.

26 Zamborini, F.P., Leopold, M.C., Hicks, J.F., Kulesza, P.J., Malik, M.A. and Murray, R.W. (2002) *Journal of the American Chemical Society*, **124**, 8958–8964.

27 Raguse, B., Chow, E., Barton, C.S. and Wieczorek, L. (2007) *Analytical Chemistry*, **79**, 7333–7339.

28 Velev, O.D. and Kaler, E.W. (1999) *Langmuir*, **15**, 3693–3698.

29 Park, S.J., Taton, T.A. and Mirkin, C.A. (2002) *Science*, **295**, 1503–1506.

30 Zheng, G., Patolsky, F., Cui, Y., Wang, W.U. and Lieber, C.M. (2005) *Nature Biotechnology*, **23**, 1294–1301.

31 Patolsky, F., Zheng, G., Hayden, O., Lakadamyali, M., Zhuang, X. and Lieber, C.M. (2004) *Proceedings of the National Academy of Sciences of the United States of America*, **101**, 14017–14022.

32 Piner, R.D., Zhu, J., Zu, F., Hong, S. and Mirkin, C.A. (1999) *Science*, **283**, 661–663.

33 Basnar, B., Weizmann, Y., Cheglakov, Z. and Willner, I. (2006) *Advanced Materials*, **18**, 713–718.

34 Zayats, M., Baron, R., Popov, I. and Willner, I. (2005) *Nano Letters*, **5**, 21–25.

35 Martin, C.R. (1994) *Science*, **266**, 1961–1966.

36 Hulteen, J.C. and Matrin, C.R. (1997) *Journal of Materials Chemistry*, **7**, 1075–1087.

37 Yamada, K., Gasparac, R. and Martin, C.R. (2004) *Journal of the Electrochemical Society*, **151**, E14–E19.

38 Huczko, A. (2000) *Applied Physics A*, **70**, 365–376.

39 Sides, C.R. and Martin, C.R. (2005) *Advanced Materials*, **17**, 125–128.

40 Li, N., Mitchell, D.T., Lee, Y.-P. and Martin, C.R. (2003) *Journal of the Electrochemical Society*, **150**, A979–A984.

41 Guo, Y.-G., Zhang, H.-M., Hu, J.-S., Wan, L.-J. and Bai, C.-L. (2005) *Thin Solid Films*, **484**, 341–345.

42 AlMawlawi, D., Coombs, N. and Moskovits, M. (1991) *Journal of Applied Physics*, **70**, 4421–4425.

43 Foss, C.A. Jr, Hornyak, G.L., Stockert, J.A. and Martin, C.R. (1992) *The Journal of Physical Chemistry*, **96**, 7497–7499.

44 Van-Dyke, L.S. and Martin, C.R. (1990) *Langmuir*, **6**, 1118–1123.

45 Cai, Z. and Martin, C.R. (1989) *Journal of the American Chemical Society*, **111**, 4138–4139.

46 Parthasarathy, R.V. and Martin, C.R. (1994) *Nature*, **369**, 298–301.

47 Sukeerthi, S. and Contractor, A.Q. (1999) *Analytical Chemistry*, **71**, 2231–2236.

48 Liang, W. and Martin, C.R. (1990) *Journal of the American Chemical Society*, **112**, 9666–9668.

49 Menon, V.P. and Martin, C.R. (1995) *Analytical Chemistry*, **67**, 1920–1928.

50 Brumlik, C.J. and Martin, C.R. (1991) *Journal of the American Chemical Society*, **113**, 3174–3175.

51 Brumlik, C.J., Menon, V.P. and Martin, C.R. (1994) *Journal of Materials Research*, **9**, 1174–1183.

52 Shin, C., Shin, W. and Hong, H.-G. (2007) *Electrochimica Acta*, **53**, 720–728.

53 Attard, G.S., Bartlett, P.N., Coleman, N.R.B., Elliott, J.M., Owen, J.R. and Wang, J.H. (1997) *Science*, **278**, 838–840.

54 Attard, G.S., Goltner, C.G., Corker, J.M., Henke, S. and Templer, R.H. (1997) *Angewandte Chemie-International Edition*, **36**, 1315–1317.

55 Bender, F., Chilcott, T.C., Coster, H.G.L., Hibbert, D.B. and Gooding, J.J. (2007) *Electrochimica Acta*, **52**, 2640–2648.

56 Imokawa, T., Williams, K.-J. and Denuault, G. (2006) *Analytical Chemistry*, **78**, 265–271.

57 Bender, F., Mankelow, R.K., Hibbert, D.B. and Gooding, J.J. (2006) *Electroanalysis*, **18**, 1558–1563.

58 Nelson, P.A., Elliott, J.M., Attard, G.S. and Owen, J.R. (2002) *Chemistry of Materials*, **14**, 524.

59 Whitehead, A.H., Elliott, J.M., Owen, J.R. and Attard, G.S. (1999) *Chemical Communications*, 331–332.

60 Bartlett, P.N., Birkin, P.N., Ghanem, M.A., De Groot, P. and Sawicki, M. (2001) *Journal of the Electrochemical Society*, **148**, C119–C123.

61 Evans, S.A.G., Elliott, J.M., Andrews, L.M., Bartlett, P.N., Doyle, P.J. and Denuault, G. (2002) *Analytical Chemistry*, **74**, 1322–1326.

62 Sun, F., Cai, W., Li, Y., Jia, L. and Lu, F. (2005) *Advanced Materials*, **17**, 2872–2877.

63 Huang, X., Meng, F., Pi, Z., Xu, W. and Liu, J. (2004) *Sensors and Actuators B*, **B99**, 444–450.

64 Shipway, A.N., Katz, E. and Willner, I. (2000) *ChemPhysChem*, **1**, 18–52.

65 Zhu, M., Liu, M., Shi, G., Xu, F., Ye, X., Chen, J., Jin, L. and Jin, J. (2002) *Analytica Chimica Acta*, **455**, 199–206.

66 Yu, A., Liang, Z., Cho, J. and Caruso, F. (2003) *Nano Letters*, **3**, 1203–1207.

67 Boennemann, H., Brinkmann, R. and Neiteler, P. (1994) *Applied Organometallic Chemistry*, **8**, 361–378.

68 Zhang, J., Kambayashi, M. and Oyama, M. (2004) *Electrochemistry Communications*, **6**, 683–688.

69 Zhang, J., Kambayashi, M. and Oyama, M. (2005) *Electroanalysis*, **17**, 408–416.

70 Li, J. and Lin, X.-Q. (2007) *Analytica Chimica Acta*, **596**, 222–230.

71 Manesh, K.M., Santhosh, P., Gopalan, A. and Lee, K.P. (2008) *Talanta*, **75**, 1307–1314.

72 Lu, Y., Yang, M., Qu, F., Shen, G. and Yu, R. (2007) *Bioelectrochemistry (Amsterdam, Netherlands)*, **71**, 211–216.

73 Selvaraju, T. and Ramaraj, R. (2005) *Journal of Electroanalytical Chemistry*, **585**, 290–300.

74 Wang, S., Yin, Y. and Lin, X. (2004) *Electrochemistry Communications*, **6**, 259–262.

75 Wang, H., Huang, Y., Tan, Z. and Hu, X. (2004) *Analytica Chimica Acta*, **526**, 13–17.

76 Chaki, N.K. and Vijaymohanan, K. (2002) *Biosensors & Bioelectronics*, **17**, 1–12.

77 Gooding, J.J. and Hibbert, D.B. (1999) *Trends in Analytical Chemistry*, **18**, 525–533.

78 Willner, I. (2002) *Science*, **298**, 2407–2408.

79 Hall, E.A.H., Gooding, J.J. and Hall, C.E. (1995) *Mikrochimica Acta*, **121**, 119–145.

80 Ruzgas, T., Csoregi, E., Emneus, J., Gorton, L. and Marko-Varga, G. (1996) *Analytica Chimica Acta*, **330**, 123–138.

81 Varfolomeev, S.D., Kurochkin, I.N. and Yaropolov, A.I. (1996) *Biosensors & Bioelectronics*, **11**, 863–871.

82 Liu, S.Q., Leech, D. and Ju, H.X. (2003) *Analytical Letters*, **36**, 1–19.

83 Chen, D., Wang, G. and Li, J.H. (2007) *Journal of Physical Chemistry C*, **111**, 2351–2367.

84 Heller, A. (1990) *Accounts of Chemical Research*, **23**, 128–134.

85 Hecht, H.J., Schomburg, D., Kalisz, H. and Schmid, R.D. (1993) *Biosensors & Bioelectronics*, **8**, 197–203.

86 Liu, J., Paddon-Row, M.N. and Gooding, J.J. (2004) *The Journal of Physical Chemistry B*, **108**, 8460–8466.

87 Xiao, Y., Patolsky, F., Katz, E., Hainfeld, J.F. and Willner, I. (2003) *Science*, **299**, 1877–1881.

88 Holmlin, R.E., Ismagilov, R.F., Haag, R., Mujica, V., Ratner, M.A., Rampi, M.A. and Whitesides, G.M. (2001) *Angewandte Chemie-International Edition*, **40**, 2316.

89 Brown, K.R., Fox, A.P. and Natan, M.J. (1996) *Journal of the American Chemical Society*, **118**, 1154–1157.

90 Liu, T., Zhong, J., Gan, X., Fan, C.H., Li, G.X. and Matsuda, N. (2003) *ChemPhysChem*, **4**, 1364–1366.

91 Jensen, P.S., Chi, Q., Grumsen, F.B., Abad, J.M., Horsewell, A., Schiffrin, D.J. and Ulstrup, J. (2007) *Journal of Physical Chemistry C*, **111**, 6124–6132.

92 Guiseppi-Elie, A., Lei, C.H. and Baughman F R.H. (2002) *Nanotechnology*, **13**, 559–564.

93 Jiang, L., McNeil, C.J. and Cooper, J.M. (1995) *Journal of the Chemical Society. Chemical Communications*, 1293–1295.

94 Gooding, J.J. (2005) *Electrochimica Acta*, **50**, 3049–3060.

95 Zhao, Y.D., Zhang, W.D., Chen, H. and Luo, Q.M. (2002) *Analytical Sciences*, **18**, 939–941.

96 Chou, A., Bocking, T., Singh, N.K. and Gooding, J.J. (2005) *Chemical Communications*, 842–844.

97 Gooding, J.J., Chou, A., Liu, J.Q., Losic, D., Shapter, J.G. and Hibbert, D.B. (2007) *Electrochemistry Communications*, **9**, 1677–1683.

98 Gao, M., Huang, S.M., Dai, L.M., Wallace, G., Gao, R.P. and Wang, Z.L. (2000) *Angewandte Chemie-International Edition*, **39**, 3664–3667.

99 Gao, M., Dai, L.M. and Wallace, G.G. (2003) *Electroanalysis*, **15**, 1089–1094.

100 Yang, Y.Y., Huang, S.M., He, H., Mau, A.W.H. and Dai, L.M. (1999) *Journal of the American Chemical Society*, **121**, 10832–10833.

101 Li, J., Cassell, A., Delzeit, L., Han, J. and Meyyappan, M. (2002) *The Journal of Physical Chemistry B*, **106**, 9299–9305.

102 Koehne, J., Chen, H., Li, J., Cassell, A.M., Ye, Q., Ng, H.T., Han, J. and Meyyappan, M. (2003) *Nanotechnology*, **14**, 12391245.

103 Koehne, J., Li, J., Cassell, A.M., Chen, H., Ye, Q., Ng, H.T., Han, J. and Meyyappan, M. (2004) *Journal of Materials Chemistry*, **14**, 676–684.

104 Zhang, Y.G., Chang, A.L., Cao, J., Wang, Q., Kim, W., Li, Y.M., Morris, N., Yenilmez, E., Kong, J. and Dai, H.J. (2001) *Applied Physics Letters*, **79**, 3155–3157.

105 Liu, Z.F., Shen, Z.Y., Zhu, T., Hou, S.F., Ying, L.Z., Shi, Z.J. and Gu, Z.N. (2000) *Langmuir*, **16**, 3569–3573.

106 Yu, X.F., Mu, T., Huang, H.Z., Liu, Z.F. and Wu, N.Z. (2000) *Surface Science*, **461**, 199–207.

107 Diao, P., Liu, Z.F., Wu, B., Nan, X., Zhang, J. and Wei, Z. (2002) *ChemPhysChem*, 898–901.

108 Gooding, J.J., Rahmat, W., Liu, J.Q., Yang, W.R., Losic, D., Orbons, S., Mearns, F.J., Shapter, J.G. and Hibbert, D.B. (2003) *Journal of the American Chemical Society*, **215**, 9006–9007.

109 Yu, X., Chattopadhyay, D., Galeska, I., Papadimitrakopoulos, F. and Rusling, J.F. (2003) *Electrochemistry Communications*, **5**, 408–411.

110 Patolsky, F., Weizmann, Y. and Willner, I. (2004) *Angewandte Chemie-International Edition*, **43**, 2113–2117.

111 Yu, J.X., Shapter, J.G., Johnston, M.R., Quinton, J.S. and Gooding, J.J. (2007) *Electrochimica Acta*, **52**, 6206–6211.

112 Yu, J.X., Losic, D., Marshall, M., Bocking, T., Gooding, J.J. and Shapter, J.G. (2006) *Soft Matter*, **2**, 1081–1088.

113 Liu, J.Q., Chou, A., Rahmat, W., Paddon-Row, M.N. and Gooding, J.J. (2005) *Electroanalysis*, **17**, 38–46.

114 Willner, I., Heleg-Shabtai, V., Blonder, R., Katz, E. and Tao, G.L. (1996) *Journal of the American Chemical Society*, **118**, 10321–10322.

115 Katz, E., Riklin, A., Heleg-Shabtai, V., Willner, I. and Bückmann, A.F. (1999) *Analytica Chimica Acta*, **385**, 45–58.

116 Zayats, M., Katz, E. and Willner, I. (2002) *Journal of the American Chemical Society*, **124**, 2120–2121.

117 Zayats, M., Katz, E. and Willner, I. (2002) *Journal of the American Chemical Society*, **124**, 14724–14735.

118 Hess, C.R., Juda, G.A., Dooley, D.M., Amii, R.N., Hill, M.G., Winkler, J.R. and Gray, H.B. (2003) *Journal of the American Chemical Society*, **125**, 7156–7157.

119 Contakes, S.M., Juda, G.A., Langley, D.B., Halpern-Manners, N.W., Duff, A.P., Dunn, A.R., Gray, H.B., Dooley, D.M., Guss, J.M. and Freeman, H.C. (2005) *Proceedings of the National Academy of Sciences of the United States of America*, **102**, 13451–13456.

120 Langley, D.B., Brown, D.E., Cheruzel, L.E., Contakes, S.M., Duff, A.P., Hilmer, K.M., Dooley, D.M., Gray, H.B., Guss, J.M. and Freeman F H.C. (2008) *Journal of the American Chemical Society*, **130**, 8069–8078.

121 Sikes, H.D., Smalley, J.F., Dudek, S.P., Cook, A.R., Newton, M.D., Chidsey, C.E.D. and Feldberg, S.W. (2001) *Science*, **291**, 1519–1523.

122 Creager, S., Yu, C.J., Bamdad, C., O'Connor, S., MacLean, T., Lam, E., Chong, Y., Olsen, G.T., Luo, J., Gozin, M. and Kayyem, J.F. (1999) *Journal of the American Chemical Society*, **121**, 1059–1064.

123 Wei, J.J., Liu, H.Y., Khoshtariya, D.E., Yamamoto, H., Dick, A. and Waldeck, D.H. (2002) *Angewandte Chemie-International Edition*, **41**, 4700–4703.

124 Wei, J.J., Liu, H.Y., Niki, K., Margoliash, E. and Waldeck, D.H. (2004) *The Journal of Physical Chemistry B*, **108**, 16912–16917.

125 Wei, J.J., Liu, H.Y., Dick, A.R., Yamamoto, H., He, Y.F. and Waldeck, D.H. (2002) *Journal of the American Chemical Society*, **124**, 9591–9599.

126 Adenier, A., Cabet-Deliry, E., Lalot, T., Pinson, J. and Podvorica, F. (2002) *Chemistry of Materials*, **14**, 4576–4585.

127 Downard, A.J. (2000) *Electroanalysis*, **12**, 1085–1096.

128 Gooding, J.J. (2008) *Electroanalysis*, **20**, 573–582.

129 Blanford, C.F., Heath, R.S. and Armstrong, F.A. (2007) *Chemical Communications*, 1710–1712.

130 Sumner, J.J. and Creager, S.E. (2001) *The Journal of Physical Chemistry B*, **105**, 8739–8745.

131 Liu, G.Z. and Gooding, J.J. (2006) *Langmuir*, **22**, 7421–7430.

132 Liu, G.Z., Paddon-Row, M.N. and Gooding, J.J. (2007) *Electrochemistry Communications*, **9**, 2218–2223.

133 Liu, J., Gooding, J.J. and Paddon-Row, M.N. (2005) *Chemical Communications*, 631–633.

134 Liu, J.Q., Paddon-Row, M.N. and Gooding, J.J. (2006) *Chemical Physics*, **324**, 226–235.

135 Chi, Q., Zhang, J. and Dong, S.J. (1994) *Electrochimica Acta*, **39**, 2431–2438.

136 Bourdillon, C., Demaille, C., Gueris, J., Moiroux, J. and Saveant, J.-M. (1993) *Journal of the American Chemical Society*, **115**, 12264–12269.

137 Gooding, J.J., Erokhin, P., Losic, D., Yang, W.R., Policarpio, V., Liu, J.Q., Ho, F.M., Situmorang, M., Hibbert, D.B. and Shapter, J.G. (2001) *Analytical Sciences*, **17**, 3–9.

138 Umek, R.M., Lin, S.W., Vielmetter, J., Terbrueggen, R.H., Irvine, B., Yu, C.J., Kayyem, J.F., Yowanto, H., Blackburn, G.F., Farkas, D.H. and Chen, Y.P. (2001) *The Journal of Molecular Diagnostics*, **3**, 74–84.

139 Delamar, M., Hitmi, R., Pinson, J. and Saveant, J.M. (1992) *Journal of the American Chemical Society*, **114**, 5883–5884.

140 Liu, G.Z., Bocking, T. and Gooding, J.J. (2007) *Journal of Electroanalytical Chemistry*, **600**, 335–344.

141 Ligler, F.S. and Rowe Taitt, C.A. (2002) *Optical Biosensors: Present and Future*, Elsevier.

142 Liu, G., Paddon-Row, M.N. and Gooding, J.J. (2008) *Chemical Communications*, 3870–3872.

143 Lahann, J. and Langer, R. (2005) *MRS Bulletin*, **30**, 185–188.

144 Lahann, J., Mitrogotri, S., Tran, T.N., Kaido, H., Sundaram, J., Choi, I.S., Hoffer, S., Somorjai, G.A. and Langer, R. (2003) *Science*, **299**, 371–374.

145 Wang, X.M., Katz, E. and Willner, I. (2003) *Electrochemistry Communications*, **5**, 814–818.

146 Wang, X.M., Kharitonov, A.B., Katz, E. and Willner, I. (2003) *Chemical Communications*, 1542–1543.

147 Jiang, X.Y., Ferrigno, R., Mrksich, M. and Whitesides, G.M. (2003) *Journal of the American Chemical Society*, **125**, 2366–2367.

148 Xia, Y. and Whitesides, G.M. (1998) *Angewandte Chemie-International Edition*, **37**, 551–575.

149 Yeo, W.-S. and Mrksich, M. (2004) *Advanced Materials*, **16**, 1352–1356.

150 Yeo, W.S., Yousaf, M.N. and Mrksich, M. (2003) *Journal of the American Chemical Society*, **125**, 14994–14995.

151 Yousaf, M.N., Houseman, B.T. and Mrksich, M. (2001) *Proceedings of the National Academy of Sciences of the United States of America*, **98**, 5992–5996.

152 Yeo, W.S. and Mrksich, M. (2006) *Langmuir*, **22**, 10816–10820.

153 Wang, J. and Carlisle, J.A. (2006) *Diamond and Related Materials*, **15**, 279–284.

154 Zhou, Y.L. and Zhi, J.F. (2006) *Electrochemistry Communications*, **8**, 1811–1816.

155 Vakurov, A., Simpson, C.E., Daly, C.L., Gibson, T.D. and Millner, P.A. (2004) *Biosensors & Bioelectronics*, **20**, 1118–1125.

156 Yeo, W.S. and Mrksich, M. (2004) *Advanced Materials*, **16**, 1352.

157 Hirsch, R., Katz, E. and Willner, I. (2000) *Journal of the American Chemical Society*, **122**, 12053–12054.

158 Cass, A.E.G., Davis, G., Francis, G.D., Hill, H.A.O., Aston, W.J., Higgins, I.J., Plotkin, E.V., Scott, L.D.L. and Turner, A.P.F. (1984) *Analytical Chemistry*, **56**, 667–671.

159 Ichia, L.S.-H., Katz, E., Wasserman, J. and Willner, I. (2002) *Chemical Communications*, 158–159.

160 Calabrese, G.S., Buchanan, R.M. and Wrighton, M.S. (1983) *Journal of the American Chemical Society*, **105**, 5594–5600.

161 Wang, J. and Kawde, A.-N. (2002) *Electrochemistry Communications*, **4**, 349–352.

162 Wang, J., Musameh, M., Laocharoensuk, R., González-García, O., Oni, J. and Gervasio, D. (2006) *Electrochemistry Communications*, **8**, 1106–1110.

163 Musameh, M. and Wang, J. (2005) *Langmuir*, **21**, 8565–8568.

164 Katz, E., Sheeney-Haj-Ichia, L., Bückmann, A.F. and Willner, I. (2002) *Angewandte Chemie-International Edition*, **41**, 1343–1346.

165 Katz, E., Sheeney-Haj-Ichia, L., Basnar, B., Felner, I. and Willner, I. (2004) *Langmuir*, **20**, 9714–9719.

166 Katz, E., Baron, R. and Willner, I. (2005) *Journal of the American Chemical Society*, **127**, 4060–4070.

167 Moore, A.N.J., Katz, E. and Willner, I. (1996) *Journal of Electroanalytical Chemistry*, **417**, 189–192.

168 Katz, E., Weizmann, Y. and Willner, I. (2005) *Journal of the American Chemical Society*, **127**, 9191–9200.

169 Katz, E. and Willner, I. (2005) *Angewandte Chemie-International Edition*, **44**, 4791–4794.

170 Katz, E. and Willner, I. (2006) *Electrochemistry Communications*, **8**, 879–882.

171 Wang, J., Scampicchio, M., Laocharoensuk, R., Valentini, F., Gonzalez-Garcia, O. and Burdick, J. (2006) *Journal of the American Chemical Society*, **128**, 4562–4563.

172 Laocharoensuk, R., Bulbarello, A., Hocevar, S.B., Mannino, S., Ogorevc, B. and Wang, J. (2007) *Journal of the American Chemical Society*, **129**, 7774–7775.

173 Loaiza, Óscar A., Laocharoensuk, R., Burdick, J., Rodríguez, Marcella C., Pingarron, Jose M., Pedrero, M. and Wang, J. (2007) *Angewandte Chemie-International Edition*, **46**, 1508–1511.

174 Piccin, E., Laocharoensuk, R., Burdick, J., Carrilho, E. and Wang, J. (2007) *Analytical Chemistry*, **79**, 4720–4723.

175 Jimenez, J., Sheparovych, R., Pita, M., Narvaez Garcia, A., Dominguez, E., Minko, S. and Katz, E. (2008) *The Journal of Physical Chemistry C*, **112**, 7337–7344.

176 Zhai, Y., Zhai, J., Wen, D., Zhou, M., Zhang, L. and Dong, S. (2008) *Electrochemistry Communications*, **10**, 1172–1175.

177 Madueno, R., Raisanen Minna, T., Silien, C. and Buck, M. (2008) *Nature*, **454**, 618–621.

2

Electrochemically Active Polyelectrolyte-Modified Electrodes

Mario Tagliazucchi and Ernesto J. Calvo

2.1

Introduction

A polyelectrolyte solution contains the salt of a polyion, a polymer comprised of repeating ionized units. In dilute solutions, a substantial fraction of sodium ions are bound to polyacrylate at concentrations where sodium acetate exhibits only dissociated ions. Thus counterion binding plays a central role in polyelectrolyte solutions [1]. Close approach of counterions to polyions results in mutual perturbation of the hydration layers and the description of the electrical potential around polyions is different to both the Debye–Huckel treatment for soluble ions and the Gouy–Chapman model for a surface charge distribution, with Manning condensation of ions around the polyelectrolyte.

Coulombic, van der Waals, entropic and osmotic forces are coupled in a nontrivial way and give rise to important charge regulation in polyelectrolyte systems. The salt concentration is also an important factor to define the structure and thermodynamic properties of polyelectrolyte solutions. In weak polyelectrolytes the ionization equilibrium is also coupled to these interactions and thus the pK of ionizable groups depends on the organization of the interface and differs from that for the isolated molecule.

Polyelectrolyte complexes formed by polyion pairing are of special interest, including protein–polyelectrolyte interactions such as protein–DNA complexes. A special case of polyelectrolyte complexes are polyelectrolyte multilayers (PEM) on surfaces formed by ion pairing, van der Waals interactions and counterion release of oppositely charged polyelectrolytes [2, 3].

In this chapter we describe the use of polyelectrolytes carrying redox-active centers on electrode surfaces with particular emphasis on organized layer-by-layer redox polyelectrolyte multilayers (RPEM). In redox-active polyelectrolyte multilayers the polyion–polyion intrinsic charge compensation can be broken by ion exchange driven by the electrochemical oxidation and reduction forming extrinsic polyion-counterion pairing. In this chapter we describe the structure, dynamics and applications of these systems.

2.1.1
Chemically Modified Electrodes

In the last 30 years considerable progress has been made in the development of 'tailor-made' electrode surfaces by chemical modification [4–12] of electrodes surfaces with electroactive polymer films. A comprehensive description of electroactive polymer-modified electrodes can be found in the book edited by M. Lyons [13].

The redox groups can be introduced by coordination, electrostatic binding or covalent attachment to the polymer backbone.

Many of these systems employ charged polymers or polyelectrolytes that confer on them particular properties due to the existence of electrical charges in the polymer structure. Oyama and Anson [14, 15] introduced polyelectrolytes at electrode surfaces by using poly(vinylpiridine), PVP, and poly-(acrylonitrile) to coordinate metal complexes via the pyridines or nitrile groups pending from the polymer backbone. Thomas Meyer's group at North Carolina [16, 17] also employed poly(vinylpyridine) to coordinate Ru, Os, Re and other transition-metal complexes by generating an open coordination site on the precursor-metal complex.

Oyama and Anson [18, 19] introduced in 1980s ion-exchange polymers on electrodes by incorporating redox-active counterions to an electrode modified with polyelectrolytes by 'electrostatic binding'. The polycation poly(vinylpyridine) (PVP) was used to bind $Fe(CN)_6^{3/4-}$ [18] and deprotonated poly(acrylic acid) to bind $Ru(NH_3)_6^{2/3+}$[19]. Other cationic polyelectrolytes besides poly(vinylpyridine) such as poly(lysine) and several anions with multiple charge like $Fe(CN)_6^{3/4-}$, $IrCl_6^{3-}$, $Mo(CN)_8^{4-}$, and so on were employed. Among the polyanions, poly(styrene sulfonate), PSS was one of the first choices with redox-active cations such as $Ru(bpy)_3^{3/2+}$ and, $Co(bpy)_3^{3+}$. Of special interest is the use of perfluoro sulfonated poly(ethylene), Dupont de Nemours' Nafion, with fluorocarbon hydrophobic backbone and sulfonates that provide hydrophilic environment. The groups of Anson, Bard and Martin studied extensively redox cations by electrostatic binding of $Ru(bpy)_2$, $Fe(bpy)_3^{2+}$, $Os(bpy)_3^{2+}$, methylviologen, $Co(bpy)_3^{2+}$, $Co(terpy)_3^{2+}$, and so on (terpy = 2,2′: 6′2″-terpyridine) into Nafion.

The third approach has been to graft the redox couple by means of a covalent bond to the polyelectrolyte backbond as described early in 1965 in the book of Cassidy and Kun [20]. Several of these systems are charged polymers in at least one oxidation state, like poly(viologen), poly(vinylferrocene), and so on. Examples of polyelectrolytes like polyacrylic acid with covalently bound viologen were reported by Fernández, Katz and coworkers [21], hydroquinone [22] and Anson *et al.* with bound ferrocene [23].

The existence of charge in these polyelectrolyte-modified electrodes is responsible for some interesting features of the electrochemical response:

a. The effect of electrolyte concentration on the apparent redox potential of the redox couple entrapped in a charged matrix. This has been discussed by Anson and Redepening [24] and by Doblhofer and Vorotyntsev [25] in terms of Donnan or membrane potential with respect to the reference electrode in the external solution.

b. The effect of solution pH on the apparent redox potential for pH-independent redox couples [21].

c. Ion and solvent exchange between the polyelectrolyte film and the bathing electrolyte as the redox charge is changed by oxidation and reduction of the chemically modified electrode. This has been extensively studied by the electrochemical quartz crystal microbalance [26–30], by probe-beam deflection [28, 31] and scanning electrochemical microscopy (SECM) [32].

d. Exchange of ions and solvent between a polyelectrolyte layer at an electrode surface and the electrolyte solution adjacent to the layer produces swelling/deswelling and viscoelastic changes of the polymer film by uptake and release of the solvent with mechanical-work terms contributing to the free energy of the system.

e. Exclusion of ions of the same charge as those in the polyelectrolyte backbone and high partition coefficient for counterions depending on the redox state of the film [25].

f. Diffusion-like propagation of charge due to electron hopping of electrons between neighboring redox sites by segmental motion. The diffusion coefficients are very dependent on the concentration of redox sites [13] and the system undergoes a change of charge-propagation mechanism when the percolation limit is reached at high concentration [33].

g. Existence of a mixed mechanism of electron hopping due to polymer segmental motion and physical diffusion of counterions to compensate charge [34].

2.1.2
Redox Hydrogels

Hydrogels are crosslinked polymer networks with entrapped solvent. In the case of hydrogels containing polyectrolytes, in addition to solvent, ions and salt can be found in the gel as determined by the Donnan partition. This arises from the exclusion of ions of the same charge that sets a membrane potential at the gel/external electrolyte interface.

Adam Heller demonstrated that the electrical communication between the $FADH_2$ prosthetic group in glucose oxidase and electrodes can be facilitated by electrostatic complexing the negatively charged enzyme in a solution of pH above the isoelectric point ($pI = 4.2$) with a cationic polyelectrolyte quaternized poly(vinylpyridine) and poly (vinylpyridine)-Os $(bpy)_2Cl$ redox-mediator copolymer [35]. Based on this concept Heller further introduced a two-component epoxy technique combining glucose oxidase (GOx) with the redox polycationic mediator crosslinked with a bifunctional reagent to yield a self-contained biosensor.

Three-dimensional wired enzyme structures, based on crosslinking the redox polymer chains and binding these to glucose oxidase lysine amines, were subsequently designed and syntesized [36, 37]. An example of a polymerization reaction is

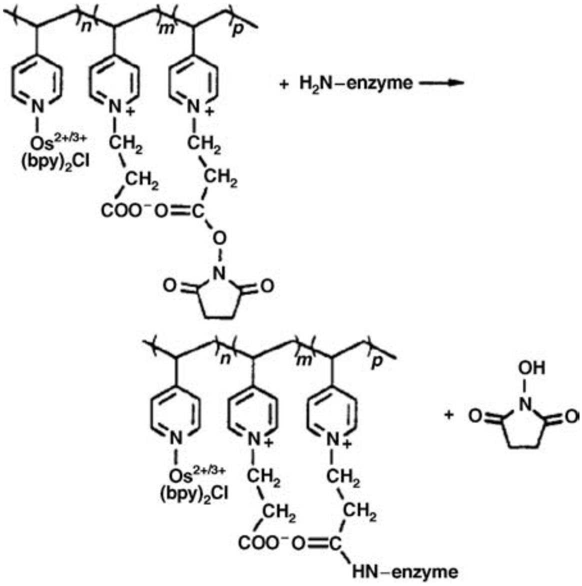

Figure 2.1 Chemical structure of osmium derivatized polyelectrolyte–enzyme system developed by Heller. Taken from Ref. [37].

shown in the Figure 2.1. In the resulting network, one pyridine ring in about five carries an $[Os(bpy)_2Cl]^{1+/2+}$ center. A variation of this crosslinking strategy is via the reaction of a commercially available, water-soluble di-epoxide with the pendant amine functions on the polymer as well as with amine functions of surface lysines in the enzyme glucose oxidase [38, 39].

Redox hydrogels provide three-dimensional electron conductivity in a high-water environment, where the stability of biomolecules such as enzymes is increased. Electron diffusion in redox hydrogels takes place by collisional self-exchange between neighboring redox centers through segmental motion of highly flexible polymer chains. Two extreme limits are: electron hopping and percolation of charge above certain concentration threshold [33, 40]. It should be mentioned that unprecedented fast diffusion ($D_{app} \sim 5.8 \times 10^{-6}\,cm^2\,s^{-1}$) has been recently reported by Mao *et al.* [41] for a 13-atom spacer arm between the $Os^{2+/3+}$ redox complex and the polyelectrolyte backbone complex consistent with the predictions of Blauch and Savéant, as discussed below [33, 40].

2.1.3
Redox Polyelectrolyte Monolayers

A large number of examples of redox polyelectrolyte monolayers have been reported [42]. Anson described the adsorption of poly(acrylic acid) onto glassy carbon with electrostatic binding of $Ru(NH_3)_6{}^{3+}$ and $Co(NH_3)_6{}^{3+}$ ions from solution [43]. Finklea [44] adsorbed poly(4-vinyl-I-methyl-pyridinium methylsulfate) on self-assembled mercapto-undecanoic self-assembled monolayer (SAM) on gold electrodes to form a bilayer structure. Further, adsorption of anionic redox ions such as $[Fe(CN)_6]^{-4}$, $Cu(EDTA)^{2-}$, $Cr(EDTA)^{-}$ and ferrocene carboxylate, $Fc\text{-}COO^{-}$ showed redox activity. In both cases the top layer of these layered polyelectrolyte films contains many ion sites that can bind redox ions by ion exchange with the electrolyte solution. Homo polypeptides such as poly(L-lysine) and poly(L-glutamic acid) have been employed to form layered polyelectrolyte films with $Fe(CN)_6{}^{3-/4-}$ electrostatically adsorbed onto ammonium sites in poly(lysine) [45]. Modified electrodes with polyelectrolytes monolayers have also been deposited using the Langmuir–Blodgett technique [46–48].

An interesting polyelectrolyte monolayer is redox-functionalized dendrimers adsorbed on electrodes with multiple redox states. Each dendrimer in this system is an isolated molecular object of well-defined shape [49, 50]. Cyclic voltammetry in the megavolt per second range has been used to probe the dynamics of charge transport that can be related to the morphology of the adsorbed dendrimer (i.e. the contact angle between the dendrimer and the surface) through a model describing electron hopping in spherical shells.

2.1.4
Redox Polymer Brushes and Grafted DNA

Linear polymer and polyelectrolyte brushes end-labeled with a redox moiety have been extensively used by Moiroux, Demaille, Anne and coworkers to probe the link between the electrochemical response and polymer dynamics. In these systems, chain motions determine the position of the terminal electroactive groups and therefore the scan-rate dependence of the experimental current–potential waves. Ultimately, simple theoretical models can be employed to relate the experiments to molecular features of the polymer, such as its length and flexibility. It is interesting to note that polymer dynamics assists charge propagation also in the case of the polyelectrolyte-modified electrodes discussed above. However, in those systems the redox sites are randomly distributed alongside the polymer backbone and therefore chain motions become convoluted with electron hopping. This situation gives rise to a voltammetric behavior that is well described in terms of the diffusion of charge in a homogeneous film characterized by an effective diffusion constant, D_{app} [51, 52].

The different experimental systems used to relate the electrochemical response with chain dynamics are shown in Figure 2.2. Flexible polyethylene glycol (PEG) chains bearing terminal ferrocene groups have been attached to surfaces (Figure 2.2a) [54, 55], supramolecular self-assembled monolayers (Figure 2.2b) [56] and multilayers (Figure 2.2c) [201] of immunoglobulins. In addition, a redox enzyme was attached at the end of the multilayer to study wiring by PEG-Ferrocene (Figure 2.2d) [201]. In all these systems, diffusion of the terminal ferrocene groups is constrained by the presence of PEG chains (bound diffusion). When the polymeric tether is modeled as an harmonic spring, the ferrocene groups follow a Gaussian distribution around their anchoring point:

$$C(x) = C^{*}\exp\left(\frac{-k_{\mathrm{spr}}x^{2}}{2RT}\right) \tag{2.1}$$

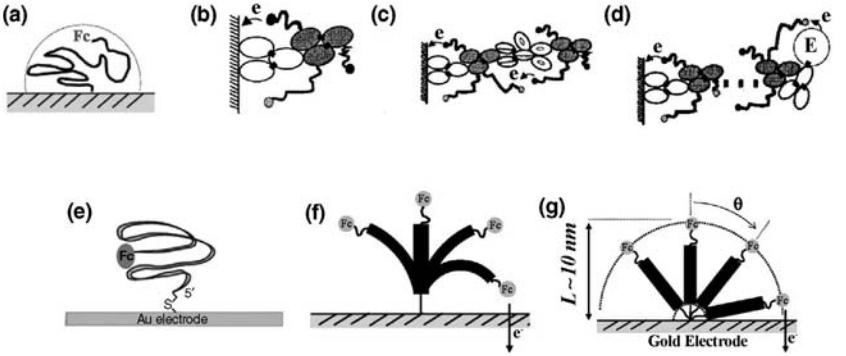

Figure 2.2 Different experimental system used for probing the relationship between chain dynamics and electrochemical response. (a) Ferrocene-labeled polyethylene glycol (PEG-Fc) attached to a surface. (b) PEG-Fc attached to an immonoglobulin monolayer. (c) PEG-Fc attached to an immonoglobulin multilayer. (d) The same as c, but with an additional redox enzyme layer. (e) Ferrocene-labeled ssDNA. (f) Elastic bending of ferrocene labeled dsDNA tethered to the surface with a short linker. (g) Rotational diffusion of ferrocene-labeled dsDNA tethered to the surface with a long linker. Taken from Refs. [58, 59, 201, 202].

where C is the concentration of ferrocene sites at a distance x from the equilibrium point, R is the gas constant, T is the temperature and k_{spr} is the spring force constant. This inhomogeneous distribution of redox sites determines the experimental voltammetric curve.

Current–potential curves have also been recorded for ssDNA and dsDNA [58, 59, 202] end-labeled with ferrocene moieties, which are interesting systems for electrochemical DNA sensing [60]. The diffusion of terminal ferrocene attached to flexible ssDNA is faster that the timescale accessible to cyclic voltammetry and therefore thin-layer behavior is observed. Upon hybridization, the system becomes stiffer and the propagation of redox charge is slower. In the case of dsDNA two different models has been proposed to explain the expererimental results. For short surface–DNA linkers, bending of DNA rods was proposed to be the operating mechanism (Figure 2.2f) [202], while rotational diffusion would be responsible for charge transport when long linkers are used (Figure 2.2g) [59]. Each of the mechanisms presented above has a characteristic distribution of electroactive groups and therefore follows a different diffusion equation.

Recently, pH-responsive redox brushes have been described by Katz and Minko [61]. It has been shown that the electrochemical response of PVP-Os grafted to ITO completely disappears when going from pH 4 to pH > 6, which was attributed to film collapse due to deprotonation of pyridine units. The same effect was not observed for randomly adsorbed polyelectrolytes.

2.1.5
Layer-by-Layer Polyelectrolyte Multilayers

In 1991 Decher and coworkers introduced a new method to prepare multilayered thin films by electrostatic interaction between oppositely charged polyelectrolytes [3, 62, 63]. In this fashion, thin molecular films comprised of charged polymers, proteins, DNA, and so on can be built up by sequential electrostatic adsorption layer-by-layer simply by alternate immersing a solid substrate in solutions of positively and negatively charged polyelectrolytes.

The layer-by-layer method allows the thickness and internal structure of redox-active films to be defined to a degree that cannot be realized with traditional methods such as spin and dip coating or electropolymerization. Control of the film thickness with nanometer precision and surface charge, not only on flat surfaces but also on curved and rough surfaces and even on colloidal particles, can be achieved by choosing the number of layers, the type of building blocks (which can be almost anything bearing electrostatic charges) and/or the processing conditions (deposition pH, salt concentration, etc.).

Electrode preparation by the LbL method is schematized in Figure 2.3 [3, 64]. We start with a metallic or semiconductor electrode bearing a surface electrical charge (negative in this case). This surface charge is usually conferred to the substrate by chemical reaction: charged thiols are used for gold and silver, silanes for ITO and diazonium salts for carbon surfaces. The electrode is immersed in a solution of an oppositely charged polyelectrolyte that adsorbs on the surface. If this polyelectrolyte

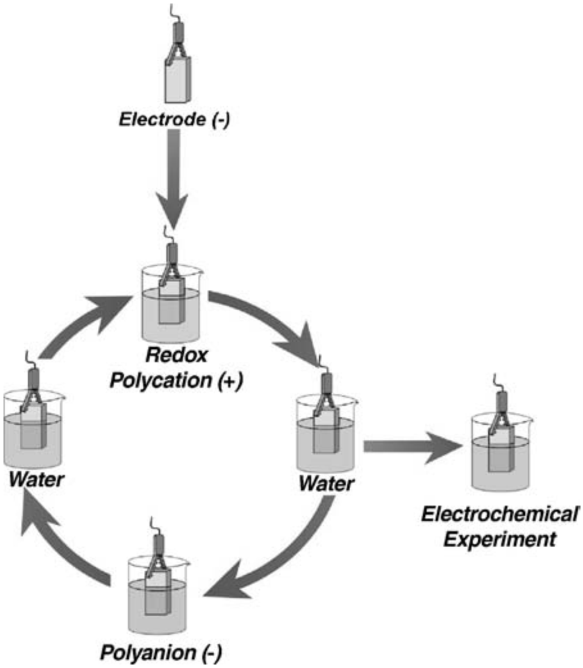

Figure 2.3 Simple schematic of the layer by layer-deposition method. The initially negatively charged substrate is immersed in a solution of a polycation for ~15 min and rinsed with water. During this process a polycation layer is adsorbed and therefore the surface polarity is reversed. The sustrate is now immersed in a polyanion solution for ~15 min and rinsed again with water. This process is repeated after the desired number of layers is achieved.

carries electrochemically active groups, the polyelectrolyte multilayer (PEM) results in a chemically modified electrode [65]. Different redox polyelectrolytes that have been used in PEMs are shown in Figure 2.4. After rinsing, the electrode is dipped in a solution of a polyelectrolyte bearing opposite charge. During each adsorption step the surface charge is completely reversed and therefore the adsorption/rising steps can be repeated the desired number of times with the same or different polyelectrolytes until the target modified electrode is obtained.

The monotonic increase of immobilized material with the number of deposition cycles in the LbL technique is what allows control over film thickness on the nanometric scale. Film growth in LbL has been very well characterized by several complementary experimental techniques such as UV-visible spectroscopy [66, 67], quartz crystal microbalance (QCM) [68–70], X-ray [63] and neutron reflectometry [3], Fourier transform infrared spectroscopy (FTIR) [71], ellipsometry [68–70], cyclic voltammetry (CV) [67, 72], electrochemical impedance spectroscopy (EIS) [73], ζ-potential [74] and so on. The complement of these techniques can be appreciated, for example, in the integrated charge in cyclic voltammetry experiments or the redox capacitance in EIS for redox PEMs: The charge or redox capacitance is not necessarily that expected for the complete oxidation/reduction of all the redox-active groups that can be estimated by other techniques because of the experimental timescale and charge-transport limitations.

Even thought the layer-by-layer method has been originally described for the alternate adsorption of oppositely charged linear polyelectrolytes [64], the list of possible building blocks now includes nanoparticles [75, 76], enzymes [77–79], viruses [80], inorganic clusters [81–86], dendrimers [87, 88], and so on. Following the work of Hodak *et al.* [77], several authors proposed the assembly of enzymes and redox polyelectrolytes to be used as biosensors. Recently, a number of reports have also included metal nanoparticles or carbon nanotubes in redox PEMs in order to improve their electrochemical and electrocatalytic properties [89, 90]. At present, the LbL films based on nonelectrostatic interactions such as hydrogen bonding, covalent reaction and coordination chemistry, and so on, have been disclosed. Covalent crosslinking of redox-active films has been proposed as a way to increase electrode stability [91] and life, but can also cause a decrease in the mobility of redox sites and thus in redox response [92]. Multilayer films based on coordination chemistry are usually electroactive due to the presence of transition metals, some of which have a rich redox chemistry [93].

2.2
Structure

Polyelectrolyte films are comprised of the polyelectrolytes, solvent and ions, the latter mainly located at the film/solution interface, see below. Solvent content in PEMs can be aproximately 40% [94, 95], being the actual value dependent on film history (drying and reswelling steps) and for dry films on environmental humidity [95, 96]. PEMs are therefore highly swollen structures, but its water content is below that found in

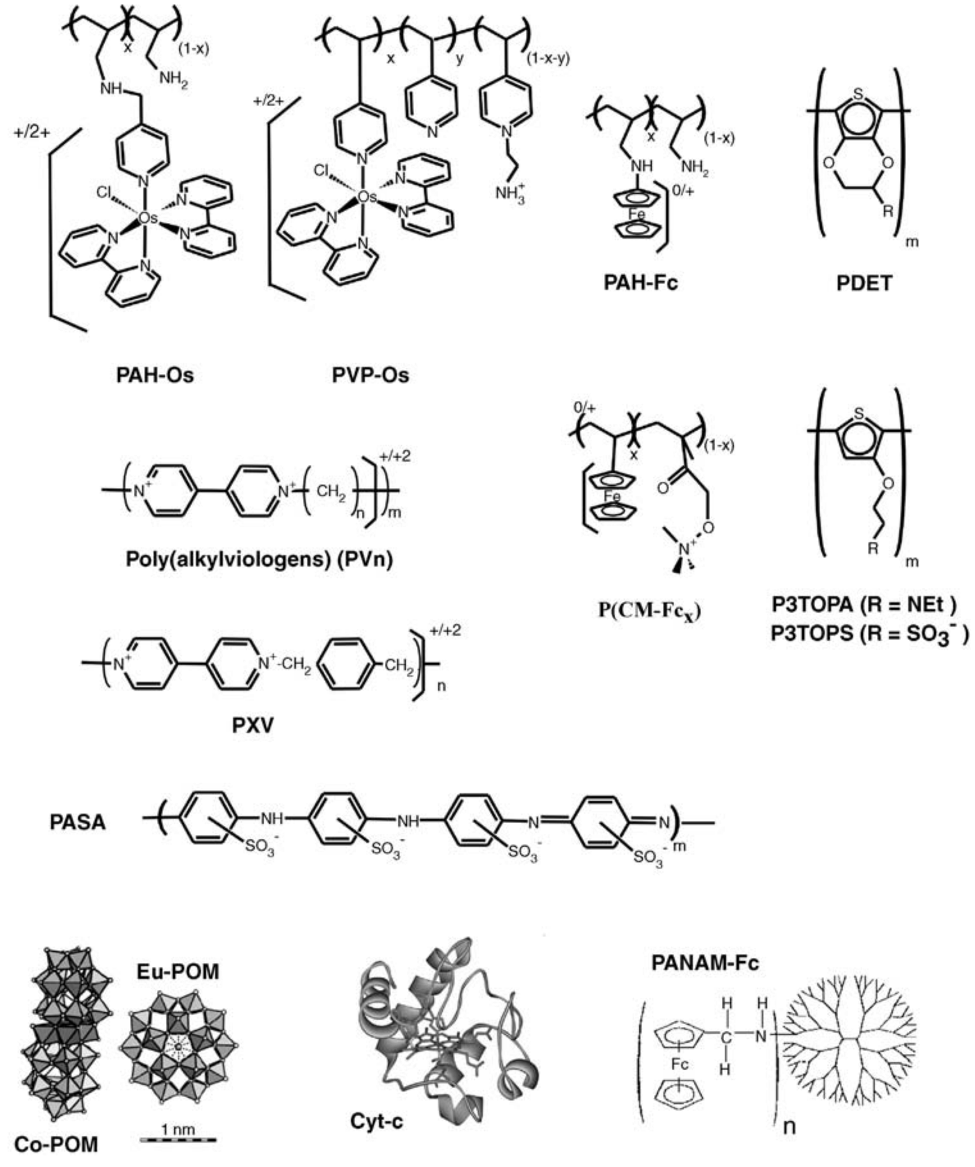

Figure 2.4 Redox-active building blocks used in LbL self-assembly. PAH-Os: Osmium pyridil-bipyridil modified poly(allylamine) [28, 68, 69, 72, 148, 150–154, 184, 185, 191, 203–205]; PVP-Os: Osmium-bipyridyl-modified quaternized poly(4-vinylpyridine) [102, 206, 207]; PAH-Fc: Ferrocene-modified polyallylamine [77, 101, 208]; P(CM-Fc$_x$): Poly(vynil ferrocene) copolymer [224]; PV*n*: Polyalkylviologens (PV*n*, *n*: number of methylene groups) [67, 104, 209–212]; PXV: Poly(p-xylylenviologen) [211, 212]; PASA: Sulfonated polyaniline [213] [92, 214, 215]; P3TOPS and P3TOPA: Poly(alkoxythiophene) derivatives [103]; Co-POM: $[Co_4(H_2O)_2P_4W_{30}O_{112}]^{16-}$, Eu-POM: $[Eu(H_2O)P_5W_{30}\ O_{110}]^{12-}$ [216] (for other polyoxometallates see Refs. [81–84, 217]); Cyt. c: Cytochrome c [92, 214, 215, 218]; PANAM-Fc: poly(amidoamine) [87, 88].

hydrogels (60% [97]), probably due to the high electrostatic crosslinking, owing to intrinsic polyelectrolyte–polyelectrolyte compensation. However, from these values it can be expected that redox PEMs behave much more like redox hydrogels than hydrophobic films such as Langmuir–Blodgett films [46–48] or electroprecipitated poly(vinylferroce) [98].

2.2.1
Polyelectrolye Interpenetration

The inner structure of polyelectrolyte multilayer films has been studied by neutron and X-ray reflectivity experiments by intercalating deuterated PSS into a nondeuterated PSS/PAH assembly [94, 99]. An important lesson from these experiments is that polyelectrolytes in PEMs do not present well-defined layers but are rather interpenetrated or fussy systems. As a consequence, polyelectrolyte chains deposited in an adsorption step are intertwined with those deposited in the three or four previous adsorption cycles. When polyelectrolyte mobility is increased by immersion in NaCl 0.8 M, the interpenetration increases with time as the system evolves towards a fully mixed state in order to maximize its entropy [100]. From the point of view of redox PEMs, polyelectrolyte interpenetration is advantageous in the sense that two layers of a redox polyelectrolyte can be in electrochemical contact even if they are separated by one or more layers of an electroinactive polyion. For example, electrical connectivity between a layer of a redox polymer and the electrode is maintained even when separated by up to 2.5 insulating bilayers [67, 101–103].

2.2.2
Compensation of Polyelectrolyte Charges

Inside PEMs, overlapping Gaussian profiles for positively and negatively charged chains are predicted to yield an electrostically neutral phase [2]. Schlenoff has demonstrated complete release of radiolabeled mobile counterions from a PEM upon adsorption of an additional polyelectrolyte layer, suggesting full polyion–polyion charge compensation (intrinsic compensation) for the as-prepared film [104]. Exposing the as-prepared film to an external electrolyte solution produces the dissociation of some of these polyion–polyion bonds with the simultaneous incorporation of an anion and a cation per broken bond to compensate the newly created charges (extrinsic charge compensation) [105, 106]. It should be noted that in the original work of Schlenoff [104], strong polyelectrolytes were used. The presence of acid–base or redox equilibria opens up new possibilities to achieve extrinsic compensation by protonation/deprotonation or oxidation/reduction, as is exemplified in Section 2.3.2.

2.2.3
Film Inner Structure

The structure of nanometer-thick PEM films is inhomogeneous along the direction normal to the electrode due to the presence of the surface. Decher has developed a qualitative three-zone model to describe the PEM structure [3]. The first zone, composed of a few polyelectrolyte layers, is located closest to the substrate and therefore is more susceptible to its influence. As an example of the influence of the surface, consider the smaller thickness and mass per bilayer during the first dipping cycles when compared by the following adsorption steps [3, 107]. Zone II exists between zone I and the charged region in contact with the electrolyte, zone III, and, as previously discussed, it is assumed to be free of mobile ions. The environment felt by polyelectrolyte chains in zone III drastically differs from that in zones I and III since charge compensation is mainly achieved in this case by mobile ions and not by polyion–polyion compensation. As a consequence, polyelectrolytes in zone III form a more permeable [108], mobile [109] and swollen layer [110]. Not only does the film structure depend on the distance from the underlying surface, but also the presence of an inhomogeneous electric field results from a nonuniform concentration profile of protons across the multilayer [111]. It has also been shown that the electrostatic charge in zone III can alter the properties in zones I and II, even for thick multilayers. For instance, Granick and Xie have assembled multilayers of the strong polyions QPVP (quaternized poly(vinylpyridine)) and PSS on top of layers of the weak polyelectrolyte PMA poly(methyacrylic acid)) and showed that the degree of ionization of the carboxylic groups in PMA oscillates between 30% and 80% depending on the charge of the topmost adsorbed layer [53, 57]. This effect is particularly long ranged since oscillations continue for films of more than 10 layers.

2.2.4
Effect of the Assembly pH

The ionic strength [3, 112–115] and (for weak polyelectrolytes) the pH [114] of the assembly solutions play a major role in determining the structure of self-assembled multilayers. Rubner has shown that dramatic changes in the thickness per bilayer and surface roughness can be caused by small changes in the adsorption pH [114]. This result has been explained in terms of the lineal charge density of the polyelectrolyte chains. Highly charged polyelectrolytes ($\mathrm{pH} \gg \mathrm{p}K\mathrm{a}$ for polyacids or $\mathrm{pH} \ll \mathrm{p}K\mathrm{a}$ for polybases) adopt rod-like conformations to minimize electrostatic energy and therefore produce thin, smooth and compact films. On the other hand, coiled conformations prevail for poorly charged polymers ($\mathrm{pH} \ll \mathrm{p}K\mathrm{a}$ for polyacids or $\mathrm{pH} \gg \mathrm{p}K\mathrm{a}$ for polybases) giving rise to thick, rough and floppy films. The effects of assembly pH have consequences for the design of PEM-modified electrodes. The most immediate one is the ability to increase the total redox charge per bilayer by lowering the charge density of the polyelectrolytes. For example, the redox charge for PAH-Os_3/GOx_3 electrodes increases from $5.7\,\mu\mathrm{C\,cm^{-2}}$ to $148\,\mu\mathrm{C\,cm^{-2}}$ when the assembly pH varies from 5.5 to 8.75 (note that the PAH-Os is a polybase and therefore its charge density decreases with solution pH) [69]. Since PAH-Os is adsorbed in coiled conformations at high pH, the amount of enzyme that can be immobilized under such conditions is also higher. As a consequence of the increased redox charge and enzyme loading, the sensitivity of the electrode is improved: the catalytic current under glucose saturation increases from 0.025 to $30\,\mu\mathrm{C\,cm^{-2}}$ between the pH limits mentioned above. Finally, the assembly pH impacts on the inner composition of the polyelectrolyte film and can cause an excess of either positive or negative groups. The internal ionization degree in as-prepared polyelectrolyte films can be determined by FTIR and XPS techniques [107]. For example, the ionization degrees of the amino groups for multilayers prepared at pH 8.3 and pH 5.5 determined by fitting the XPS N 1s peak are 81 and 97%, respectively. These differences in film composition also have an impact in the electrochemical response (see Section 2.3.2).

2.2.5
Theoretical Description

While the structure of nonredox polymer and polyelectrolytes thin layers has received much attention in the past [116, 117], only recently has a molecular theory able to treat, from a molecular point of view, redox polyelectrolytes adsorbed on electrodes, been presented [118–120]. The formulation of the theory, its scope, advantages and limitations will be discussed in detail in Section 2.5.2, and therefore we will limit ourselves to show here some predictions that are relevant for the understanding of the structure of polyelectrolyte-modified electrodes. The theory was applied to study the particular system depicted in Figure 2.5, which consists of a single layer of PAH-Os adsorbed on a gold surface thiolated with negatively charged mercapto

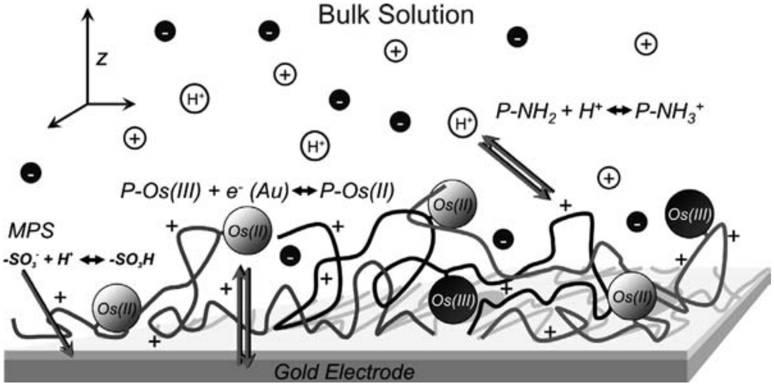

Figure 2.5 Schematic representation of the Au/MPS/PAH-Os/solution interface modeled in Refs. [118–120] using the molecular theory for modified polyelectrolyte electrodes described in Section 2.5. The red arrows indicate the chemical equilibria considered by the theory. The redox polymer, PAH-Os (see Figure 2.4), is divided into the poly(allyl-amine) backbone (depicted as blue and light blue solid lines) and the pyridine–bipyridine osmium complexes. Each osmium complex is in redox equilibrium with the gold substrate and, depending on its potential, can be in an oxidized Os(III) (red spheres) or in a reduced Os(II) (blue sphere) state. The allyl-amine units can be in a positively charged protonated state (plus signs on the polymer backbone lines) or in a neutral deprotonated state, which are related by an acid–base equilibrium. The self-assembled layer of a mercapto-propane sulfonate, MPS, is covalently adsorbed on top of the gold substrate (depicted as a yellow layer covering the electrode). The sulfonate groups in MPS are in acid–base equilibrium with protons in solution and thus could be in a protonated or in a deprotonated state. The polymer-modified electrode is immersed in an aqueous electrolyte solution containing salt ions, protons and hydroxyls in thermodynamic equilibrium which a bulk solution. The normal direction from the electrode is denoted by *z* and has its origin on the metal surface. Taken from Ref. [118].

propylsufonate, MPS. The polymer has two parts (see structure in Figure 2.4), namely a polymeric backbone comprised of repeating allyl-amine units and the anchored redox sites. The amino groups in the polymer backbone and the sulfonate groups in the thiol molecules participate in their respective acid–base equilibria and can be either charged or neutral. The redox sites participate in a redox equilibrium and can exist as Os(II) or Os(III). The modified electrode is immersed in an aqueous electrolyte solution containing salt ions, protons and hydroxyls ions. Despite the molecular complexity of the problem, the molecular theory is able to predict the structure, molecular organization and electrochemical behavior of this system taking into account all the molecular details, namely the size, conformations, charge and shape of all the species in the interface as well as the molecular interaction between them and the presence of the chemical equilibria.

The density profile of PAH-Os predicted by the theory is shown in Figure 2.6a in terms of the fraction of the available volume occupied by the polymer (volume

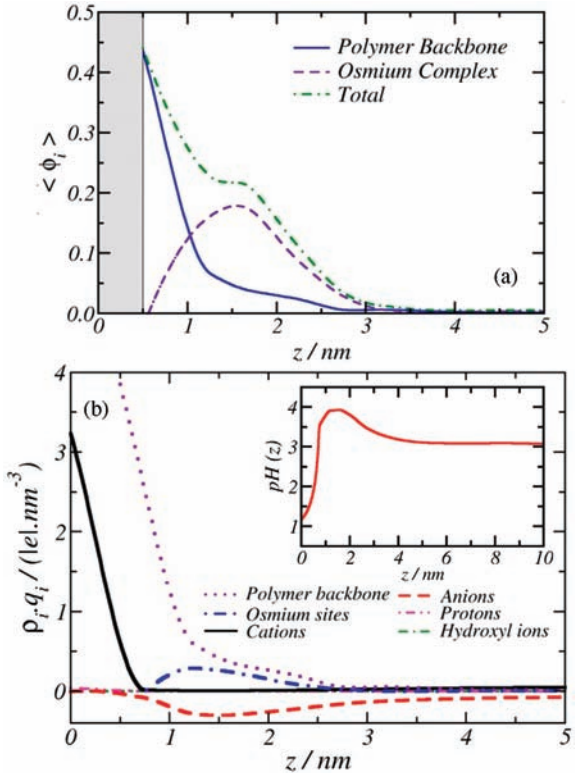

Figure 2.6 (a) Volume-fraction profiles for the polymer backbone (full line), the redox sites (dashed line), and the whole redox polymer (dot-dashed line) predicted by the molecular theory (Section 2.5) for a single layer of PAH-Os on a thiolated gold electrode. (salt concentration = 0.1 M, pH = 3). The shaded region ($z < 0.5$ nm) is occupied by the thiol layer. (b) Charge-density profile for each of the charged molecular species considered by the theory. Inset: local pH vs. distance from the electrode. Taken from Ref. [118].

fraction). The polymer adopts a compact distribution on the surface in order to maximize polymer–polymer and polymer–surface van der Waals interactions with an average volume fraction of approximately 0.3. This left ~70% of the volume for the electrolyte solution, which is in qualitative agreement with the picture of a highly swollen system presented above for PEMs and hydrogels. The polymer density profile also shows a long tail that reaches approximately 12 nm from the surface, which is consistent with a population of dangling segments adopting extended conformations to minimize electrostatic repulsions. Calculations show that these tails are much more responsive to changes in solution pH and ionic strength than the compact layer on the surface. The total density profile shown in Figure 2.6A can be split into two components corresponding to the osmium sites and the polymer backbone. An interesting finding is that the bulky osmium complexes are excluded from the surface by the small and flexible polymer chains. From the profile in Figure 2.6A, we can calculate a theoretically predicted average thickness that can be qualitatively compared with ellipsometric measuments. For example, the *in-situ* ellipsometric thickness for a completely reduced layer on PAH-Os on Au/MPS immersed in a 0.2 M KNO_3 pH 7.3 buffer solution was measured to be 1.5 nm [73] in good agreement with the predicted value of 1.2 nm in the same conditions. Based on this result and the very good agreement that exists between the predicted and measured voltammetric behavior in solutions of different pHs and ionic strength, we are confident in the ability of the theory to provide the structural information discussed in this section, which would otherwise be very difficult or impossible to determine from experiments.

In Figure 2.6B the density profiles for the polymer components and the mobile ions are shown in terms of charge concentrations (charges per unit volume). The figure shows a large excess of cations inside the thiol layer ($z < 0.5$ nm, where z is the distance from the surface, see Figure 2.5) to compensate for the large charge arising from the sulfonate groups from MPS. In the polymer region, $0.5\text{ nm} < z < 2.5$ nm, the positive charges of osmium sites and amino groups are mainly compensated by an excess of anions.

Finally, for large z both the concentration of anions and cations reach their bulk values. The curves for protons and hydroxyl ions are not distinguishable due to their very low concentration, but the pH (defined as $-\log[H^+]$) in the inset of Figure 2.6B shows dramatic changes in the local concentration of protons larger than 3 orders of magnitude within 1 nm.

We will now focus our attention on the electrostatic potential profile, Figure 2.7. The electrostatic potential and the lateral osmotic pressure are the interaction fields in the theory that self-consistently determine (and are determined by) the concentration of all the molecular species in the system. Figure 2.7 shows that the electrostatic potential is positive on the surface as a result of the applied potential on the metal. The sharp drop observed in the thiol layer is caused by its negative charge. The potential changes its sign again in the polymer region as a consequence of the charges in the polymer and finally decays, following a long tail of positive potential that reflects the dangling polymer tails. It is interesting to note that the inversion of the electrostatic potential of the initially negatively charged surface by the polymer layer would allow a

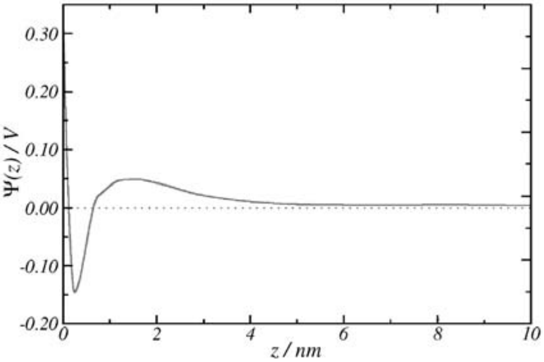

Figure 2.7 The electrostatic potential as a function of the distance from the metal (full line, left axis) calculated for a Au/MPS/PAH-Os electrode with the PAH-Os molecular model for the same conditions as Figure 2.6. Taken from Ref. [118].

second layer of a negatively charged polyelectrolyte to be adsorbed, and therefore is the first step towards the construction of a PEM by multiple adsorption points.

An interesting consequence of the highly nonuniform electrostatic potential and distribution of the molecular species is that the local activity coefficients of the chemical species taking part in chemical equilibria depend on their exact location at the interface. As an example, Figure 2.8 shows that the oxidation fraction of the osmium sites is a nonuniform function of the distance to the electrode. The consequences of this finding for the electrochemical response will be discussed in Section 2.3.4.

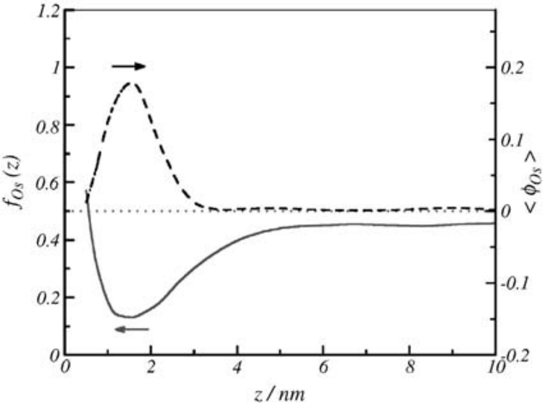

Figure 2.8 Fraction of oxidized redox sites (solid line, left axis) and osmium site volume fraction (dashed line, right axis) as a function of the distance from the electrode at $E = E^0_{\mathrm{os(II)/os(III)}}$ calculated with the molecular theory for the same conditions as Figure 2.6. Taken from Ref. [118].

2.3
Electrochemical Response

2.3.1
Ideal Response

Thin-film ideal or Nernstian behavior is the starting point to explain the voltammetric behavior of polyelectrolyte-modified electrodes. This condition is fulfilled when (i) the timescale of the experiment is slower than the characteristic timescale for charge transport (l^2/D_{app}, with l the film thickness) in the film, that is all redox within the film are in electrochemical equilibrium at any time, (ii) the activity of redox sites is equal to their concentration and (iii) all couples have the same redox potential. For these conditions, anodic and cathodic current–potential waves are mirror images (zero peak splitting) and current is proportional to the scan rate [121]. Under this regime, there exists an analytical expression for the current–potential curve:

$$i = i_{\mathrm{dl}} + \frac{F^2 v \Gamma_{\mathrm{Os}}}{RT} \frac{\exp\left[\left(\frac{F}{RT}\right)(E - E^{o'})\right]}{\left[1 + \exp\left(\frac{F}{RT}\right)(E - E^{o'})\right]^2} \tag{2.2}$$

where Γ_{Os} is the total osmium surface coverage, v is the scan rate and i_{dl} is the double-layer charging current. Note that it is not possible to obtain kinetic information from experiments performed under this regime. Figure 2.9 shows a voltammogram for a PAH-Os/PVS-modified electrode in experimental conditions closely corresponding to an ideal behavior.

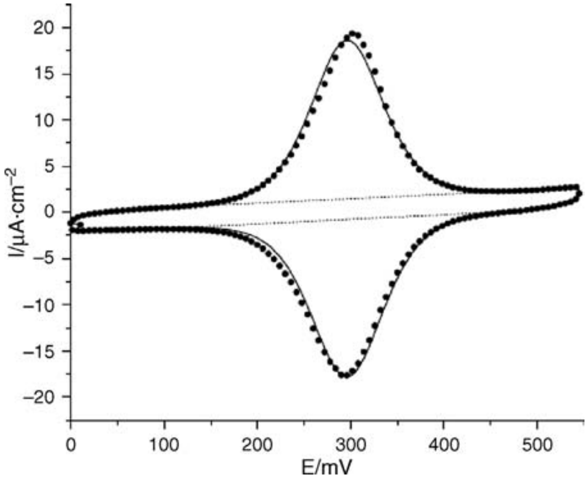

Figure 2.9 Cyclic voltammetry of $(\text{PAH-Os})_4(\text{PVS})_4(\text{PAH-Os})$ in 0.2 M KNO_3, 20 mM TRIS buffer of pH 7.4 (points). Ideal voltammetry behavior is observed. Curve: best fit to reversible thin-layer voltammetric equation 2.2. Best fit to Equation 2.2 is shown in solid line. Taken from Ref. [153].

2.3.2
Peak Position and Donnan Potential

Due to the presence of interactions, the apparent redox potential of a redox couple inside a polyelectrolyte film can differ from that of the isolated redox couple in solution (i.e. the standard formal redox potential) [121]. In other words, the free energy required to oxidize a mole of redox sites in the film differs from that needed in solution. One particular case is when these interations have an origin in the presence of immobile electrostatically charged groups in the polymer phase. Under such conditions, there is a potential difference between this phase and the solution (reference electrode in the electrolyte), known as the Donnan or membrane potential that contributes to the apparent potential of the redox couple. The presence of the Donnan potential in redox polyelectrolyte systems was demonstrated for the first time by Anson [24, 122]. Considering only this contribution to peak position, we can write:

$$E_{\mathrm{app}}^{1/2} = E^0 + \Delta\phi_{\mathrm{DONNAN}} \tag{2.3}$$

where $E_{\mathrm{app}}^{1/2}$ is the apparent redox potential measured, for example, by cyclic voltammetry, E^0 is the standard redox potential of the redox couple and $\Delta\phi_{\mathrm{DONNAN}}$ is the Donnan potential given by [25, 107]:

$$\Delta\phi_{\mathrm{D}} = \frac{\mathrm{RT}}{F}\ln\left[\frac{C_{\mathrm{F}} + (C_{\mathrm{F}}^2 + 4C_{\mathrm{S}}^2)^{1/2}}{2C_{\mathrm{S}}}\right] \tag{2.4}$$

where C_{S} is the bulk salt concentration and C_{F} is the concentration of immobile charge inside the film.

Equation 2.4 shows that the Donnan potential strongly depends on salt concentration. This can be explained as follows: when the concentration of immobile charges inside the film is larger than the electrolyte concentration, salt ions of the same charge as the immobile groups are excluded from the film, while those of equal charge are incorporated to maintain electroneutrality (see Figure 2.10). The film is said to be permselective to the latter ions. One can think of the Donnan potential as the electrostatic potential difference required to maintain this imbalance in the concentration of mobile ions. In Equation 2.4 $C_{\mathrm{F}} > 0$ implies positive Donnan potentials and anion permselectivity, whereas $C_{\mathrm{F}} < 0$ yields negative Donnan potentials and cation permselectivity. At the other limit, when the electrolyte concentration is larger than the concentration of immobile charges in the film, the concentration of mobile ions is similar in the film and the solution and thus the Donnan potential vanishes (Donnan breakdown).

We can now combine Equations 2.3 and 2.4:

$$E_{\mathrm{app}}^{1/2} = E^0 + \frac{RT}{F}\ln\left[\frac{C_{\mathrm{F}} + (C_{\mathrm{F}}^2 + 4C_{\mathrm{S}}^2)^{1/2}}{2C_{\mathrm{S}}}\right] \tag{2.5}$$

Equation 2.5 provides a way to determine the concentration and sign of immobile charges inside the film and also to probe whether the peak shift is caused by the presence of an interfacial potential or an alternative explanation is required. As an

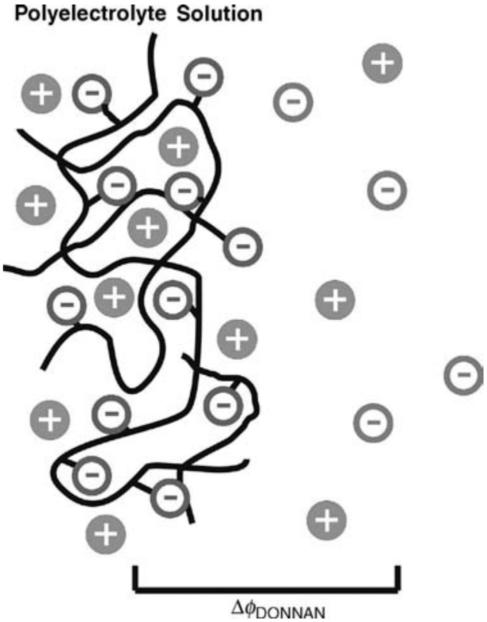

Figure 2.10 Scheme showing the Donnan partition of mobile ions between the solution and a polymeric phase bearing an excess of negative charges. While positive ions are incorporated in the film to mantain electroneutrality, negative ions are excluded from it. This situation give rise to an interfacial potential (Donnan potential) at the interface.

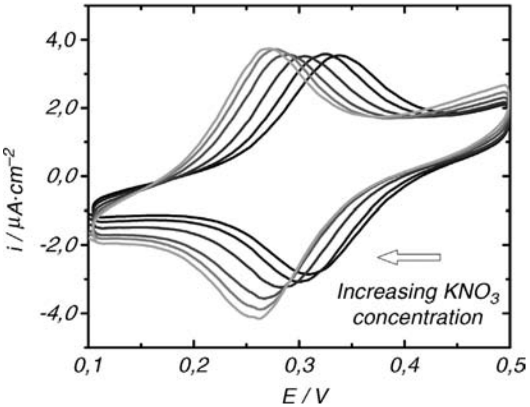

Figure 2.11 Cyclic voltammograms of $(PAH\text{-}Os)_4(PVS)_4PAH\text{-}Os$ multilayer modified Au electrode self-assembled from PVS and PAH-Os solutions of pH 8.3 and measured in pH 7.3 solutions of different KNO_3 concentration: 8, 40, 137, 481, 932 and 1500 mM. Sweep rate 0.025 mV s^{-1}. Taken from Ref. [107].

example in Figure 2.11 we show cyclic voltammperograms for a PAH-Os/PVS multilayer at different salt concentrations showing the peak shift due to the presence of interfacial potential.

Owing to the presence of both positive and negative polyions in PEM, the polarity of net immobile charge can be controlled at will by the choice of the outmost layer and the relationship between assembly and testing solution pHs [107]. Note that three approximations are used when applying Equation 2.5 to analyze LbL systems. First, the distribution of noncompensated immobile charges in PEM is inhomogeneous and mainly located in film/electrolyte interface (Decher's zone III), thus C_F should be regarded as an effective averaged concentration of charges. Second, we assume that the ionization degree of pH-dependent groups does not depend on external salt concentration. Third, during film oxidation and reduction charges are created and destroyed in the film, we neglect these changes in C_F.

Figure 2.12 shows the C_F values resulting from fitting peak potentials measured in CV as a function of ionic strength with Equation 2.5 for PAH-Os/PVS films finished either in positive or negative polyions and assembled and tested at different pHs. Interestingly, not always do films finished in PVS have $C_F < 0$ and films capped with PAH-Os have $C_F > 0$, which means that uncompensated charges at the electrolyte/film interface are not the only contribution to C_F. The other contribution arises from

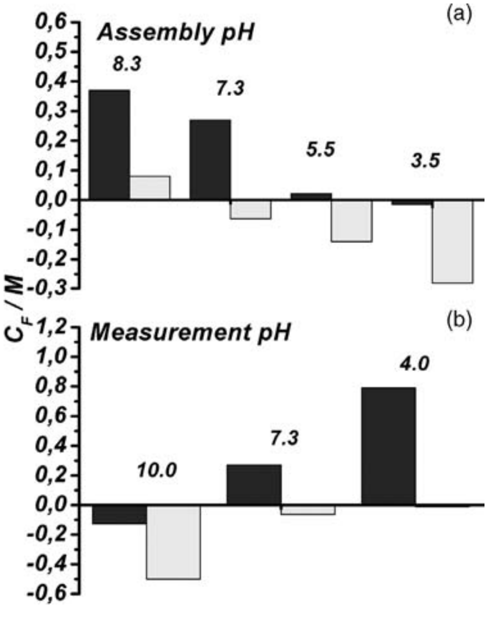

Figure 2.12 Concentration of immobile charges in the Donnan model (C_F), obtained by fitting cyclic voltammetry peak positions to Equation 2.5. Experiments were performed for $(PAH\text{-}Os)_4(PVS)_4PAH\text{-}Os$ (black bars, positively charged capping layer) and $(PAH\text{-}Os)_5(PVS)_5$ (grey bars, negatively charged capping layer) self-assembled multilayers at different assebly and testing pHs. Taken from Ref. [107].

the acid–base equilibrium of amino groups in PAH-Os. During self-assembly, unprotonated amino groups do not participate in polyion–polyion pairing and therefore can be protonated if the electrochemical experiment is performed in acid conditions. Furthermore, if the electrochemical experiments are carried out in basic conditions, unprotonation of amines produce an excess of sulfonates. The fraction of protonated amines in the freshly prepared films depends on the assembly pH, as was proved by FTIR and XPS spectroscopies (see Section 2.2.5). The concentration of immobile charge, C_F, is ruled by the relationship between the assembly solution pH and the testing solution pH. Based on Figure 2.12 we elaborated these simple and general rules to determine the type of ion-permselectivity for LbL films:

(i) If the testing solution pH < self-assembling solution pH, protonation of the PAH amines occurs, $\Delta\phi_{\mathrm{DONNAN}}$ and C_F are positive and the film is an anion exchanger.
(ii) If the testing solution pH > self-assembling solution pH, the amines in the film become deprotonated, $\Delta\phi_{\mathrm{DONNAN}}$ and C_F are negative and the film is a cation exchanger.
(iii) Finally, if the testing solution pH ≈ self-assembling solution pH, the degree of protonation of amines in the film remains unchanged and $\Delta\phi_{\mathrm{DONNAN}}$ and C_F are positive or negative depending on the polarity of the outmost layer.

Manipulation of the Donnan potential in random polymer-modified electrodes can also be achieved. In the case of cast redox polyelectrolyte-modified electrodes one can control ion permselectivity by mixing the redox polymer with an oppositely charged polyelectrolyte in an appropriate ratio before film casting [123]. The same strategy can be followed in electropolymerized films by mixing the electroactive monomer with one of opposite charge [124].

One of the main assumptions of the Donnan partition model is that two well-defined phases (polymer and solution) exist and the electrostatic potential presents a sharp transition between them. This approximation is fulfilled when the typical decay length of the electrostatic potential (Debye length) is much shorter than the film thickness. The other limiting situation is that where all the redox sites are located in a plane and thus the Debye length is larger than the film thickness. This situation can be described by the surface potential model:

$$\Delta\phi_S = \frac{2RT}{F}\operatorname{arcsinh}\left(\frac{\sigma_M}{[8c_s\varepsilon_r\varepsilon_0 kT]^{1/2}}\right) \tag{2.6}$$

where $\Delta\phi_S$ is the surface–solution potential difference and σ_M is the charge density of the surface.

We shall now consider what happens when the film thickness is of the order of the Debye length. In such a situation, no analytical expressions can be derived and numerical calculations should be used [125]. The real situation could be even more complicated, since an ill-defined film thickness can exist, like the example in Figure 2.6. We can use the molecular theory to obtain a self-consistently determined electrostatic potential profile across the interface as was shown in Figure 2.7 (see

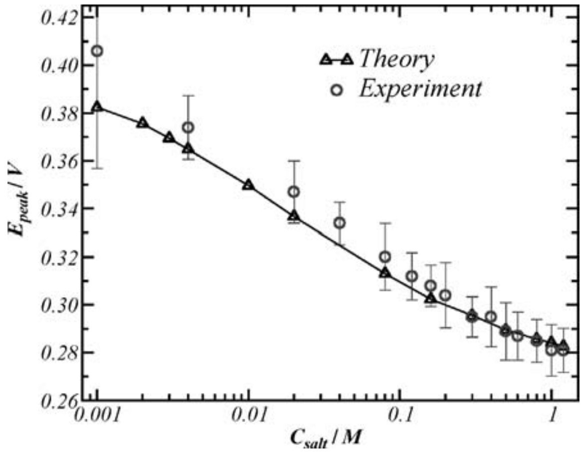

Figure 2.13 Plots of peak potential position vs. salt concentration in the bulk solution determined from the experimental and theoretical redox waves for pH = 3. Taken from Ref. [118].

Sections 2.2.5 and 2.5). This potential distribution has an influence in the predicted current–potential curves and finally in the peak potential vs. concentration plots. In Figure 2.13 we show the comparison between the predicted and measured peak potential vs. concentration plots for a single PAH-Os layer on a thiolated gold electrode and pH 3.

The data in Figure 2.13 can be fitted to Equations 2.5 or 2.6 to analyze by means of the molecular theory whether these limiting cases are applicable. We can compare, for example, the best-fitted value of $\Delta\phi_S$ in Equation 2.6 ($3.02\,\mu C\,cm^{-2}$) with that obtained by summing the charge density of the negative MPS and the positively charged PAH-Os. This calculation for a fully ionized thiol layer results in a surface charge ($-7.14\,\mu C\,cm^{-2}$) that does not correspond to the fitted value. However, if we consider the protonation of sulfonate groups predicted by the theory (which is a consequence of charge regulation [118]) then the fitted value agrees with the expected one ($3.18\,\mu C\,cm^{-2}$).

The molecular theory can also be used to examine in detail the coupling that exists between redox and acid–base equilibrium in the film [119]. A manifestation of this coupling is the dependence of the apparent redox potential of the couple with the solution pH, even for a pH-independent redox couple such as the osmium pyridine–bypyridine complex. This effect, discussed above for multilayer films, were also measured for a single layer PAH-Os. In Figure 2.14, the experimental results are compared with the prediction of the molecular theory. This figure shows two regions: for pH < 10 the number of positive charges in the film (given by the amines and the osmium complexes) remains constant and so does the peak potential. For 10 < pH < 12 deprotonation of amines with increasing pH leads to a decrease of peak potential. We expect at pH > 12, all the amines to become neutral and the peak position should be pH independent again. Note that this mechanism resembles

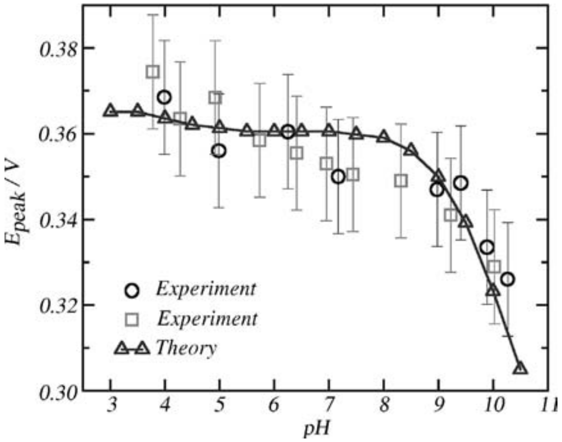

Figure 2.14 Comparison between theoretical and experimental ($\nu = 0.025$ V/s) voltammetric peak potential for electrolyte solutions of different pH (prepared from 1 mM NaOH and HNO_3 solutions containing 4 mM $NaNO_3$). Two different sets of experimental data are presented. Taken from Ref [119].

the behavior of $1e^-/1H^+$ couples [126], with the difference that here we have an electrostatic coupling between the pH-independent redox couple and the pH-dependent electroinactive acid–base group in the polyelectrolyte.

2.3.3
Coupling Between the Acid–Base and Redox Equilibria

Besides the dependence of peak potential with solution pH, there is other evidence of the acid–base and redox coupling, namely the prediction of amine deprotonation during film oxidation. Deprotonation is a response to the creation of Os(III) sites that increment the concentration of positive charges in the film. This is an example of charge regulation: a chemical equilibrium at the interface is displaced as the system tries to reduce its electrostatic charge.

It is interesting to find out the optimal conditions for the coupling between redox and acid–base equilibria. To do that, we will look at the variation of the average charged fraction upon oxidation $\Delta_{ox}\langle f_c \rangle$, defined as

$$\Delta_{ox}\langle f_c \rangle = \langle f_c \rangle(E = 0.6\,\mathrm{V}) - \langle f_c \rangle(E = 0.0\,\mathrm{V}) \tag{2.7}$$

In this equation $\langle f_c \rangle$ is the average fraction of charged amino groups in the film. Figure 2.15a shows how $\Delta_{ox}\langle f_c \rangle$ depends on the electrolyte composition and bulk pH. The maximum effect is observed at high pH and low salt concentration. The latter condition can be explained considering that at high salt concentrations, the system prefers to compensate newly created charges by counterion uptake rather than by displacing a chemical equilibrium. In Figure 2.15b we observed the pH dependence

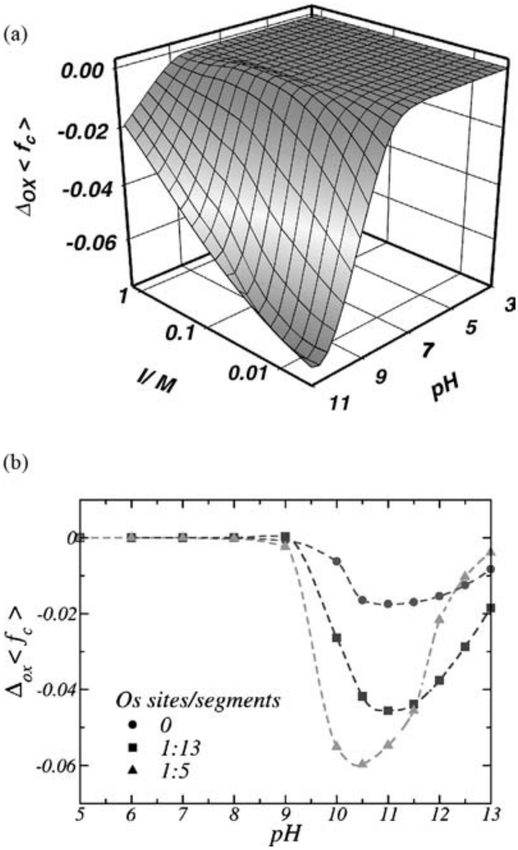

Figure 2.15 (a) Variation in the average fraction of charged amino groups from the fully reduced ($E = 0.0$ V) to the fully oxidized ($E = 0.6$ V) state (defined by Equation 2.7) calculated for solutions of different the pH and ionic strength. (b) Change in the average fraction of protonated amino groups during film oxidation as a function of solution pH for PAH-Os chains with different fraction of osmium sites to polymer segments. Calculations were performed at $I = 0.12$ M. Taken from Ref. [119].

of $\Delta_{\text{ox}}\langle f_c \rangle$ for fixed low salt concentration ($C_{\text{salt}} = 0.12$ M) and different ratios of osmium sites to allylamine units (including the situation of a nonredox film). We observe that the coupling is optimum when the solution pH is close to the apparent p*K*a (~11). This figure also shows that coupling between acid–base and redox equilibria is strongly favored by higher osmium concentrations.

2.3.4
Peak Width

For a 1e$^-$ couple, the Nernstian behavior predicts a peak full width at half-height (FWHH) of 90.6 mV. Real peak FWHH usually differs from that value. This observation has been explained by two different phenomenological models, proposed by Brown and Anson [127] and by Albery *et al.* [128]. The former assumes that due to the presence of lateral interactions between oxidized and reduced sites the free energy for oxidation depends on the fraction of oxidized sites:

$$E = E^{0'} + \frac{RT}{F}\ln\left(\frac{f_{\mathrm{Ox}}}{1-f_{\mathrm{Ox}}}\right) - \frac{RT}{F}\Gamma f_{\mathrm{Ox}} r \tag{2.8}$$

where $E^{0'}$ is the standard redox potential of the couple, f_{Ox} is the fraction of oxidized sites, Γ is the total redox site coverage and r is an interaction parameter (equal to $r_{\mathrm{O}} + r_{\mathrm{R}}$ in Anson's original work). In other words, the apparent potential of the couple ($E^{0'} - RTF^{-1}\,\Gamma f_{\mathrm{Ox}} r$) depends on the electrode potential. On the other hand, Albery's model considers that not all the redox sites in the film have the same redox potential, but a Gaussian distribution of apparent redox potential exists. Both models rely on a fitting parameter: r in the case of Brown and Anson and the width of the Gaussian distribution in Albery's model. Other models predict peak broadening such as that of Smith and White for the interfacial potential distribution in monolayer-coated electrodes [129] and Redepenning's model that takes into account the effect of charges created during a potential scan in the Donnan potential [130].

The molecular theory described in Section 2.5 is able to quantitatively predict FWHH for a single layer of PAH-Os on an electrode without the need for using adjustable fitting parameters (see Figure 2.16). It is interesting to note that the models of Brown and Anson and Albery (as well as the Donnan partition model for peak position) are limiting cases of the molecular theory, therefore the fitting parameters of these simpler models are predicted by the theory. For example, in Figure 2.8 we

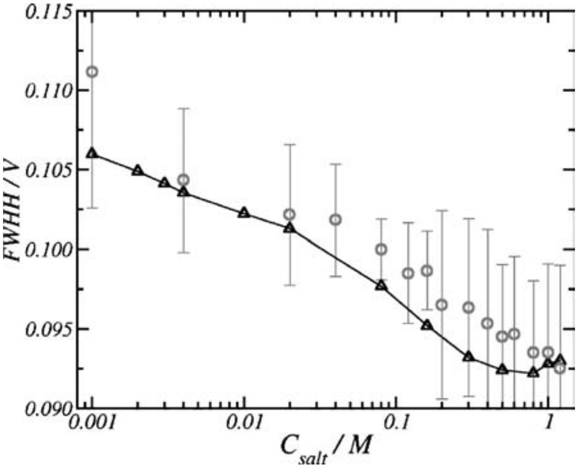

Figure 2.16 Peak width vs. salt concentration in the bulk solution determined from the experimental and theoretical redox waves in the same conditions of Figure 2.13. Taken from Ref. [118].

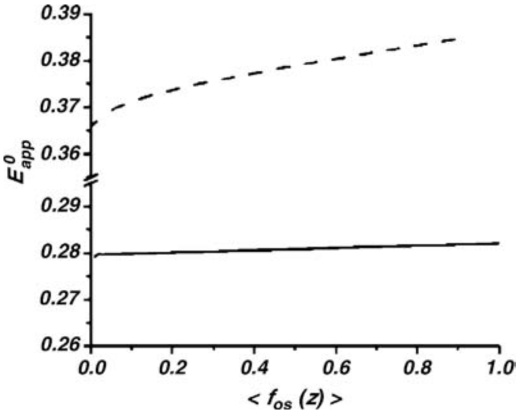

Figure 2.17 Formal Os(III)/Os(II) redox potential as a function of the average fraction of oxidized osmium sites for $C_{salt} = 1$ mM (dashed lines) or 1.2 M (solid line). From the slope it is possible to predict the lateral interaction parameters in Brown and Anson model, Equation 2.8. Taken from Ref. [120].

show an inhomogeneous fraction of oxidized osmium groups as a function of their distance to the electrode surface, which implies a z-dependent distribution of apparent redox potentials, which is conceptually equivalent to Albery's model. In addition, we can calculate the potential dependence of the average Os(III)/Os(II) apparent formal potential in the film defined as [120]:

$$E^0_{app} = E - \frac{RT}{F}\ln\left(\frac{\langle f_{Ox}\rangle}{1-\langle f_{Ox}\rangle}\right) \tag{2.9}$$

where $\langle f_{Ox}\rangle$ is the z-averaged oxidation fraction at an electrode potential E predicted by the molecular theory. In Figure 2.17 we show that the apparent formal potential predicted by the theory depends on the osmium-site oxidation fraction in the film, in line with the explanation of peak broadening based on lateral interactions.

2.3.5
Nonreversible Electrochemistry: Charge Transport

When the characteristic time for charge diffusion is lower than the experiment timescale, not all the redox sites in the film can be oxidized/reduced. From experiments performed under these conditions, an apparent diffusion coefficient for charge propagation, D_{app}, can be obtained. In early work choroamperometry and chronocoulometry were used to measure D_{app} for both electrostatically [131, 225] and covalently bound [132, 133] redox couples. Laviron showed that similar information can be obtained from cyclic voltammetry experiments by recording the peak potential and current as a function of the potential scan rate [134, 135]. Electrochemical impedance spectroscopy (EIS) has also been employed to probe charge transport in polymer and polyelectrolyte-modified electrodes [71, 73, 131, 136–138]. The methods described above require a balance of the flux of ions in and out of the film to maintain charge electroneutrality during redox switching. This process can be the rate-limiting step and therefore must be considered in the analysis of transient responses [34, 139]. The limitation was solved by Murray using steady-state techniques, where a time-independent gradient of the fraction of oxidized and reduced states is forced and therefore counterion flow is not required. In the steady state, sandwich [140] and microband electrode configurations [141] were employed. In the former, a gold layer was evaporated on a redox polymer film deposited on a conductive substrate, thus providing a second electrode. In the microband electrode, on the other hand, the polymer is deposited across the gap between two metallic band electrode contacts. In both cases, the current that flows across the system is given by:

$$i = nFCAD_{\mathrm{app}}d^{-1} \tag{2.10}$$

where d is microband separation or the film thickness in the sandwich-electrode configuration, and C is the concentration of redox-active groups.

From a theoretical point of view, charge propagation in films containing space-distributed redox centers can be achieved either by the physical displacement of the sites or by the transference (hopping) of electrons from neighboring reduced to oxidized sites or by the combination of both processes. In the case of free diffusing couples immobilized in oppositely charged polyelectrolytes, both processes occur and an apparent diffusion coefficient can be defined and measured [136, 142, 143]:

$$D_{\mathrm{app}} = D_{\mathrm{Phys}} + D_{\mathrm{e}} \tag{2.11}$$

with D_{phys} the constant for physical diffusion and D_{e} the diffusion constant for the electron-hopping process. For an immobile assembly of redox centers:

$$D_{\mathrm{e}} = \frac{k_{\mathrm{ex}}C_{\mathrm{E}}\delta^2}{6} \tag{2.12}$$

where k_{ex} is the bimolecular rate constant for electron self-exchange, δ is the center-to-center separation during self-exchange and C_{E} is the concentration of redox sites. The concentration dependence D_{e} in polyelectrolytes with freely diffusible redox centers has been addressed by Buttry and Anson [225], using the redox couples $[\mathrm{Co(bpy)_6}]^n$ (with $n = 2+/+$ or $3+/+2$). Since the couple $[\mathrm{Co(bpy)_6}]^{3+/2+}$ has a very low electron exchange rate constant, it was possible to identify from the measured values of D_{app} as a function of the redox concentration the contributions from D_{phys} and $D_{\mathrm{e-}}$. Another method to separate the contributions to D_{app} based on permeation studies was proposed by White, Leddy and Bard [131].

In the case of redox sites covalently bound to a polymer backbone, when only D_{e} contributes to charge transport, Equation 2.12 has systematically failed to explain the dependence of D_{app} with the concentration of redox sites. Blauch and Savéant have shown that for completely immobile centers, charge transport is basically a percolation process: random distribution of isolated clusters of electrochemically connected sites [33, 40]. Only by dynamic rearrangements can these clusters become in contact and charge transport occur, giving rise to the concept of bound diffusion where each site in the polymeric structure moves around its equilibrium position. To a first approximation, this motion can be regarded as harmonic, so we write:

$$D_{\mathrm{app}} = \frac{k_{\mathrm{bim}}(\delta^2 + 3\lambda^2)C^*}{6} \tag{2.13}$$

where k_{bim} is the bimolecular activation-limited rate constant for electron hopping $k_{\mathrm{bim}} = \frac{k_{\mathrm{ex}}k_{\mathrm{D}}}{(k_{\mathrm{ex}} + k_{\mathrm{D}})}$, k_{D} is the diffusion limited bimolecular rate constant and δ is the distance between adjacent redox centers in the film, while λ represents the mean displacement of a redox center out of its equilibrium position. This distance can be related to an imaginary spring $\lambda = (2k_{\mathrm{B}}\mathrm{T}/f_{\mathrm{s}})^{1/2}$, where k_{B} is the Boltzmann constant, T the temperature, and f_{s} is the spring force constant. While in this model, physical displacement of electroactive groups is not important as a long-range conducting mechanism, it is crucial to assist the electron-hopping process. Savéant and Blauch further investigated the bound diffusion model using both analytical methods and Monte Carlo simulations. Long linkers between the polymer and the electroactive groups can dramatically help by allowing the redox sites to explore larger spatial regions around their equilibrium positions. Experimental validation of this model was achieved by Mano and Heller, who synthesized a redox polymer bearing a long 13-atom spacer [41] that presents an unprecedented diffusion coefficient of $5.8 \times 10^{-6}\,\mathrm{cm^2\,s^{-1}}$, which is more than five orders of magnitude higher that those typically reported for redox polymers and very close to that of a freely diffusing molecule.

The simple models discussed above have shed light on the mechanism of charge transport, experimental observations are usually complicated by the effect of experimental variables on the structure and composition of the polymeric matrix. For example crosslinking of polymer films (which is often employed to improve film stability) partially or completely hinders charge transport [52] due to the slowdown of segmental motions and the consequent failure of redox sites to come close enough to allow an electron-transfer event. On the other hand, charge propagation can be improved by film swelling giving rise to more flexible structures [144].

Another important aspect is the effect of solution composition, that is, mobile ions and solvent. It has been demonstrated that some ions are able to ionically crosslink polymer films, decreasing the charge diffusion coefficient [145, 146, 148]. We have observed dramatic specific ionic effects, which can reduced D_{app} from $1.8 \times 10^{-10}\,\mathrm{cm^2\,s^{-1}}$ in chloride solutions to $6.6 \times 10^{-15}\,\mathrm{cm^2\,s^{-1}}$ in perchlorate electrolyte [148]. Experiments in solution contating both $\mathrm{Cl^-}$ and $\mathrm{ClO_4}^-$ showed that the effect arises from the presence of $\mathrm{ClO_4}^-$ and not by the absence of $\mathrm{Cl^-}$, supporting the ionic crosslink hypothesis. A similar mechanism has been proposed to explain the more irreversible shape of voltammperograms for PAH-Os/PVS films assembled at low pH (pH 3.5–5.5) when compared to those assembled at high pH (pH 8.3). Since PAH-Os/PVS films assembled at lower pH are thinner than those obtained at high pH (See Section 2.2.5), diffusion limitations are expected to occur first for the latter. The only possible explanation for the experimental results is therefore that the apparent electron-hopping diffusion coefficient decreases with the assembly pH. We ascribed this effect to the slowdown of segmental motions (and hence to the mobility of redox sites) by the compact structure expected for films assembled at low pH, compared to the rather floppy films obtained at higher pH.

2.4
Dynamics of Solvent and Ion Exchange

For each electron that flows across the polymer/electrode interface during the electrochemical oxidation of the redox sites in film, one positive charge is created. To maintain electroneutrality, the system can (i) incorporate anions or release cations, with the subsequent solvent uptake or release to keep the osmotic balance or (ii) protonate/unprotonate acid–base groups present in the film. The prevailing operating mechanism will be that which leads to a final state of minimal free energy. For instance, the Donnan potential model can be used to decide whether anions or cations or both would be exchanged during redox switching. Solvent exchange and coupling with acid–base equilibria can also be predicted, but require a more sophisticated molecular theory [119]. In addition, to determine which of these processes are likely to occur for each system we will also discuss in this section the rate at which they take place, that is, the dynamics of solvent and ion exchange.

2.4.1
Ion Exchange

As was mentioned before, charge compensation during oxidation in redox polyelectrolyte systems can be achieved by anion uptake or cation release. For example, for a PAH-Os/PVS-modified electrode, we can write:

$$[\mathrm{PAH{-}Os(II)^{+}\,PVS^{-}}]_{\mathrm{poly}} + \mathrm{A}^{-}_{\mathrm{aq}} \rightarrow [\mathrm{PAH{-}Os(III)^{2+}\,PVS^{-}A^{-}}]_{\mathrm{poly}} + \mathrm{e}^{-} \tag{2.14}$$

$$[\mathrm{PAH{-}Os(II)^{+}\,C^{+}.2PVS^{-}}]_{\mathrm{poly}} \rightarrow [\mathrm{PAH{-}Os(III)^{2+}\,2PVS^{-}}]_{\mathrm{poly}} + \mathrm{C}^{+} + \mathrm{e}^{-} \tag{2.15}$$

Different *in-situ* techniques provide information on ion exchange. Probe-beam deflection (PBD) measures how the refractive-index gradients in the solution adjacent to the electrode/electrolyte interface changes due to ionic fluxes [149]. In this technique, positive deflections indicate the flux of ions towards the electrode, and therefore for anodic potential jumps it means anion uptake. Cation release gives rise, under these conditions, to a negative deflection. This technique provided direct evidence of ion exchange in PAH-Os/PSS multilayers [150]. PBD oxidation transitents (Figure 2.18) show the presence of a positive peak due to anion uptake, but also a negative prepeak originated in the release of cations. Due to the difference in diffusion of proton and chloride, fitting the transitents in Figure 2.18 to the PBD analytical expressions, yields the ratio of exchanged anions to exchanged cations ($C_{\mathrm{sanion}}/C_{\mathrm{scation}}$), which gave 4.2 for positively capped multilayers and 1.4 for

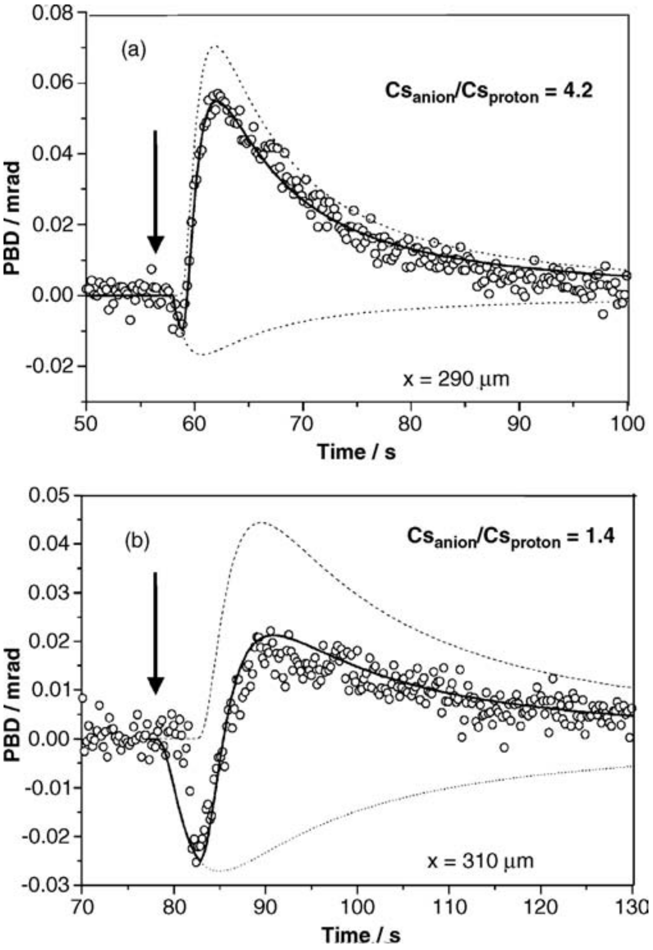

Figure 2.18 Probe-beam deflection oxidation transients for (a) positively capped $(PAH\text{-}Os)_{15}(PSS)_{14}$ and (b) negatively capped $(PAH\text{-}Os)_{15}(PSS)_{15}$ in 0.01 M HCl. Anion uptake/cation release appears as a positive/negative PBD signal. Taken from Ref. [150].

negatively capped ones. As expected, anion exchange contributes more to charge compensation for positively capped films than for those with a negative topmost layer. Note also that anion exchange is the main charge-compensation mechanism even for negatively capped films. We can explain this result considering the rules of ion exchange described in Section 2.3.2, since the testing solution (HCl 10 mM) is more acid that the assembly solutions.

Ion exchange in LbL films has been also studied using radiolabeled $^{45}Ca^{2+}$ ions [104] by Schlenoff and coworkers. In that case, poly(butylviologen)/PSS multilayers showed the exchange of Ca^{2+} in a stoichometric ratio with the charge passed through the electrode, an indication of cation permselectivity.

2.4.2
Solvent Exchange

An electrochemical quartz crystal microbalance (EQCM) is able to measure *in-situ* charges in film mass and viscoelasticity [148, 151, 153]. An important characteristic of this technique is that the exchanged mass during redox switching has contributions from both ions and solvent. EQCM experiments for PAH-Os/PVS and PAH-Os/GOx systems indicate mass gain during oxidation and loss during reduction. The amount of exchanged mass can only be explained by water fluxes that are well above ionic hydratation [148, 153] (around 30 water molecules per electron, see Table 2.1). In the case of cation permeselective films, this water flux is suggested to mask the release of cations [107]. Further molecular evidence of water uptake/release during the anodic/catodic scans has been obtained by observing the associated water IR band at 3450 cm^{-1} by subtractively normalized interfacial Fourier transform infrared spectroscopy (SNIFTIRS) [153, 154].

Indirect evidence for solvent exchange can also be gained by *in-situ* ellipsometry. This technique can provide information of film thickness and optical properties as a function of the electrode potential. Figure 2.19 shows that the film swells during oxidation and shrinks during reduction, in agreement with EQCM measurements. A decrease in the refractive index from 1.42 to 1.38 during oxidation also supports the uptake of water, which has a refractive index of 1.33.

2.4.3
Specific Ionic Effects

We have studied the electrochemical behavior and redox-driven mass changes for PAH-Os/PVS films immersed in solutions of salts with a common anion and different cations and a common cation and different anions [148]. The electrochemical and

Table 2.1 Results from CV, EIS and EQCM measurements for (PAH-Os$_5$)/(PVS$_4$) electrode in 10 mM solutions of different 1 : 1 electrolytes.

	Electrolyte	Q_{ox} μC cm^{-2}	$E_{1/2}$ V^{-1}	($E_p^{ox} - E_p^{red}$) V^{-1}	$\Delta m/\Delta q^1$ g C^{-1}	Δm g mol^{-1} (×10^3)	D_{app}/cm^2 s^{-1}
	NaCl	19.2	0.365	0.027	64 ± 9	615 ± 90	1.8×10^{-10}
Common	NaF	20.7	0.374	0.036	72 ± 9	692 ± 90	
cation	$NaNO_3$	21.1	0.359	0.025	19 ± 9	185 ± 90	
	$NaBF_4$	18.9	0.378	0.031	20 ± 9	195 ± 90	
	$NaClO_4$	17.5	0.343	0.041	6 ± 9	58 ± 90	6.6×10^{-15}
Common	CsCl	18.7	0.364	0.025	58 ±9	564 ± 90	
anion	LiCl	19.8	0.369	0.028	62 ± 9	596 ± 90	
	HCl	17.2	0.394	0.034	69 ±v9	662 ± 90	

Q_{ox}: CV anodic peak charge, $E_{1/2}$: average peak potential, $E_p^{ox} - E_p^{red}$: peak separation, Δm/Δq: exchanged mass to redox charge ratio for complete film oxidation, $\Delta m/\Delta$mol exchanged mass per mole of electrons and D_{app}: apparent diffusion coefficient measured by EIS.

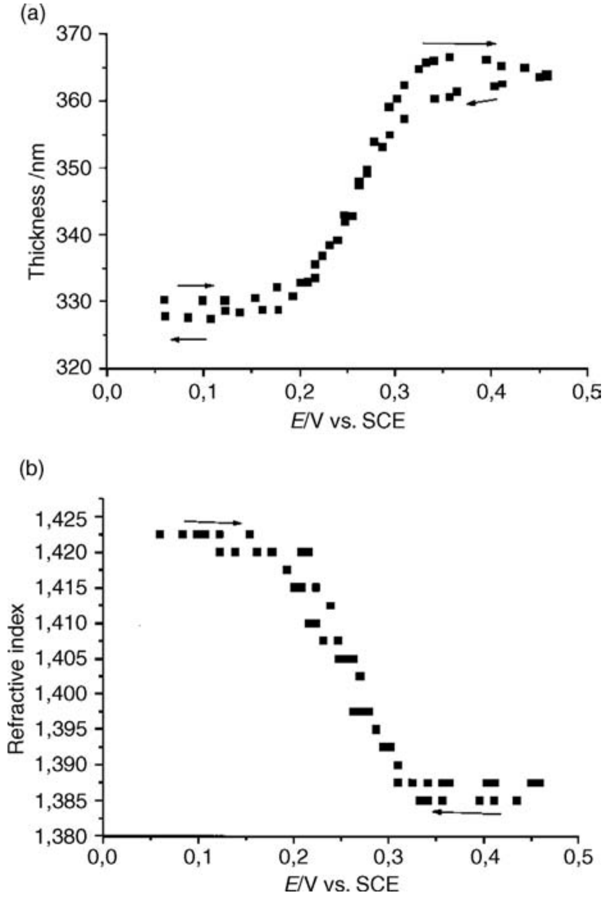

Figure 2.19 Ellipsometric thickness (a) and refraction index (b) as a function of electrode potential for a (PAH-Os)$_7$(GOx)$_7$ multilayer. Scan rate: 5 mV s^{-1}. Taken from Ref. [68].

EQCM experiments are summarized in Table 2.1, which shows the CV anodic peak charge (Q_{ox}), the average peak potential ($E_{1/2}$), peak separation ($E_p^{ox}-E_p^{red}$), the exchanged mass to redox charge ratio for complete film oxidation ($\Delta m/\Delta q$), the exchanged mass per mole of electrons (Δm/Δmol) and apparent diffusion coefficient measured by EIS (D_{app}). Table 2.1 shows some important results previously discussed, namely the inhibition effect of ClO_4^- on charge propagation, which makes voltammograms more irreversible for solutions containing this anion; the shift of peak position in HCl solution due to changes in the Donnan potential induced by amine protonation; and the exchanged molar masses under permselective conditions, larger than the molecular masses of the salt ions, indicating water exchange. There are also two salient features arising from specific ionic effects. First, Table 2.1 shows that the cation has little effect on the solvent and ion exchange (EQCM data), while large differences in molar masses of exchanged species were observed for different anions. This could be related to the anion permselectivity present in the films used in the study [107, 148]. Second, the exchanged molar masses for the anions follow a well-known Hoiffmeinster series, ordered by the exchanged mass, we have: $F^- > Cl^- > NO3^- > BF_4{}^- \gg ClO_4{}^-$. We ascribe this effect to the formation of polymer–anion ion pairs for the more hydrophobic anions, which leads to electrostatic crosslinking, and thus constrains film swelling.

2.4.4
Break-In

During continuous redox cycling, the first cycle usually differs from the following ones. This effect is referred as break-in. In poly(vinylferrocene), PVF, films this has been related to the incorporation of solvent and ions into the film, decreasing its resistivity [132]. This effect has been observed for several polyelectrolyte and polymer-modified electrodes, for example, polyaniline [155].

Break-in condition effects of this type has also been observed in redox PEMs. For example, the first voltammogram of a series always shows a larger anodic to cathodic peak separation than the subsequent ones [153]. We have performed *in-situ* EQCM studies applying a square-wave perturbation to the electrode potential, the resulting mass transients are shown in Figure 2.20a. As was discussed above, the mass increases during oxidation and reduces after reduction. However, for the freshly prepared films, the mass exchanged during the oxidation process is smaller than during reduction and therefore QCM signal increases with successive cycles. After $\sim$12 cycles a steady state is achieved and now the mass incorporated during oxidation is exactly the same as that of the released during reduction. The film can be reverted to its original state after switching off the perturbation and holding the electrode at a reductive negative potential for $\sim$1 h (Figure 2.20b).

The increase in film mass observed by EQCM during the break-in could be originated by the accumulation of water, mobile ions or both. We used SNIFTIRS to show that the water content in the film increases during cycling [153]. The role of mobile ions has been addressed for the first time by Schlenoff *et al.* using radiolabeled $^{45}Ca^{2+}$ ions. These cations flowed into poly(butylviologen)/PSS multilayers during the cathodic scan, but during the oxidation a small fraction was not expelled. As a consequence, an increase in Ca^{2+} content occurred for the following cycles [104]. The authors suggested that anion uptake occurs during reduction in the same proportion to the fraction of Ca^{2+} that was retained in the film in order to the assure charge compensation. Probe-beam deflection (PBD) has also shown differences both in the deflection signal and the electrical current transients between the first and successive oxidation–reduction cycles for freshly prepared PAH-Os/PSS films in HCl 10 mM [28] (panel A in Figure 2.22). Both the PBD signal and the electrode current show a decrease with the number of cycles. This decrease in redox current is clearly not caused by loss of electroactive material since, as happens with film mass in EQCM, the electrochemical response is recovered after holding the system at a reducing potential for a rest period (panels B–D in Figure 2.22). A possible explanation for this decay in the current could be the effect known as charge trapping [156], where potential cycling causes some reduced or oxidized sites to become isolated and therefore unable to contribute further

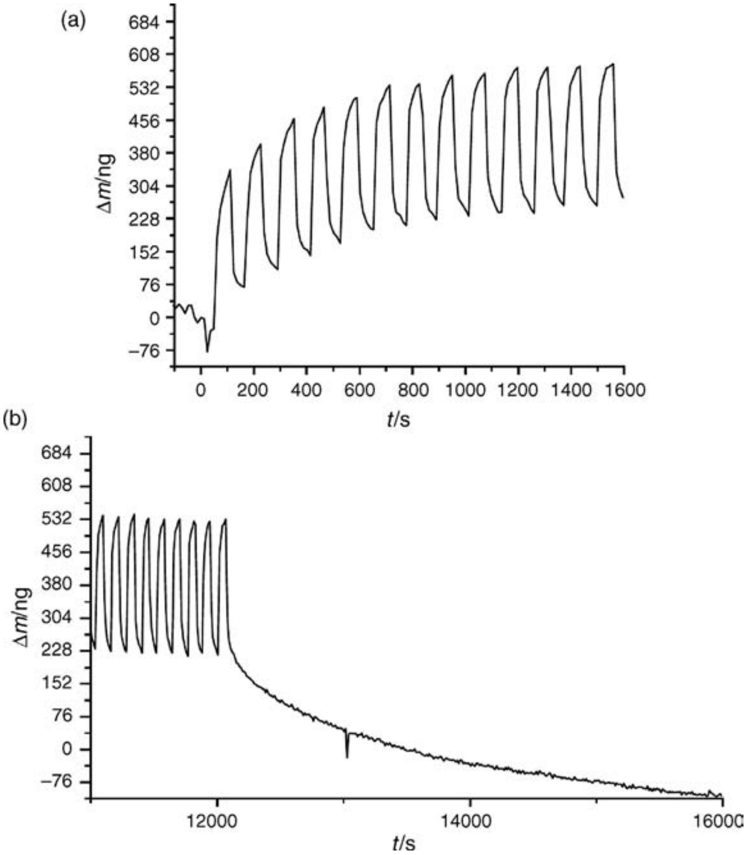

Figure 2.20 EQCM gravimetric response of $(PAH\text{-}Os)_{15}(PSS)_{14}$ multilayer in 10 mM NaCl for continuous perturbation with a square-wave potential of frequency 0.5 min^{-1} and potential limits of 0.1 and 0.6 V. (a) First cycle (b) Electrode mass transient after switching off to 0.10 V. Taken from Ref. [153].

to the redox charge. Figure 2.22 also shows that the electrochemical response for the electrode rested at a negative potential decays when redox cycling is restarted, which suggest a secondary break-in effect.

2.5
Molecular Description of Redox Polyelectrolyte-Modified Electrodes

2.5.1
Formulation of the Molecular Theory

In Sections 2.2 and 2.3 we have anticipated some results from the molecular theory for polyelectrolyte-modified electrodes. We will briefly discuss here the formulation

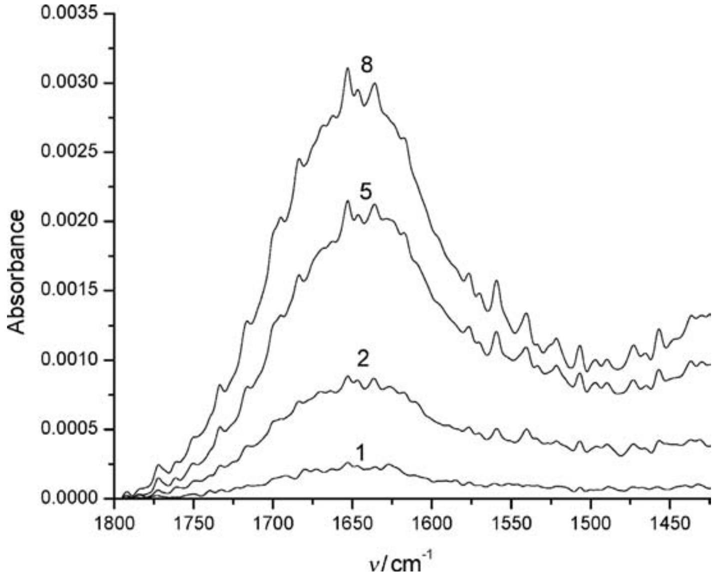

Figure 2.21 FT-IRRAS spectra for the H_2O band 1648 cm^{-1} (PAH-Os(II))$_{15}$(PSS)$_{15}$. Numbers indicate the oxidation–reduction cycle number. Taken from Ref. [153].

of the theory, which is based in the molecular theory developed by Szleifer and coworkers. For an indepth analysis the reader is referred to the original references [118–120].

The system under analysis, a single layer of PAH-Os adsorbed on a thiol-modified gold electrode, has been shown in Figure 2.5. Figure 2.23 is an explicative chart included to assist the reader to follow the steps required to formulate and solve the theory. We start by writing down the free energy of the system as a function of densities of all the mobile species in the system (solvent, protons, hydroxyl ions and salt ions), the probabilities of all possible conformations for polymer chains, the electrostatic potential and the degrees of protonation and oxidation for acid–base and redox groups, respectively. We write this free energy as

$$\begin{aligned} F = & -TS_{\mathrm{w,mix}} - TS_{\mathrm{A,mix}} - TS_{\mathrm{C,mix}} - TS_{\mathrm{H^+,mix}} - TS_{\mathrm{OH^-,mix}} - TS_{\mathrm{pol}} - TS_{\mathrm{MPS}} \\ & - TS_{\mathrm{NH_2/NH_3^+}} - TS_{\mathrm{SO_3^-/HSO_3}} - TS_{\mathrm{Os(III)/Os(II)}} + F_{\mathrm{e^-}} + F_{\mathrm{vdW}} + F_{\mathrm{Elec}} \\ & + F_{\mathrm{P\text{-}S}} + F_0 + F_{\mu_{\mathrm{C}}} + F_{\mu_{\mathrm{A}}} \end{aligned} \tag{2.16}$$

Equation 2.16 contains contributions from the translational entropy of the mobile species, the conformational entropy of polymer chains, the free energy associated with the different chemical equilibria in the system, the polymer-polymer and polymer–surface van der Waals (vdW) interaction energies, the electrostatic interaction energies and the repulsive interactions between all the different molecular species. The expressions for each of these terms are shown in Table 2.2, while the definition of the symbols is given in Appendix. Note that in Table 2.2, the densities,

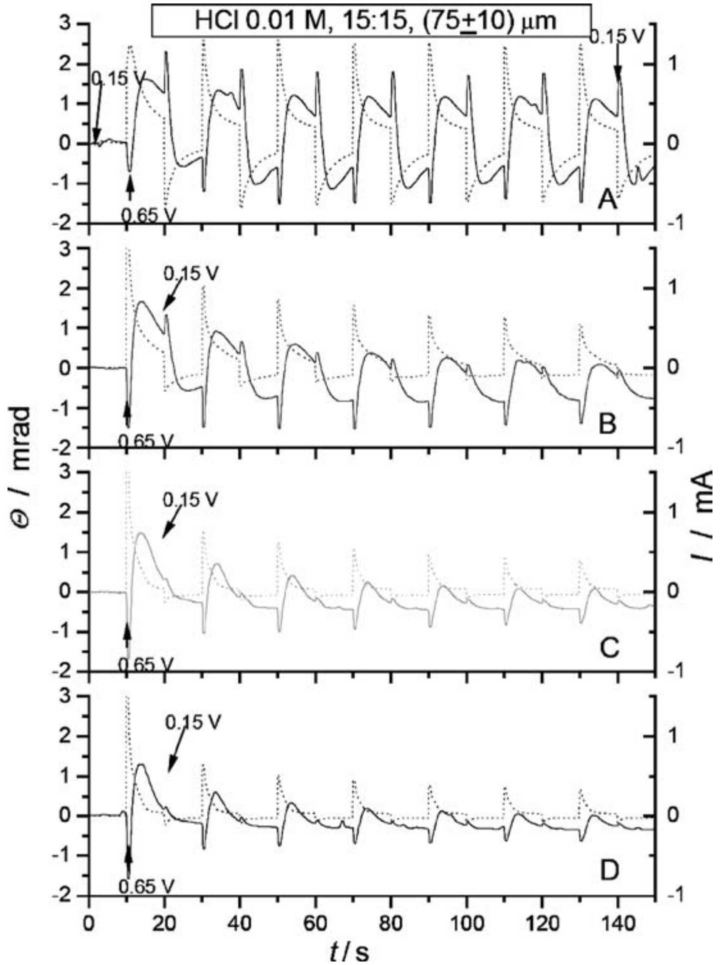

Figure 2.22 Chronoamperometric current transients (dotted lines) and probe-beam deflection transients (solid lines) during the oxidation-reduction cycles of $(PAH\text{-}Os)_{15}(PSS)_{14}$ PEM film in 10 mM HCl solution. Panels A–D show consecutive oxidation–reduction steps with a wait time of 180 s at the end of each train in the reduced state. Taken from Ref. [28].

the electrostatic potential and ionization and oxidation fractions are functions only of the distance from the electrode surface, z (see Figure 2.5). This is because we use a mean-field approximation in the x-y plane and consider only inhomogeneities in the z-direction. While this is not required by the theory, it greatly simplifies solving the equations. We now perform a functional minimization of the free energy considering two constraints: the global electroneutrality and the packing constraint, which accounts for repulsive interactions (see Table 2.2). This process provides us with an expression for the density profile of mobile ions and solvent molecules, $\rho_i(z)$; the

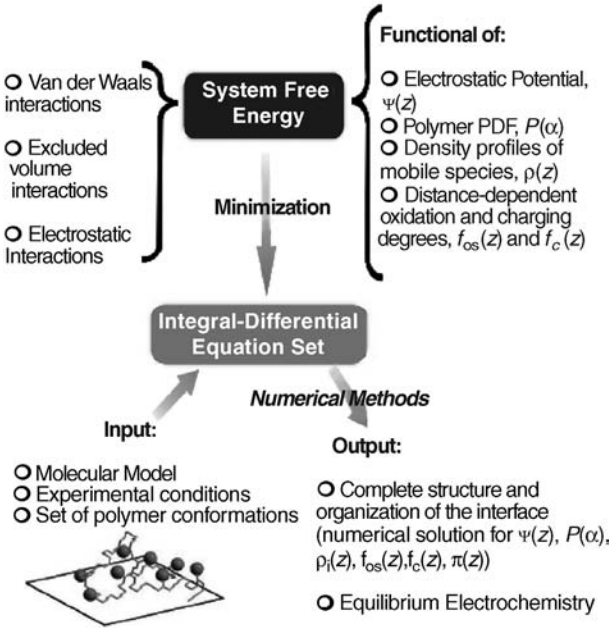

Figure 2.23 Flow chart showing the steps involved in writing down and solving the molecular theory. Taken from Ref. [120].

probability distribution function for the polymer, $P(\alpha)$; the protonation fraction of amines and sulfonates, $f_c(z)$ and $f_{c,MPS}(z)$; the osmium oxidation degree, $f_{Os}(z)$ and $\psi(z)$ the distance-dependent electrostatic potential.

The density profiles for mobile species are:

$$\rho_w(z)v_w = \rho_w^{bulk}v_w\exp(-v_w\beta[\pi(z)-\pi^{bulk}]) \tag{2.17}$$

$$\rho_i(z)v_w = \rho_i^{bulk}v_w\exp(-v_i\beta[\pi(z)-\pi^{bulk}]-q_i\beta[\psi(z)-\psi^{bulk}]) \tag{2.18}$$

where $\beta = 1/k_BT$ is the inverse absolute temperature, $\pi(z)$ is a Lagrange multiplier associated with the packing constraint, which can be regarded as a lateral osmotic pressure [117] and v_w is the molecular volume of the solvent. In Equation 2.18, $i = A$, C, H^+ or OH^- for solvent, protons, hydroxyl ions and salt ions and $v_i(z)$ and q_i are the molecular volume and charge of the species I, respectively.

The probability of having a polymer chain in conformation α is given by

$$\begin{aligned} P_P(\alpha) = \frac{1}{\xi}\exp\Bigg\{ &-\int n_P(z,\alpha)[\ln(f_c(z)) + q_{NH_3^+}\beta\psi(z)]dz + \\ &-\int n_{Os}(z,\alpha)[q_{Os(II)}\beta\psi(z) + \ln(1-f_{Os}(z))]dz - \beta U_{PS}(\alpha) \\ &-\int[v_P(z,\alpha)+v_{Os}(z,\alpha)]\Bigg[\beta\pi(z) + \int\beta\chi(|z-z'|)(\langle\phi_P(z')\rangle + \langle\phi_{Os}(z')\rangle)dz'\Bigg]dz\Bigg\} \end{aligned} \tag{2.19}$$

Table 2.2 Contributions to the system free energy considered by the molecular theory for poleyelectrolyte modified electrodes, Equation 2.16.

Terms of the free energy		
Term in eq.	**Contribution to the free energy**	**Expression**
$\frac{S_{i,\mathrm{mix}}}{Ak_\mathrm{B}}$	Translational entropy of mobile ions and water molecules (i: A, C, OH−, H+, w)	$-\int\rho_i(z)[\ln(\rho_i(z)v_w)-1]\mathrm{d}z$
$\frac{S_\mathrm{pol}}{Ak_\mathrm{B}}$	Conformational entropies of polymer chains	$-\frac{N_\mathrm{P}}{A}\left[\sum_\alpha P_\mathrm{P}(\alpha)\ln P_\mathrm{P}(\alpha)\right]$
$\frac{S_\mathrm{MPS}}{Ak_\mathrm{B}}$	Conformational entropies of thiol molecules	$-\frac{N_\mathrm{MPS}}{A}\left[\sum_\gamma P_\mathrm{MPS}(\gamma)\ln P_\mathrm{MPS}(\gamma)\right]$
$\frac{S_{\mathrm{NH_2/NH_3^+}}}{Ak_\mathrm{B}}$	Amine acid–base equilibrium mixing entropy	$-\int\langle n_\mathrm{P}(Z)\rangle[f_\mathrm{c}(z)\ln(f_\mathrm{c}(z))$ $+(1-f_\mathrm{c}(z))\ln(1-f_\mathrm{c}(z))]\mathrm{d}z$
$\frac{S_{\mathrm{SO_3^-/HSO_3}}}{Ak_\mathrm{B}}$	Sulfonate acid–base equilibrium mixing entropy	$-\int\langle n_\mathrm{MPS}(z)\rangle[f_\mathrm{c,MPS}(z)\ln(f_\mathrm{c,MPS}(z))$ $+(1-f_\mathrm{c,MPS}(z))\ln(1-f_\mathrm{c,MPS}(z))]\mathrm{d}z$
$\frac{S_{\mathrm{Os(III)/Os(II)}}}{Ak_\mathrm{B}}$	Osmium redox equilibrium mixing entropy	$-\int\langle n_\mathrm{Os}(z)\rangle[f_\mathrm{Os}(z)\ln(f_\mathrm{Os}(z))$ $+(1-f_\mathrm{Os}(z))\ln(1-f_\mathrm{Os}(z))]\mathrm{d}z$
$\frac{\beta F_{\mathrm{e^-}}}{A}$	Electrical work to achieve the final redox state of the system from electrons in the environment.	$E_\mathrm{eq}^\mathrm{abs}\beta\lvert e\rvert\int\langle n_\mathrm{Os}(z)\rangle[1-f_\mathrm{Os}(z)]\mathrm{d}z$
$\frac{\beta F_\mathrm{vdW}}{A}$	van der Waals (vdW) polymer–polymer interactions	$\int\int\frac{\beta\chi(\lvert z-z'\rvert)}{2}[\langle\phi_\mathrm{Os}(z)\rangle+\langle\phi_\mathrm{P}(z)\rangle][\langle\phi_\mathrm{Os}(z')\rangle$ $+\langle\phi_\mathrm{P}(z')\rangle]\mathrm{d}z\mathrm{d}z'$
$\frac{\beta F_\mathrm{Elec}}{A}$	Coulombic interactions	$\beta\int\left[\langle\rho_\mathrm{Q}(z)\rangle\psi(z)-\frac{1}{2}\varepsilon(z)(\nabla_z\psi(z))^2\right]\mathrm{d}z$
$\frac{\beta F_\mathrm{P\text{-}S}}{A}$	van der Waals (vdW) polymer–surface interactions	$\frac{N_\mathrm{P}}{A}\left[\sum_\alpha P_\mathrm{P}(\alpha)\beta U_\mathrm{PS}(\alpha)\right]$
$\frac{\beta F_0}{A}$	Standard chemical potentials (μ_i^0) for those species participating in chemical equilibria	$\int\langle n_\mathrm{P}(z)\rangle(f_\mathrm{c}(z)\beta\mu^0_{\mathrm{NH_3^+}}+(1-f_\mathrm{c}(z))\beta\mu^0_{\mathrm{NH_2}})\mathrm{d}z$ $+\int\langle n_\mathrm{MPS}(z)\rangle(f_\mathrm{c,MPS}(z)\beta\mu^0_{\mathrm{SO_3^-}}$ $+(1-f_\mathrm{c,MPS}(z))\beta\mu^0_{\mathrm{HSO_3}})\mathrm{d}z$ $+\int\langle n_\mathrm{Os}(z)\rangle(f_\mathrm{Os}(z)\beta\mu^0_{\mathrm{Os(III)}}$ $+(1-f_\mathrm{Os}(z))\beta\mu^0_{\mathrm{Os(II)}})\mathrm{d}z$ $+\int\mu^0_{\mathrm{H^+}}\rho_{\mathrm{H^+}}(z)\mathrm{d}z+\int\mu^0_{\mathrm{OH^-}}\rho_{\mathrm{OH^-}}(z)\mathrm{d}z$
$\frac{\beta F_{\mu_i}}{A}$	Chemical potentials of anions ($i=\mathrm{A}$) and cations ($i=\mathrm{C}$)	$-\beta\mu_i\int\rho_i(z)\mathrm{d}z$

(*Continued*)

Table 2.2 (*Continued*)

Minimization constraints	
Constraint	**Expression**
Global electroneutrality	$\int \langle \rho_Q(z) \rangle dz + \sigma_M = 0$
Packing constraint	$\sum_i \langle \phi_i(z) \rangle = 1$

where $n_i(z,\alpha)$ and $v_i(z,\alpha)$ are the number and volume of allylamine segments or osmium sites ($i = \mathrm{P}$, Os, respectively) that a PAH-Os chain in conformation α has at z, $U_{PS}(\alpha)$ is the polymer–surface interaction energy for a chain in conformation $\beta\chi(|z-z'|)$ is a distance-dependent van der Waals interaction parameter [63], ξ is a normalization constant and $\langle \phi_i(z) \rangle$ is the average volume fraction of species i at z.

In Equations 2.17–2.19, the Boltzmann factor contains contributions arising from the different interactions considered by the molecular theory. For example, $\pi(z)$ and $\psi(z)$ represent the repulsive and electrostatic interaction fields at z. It should be stressed that these fields are unknowns for the theory and that they depend on the distribution of all the different species across the film, that is, Equations 2.17–2.19. This has two consequences. First, a self-consistent solving process must be used, which means that simplicity is sacrificed in the theory in order to study the system in all its molecular complexity. Second, their interactions in the system are highly coupled and nonlocal [157].

For the acid–base equilibrium of the allyl-amines and thiol groups, the equilibrium constants are given by:

$$K_b^0 = \exp\left[-\beta \Delta G_c^0\right] = \frac{\rho_{OH^-}(z) f_c(z)}{1 - f_c(z)} \exp\left(v_{OH^-} \beta \left[\pi(z) - \pi^{bulk}\right]\right) \tag{2.20}$$

$$K_{a,MPS}^0 = \exp\left[-\beta \Delta G_{c,MPS}^0\right] = \frac{\rho_{H^+}(z) f_{c,MPS}(z)}{1 - f_{c,MPS}(z)} \exp\left(v_{H^+} \beta \left[\pi(z) - \pi^{bulk}\right]\right) \tag{2.21}$$

In this expression, K_b^0 is the thermodynamic equilibrium constant, which can be multiplied by N_A/ρ_w^{bulk} (with N_A equal to Avogadro's number) to obtain the commonly used equilibrium constants based on the molar bulk concentration reference state. It is important to note that the exponential term in the right-hand side of Equations 2.20 and 2.21 is an activity coefficient term. This term depends on the interaction field $\pi(z)$, which is nonlocal and therefore it couples with all the interactions and chemical equilibria in all regions of the film.

A generalized Nernst equation for this redox couple is also provided by the theory

$$E_{eq}^{abs} = E_{Os(III)/Os(II)}^{0,abs} + \frac{RT}{F} \ln^\circ \left(\frac{f_{Os}(z)}{1 - f_{Os}(z)} \right) + \frac{(q_{ox} - q_{red})}{|e|} \psi(z) \tag{2.22}$$

where E_{eq}^{abs} is the electrode potential and $E_{Os(II)/Os(III)}^{0,abs}$ is the standard thermodynamic redox potential in the absolute scale. Here again, the nonlocal effect is hidden in the fact that both $\psi(z)$ and $f_{\mathrm{Os}}(z)$ are strongly coupled with the other interaction fields at all distances from the surfaces.

Finally, the extremum of the free energy with respect to $\psi(z)$ yields the generalized Poisson–Boltzmann (GPB) equation for electrostatics

$$\nabla(\varepsilon(z)\nabla\psi(z)) = -\langle\rho_Q(z)\rangle \tag{2.23}$$

where $\varepsilon(z)$ is the local dielectric constant and $\langle\rho_Q(z)\rangle$ is the total average charge at distance z from the metal electrode.

We now have a set of integral-differential equations given by Equations 2.17 to 2.23 and the packing constraint in Table 2.2. We need to feed this system with the molecular information of the particular system: size, charge, charge distribution, and conformations of all the participating species, the strength of the interactions, that is, the van der Waals coefficients and the standard free energy for the appropriate acid–base and redox reactions. Table 2.3 summarizes this information. We also need the experimental conditions, that is bulk salt concentration, pH, electrode potential and surface coverage of polymer chains and thiol molecules.

The numerical solution of the theory provides us with the complete picture of the interface, namely the functions $\psi(z)$, $\rho_i(z)$, $\pi(z)$, $P(\alpha)$, $f_c(z)$, $f_{c,\mathrm{MPS}}(z)$ and $f_{\mathrm{Os}}(z)$. These functions can also be used to calculate the equilibrium electrochemistry. To do this we solve the theory for increasing electrode potentials and calculate the redox and

Table 2.3 Molecular model used in the molecular theory for gold/MPS/PAH-Os/electrolyte system.

Solution species

Specie	**Electrostatic charge q_i**	**Molecular volume, ν_i**
Water	0	30 Å^3
Cation	+1	33.5 Å^3
Anion	−1	33.5 Å^3
Proton	+1	30 Å^3
Hydroxyl ions	−1	30 Å^3

Grafted species

Specie	Electrostatic charge q_i	Molecular (segment) volume, ν_i	Equilibrium constant	Surface density (mol cm^{-2})
Polymer segment (allyl-amine)	+1 (NH_3^+) 0 (NH_2)	113 Å^3	$pK_b = 11.0$	3.5×10^{-10}
Thiol molecule	−1 (SO_3^-) 0 (HSO_3)	580 Å^3	$pK_a = 0.0$	4.6×10^{-10}
Redox site (osmium complex)	+2 (Os^{III}) +1 (Os^{II})	1770 Å^3	$E^0_{Os(III)/Os(II)} =$ 0.265 V (vs. Ag/AgCl)	2.65×10^{-11}

nonredox contributions to the electrode capacitance by rewriting as:

$$C_{\text{redox}} = F\frac{\partial \Gamma_{\text{Os(III)}}}{\partial E_{\text{eq}}^{\text{abs}}} = F\frac{\partial \int \langle n_{\text{Os}}(z)\rangle f_{\text{Os}}(z)\mathrm{d}z}{\partial E_{\text{eq}}^{\text{abs}}} \tag{2.24}$$

$$C_{\text{non-redox}} = \frac{\partial \sigma_{\text{M}}}{\partial E_{\text{eq}}^{\text{abs}}} = \frac{\partial\left(-\varepsilon(0)\frac{\partial \psi}{\partial z}(0)\right)}{\partial E_{\text{eq}}^{\text{abs}}} \tag{2.25}$$

where $\Gamma_{\text{Os(III)}}$ is the surface concentration of Os(III) and σ_{M} the charge in the metal. The total capacitance is given by the sum of C_{redox} and $C_{\text{non-redox}}$. We can use Equations 2.24 and 2.25 to calculate current potential waves and from them, the peak potentials (Figures 2.13 and 2.14) and widths (Figure 2.16) for different conditions, which are in excellent agreement with the experiments.

2.5.2
Comparison with Phenomenological Models, Advantages and Limitations

From a survey of the literature in chemically modified electrodes [13], one can identify simple phenomenological models that have been very successful for the analysis of a particular aspect of the experimental data. Such models are, for instance, the Donnan partition model [24, 122], the Laviron [158], Albery [159] and Anson models [127] to account for the nonideal peak width, the Smith and White model for the interfacial potential distribution [129], and so on. Most of these models contain one or more adjustable parameters that give some partial information about the system. For example, the lateral interaction model proposed by Anson [127] provides a value for the lateral interactions between oxidized and reduced sites, but does not explain the origin of the interactions, neither does it predict how they depend on the experimental conditions or the polymer structure. In addition, none of these models provide information on the interfacial structure.

The molecular theory presented above seeks to provide, from a first-principles calculation an all-in-one description of the electrochemical, thermodynamic and structural properties of the system, some of which cannot be accessed from the experiments. As an example, the theory can predict the density profile for the redox polymer and its components (Figure 2.6), the electrostatic potential profile across the interface (Figure 2.7), the fraction of protonated amino groups or oxidized osmium sites at different positions from the surface (Figure 2.8), and so on for any given experimental condition. Providing that the molecular model is known, it requires nonadjustable parameters and therefore it is a predictive theory. Since the models mentioned in the previous paragraph can be considered limiting cases of the theory, it can be used to test their validity under limiting cases or to predict their parameters (see Reference [120] Sections 2.3.2 and 2.3.4). The price of these advantages is a complexity that exceeds simpler models, but it is necessary to obtain a complete picture of these complicated systems (which cannot be accessed nowadays through molecular simulations due their size). The main limitation of the current formulation of the theory is that it is an equilibrium theory and therefore only accounts for the equilibrium electrochemistry (low scan rate). This limitation would be overcome in the future by coupling the theory to a generalized diffusion approach [160].

2.6
Applications

We will discuss here applications of polyelectrolyte-modified electrodes, with particular emphasis on layer-by-layer self-assembled redox polyelectrolyte multilayers. The method offers a series of advantages over traditional technologies to construct integrated electrochemical devices with technological applications in biosensors, electrochromic, electrocatalysis, corrosion prevention, nanofiltration, fuel-cell membranes, and so on.

Unique features of the LbL films are flexibility in the design, control over film composition, structure, thickness, surface charge and the almost endless list of building blocks that can be used. The method is also environmentally friendly since it does not require the use of nonaqueous solvents and can be applied to substrates of any shape and size, allowing deposition of polymers from aqueous solutions in a cost-effective technology. The latter characteristic made it very appealing for the modification of large-area electrode materials commonly used in electrochemistry. The long assembly times that are probably the main limitation of the technique, have been eliminated by using spin- [161], spray- [162] or electrophoretic-assisted deposition [163, 164]. Table 2.4 presents a summary of some of the proposed applications for redox-active PEMs. Excellent reviews can be found in the literature covering the applications of PEMs to other technologies [3, 165–169].

2.6.1
Amperometric Enzymatic Electrodes

The aim of electrochemical biosensors is the molecular recognition of a target biomolecule and the generation of an optical or electrical signal by transducing the concentration of an analyte into an amperommetric or potentiommetric signal. The use of redox polyelectrolytes as electron relays in enzymatic electrodes was first proposed by Heller, who wired GOx with a cationic polyelectrolyte quaternized poly (vinylpyridine) and poly (vinylpyridine)-Os (bpy)$_2$Cl redox-mediator copolymer [35]. While the first-generation biosensors relied on detecting the H_2O_2 generated during oxygen reduction by the enzyme [170], in an immobilized mediator system, the redox sites in the polymer 'wires' the enzyme to the electrode. The latter strategy solves two important drawbacks of first-generation sensors, namely the interference from electroactive species and the signal dependence on the partial O_2 pressure [171, 172]. In addition, the use of covalently bound couples rules out the leaching of toxic species into the solution, allowing *in-vivo* measurements.

Structurally well-defined enzyme electrodes wired by redox polymers have been constructed using different interactions, such as antigen–antibody [173–175] or avidin–biotin [176–181]. Hodak *et al.* described for the first time the layer-by-layer

Table 2.4 Applications of PEM-modified electrodes.

Application	Polycation	Polyanion	Ref.
Amperometric glucose biosensors	Ferrocene-modified polyallylamine (PAH-Fc)	Glucose oxidase (GOx)	[77]
	Osmium-pyridil-bipyridyl-modified Polyallylamine (PAH-Os)	Glucose oxidase (GOx)	[68, 69, 151, 184, 185, 191, 203–205]
Nitrite sensor	Osmium-bipyridyl-modified quaternized poly(4-vinylpyridine) (PVP-Os)	PSS or poly[aniline-co-N-(3-sulfopropyl)aniline (PAPSH)	[206]
Ascorbic acid sensor	Osmium (4,4′-dimethyl-2,2′-bipyridil)-modified poly(vynil imidazole)	Citrate-capped gold nanoparticles	[207]
Fructose, H_2O_2 and methanol sensors	Osmium-bipyridyl-modified quaternized poly(4-vinylpyridine) (PVP-Os)	Fructose dehydrigenase (FDH), Horseradish peroxidase (HRP) or alcohol oxidase	[102]
Superoxide sensor	Cytochrome c (cyt. c)	Poly(anilinesulfonic acid) (PASA)	[92, 214, 215]
Nitrate sensor	Viologen-functionalized polyvinylpyridinium (PV)	Nitrate reductase	[189]
Electrochromic devices	Poly(butanyl viologen) (PBV)	PSS	[67, 104, 209]
	poly(diallyldimethylammonium chloride) (PDDA)	Poly(alkoxythiophene) derivatives (P3TOPS and P3TOPA)	[103]
	Positive charged water-soluble polythiophenes	Negative charged water-soluble polythiophenes	[220–222]
	Poly(diallyldimethylammonium chloride) (PDDA) or polyethylene amine (PEI)	Iron hexacyanoferrate (Prussian Blue)	[29, 63]
	Linear poly(ethylene amine) (LPEI) Polyaniline (PANI)	PEDOT:PSS PANI poly(2-acrylamido-methane-2-propanesulfonic acid) PAMPS	[196]
	LPEI	Ruthenium Purple	[197]
	PAH	Polyoxometallates	[85, 86, 198]
Photochromic/ electrochromic devices	Poly(diallyldimethylammonium chloride) (PDDA)	Sodium decatungstate	[223]
Electrocatalytic devices	Poly(allyl-amine) (PAH)	Wheel-shaped (Mo36 and Mo46); crown-shaped (Mo54); sphere-shaped $Mo_8V_2O_{28}.7H_2O$	[81–84]

Table 2.5 Data for the oxidation of GOx($FADH_2$) by ferrocenium in different enzyme electrodes (taken from [147].)

Enzyme–mediator system	$k/M^{-1}\,s^{-1}$
GOx soln. + FcMeOH soln.	1.2×10^7
GOx immob. biotin + FcMeOH soln.	1.2×10^7
GOx immob. biotin + PEGFc soln.	2.2×10^5
GOx immob. biotin + PEGFc attached	1.6×10^6
GOx immob. IgG + PEGFc soln.	6.0×10^5
GOx immob. IgG + PEGFc attached	1.0×10^4

self-assembly of a redox polymer (ferrocene-derivatized PAH) and an enzyme (GOx) to yield a totally immobilized multilayer biosensor [77]. The sensitivity of the biosensor to glucose increases with the number of layers, as shown in Figure 2.24 [77, 182]. Several papers employing similar strategies followed that initial report, involving in general redox polymers based on osmium complexes [182–186] or ferrocenes [187, 188] (see Figure 2.4). Polyviologen has also been used to wire nitrite reductase, due its negative redox potential close to −0.5 V [189].

The LbL methods have been also used to prepare spatially ordered bienzymatic electrodes, two examples are shown in Figure 2.25. In the first one, glucose is aerobically oxidized by GOx in the outer layers to produce hydrogen peroxide that is thereafter reduced by soybean peroxidase (SBP) wired to the electrode with PAH-Os [182]. This system responds both to H_2O_2 and to glucose, but in the

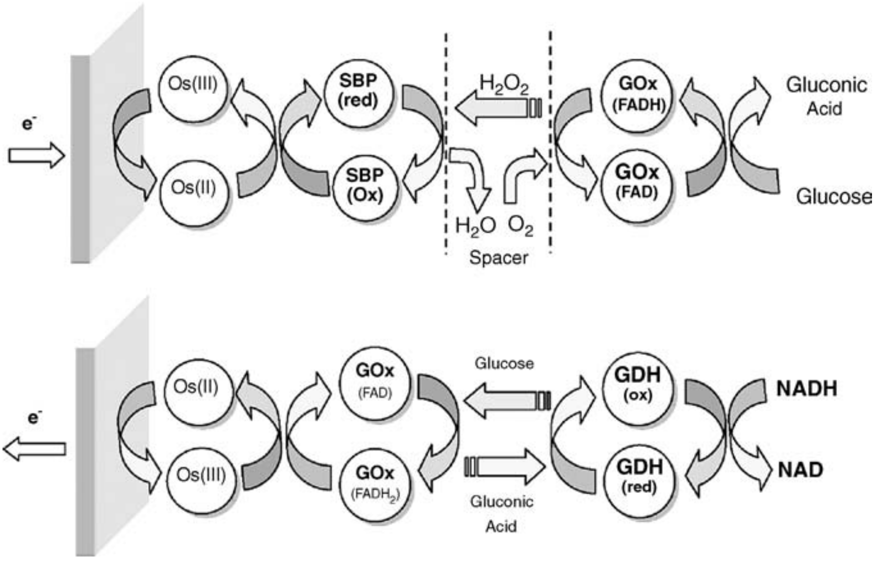

Figure 2.24 Diagrams of bienzymatic spatially ordered electrodes built using the LbL method. SBP: Soybean peroxidase, GOx: Glucose oxidase, GDH glucose dehydrogenase.

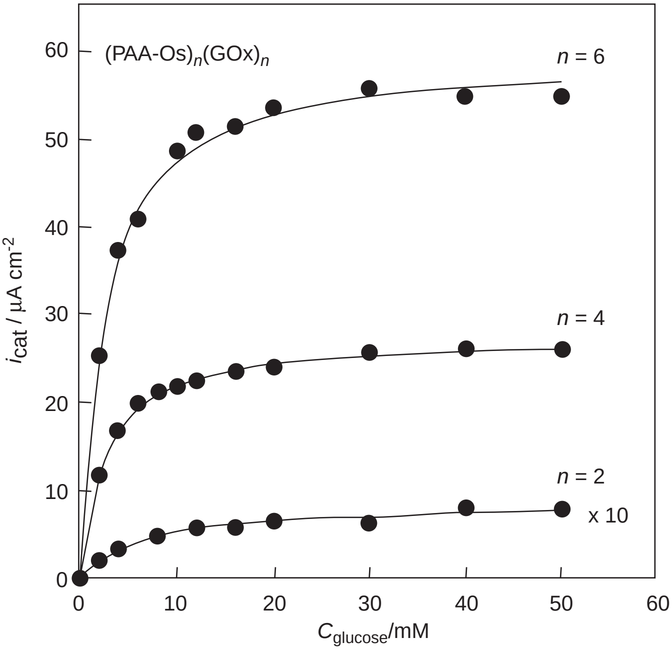

Figure 2.25 Dependence of the catalytic current for the oxidation of β-D-glucose mediated by the redox polyelectrolyte film for different number of GOx layers self-assembled with (PAH-Os)$_n$(GOx)$_m$ ($n = m = 2, 4, 6$). Taken from [182].

latter case the electrochemical signal can be suppressed by thoroughly eliminating the dissolved oxygen using Ar bubbling. A similar system has been proposed for methanol quantification replacing the GOx by alcohol dehydrogenase, which otherwise cannot be directly wired by the redox polymer [190]. The second example consists of a PAH-Os/GOx glucose sensor coated with a layer glucose dehydrogenase (GDH) that reduces gluconic acid back to glucose in presence of β-NADH$_2$. This extra layer recycles glucose, producing the amplification of the catalytic current to more than double the value recorded in absence of β -NADH$_2$ [182].

The major part of the reports discussed above provides only a qualitative description of the catalytic response, but the LbL method provides a unique opportunity to quantify this response in terms of enzyme kinetics and electron-hopping diffusion models. For example, Hodak *et al.* [77] demonstrated that only a fraction of the enzymes are wired by the polymer. A study comprising films with only one GOx and one PAH-Os layer assembled in different order on cysteamine, MPS and MPS/PAH substrates [184] has shown a maximum fraction of 'wired enzymes' of 30% for the maximum ratio of mediator-to-enzyme, $[\mathrm{Os}]/[\mathrm{GOx}] \approx 100$, while the bimolecular FADH$_2$ oxidation rate constant remained almost the same, about $5–8 \times 10^3\ \mathrm{M}^{-1}\ \mathrm{s}^{-1}$ in all cases. This result suggests that the wiring efficiency depends on the ability of the tethered redox groups to reach the FAD site at the enzyme by segmental motion of the polymer chains. In other experiments, an active GOx layer was assembled in different

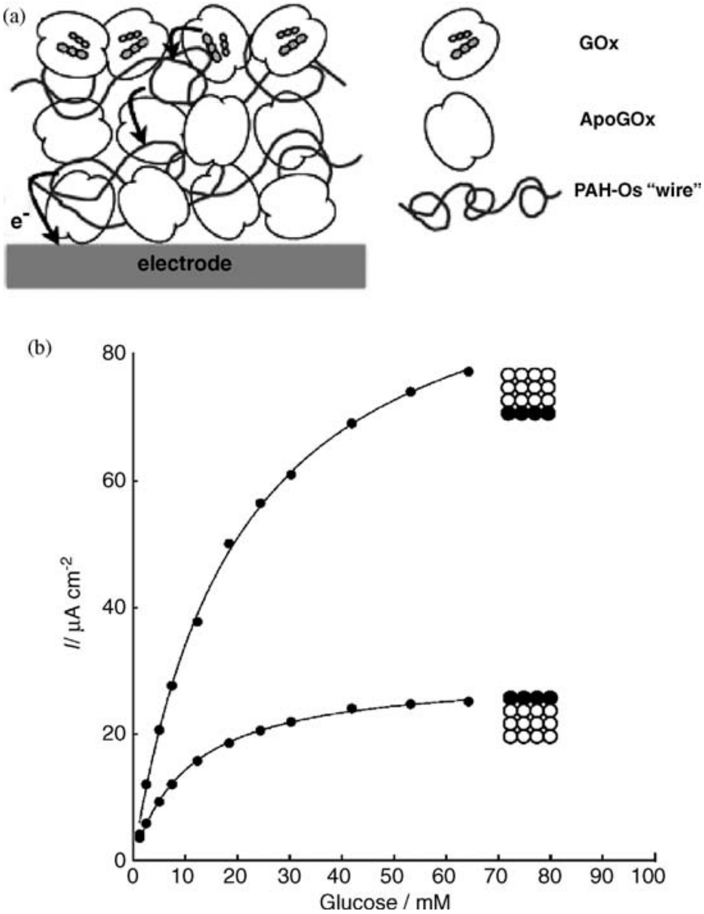

Figure 2.26 (a) Scheme for an electrostatically self-assembled multilayer $(PAHOs)_4(Apo\text{-}GOx)_3(GOx)$ electrode. (b) Catalytic current response to β-d-glucose concentration for self-assembled nanostructured thin films of PAH-Os/GOx/(PAH-Os/$(ApoGOx)_3$ and $(PAH\text{-}Os/ApoGOx)_3$/PAH-Os/GOx, where ApoGOx is FAD-free glucose oxidase. Taken from Ref. [219].

positions in a FAD-free GOx (Apo-GOx)/PAH-Os multilayer (Figure 2.26a). The electrocatalytic response of these systems (Figure 2.26b) decreases as the enzyme active layer is moved out from the surface, following a diffusion-like law [191]. Limitations in charge transport through the multilayer are therefore other important issues that could affect the fraction of wired enzymes. It is interesting to note that this kind of experiment is not possible with conventional ramdom films or hydrogels.

A quantitative model for the electrocatalyitic response of enzymatic amperometric biosensors requires consideration of the diffusion of all the involved species and the kinetics of the redox–enzyme catalytic cycle, as is depicted in Figure 2.27.

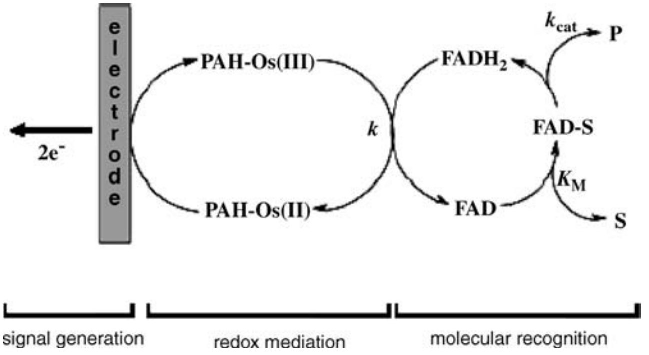

Figure 2.27 Double catalytic cycle that gives rise to the current in the presence of β-D-glucose. GOx(FAD) oxidizes the enzyme substrate β-D-glucose to yield the reduced form of the enzyme GOx($FADH_2$) that is then reoxidized by the osmium polymer mediator PAH-Os(III). This process yields PAH-Os(II). Electrons should diffuse to the electrode surface by electron hopping between adjacent osmium redox sites in the polymer film and finally the osmium sites in contact with the electrode generate of an amperometric catalytic anodic current. k_{cat}: rate constant for dissociation of enzyme–substrate complex, K_{MS}: Michaelis constant, k: second-order rate constant for the reaction between the enzyme and the mediator. Taken from Ref. [69].

This kinetic-diffusion problem in the steady state can be described by the coupled second-order differential equations:

$$D_M \frac{d^2 m(x,t)}{dx^2} = \frac{k k_{cat} m\, s\, e_\Sigma}{k\, s(K_{MS}+s)+k_{cat} s} \tag{2.26}$$

$$D_S \frac{d^2 s(x,t)}{dx^2} = \frac{k k_{cat} m\, s\, e_\Sigma}{k\, m(K_{MS}+s)+k_{cat} s} \tag{2.27}$$

where m and s are the concentration of the oxidized mediator and the substrate, D_M and D_S are the respective diffusion coefficients, k_{cat} is the rate constant for dissociation of the enzyme–substrate complex, K_{MS} is the Michaelis constant and k is the second-order rate constant for the reaction between the enzyme and the mediator, e_Σ is the total enzyme concentration, (see Figure 2.27).

Equations 2.26 and 2.27 cannot be solved analytically except for a series of limiting cases considered by Bartlett and Pratt [147, 192]. Since fine control of film thickness and organization can be achieved with LbL self-assembled enzyme polyelectrolyte multilayers, these different cases of the kinetic case-diagram for amperometric enzyme electrodes could be tested [147]. For the enzyme multilayer with entrapped mediator in the mediator-limited kinetics (enzyme–mediator reaction rate-determining step), two kinetic cases deserve consideration in this system: in both cases I and II, there is no substrate dependence since the kinetics are mediator limited and the current is potential dependent, since the mediator concentration is potential dependent. Since diffusion is fast as compared to enzyme kinetics, mediator and substrate are both approximately at their bulk concentrations throughout the film in case I. The current is first order in both mediator and enzyme concentration and k, the enzyme reoxidation rate. It increases linearly with film thickness since there is no substrate polarization. On increasing the rate of mediator–enzyme reaction or the film thickness) we cross the border from case I to II

$$I_{\mathrm{I}} = nFAa_{\varepsilon}m_{\Sigma}ke_{\Sigma}L \tag{2.28}$$

where m_{Σ} is the total concentration of the redox mediator, a_{ε} is $1/(1+\exp[-(E-E^0)nF/RT])$, L is the thickness of the film.

In case II, the mediator is exhausted within the film before reaching the outside. The reaction occurs only in a first-order layer and the current becomes independent of film thickness, half-order in enzyme concentration, k and D_{M} (mediator diffusion coefficient within the film).

$$I_{\mathrm{II}} = nFAa_{\varepsilon}m_{\Sigma}(D_{\mathrm{M}}ke_{\Sigma})^{1/2} \tag{2.29}$$

In case V for the enzyme–substrate limiting case, the current is independent of mediator concentration and thus of the potential, while there is a Michaelis–Menten dependence on substrate concentration. Case V is similar to case I since the concentrations of both substrate and mediator remain almost constant throughout the film, while in case IV the substrate is depleted and never reaches the electrode surface

$$I_{\mathrm{V}} = \frac{nFALe_{\Sigma}k_{\mathrm{cat}}K_{\mathrm{S}}s_{\mathrm{bulk}}}{K_{\mathrm{MS}} + K_{\mathrm{S}}s_{\mathrm{bulk}}} \tag{2.30}$$

where K_{S} is the partition coefficient for the substrate and s_{bulk} is the substrate bulk concentration.

A special case of the thin-film approximation considers that the substrate can diffuse within the film with negligible depletion. This corresponds to both Case V (unsaturated enzyme), Case I (saturated enzyme) and the border between them. A thin film is the only situation where we can fit experimental data to a theoretical calibration curve for the whole range of glucose concentrations with:

$$I = \frac{nFALe_{\Sigma}k_{\mathrm{cat}}}{1 + \frac{k_{\mathrm{cat}}}{km} + \frac{K_{\mathrm{MS}}}{s_{\mathrm{bulk}}}} \tag{2.31}$$

In the boundary between cases I and V, which corresponds to $E_{1/2} = E^{o'}$, and the half-wave potential shifts with the substrate concentration

$$\exp\left[-\frac{(E_{1/2}-E^0)F}{RT}\right] = \frac{km_{\Sigma}K_{\mathrm{MS}}}{k_{\mathrm{cat}}s_{\mathrm{bulk}}} + \frac{km_{\Sigma}}{k_{\mathrm{cat}}} - 1 \tag{2.32}$$

As a consequence, the half-wave potential of the catalytic waves $E_{1/2}$ in glucose solutions shifts to more negative values with respect to the formal standard redox potential of the Os(III)/Os(II) redox couple, $E^{o'}$. This corresponds to the transition from the enzyme–substrate rate-determining step to the enzyme–mediator control [147, 193] (i.e. cases I and V in the kinetic case diagram) and is shown in Figure 2.28 taken from Ref. [186]. From the slope and the intercept the value $K_{\mathrm{MS}} = 19$ mM can be obtained. This trend has also been shown by Bartlett and Pratt [147] and Savéant and coworkers [194] for glucose oxidase, and Andreau *et al.* for horseradish peroxidase [195].

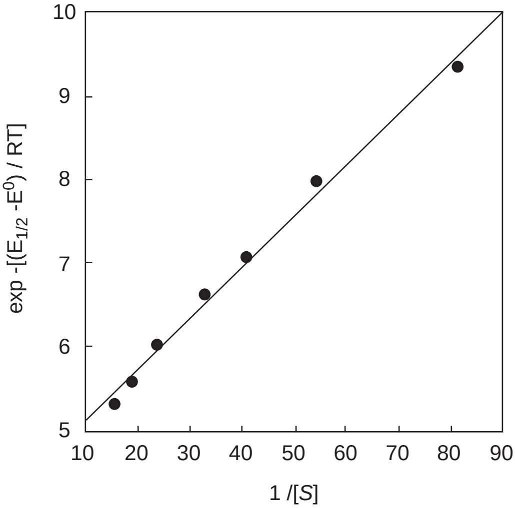

Figure 2.28 Diagnostic plot of Equation 2.32 taken from Ref. [147].

The boundary between cases I-II has been explored by Flexer *et al.* [69] with LbL self-assembled GOx multilayers and poly(bipyridine-pyridine) redox polymer (PAH-Os). Figure 2.29 shows the catalytic response in excess glucose as a function of the number of self-assembled polymer–enzyme bilayers. For the first bilayers (thin films)

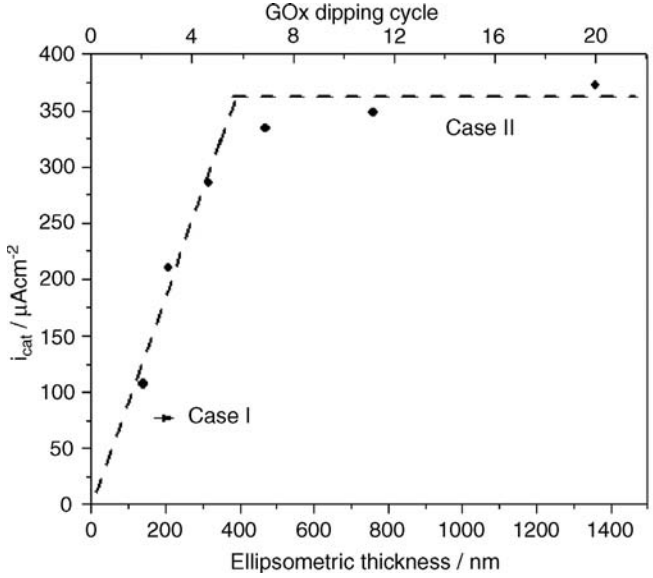

Figure 2.29 Plot of catalytic current for layer-by-layer self-assembled GOx and PAH-Os at 0.55 V in 60 mM glucose for increasing film ellipsometric thickness. Lines indicate limiting cases I and II. Taken from Ref. [147].

the current increases proportionally with the number of enzyme layers as expected for case I. However, for thicker enzyme films the catalytic current is no longer proportional to the film thickness and reaches a plateau when the conditions for Case II are reached. The boundary condition between Cases I and II appears at $L = (D_M/ke_\Sigma)^{1/2}$and this critical thickness is reached after some ten dipping cycles or 770 nm in Figure 2.29 for $D_M = 1.2 \times 10^{-9}\,\text{cm}^2\,\text{s}^{-1}$, $k = 2 \times 10^4\,\text{M}^{-1}\,\text{s}^{-1}$, $e_\Sigma = 5 \times 10^{-4}\,\text{M}$.

2.6.2
Electrochromic Devices

Electrochromic materials are electroactive compounds whose visible spectra depend on the oxidation state. Possible applications are smart windows, displays, mirrors, and so on. Among the most important performance aspects in electrochromic materials, the reversibility and lifetime of the material to repeated cycles, the time of response (usually in order of seconds), the colors of the oxidized/reduced forms and the change in absorbance upon redox switching (contrast) are of interest.

The first demonstration of a PEM with electrochromic properties was disclosed by Schlenoff and coworkers [66], using poly(butanylviologen)/PSS films. While this film exhibited strong electrochromic response, it still required the use of an outer electrolyte solution. DeLongchamp and Hammond disclosed for the first time a solid-state device comprised of two electrochromic PEM-modified ITO electrodes separated by a 200-μm thick poly(2-acrylamido-methane-2-propanesulfonic acid), proton-conducting PAMPS membrane (see Figure 2.30) [196]. Both PEMs used in

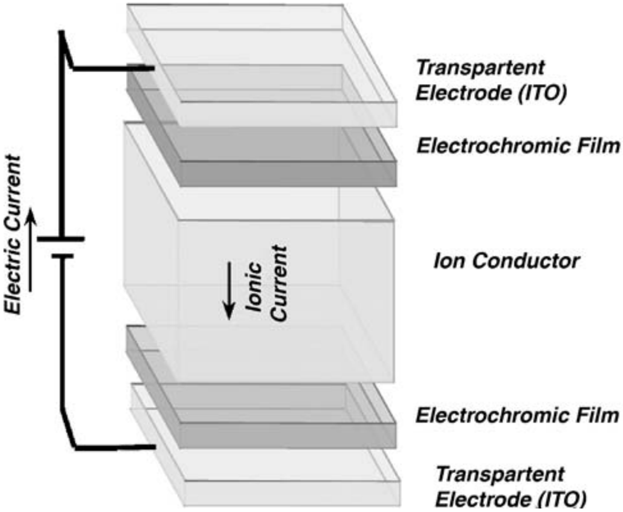

Figure 2.30 Scheme of a solid electrochromic device. The device can operate with two electrochromic films as shown or with an electrochromic and an ion-storage film.

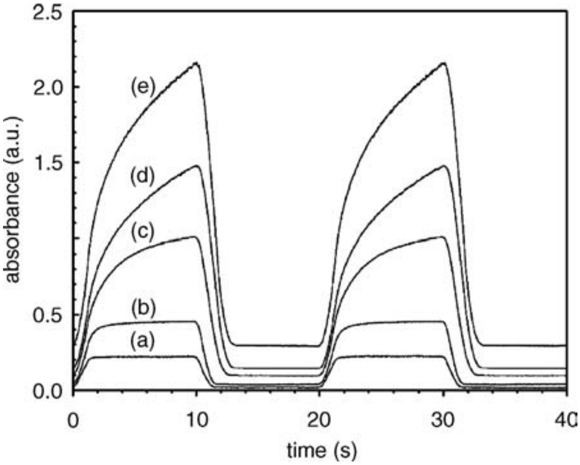

Figure 2.31 Effect of film thickness on the absorbance response of a PXV/PEDOT:PSS films bearing (a) 20; (b) 30; (c) 40; (d) 50 and (e) 60 bilayers. Square-wave potential between 0.5 V and −0.9 V and a period of 20 s was employed. Taken from [196].

this work were electrochromic and present complementary color: the PEDOT-PSS/LPEI anode is blue in the reduced state and pale blue in the oxidized form, while the PANI/PAMPS cathode is pale yellow in the reduced form and green in the (emeraldine) oxidized form.

The ability of the LbL method to accurately control film thickness through the number of layers is an important consideration for device design. For instance, Figure 2.31 shows that films bearing a large number of layers have high contrast but slow response, whereas the opposite is true for thin multilayers. DeLongchamp and Hammond reported one of the highest contrast for PEM-based devices of 82.1% [196] using PXV/PEDOT-PSS. Very recently, an impressive contrast of 84% was reported by Jain *et al.* [197]. The authors used Ruthenium Purple crystals and LPEI to build high-constrast solid-state devices with fast subsecond response times. Similar electrochromic hybrid inorganic/polymeric materials based on Prussian Blue [196], POMs [85, 86, 198], WO_3 [199, 200] and MnO_2 [200] have been reported in the literature.

2.7
Conclusions

Electrode surfaces can be modified by redox polyelectrolytes via a sol-gel process, yielding random redox hydrogels or by layer-by-layer self-assembly of different redox and nonredox polyelectrolytes by alternate electrostatic adsorption from solutions containing the polyelectrolytes to produce highly organized redox-active ultrathin multilayers.

The polyelectrolyte-modified electrodes show characteristic features such as Donnan permselectivity, ion and solvent exchange during redox switching, swelling and viscoelastic changes associated with changes in the redox state, electron-hopping-bound diffusion by segmental motion of polyelectrolyte chains carrying the redox moieties, counterion diffusion, and so on.

The LbL strategy to chemically modify electrodes with redox polyelectrolyte films has become an important tool for the fabrication of devices and electrodes with important future applications in biosensors, electrochromic devices, electrocatalysts, corrosion-resistant coatings, and so on.

Hybrid inorganic–organic–biological components can easily be built into highly organized films on materials surfaces of any shape and composition, with advantages over other layered coatings such as Langmuir–Blodgett films for real applications.

The unique ability of these LbL redox multilayer systems with control of film thickness on the nanometer scale, the composition and thickness of each alternate layer separately as well as the surface charge by choice of the topmost layer brings about design and tailored properties of devices with important applications.

These features will not only result in new industrial applications but in new ways to investigate mechanisms of charge and mass transport following molecular recognition, and ion and solvent exchange during redox switching that would otherwise be impossible with random hydrogels built with the same polyelectrolyte component building blocks. Modern computational techniques allow a molecular description of these complex systems where nonlocal coupling of different interaction fields determine the film properties.

Emerging new technologies such as spray deposition of alternate polyelectrolyte layers in LbL multilayers will reduce the deposition time to 1 s per layer, which will open up possibilities of real applications in electrochemical science and technology.

Appendix: List of abbreviations

N_P/A	number of polymer chains per unit area
N_{MPS}/A	number of thiol molecules per unit area
β	inverse temperature, $(k_{B.}T)^{-1}$.
k_B	Boltzmann constant
e	elemental charge
F	Faraday constant
$K^0_{a,MPS}$	Thermodynamic equilibrium constant for amine deprotonation
$K^0_{b,MPS}$	Thermodynamic equilibrium constant for thiol sulfonate protonation
$E^{0,abs}_{Os(II)/Os(III)}$	Standard reduction potential for the Os(II)/Os(III) couple in PAH-Os
v_i	molecular volume of the species i (i = w, H + , OH-, C, A for water molecules, proton, hydroxyls, cations and anions respectively)

q_i	charge of the species i in units of elemental charge
$\rho_i\ (z)$	number density of species i at z
$\phi_i(z)$	volume fraction of the species i at z
$P_P(\alpha)$	probability of having a polymer chain in the conformation α
$P_{MPS}(\gamma)$	probability of having a thiol chain in conformation γ
$f_c(z)$	fraction of charged amino groups at z
$\langle f_c\rangle$	average fraction of charged amino groups
$\Delta_{ox}\langle f_c\rangle$	change in the average fraction of charged amino groups upon oxidation
$f_{c,MPS}(z)$	fraction of charged sulfonate groups at z
$\langle f_{c,MPS}\rangle$	average fraction of charged sulfonate groups
$\Delta_{ox}\langle f_{c,MPS}\rangle$	change in the average fraction of charged sulfonate groups upon oxidation
$\langle z\rangle$	average film thickness
$\Delta_{ox}\langle z\rangle$	change in the average film thickness upon oxidation
$f_{Os}(z)$	fraction of oxidized osmium sites at z
$n_P(z, \alpha)$	number of polymer allyl-amine segments that a chain in conformation α has at z
$n_{Os}(z, \alpha)$	number of osmium sites that a chain in conformation α has at z
$v_P(z, \alpha)$	volume occupied at z by polymer segments for a chain in conformation α
$v_\mathrm{Os}(\mathrm{z}, \alpha)$	volume occupied at z by the redox sites for chain in conformation α
$\langle n_P\ (z)\rangle$	average density of polymer segments at z, $\sum_\alpha P_P(\alpha)n_P(z,\alpha)$
$\langle n_{MPS}(z)\rangle$	average density of thiols at z
$\langle n_{Os}\ (z)\rangle$	average density of redox sites at z, $\sum_\alpha P_P(\alpha)n_{Os}(z,\alpha)$
$\langle\phi_P\ (z)\rangle$	average volume fraction occupied by the polymer backbone at z, $\sum_\alpha P_P(\alpha)v_P(z,\alpha)$
$\langle\phi_{MPS}\ (z)\rangle$	average volume fraction occupied by the thiol at z
$\langle\phi_{Os}\ (z)\rangle$	average volume fraction of osmium sites at z, $\sum_\alpha P_P(\alpha)v_{Os}(z,\alpha)$
E_{eq}^{abs}	electrode potential of the metal in the absolute scale
E	electrode potential against Ag/AgCl reference electrode
ψ_M	Electrostatic charge on the metal
C_{redox}	Electrode redox capacitance
$C_{non\text{-}redox}$	Electrode non-redox capacitance
$\chi(\lvert z-z'\rvert)$	distance dependent vdW interaction parameter
$\psi\ (z)$	(outer) electrostatic potential at z
$\varepsilon\ (z)$	z-dependent dielectric coefficient
$\langle\rho_Q(z)\rangle$	average density of charges at z
$Ups(\alpha)$	van der Waals interaction energy between the surface and a polymer chain in conformation α
μ_i^0	standard chemical potential for the species i participating in a chemical equilibrium
μ_i	chemical potential for a mobile species i
$\pi(z)$	Lagrange multiplier enforcing the packing constraint at z (lateral osmotic pressure)

λ	Lagrange multiplier assuring global electroneutrality (additive constant to the electrostatic potential)
ξ	normalization constant assuring $\Sigma_{\alpha} P(\alpha) = 1$

References

1 Manning, G.S. (1979) *Accounts of Chemical Research*, **12**, 443.

2 Decher, G. (1997) *Science*, **277**, 1232.

3 Decher, G. and Schlenoff, B.J. (2003) *Multilayer Thin Films*, Wiley-VCH, Weinheim.

4 Fujihira, M., Rusling, J.F. and Rubinstein, I. (2006) in *Encyclopedia of Electrochemistry*, 1st edn (ed. A.J. Bard and M. Stratmann), vol. 10, Wiley-VCH, Weinheim.

5 Moses, P.R., Wier, L. and Murray, R.W. (1975) *Analytical Chemistry*, **47**, 1882.

6 Murray, R.W. (1980) *Accounts of Chemical Research*, **13**, 135.

7 Murray, R.W. (1984) in *Electroanalytical Chemistry Vol. 13: Chemically Modified Electrodes* (ed. A.J. Bard), Marcel Dekker, New York, p. 191.

8 Murray, R.W. (1992) in *Molecular Design of Electrode Surfaces Introduction to Molecularly Designed Electrode Surfaces* (ed. R.W. Murray), John Wiley and Sons, Inc., New York.

9 Murray, R.W., Ewing, A.G. and Durst, R.A. (1987) *Analytical Chemistry*, **59**, A379.

10 Lane, R.F. and Hubbard, A.T. (1973) *The Journal of Physical Chemistry*, **77**, 1401.

11 Lane, R.F. and Hubbard, A.T. (1973) *The Journal of Physical Chemistry*, **77**, 1411.

12 Abruña, H.D. (1988) *Coordination Chemistry Reviews*, **86**, 135.

13 Lyons, M.E.G. (1994) *Electroactive Polymer Electrochemistry*, Plenum Press, New York.

14 Oyama, N. and Anson, F.C. (1979) *Journal of the American Chemical Society*, **101**, 739.

15 Oyama, N. and Anson, F.C. (1979) *Journal of the American Chemical Society*, **101**, 3450.

16 Samuels, G.J. and Meyer, T.J. (1981) *Journal of the American Chemical Society*, **103**, 307.

17 Samuels, G.J. and Meyer, T.J., (1981) *Journal of the American Chemical Society*, **103**, 27.

18 Oyama, N. and Anson, F.C. (1980) *Journal of the Electrochemical Society*, **127**, 247.

19 Oyama, N. and Anson, F.C. (1980) *Journal of the Electrochemical Society*, **127**, 249.

20 Cassidy, H.G. and Kun, K.A. (1965) *Oxidation Reduction Polymers (Redox Polymers)*, Wiley-Interscience, New York.

21 Katz, E., de Lacey, A.L., Fierro, J.L.G., Palacios, J.M. and Fernández, V.M. (1993) *Journal of Electroanalytical Chemistry*, **358**, 261.

22 Moulay, S. and Mehdaoui, R. (2004) *Reactive & Functional Polymers*, **61**, 265.

23 Hatozaki, O. and Anson, F.C. (1997) *Journal of Electroanalytical Chemistry*, **420**, 195.

24 Redepenning, J. and Anson, F.C. (1987) *The Journal of Physical Chemistry*, **91**, 4549.

25 Doblhofer, K. and Vorotyntsev, M. (1994) in *Electroactive Polymer Electrochemistry. Fundamentals* (ed. M.E.G. Lyons), Plenum, New York, p. 375.

26 Kelly, A.J. and Oyama, N. (1991) *Journal of Physical Chemistry*, **95**, 9579.

27 Hillman, A.R., Hughes, N.A. and Bruckenstein, S. (1994) *Analyst*, **119**, 167.

28 Grumelli, D.E., Garay, F., Barbero, C.A. and Calvo, E.J. (2006) *Journal of Physical Chemistry B*, **110**, 15345.

29 Etchenique, R.A. and Calvo, E.J. (1997) *Analytical Chemistry*, **69**, 4833.

30 Calvo, E.J., Danilowicz, C. and Etchenique, R. (1995) *Journal of the Chemical Society-Faraday Transactions*, **91**, 4083.

31 Henderson, M.J., Hillman, A.R. and Vieil, E. (1998) *Journal of Electroanalytical Chemistry*, **454**, 1.

32 Jeon, I.C. and Anson, F.C. (1992) *Analytical Chemistry*, **64**, 2021.

33 Blauch, D.N. and Savéant, J.M. (1993) *The Journal of Physical Chemistry*, **97**, 6444.

34 Mathias, M.F. and Haas, O. (1993) *Journal of Physical Chemistry*, **97**, 9217.

35 Degani, Y. and Heller, A. (1989) *Journal of the American Chemical Society*, **111**, 2357.

36 Gregg, B.A. and Heller, A. (1990) *Analytical Chemistry*, **62**, 258.

37 Heller, A. (1990) *Accounts of Chemical Research*, **23**, 128.

38 Gregg, B.A. and Heller, A. (1991) *Journal of Physical Chemistry*, **95**, 5970.

39 Gregg, B.A. and Heller, A. (1991) *Journal of Physical Chemistry*, **95**, 5976.

40 Blauch, D.N. and Savéant, J.-M. (1992) *Journal of the American Chemical Society*, **114**, 3323.

41 Mao, F., Mano, N. and Heller, A. (2003) *Journal of the American Chemical Society*, **125**, 4951.

42 Bruening, M.L. and Rusling, J. (2006) in *Modified Electrodes. Encyclopedia of Electrochemistry Vol. 10: Synthesis of Layered Polyelectrolyte Films* (eds A.J. Bard, M. Stratmann, M. Fujihira, J.F. Rusling and I. Rubinstein), Wiley-VCH, Weinheim.

43 Jiang, R.Z. and Anson, F.C. (1992) *Journal of Physical Chemistry*, **96**, 10565.

44 Lowy, D.A. and Finklea, H.O. (1997) *Electrochimica Acta*, **42**, 1325.

45 Cheng, Y.F. and Corn, R.M. (1999) *Journal of Physical Chemistry B*, **103**, 8726.

46 Nakanishi, T. and Nakashima, N. (2006) in *Modified Electrodes Encyclopedia of Electrochemistry* Vol. 10: Langmuir–Blodgett (LB) Films on Electrodes (B) Electrochemistry (eds A.J. Bard, M. Stratmann, M. Fujihira, J.F. Rusling and I. Rubinstein, Wiley-VCH, Weinheim, p. 203.

47 Bilewicz, R. and Majda, M. (1991) *Langmuir*, **7**, 2794.

48 Bilewicz, R., Sawaguchi, T., Chamberlain, R.V. and Majda, M. (1995) *Langmuir*, **11**, 2256.

49 Amatore, C., Bouret, Y., Maisonhaute, E., Goldsmith, J.I. and Abruña, H.D. (2001) *ChemPhysChem*, **2**, 130.

50 Amatore, C., Bouret, Y., Maisonhaute, E., Goldsmith, J.I. and Abruña, H.D. (2001) *Chemistry-a European Journal*, **7**, 2206.

51 Blauch, D.N. and Savéant, J.M. (1992) *Journal of the American Chemical Society*, **114**, 3323.

52 Aoki, A. and Heller, A. (1993) *The Journal of Physical Chemistry*, **97**, 11014.

53 Xie, A.F. and Granick, S. (2002) *Macromolecules*, **35**, 1805.

54 Abbou, J., Anne, A. and Demaille, C. (2004) *Journal of the American Chemical Society*, **126**, 10095.

55 Abbou, J., Anne, A. and Demaille, C. (2006) *The Journal of Physical Chemistry. B*, **110**, 22664.

56 Anne, A., Demaille, C. and Moiroux, J. (1999) *Journal of the American Chemical Society*, **121**, 10379.

57 Xie, A.F. and Granick, S. (2001) *Journal of the American Chemical Society*, **123**, 3175.

58 Anne, A., Bouchardon, A. and Moiroux, J. (2003) *Journal of the American Chemical Society*, **125**, 1112.

59 Anne, A. and Demaille, C. (2008) *Journal of the American Chemical Society*, **130**, 9812.

60 Fan, C., Plaxco, K.W. and Heeger, A.J. (2003) *Proceedings of the National Academy of Sciences*, **100**, 9134.

61 Tam, T.K., Ornatska, M., Pita, M., Minko, S. and Katz, E. (2008) *The Journal of Physical Chemistry. C*, **112**, 8438.

62 Decher, G. and Hong, J.D. (1991) *Makromolekulare Chemie, Macromolecular Symposia*, **46**, 321.

63 Decher, G. and Hong, J.D. (1992) *Thin Solid Films*, **210/211**, 831.

64 Decher, G., Hong, J.D. and Schmitt, J. (1992) *Thin Solid Films*, **210**, 831.

65 Crespilho, F.N., Zucolotto, V., Oliveira, O.N. and Nart, F.C. (2006) *International Journal of Electrochemical Science*, **1**, 194.

66 Stepp, J. and Schlenoff, J.B. (1997) *Journal of the Electrochemical Society*, **144**, 155.

67 Laurent, D. and Schlenoff, J.B. (1997) *Langmuir*, **13**, 1552.

68 Forzani, E.S., Perez, M.A., Teijelo, M.L. and Calvo, E.J. (2002) *Langmuir*, **18**, 9867.

69 Flexer, V., Forzani, E.S., Calvo, E.J., Ludueña, S.J. and Pietrasanta, L.I. (2006) *Analytical Chemistry*, **78**, 399.

70 Baba, A., Kaneko, F., Shinbo, K., Kato, K., Kobayashi, S. and Advincula, R.C. (2000) *Molecular Crystals and Liquid Crystals*, **347**, 259.

71 Bonazzola, C., Calvo, E.J. and Nart, F.C. (2003) *Langmuir*, **19**, 5279.

72 Calvo, E.J. and Wolosiuk, A. (2002) *Journal of the American Chemical Society*, **124**, 8490.

73 Tagliazucchi, M. and Calvo, E.J. (2007) *Journal of Electroanalytical Chemistry*, **599**, 249.

74 Sukhorukov, G.B., Donath, E., Lichtenfeld, H., Knippel, E., Knippel, M., Budde, A. and Möhwald, H. (1998) *Colloids and Surfaces. A*, **137**, 253.

75 Kotov, N.A. (2003) in *Multilayer Thin Films Layer-by-Layer Assembly of Nanoparticles and Nanocolloids: Intermolecular Interactions, Structure and Materials Perspectives* (eds G. Decher and B.J. Schlenoff), Wiley-VCH, Weinheim.

76 Fendler, J.H. (2003) in *Multilayer Thin Films Layer-by-Layer Self-assembled Polyelectrolytes and Nanoplatelets* (eds G. Decher and B.J. Schlenoff), Wiley-VCH, Weinheim.

77 Hodak, J., Etchenique, R., Calvo, E.J., Singhal, K. and Bartlett, P.N. (1997) *Langmuir*, **13**, 2708.

78 Lvov, Y., Ariga, K., Ichinose, I. and Kunitake, T. (1995) *Journal of the American Chemical Society*, **117**, 6117.

79 Lvov, Y., Ariga, K. and Kunitake, T. (1994) *Chemistry Letters*, **23**, 2323.

80 Yoo, P.J., Nam, K.T., Qi, J., Lee, S.-K., Park, J., Belcher, A.M. and Hammond, P.T. (2006) *Nature Materials*, **5**, 234.

81 Ma, H., Peng, J., Han, Z., Feng, Y. and Wang, E. (2004) *Thin Solid Films*, **446**, 161.

82 Wang, L., Wang, E., Hao, N., Jiang, M., Wang, Z., Lü, J. and Xu, L. (2004) *Journal of Colloid and Interface Science*, **274**, 602–606.

83 Wang, L., Jiang, M., Wang, E.B., Duan, L.Y., Hao, N., Lan, Y., Xu, L. and Li, Z. (2003) *Journal of Solid State Chemistry*, **176**, 13.

84 Liu, S., Volkmer, D., Kurth, D.G. (2004) *Analytical chemistry*, **76**, 4579.

85 Xu, L., Zhang, H., Wang, E., Kurth, D.G. and Li, Z. (2002) *Journal of Materials Chemistry*, **3**, 654.

86 Liu, S., Kurth, D.G., Möhwald, H. and Volkmer, D. (2002) *Advanced Materials*, **14**, 225.

87 Yoon, H.C. and Kim, H.-S. (2000) *Analytical Chemistry*, **72**, 922.

88 Yoon, H.C., Hong, M.-Y. and Kim, H.-S. (2000) *Analytical Chemistry*, **72**, 4420.

89 Deng, L., Liu, Y., Yang, G., Shang, L., Wen, D., Wang, F., Xu, Z. and Dong, Shaojun (2007) *Biomacromolecules*, **8**, 2063.

90 Liu, J., Cheng, L., Song, Y., Liu, B. and Dong, S. (2001) *Langmuir*, **17**, 6747.

91 Sun, J., Cheng, L., Liu, F., Dong, S., Wang, Z., Zhang, X. and Shen, J. (2000) *Colloids and Surfaces A: Physicochemical and Engineering Aspects*, **169**, 209.

92 Beissenhirtz, M.K., Scheller, F.W. and Lisdat, F. (2004) *Analytical Chemistry*, **76**, 4665.

93 Blasini, D.R., Flores-Torres, S., Smilgies, D.-M. and Abruña, H.D. (2006) *Langmuir*, **22**, 2082.

94 Lösche, M., Schmitt, J., Decher, G., Bouwman, W.G. and Kjaer, K. (1998) *Macromolecules*, **31**, 8893.

95 Schönhoff, M., Ball, V., Bausch, A.R., Dejugnat, C., Delorme, N., Glinel, K., von Klitzing, R. and Steitz, R. (2007) *Colloids and Surfaces A: Physicochem Eng Aspects*, **303**, 14.

96 Steitz, R., Leiner, V., Siebrecht, R. and von Klitzing, R. (2000) *Colloids and Surfaces A: Physicochemical and Engineering, Aspects*, **163**, 63.

97 Battaglini, F. and Calvo, E.J. (1994) *Journal of the Chemical Society-Faraday Transactions*, **90**, 987.

98 Jureviciute, I., Bruckenstein, S., Hillman, A.R. and Jackson, A. (2000) *Physical Chemistry Chemical Physics*, **18**, 4193.

99 Schmitt, J., Grünewald, T., Decher, G., Pershan, P., Kjaer, K. and Lösche, M. (1993) *Macromolecules*, **26**, 7058.

100 Jomaa, H.W. and Schlenoff, J.B. (2005) *Macromolecules*, **38**, 8473.

101 Liu, A., Kashiwagi, Y. and Anzai, J., (2003) *Electroanalysis*, **15**, 1139.

102 Narváez, A., Suárez, G., Popescu, I.C., Katakis, I. and Domínguez, E. (2000) *Biosensors and Bioelectronics*, **15**, 43.

103 Lukkari, J., Salomäki, M., Viinikanoja, A., Ääritalo, T., Paukkunen, J., Kocharova, N. and Kankare, J. (2001) *Journal of the American Chemical Society*, **123**, 6083.

104 Schlenoff, J.B., Ly, H. and Li, M. (1998) *Journal of the American Chemical Society*, **120**, 7626.

105 Farhat, T.R. and Schlenoff, J.B. (2001) *Langmuir*, **17**, 1184.

106 Farhat, T.R. and Schlenoff, J.B. (2003) *Journal of the American Chemical Society*, **125**, 4627.

107 Tagliazucchi, M., Williams, F. and Calvo, E.J. (2007) *The Journal of Physical Chemistry. B*, **111**, 8105.

108 von Klitzing, R. and Möhwald, H. (1996) *Macromolecules*, **29**, 6901.

109 Schönhoff, M., (2003) *Journal of Physics-Condensed Matter*, **15**, 1781.

110 Carrière, D., Krastev, R. and Shönhoff, M. (2004) *Macromolecules*, **20**, 11465.

111 von Klitzing, R. and Möwald, H. (1995) *Langmuir*, **11**, 3554.

112 Arys, X., Jonas, A.M., Laschewsky, A. and Legras, R. (2000) in *Supramolecular Polymers Supramolecular Polyelectrolyte Assemblies* (ed. A. Ciferri), Marcel Dekker, New York.

113 Jaber, J.A. and Schlenoff, J.B. (2007) *Langmuir*, **23**, 896.

114 Shiratori, S.S. and Rubner, M.F. (2000) *Macromolecules*, **33**, 4213.

115 Dubas, S.T. and Schlenoff, J.B. (1999) *Macromolecules*, **32**, 8153.

116 Netz, R.R. and Andelman, D. (2003) *Physics Reports*, **380**, 1.

117 Szleifer, I. and Carignano, M.A. (1996) *Advances in Chemical Physics*, **96**, 165.

118 Tagliazucchi, M., Calvo, E.J. and Szleifer, I. (2008) *The Journal of Physical Chemistry. C*, **112**, 458.

119 Tagliazucchi, M., Calvo, E.J. and Szleifer, I. (2008) *Langmuir*, **24**, 2869.

120 Tagliazucchi, M., Calvo, E.J. and Szleifer, I. (2008) *Electrochimica Acta*, **53**, 6740.

121 Bard, A.J. and Faulkner, L.R. (2001) *Electrochemical Methods Electroactive Layers and Modified Electrodes*, John Wiley and Sons, New York.

122 Naegeli, R., Redepenning, J. and Anson, F.C. (1986) *The Journal of Physical Chemistry*, **90**, 6227.

123 Ostrom, G.S. and Buttry, D.A. (1995) *The Journal of Physical Chemistry*, **99**, 15236.

124 Barbero, C., Miras, M.C., Haas, O. and Kötz, R. (1997) *Journal of the Electrochemical Society*, **144**, 4170.

125 Ohshima, H. and Ohki, S. (1985) *Biophysical Journal*, **47**, 673.

126 Laviron, E. (1981) *Journal of Electroanalytical Chemistry*, **124**, 9.

127 Brown, A.P. and Anson, F.C. (1977) *Analytical Chemistry*, **49**, 1589.

128 Albery, W.J., Boutelle, M.G., Colby, P.J. and Hillman, A.R. (1982) *Journal of Electroanalytical Chemistry*, **133**, 135.

129 Smith, C.P. and White, H.S. (1992) *Analytical Chemistry*, **64**, 2398.

130 Redepenning, J., Miller, B.R. and Burham, S. (1994) *Analytical Chemistry*, **66**, 1560.

131 White, H., Leddy, J. and Bard, A. (1982) *Journal of the American Chemical Society*, **104**, 4811.

132 Daum, P. and Murray, R.W. (1981) *The Journal of Physical Chemistry*, **85**, 389.

133 Facci, J.S., Schmehl, R.H. and Murray, R.W. (1982) *Journal of the American Chemical Society*, **104**, 4959.

134 Laviron, E., Roullier, L. and Degrand, C. (1980) *Journal of Electroanalytical Chemistry*, **112**, 11.

135 Hunter, T.B., Tyler, P.S., Smyrl, W.H. and White, H. (1987) *Journal of Electrochemical Society*, **134**, 2198.

136 van de Steeg, H.G.M., Cohen Stuart, M.A., de Keizer, A. and Bijsterbosch, B.H. (1992) *Langmuir*, **8**, 2538.

137 Láng, G., Bácskai, J. and Inzelt, G. (1990) *Electrochimica Acta*, **38**, 773.

138 Sharp, M. and Åberg, S. (1998) *Journal of Electroanalytical Chemistry*, **449**, 137.

139 Savéant, J.M. (1988) *The Journal of Physical Chemistry*, **92**, 4526.

140 Pickup, P.G. and Murray, R.W. (1983) *Journal of the American Chemical Society*, **105**, 4510.

141 Chidsey, C.E.D. and Murray, R.W. (1986) *The Journal of Physical Chemistry*, **90**, 1479.

142 Ruff, I. and Botár, L. (1985) *The Journal of Chemical Physics*, **83**, 1292.

143 Dahms, H. (1968) *The Journal of Physical Chemistry. B*, **72**, 362.

144 Aoki, A., Rajagopalan, R. and Heller, A. (1995) *The Journal of Physical Chemistry. B*, **99**, 5102.

145 Oh, S.M. and Faulkner, L.R. (1989) *Journal of Electroanalytical Chemistry*, **269**, 77.

146 Oh, S.M. and Faulkner, L.R. (1989) *Journal of the American Chemical Society*, **111**, 5613.

147 Bartlett, P.N. and Pratt, K.F.E. (1993) *Biosensors & Bioelectronics*, **8**, 451.

148 Tagliazucchi, M., Grumelli, D. and Calvo, E.J. (2006) *Physical Chemistry Chemical Physics*, **8**, 5086.

149 Barbero, C. (2005) *Physical Chemistry Chemical Physics*, **7**, 1885.

150 Grumelli, D.E., Wolosiuk, A., Forzani, E., Planes, G.A., Barbero, C. and Calvo, E.J., (2003) *Chemical Communications*, **9**, 3014.

151 Calvo, E.J., Forzani, E. and Otero, M. (2002) *Journal of Electroanalytical Chemistry*, **538–539**, 231.

152 Tagliazucchi, M.E. and Calvo, E.J. (2007) *Journal of Electroanalytical Chemistry*, **599**, 249.

153 Tagliazucchi, M., Grumelli, D., Bonazzola, C. and Calvo, E.J. (2006) *Journal of Nanoscience and Nanotechnology*, **6**, 1731.

154 Grumelli, D., Bonazzola, C. and Calvo, E.J. (2006) *Electrochemistry Communications*, **8**, 1353.

155 Barbero, C., Kötza, R., Kalaji, M., Nyholm, L. and Peter, L.M. (1993) *Synthetic Metals*, **55**, 1545.

156 Jureviciute, I., Bruckenstein, S. and Hillman, A.R. (2000) *Journal of Electroanalytical Chemistry*, **488**, 73.

157 Nap, R., Gong, P. and Szleifer, I. (2006) *Journal of Polymer Science: Part B*, **44**, 2638.

158 Laviron, E. (1979) *Journal of Electroanalytical Chemistry*, **100**, 263.

159 Albery, W.J. and Hillman, A.R. (1984) *Journal of Electroanalytical Chemistry*, **170**, 27.

160 Fang, F. and Szleifer, I. (2006) *Proceedings of the National Academy of Sciences of the, United States of America*, **103**, 5769.

161 Cho, B.J., Char, K., Hong, J.-D. and Lee, K.-B. (2001) *Advanced Materials*, **13**, 1077.

162 Schlenoff, J.B., Dubas, S.T. and Farhat, T. (2000) *Langmuir*, **16**, 9968.

163 Ngankam, A.P. and Tassel, P.R.V. (2005) *Langmuir*, **21**, 5865.

164 Kotov, N.A., Haraszti, T., Turi, L., Zavala, G., Geer, R.E., Dekany, I. and Fendler, J.H. (1997) *Journal of the American Chemical Society*, **119**, 6821.

165 Lutkenhaus, J.L. and Hammond, P.T. (2007) *Soft Matter*, **3**, 804.

166 Hammond, P.T. (2004) *Advanced Materials*, **16**, 1271.

167 Tang, Z., Wang, Y., Podsiadlo, P. and Kotov, N.A. (2006) *Advanced Materials*, **18**, 3203.

168 Bertrand, P., Jonas, A., Laschewsky, A. and Legras, R. (2000) *Macromolecular Rapid Communications*, **21**, 319.

169 Crespilho, F.N., Zucolotto, V., Oliveira, O.N. Jr and Nart, F.C. (2006) *International Journal of Electrochemical Science*, **1**, 194.

170 Wang, J. (2008) *Chemical Reviews*, **108**, 814.

171 Zhang, S., Wang, N., Yu, H., Niu, Y. and Sun, C. (2005) *Bioelectrochemistry (Amsterdam, Netherlands)*, **67**, 15.

172 Gough, D.A., Lucisano, J.Y. and Tse, P.H.S. (1985) *Analytical Chemistry*, **57**, 2351.

173 Proux-Delrouyre, V., Demaille, C., Leibl, W., Setif, P., Bottin, H. and Bourdillon, C. (2003) *Journal of the American Chemical Society*, **125**, 13686.

174 Danilowicz, C. and Manrique, J.M. (1999) *Electrochemistry Communications*, **1**, 22.

175 Calvo, E.J., Danilowicz, C., Lagier, C.M., Manrique, J. and Otero, M. (2004) *Biosensors & Bioelectronics*, **19**, 1219.

176 Anicet, N., Bourdillon, C., Moiroux, J. and Savéant, J.-M. (1999) *Langmuir*, **15**, 6527.

177 Dequaire, M., Limoges, B., Moiroux, J. and Savéant, J.M. (2002) *Journal of the American Chemical Society*, **124**, 240.

178 Anicet, N., Anne, A., Moiroux, J. and Savéant, J.M. (1998) *Journal of the American Chemical Society*, **120**, 7115.

179 Anicet, N., Anne, A., Bourdillon, C., Demaille, C., Moiroux, J. and Savéant, J.-M. (2000) *Faraday Discussions*, **116**, 269.

180 Anzai, J., Kobayashi, Y., Nakamura, N., Nishimura, M. and Hoshi, T. (1999) *Langmuir*, **15**, 221.

181 Anzai, J., Kobayashi, Y., Suzuki, Y., Takeshita, H., Chen, Q., Osa, T., Hoshi, T. and Du, X.Y. (1998) *Sensors and Actuators B-Chemical*, **52**, 3.

182 Calvo, E.J., Battaglini, F., Danilowicz, C., Wolosiuk, A. and Otero, M., (2000) *Faraday Discussions*, **47**.

183 Calvo, E.J., Etchenique, R., Pietrasanta, L., Wolosiuk, A. and Danilowicz, C. (2001) *Analytical Chemistry*, **73**, 1161.

184 Calvo, E.J. and Wolosiuk, A. (2004) *ChemPhysChem*, **5**, 235.

185 Calvo, E.J. and Wolosiuk, A. (2005) *ChemPhysChem*, **6**, 43.

186 Calvo, E.J., Danilowicz, C.B. and Wolosiuk, A. (2005) *Physical Chemistry Chemical Physics*, **7**, 1.

187 Hou, S.F., Fang, H.Q. and Chen, H.Y. (1997) *Analytical Letters*, **30**, 1631.

188 Li, W.J., Wang, Z., Sun, C.Q., Xian, M. and Zhao, M.Y. (2000) *Analytica Chimica Acta*, **418**, 225.

189 Ferreyra, N., Coche-Guérente, L., Labbe, P., Calvo, E.J. and Solís, V.M. (2003) *Langmuir*, **19**, 3864.

190 Dominguez, E., Suarez, G. and Narvaez, A. (2006) *Electroanalysis*, **18**, 1871.

191 Calvo, E.J., Danilowicz, C. and Wolosiuk, A. (2002) *Journal of the American Chemical Society*, **124**, 2452.

192 Pratt, K. (1993) *Chemistry*, University of Southampton, Southampton.

193 Limoges, B., Moiroux, J. and Savéant, J.-M. (2002) *Journal of Electroanalytical Chemistry*, **521**, 1.

194 Limoges, B., Moiroux, J. and Savéant, J.-M. (2002) *Journal of Electroanalytical Chemistry*, **521**, 8.

195 Andreu, R., Calvente, J.J., Fawcett, W.R. and Molero, M. (1997) *Langmuir*, **13**, 5189.

196 DeLongChamp, D.M. and Hammond, P.T. (2004) *Advanced Functional Materials*, **14**, 224.

197 Jain, V., Sahoo, R., Jinschek, J.R., Montazami, R., Yochum, H.M., Beyer, F.L., Kumarb, A. and Heflin, J.R., (2008) *Chemical Communications*, **2008**, 3663**.**

198 Gao, G., Xu, L., Wang, W., An, W. and Qiu, Y. (2004) *Journal of Materials Chemistry*, **14**, 2024.

199 Huguenin, F., Zucolotto, V., Carvalho, A.J.F., Gonzalez, E. R., and Oliveira, O.N. Jr, (2005) *Chemistry of Materials*, **17**, 6739.

200 Wang, L.Z., Sakai, N., Ebina, Y., Takada, K. and Sasaki, T. (2005) *Chemistry of Materials*, **17**, 1352.

201 Anne, A., Demaille, C. and Moiroux, J. (2001) *Journal of the American Chemical Society*, **123**, 4817.

202 Anne, A. and Demaille, C. (2006) *Journal of the American Chemical Society*, **128**, 542.

203 Forzani, E.S., Otero, M., Pérez, M.A., López Teijelo, M. and Calvo, E.J. (2002) *Langmuir*, **18**, 4020.

204 Calvo, E.J., Etchenique, R., Pietrasanta, L., Wolosiuk, A. and Danilowicz, C. (2001) *Analytical Chemistry*, **73**, 1161.

205 Calvo, E.J., Danilowicz, C.B. and Wolosiuk, A. (2005) *Physical Chemistry Chemical Physics*, **7**, 1800.

206 Sun, J., Sun, Y., Zou, S., Zhang, X., Sun, C., Wang, Y. and Shen, S. (1999)

Macromolecular Chemistry and Physics, **200**, 840.

207 Qian, L., Gao, Q., Song, Y., Li, Z. and Yang, X. (2005) *Sensors and Actuators B-Chemical*, **107**, 303.

208 Liu, A. and Anzai, J. (2003) *Langmuir*, **19**, 4043.

209 Jason, S. and Schlenoff, B.J. (1997) *Journal of the Electrochemical Society*, **144**, 155.

210 Zotti, G., Zecchin, S., Vercelli, B., Berlin, A., Grimoldi, S., Bertoncello R. and Milanese, L. (2005) *Journal of Electroanalytical Chemistry*, **580**, 330.

211 Wang, X., Huang, H.X., Liu, A.R., Liu, B., Wakayama, T., Nakamura, C., Miyake, J. and Qian, D.J. (2006) *Carbon*, **44**, 2115.

212 Huang, H.X., Qian, D.J., Nakamura, N., Nakamura, C., Wakayama, T., and Miyake, J., (2004) *Electrochimica Acta*, **49**, 1491.

213 Sarkar, N., KuRam, M., Sarkar, A., Narizzano, R., Paddeu, S. and Nicolini, C. (2000) *Nanotechnology*, **11**, 30.

214 Beissenhirtz, M.K., Kafka, B., Schafer, D., Wolny, M. and Lisdat, F. (2005) *Electroanalysis*, **17**, 1931.

215 Beissenhirtz, M.K., Scheller, F.W., Stocklein, W.F.M., Kurth, D.G., Mohwald, H. and Lisdat, F. (2004) *Angewandte Chemie-International Edition*, **43**, 4357.

216 Liu, S., Kurth, D.G., Bredenkötterand, B. and Volkmer, D. (2002) *Journal of the American Chemical Society*, **124**, 12279.

217 Cheng, L., Niu, L., Gong, J. and Dong, S. (1999) *Chemistry of Materials*, **11**, 1465.

218 Dronov, R., Kurth, D.G., Mohwald, H., Spricigo, R., Leimkuhler, S., Wollenberger, U., Rajagopalan, K.V., Scheller, F.W. and Lisdat, F. (2008) *Journal of the American Chemical Society*, **130**, 1122.

219 Calvo, E. and Wolosiuk, A. (2005) *ChemPhysChem*, **6**, 43.

220 Zotti, G., Zecchin, S., Schiavon, G., Vercelli, B., Berlin, A. and Porzio, W. (2004) *Chemistry of Materials*, **16**, 2091.

221 Zotti, G., Zecchin, S., Berlin, A., Schiavon, G. and Giro, G. (2001) *Chemistry of Materials*, **13**, 43.

222 Zotti, G., Zecchin, S., Schiavon, G. and Vercelli, B. (2003) *Chemistry of Materials*, **2003**, 2222.

223 Moriguchi, I. and Fendler, J.H. (1998) *Chemistry of Materials*, **10**, 2205.

224 Fushimi, T., Oda, A., Ohkita, H. and Ito, S. (2005) *Thin Solid Films*, **484**, 318.

225 Buttry, D.A., Anson, F.C. (1981) *Journal Electroanalytical Chemistry*, **130**.

3
Electrochemistry on Carbon-Nanotube-Modified Surfaces

María José Esplandiu

3.1
Introduction

Carbon has become a widely used and practical electrode material due to its desirable properties for electrochemical applications. Available in a variety of structures, carbon electrodes provide, in general, good electrical conductivity, high thermal and mechanical stability, a wide operable potential window with slow oxidation kinetics and in many cases electrocatalytical activity. Apart from that, they are recognized as versatile and easily handled materials. Thus, carbon in the form of glassy carbon, black carbon, carbon fibers, powdered graphite, pyrolytic graphite and highly ordered pyrolytic graphite (HOPG), has played for a long time an important role in solid electrode development, also favored by its rich surface chemistry which has been exploited to influence surface reactivity [1, 2]. However, the appearance of the allotrope form of carbon nanotubes (CNT) has enhanced these properties and propelled in an unprecedented way its electrochemical and electroanalytical applications [2–19].

Apart from the promising electrochemical properties that will be exhaustively discussed through this chapter, carbon nanotubes have become a hot research topic due to their outstanding electronic, mechanical, thermal, optical and chemical properties and their biocompatibility. Near- and long-term innovative applications can be foreseen including nanoelectronic and nanoelectromechanical devices, field emitters, probes, sensors and actuators as well as novel materials for mechanical reinforcement, fuel cells, batteries, energy storage, (bio)chemical separation, purification and catalysis [20].

In this chapter, we will focus on CNTs as advanced materials for the design of electrochemical devices. The next section will be devoted to review the structure, electronic, chemical and electrochemical properties of CNTs. Section 3.3 will comprise an overview of the synthesis, purification and (bio)functionalization of CNT, as well as the modification of substrates with CNT. In Section 3.4, we will address the electrochemical applications of functionalized CNT electrodes as sensors, biosensors, electrochemical actuators and harvesting devices. The chapter will be closed with an outlook in which we will discuss the highlights of CNTs in the electrochemical field as well as the limitations, unsettled issues or challenges to be solved in relation to the implementation of CNT devices.

3.2
Structure and Properties of Carbon Nanotubes

3.2.1
Structure and Electronic Properties

The graphene layers have become the starting point to explain the structure of carbon nanotubes. Single-walled carbon nanotubes (SWNTs) can be described as graphene sheets rolled up in different ways. Indeed, the appearance of a closed cage in CNTs can be easily rationalized by considering the presence of high-energy dangling bonds at the boundaries of a finite graphene layer. The total energy of a certain number of carbon atoms in a graphene layer can be reduced by promoting the formation of a closed structure that eliminates the dangling bonds, even at the expense of increasing the strain energy.

The way the graphene sheet is wrapped up can be described by a pair of indices (*n*,*m*) that define the chiral vector, $\vec{C} = n\vec{a}_1 + m\vec{a}_2$, in which $\vec{a}_1$ and $\vec{a}_2$ are the basis vectors of the hexagonal graphene lattice [20–25] (Figure 3.1). Three different types of nanotube structures can be generated by rolling up the graphene layer: zigzag ($m = 0$), armchair ($n = m$) and chiral nanotubes (n, m). Although CNTs are closely

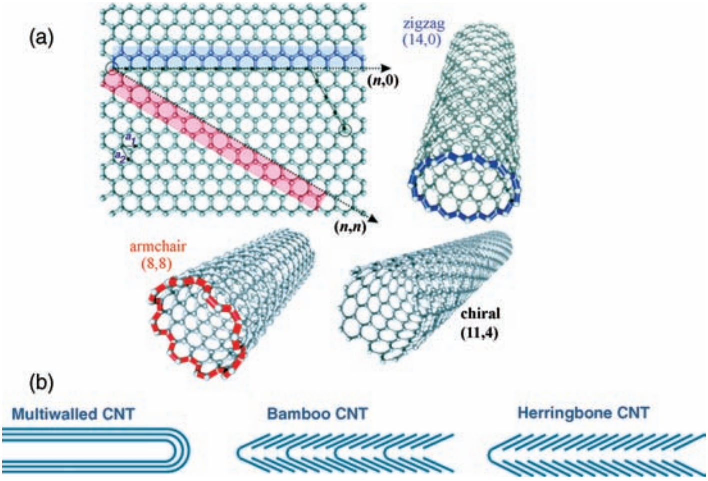

Figure 3.1 (a) Roll-up of a graphene sheet leading to three different types of SWNTs. Reprinted with permission from Ref. [25]. Copyright Wiley-VCH Verlag. (b) Different structures of multiwalled CNTs.

related to 2D graphene, the tube curvature and the quantum confinement in the circumferential direction of the nanotube bring about the unique properties that make CNTs different from graphene. One of these unusual properties is the electronic conductivity that strongly depends on the chirality and CNT diameter. CNTs can exhibit singular electronic band structures and can show metallic and semiconducting behavior. As a general rule, *n.m* tubes with *n*–*m* being an integer multiple of 3 are metallic, while the remaining tubes are semiconducting. The bandgap of semiconducting tubes can be approximated by the relation $E_g = 0.8\,\text{eV}/d$, with d being the diameter of the nanotube [26, 27]. Therefore, the bigger the diameter, the more metallic behavior is found. Moreover, carbon nanotubes can exhibit a ballistic flow of electrons with electron mean-free paths of several micrometers, and are capable of conducting very large current densities [28–30]. For instance, carbon nanotubes have been shown to withstand current densities up to $10^9\,\text{A/cm}^2$, a density that is about 2–3 orders of magnitude larger than in metals such as Al or Cu.

One of the key points when considering the electrochemical reactivity of carbon electrodes lies on the density of electronic states (DOS) that can considerably vary for different carbon materials [2]. In general, graphitic materials exhibit lower conductivity compared with metals partly due to a lower DOS. Thus, ideal three-dimensional crystalline graphite such as highly oriented pyrolytic graphite (HOPG) exhibits a small overlap between the valence and conduction bands resulting in a low DOS at the Fermi level. HOPG is considered a semimetal; however, disorder in the graphitic lattice can provide defect states at the Fermi level, increasing DOS and the metallic behavior [2]. In turn, carbon nanotubes have a variety of DOS distributions that depends on the tube diameter [26, 27, 31, 32]. As an example, Figure 3.2 illustrates the density of states (DOS) for two SWNTs of different diameter, one being

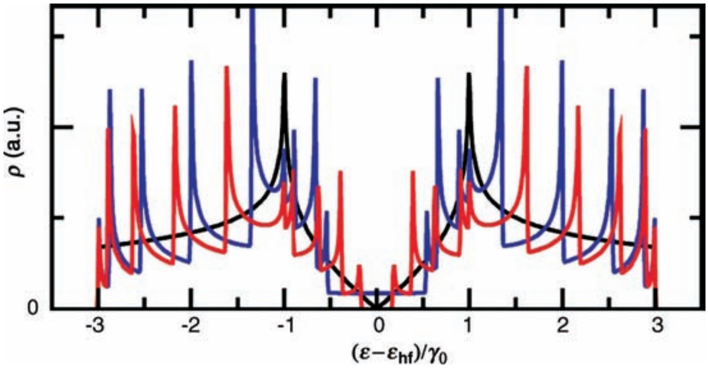

Figure 3.2 Nearest-neighbor tight-binding calculation of the density of electronic states (DOS) as a function of energy for a graphene sheet (black), a metallic (9,0) SWNT (blue), and a semiconducting (10,0) SWNT (red). $\gamma_0 = 2.7\,\text{eV}$ is the nearest-neighbor interaction energy. ε_{hf} is the half-filling energy, defined as the energy at which all bonding orbitals are filled and all antibonding orbitals are empty, yielding exactly one occupied π-orbital per carbon atom. Adapted with permission from Ref. [33]. Copyright, 2006, American Chemical Society.

metallic and the other semiconducting. The band diagram is characterized by the Van Hove singularities typical of a one-dimensional conductor that are a consequence of the size-dependent quantization of the electronic wavefunctions around the circumference. SWNTs have a rather low density of electronic states per unit energy around the Fermi level. This causes the average energy spacing between adjacent states to be much larger than that in common metals. Semiconducting SWNTs have no electronic states in the bandgap region, while metallic SWNTs have a nonzero DOS at the gap. For comparison, the figure also illustrates the symmetrical DOS for an individual layer of graphene, which is distinct from the 3D graphite in the fact that graphene is considered a zero-gap semiconductor with the DOS per unit area vanishing at the Fermi level [33].

The bonding in CNT is basically sp^2, however, the circular curvature, apart form yielding quantum confinement and quantized conductance, also causes σ–π rehybridization, an effect that is stronger as the CNT diameter decreases [34–36]. In such cases, three σ bonds are slightly out of plane and for compensation the π orbitals are more delocalized outside the tube. The electron-cloud distortion induced by the curvature, which yields a rich π-electron conjugation outside the tube, can make CNT more electrochemically active and electrically and thermally more conductive (Figure 3.3). Moreover, the latter fact, together with the combination of size, structure and topology, confer nanotubes with remarkable mechanical properties such as high stability, strength and stiffness together with low density and elastic

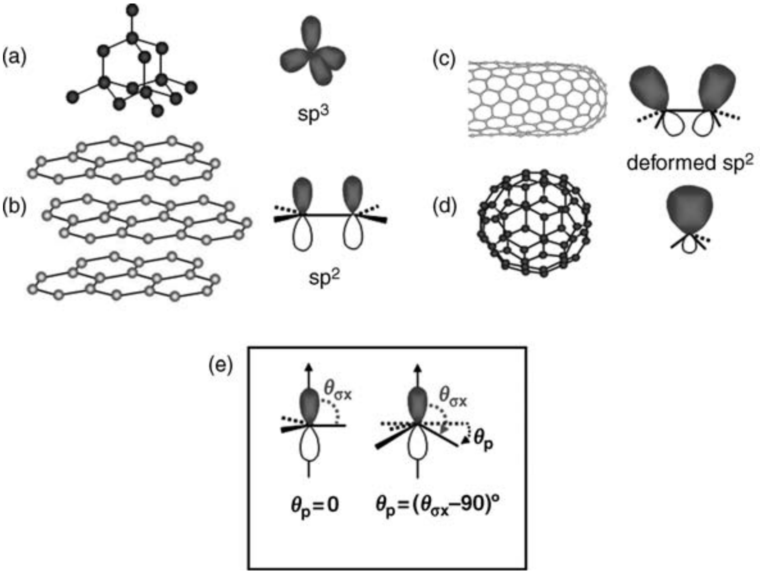

Figure 3.3 Bonding structures for different carbon materials: (a) diamond, (b) graphite, (c) carbon nanotubes and (d) fullerenes. Scheme of the pyramidalization angle (θ_p) in deformed sp^2 bonding in comparison with a trigonal structure.

deformability. That is a big difference with respect to graphite in which the sp^2 hybrid orbital form three in-plane σ bonds with an out-of-plane π orbital.

In addition to the σ–π rehybridization, the high surface area and the presence of potential topological defects (pentagons or heptagons, edges, etc.) that induce local perturbations in the electronic structure constitute key points for chemical, electrochemical and biochemical reactivity. Thus, molecular adsorption, doping and charge transfer can be more facilitated if compared with its analog graphite.

So far, we have considered CNTs formed by a single graphene wall (SWNT) with diameters ranging generally from 0.4 nm up to 1.5 nm and with an important diversity in electronic conductivity, from semiconducting to metallic behavior. However, CNTs can also be made by multiple graphene layers disposed in different arrangements. Such structures, known as multiwalled carbon nanotubes (MWNTs), typically have diameters in the range of 2–100 nm and metallic behavior. This is due to the fact that the DOS for MWNTs exhibits no gap and no significant features as a result of the average of the different graphene layer contributions. MWNTs can appear as several concentric tubes fitted one inside the other (hollow MWNTs) or with the graphene planes forming an angle with respect to the axis of the tube (herringbone or bamboo MWNTs), see schemes in Figure 3.1. The bamboo-like tubes differ from the herringbone ones in that some of the graphene layers are periodically closed along the length of the tube forming compartments. The main difference between the hollow morphology and the herringbone and bamboo ones lies on the high density of terminating edge planes that contain the last two morphological variations of MWNTs.

3.2.2
Chemical Properties

CNTs provide a high specific surface system that together with the σ–π rehybridization and the presence of structural defects facilitate different chemical processes such as (bio)chemical derivatization, intercalation, molecular adsorption, doping, charge transfer, and so on [34–40]. These characteristics are being considerably exploited for different applications such as biochemical and chemical sensing, energy storage or separation techniques. For instance, a semiconducting CNT placed as a channel in a field effect transistor configuration can be used for electronic (bio) sensing, where the (bio)molecular adsorption on CNT can lead, among other effects, to charge transfer and doping on the CNT that is reflected in a strong modulation in the electronic conductivity of the tube. Such devices hold promise as ultrasensitive sensors at the single-molecule level. A recent study has demonstrated that these devices are even able to detect single-electron transfers [41].

A good understanding of the chemical properties of CNTs is mandatory for enhancing the efficiency of practical devices and also for comprehending related fundamental processes such as their electrochemistry. In the following, we will address the chemical reactivity of CNTs and in Section 3.3.3, the different (bio) chemical functionalization procedures that can be performed for applications, will be discussed in more detail.

Although graphite, fullerene and carbon nanotubes are built from the same basic element, the chemical reactivity is substantially different among them. The chemical reactivity is higher for a CNT than for a graphene layer, but lower if compared with fullerene [34, 37]. Such behavior can be closely related to the surface curvature of the carbon structure [34–39]. The reactivity of fullerenes is mainly due to the high strain generated by the spherical geometry that affects the pyramidalization angle θ_p among carbon bonds that is defined as the difference between the σ–π orbital angle and 90° [37]. θ_p is a quantitative measure of the curvature at a tri-coordinated carbon atom. As illustrated by Figure 3.3, this angle quantifies the deviation of a carbon atom from the plane passing through the three adjacent carbon atoms. The higher the θ_p, the more reactive the species is. In a pure sp^2 hybridization (trigonal, graphene), $\theta_p = 0$. Fullerenes have a θ_p of 11.6° due to 2D curved structure that results in sp^2-sp^3 or σ–π mixing, as discussed above with CNTs (Figure 3.3). In this case, reactions that lead to a strain relief are enhanced, such as the ones related to the addition chemistry [34–39].

In the case of CNTs, the strain appears as a consequence not only of the curvature-induced pyramidalization but also from π orbital misalignment between adjacent pairs of conjugated carbon atoms that favors the chemical reactivity of the CNT walls as compared to that of flat graphene layers [37]. Furthermore, since pyramidalization angles and π-orbital misalignment angles of CNTs scale inversely with the diameter of the tubes, a differentiation is expected between the reactivity of carbon nanotubes of different diameters. A higher surface reactivity with decreasing diameter is thus expected [38].

The reactivity of different graphitic carbon allotropes is also characterized by having chemical anisotropy. Taking as a reference, for instance, the layered structure of HOPG, it is known that its basal plane is more inert than the highly reactive edges (edge HOPG) that contain unsatisfied valences or dangling bonds prone to reaction with oxygen or water [2]. Such anisotropy is also observed in adsorption processes. The same anisotropy in the chemical reactivity can be considered on CNT, since the walls behave differently from the ends, which can be either capped or just finishing in terminal edges [25, 39, 42, 43]. The chemical reactivity is increased at the capped ends (due to the presence for instance of pentagons) or at the edges of an open nanotube, which become the more reactive sites of the CNT irrespective of its diameter. Such anisotropy in the chemical reactivity will also have strong implications from the point of view of electrochemistry, and will be approached in the next sections.

Although, as mentioned before, the CNT ends exhibit a higher chemical reactivity than the walls, the presence of local defects on the walls also constitutes efficient reactive sites. For instance, when CNTs are subjected to oxidative acid treatment, the local generation of carboxylic, ketones, alcohols and ester groups leads to active sites that can be profited for (bio)molecular anchoring [16, 39, 42–44]. Such acid treatments also open the CNT capped ends, bringing about an increase of oxygen-rich terminal groups. Figure 3.4 depicts a general overview of the different oxygen functionalities that can appear at the edges of CNTs [2, 35]. Such defects together with the reactivity associated with the generated strain from the curvature and π misalignment are very important for the attachment of a wide diversity of molecules. In this context, it is expected that the chemical reactivity is increased

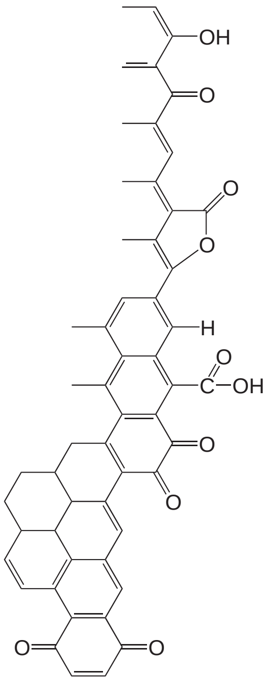

Figure 3.4 Different oxygenated functionalities that can appear at CNT edges.

in MWNTs with a higher density of reactive edges, with the favored structures being the bamboo or herringbone CNTs.

3.2.3
Electrochemical Properties

In general, the electrochemical performance of carbon materials is basically determined by the electronic properties, and given its interfacial character, by the surface structure and surface chemistry (i.e. surface terminal functional groups or adsorption processes) [1, 2]. Such features will affect the electrode kinetics, potential limits, background currents and the interaction with molecules in solution [2]. From the point of view of electroanalysis, the remarkable benefits of CNT-modified electrodes have been widely praised, including low detection limits, increased sensitivity, decreased overpotentials and resistance to surface fouling [5, 9, 11, 17].

The electronic properties of CNTs, and especially their band structure, in terms of DOS, is very important for the interfacial electron transfer between a redox system in solution and the carbon electrode. There should be a correlation between the density of electronic states and electron-transfer reactivity. As expected, the electron-transfer kinetics is faster when there is a high density of electronic states with energy values in the range of donor and acceptor levels in the redox system [2]. Conventional metals (Pt, Au, etc.) have a large DOS in the electrochemical potential

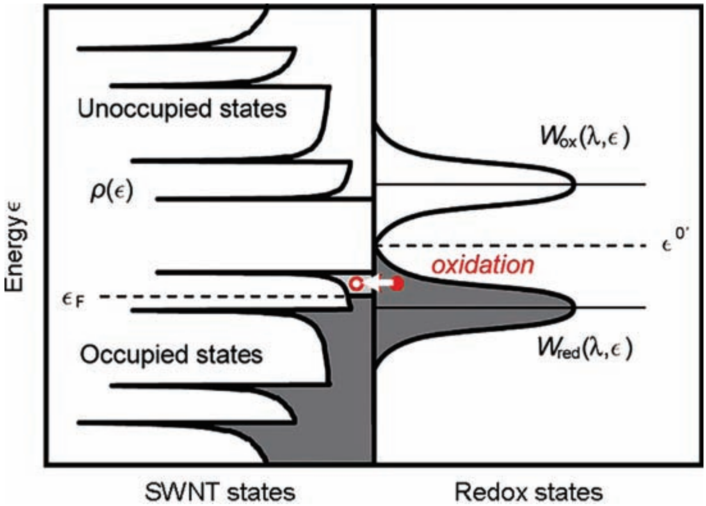

Figure 3.5 Energy diagram showing the energy overlap of the electronic states of electrode and solution under consideration. Dark shaded areas indicate occupied electronic states, and light shaded areas indicate unoccupied electronic states. The left-hand side shows the electrode states represented by the density of electronic states of a semiconducting SWNT. The right-hand side shows the redox states in solution represented by the Gaussian distributions of occupied reduced states, $W_{red}(\in)$, and unoccupied oxidized states, $W_{ox}(\in)$, centered around the standard energy of the redox couple $\in^{\circ}$. The oxidation reaction is illustrated with the arrow, indicating the electron transfer from an occupied redox state in solution to a vacant state on the electrode. Reprinted with permission from Ref. [33]. Copyright, 2006, American Chemical Society.

window, whereas carbon electrodes have a considerably lower DOS (especially in the case of HOPG) that can be incremented by the introduction of disorder. For instance, the low DOS of HOPG can be reflected in a remarkably low double-layer capacitance when the basal plane is considered [1, 2]. Interestingly, SWNTs have additionally a nontrivial variety of diameter-dependent DOS distributions and, as a consequence, a very rich electrochemical behavior is expected. As an illustration Figure 3.5 shows the DOS of a semiconducting SWNT together with the energy states of the redox system in solution [33]. In that scheme, the oxidation in the redox system occurs when the empty states of the electrode match the filled levels of the redox system (W_{red}). SWNTs of different diameters will yield different rate constants due to the structure-dependent variations in the DOS and that could be tracked by electrochemistry [33]. The theory predicts that semiconducting or metallic SWNT band structure together with their distinct van Hove singularities could be resolved in voltammetry, in a manner analogous to scanning tunneling spectroscopy [33]. The experimental handicap for such an observation lies in the fact that, until now, it is not possible to synthesize CNTs with the same structure. Even if one wants to probe the electrochemical reactivity correlation with DOS of individual SWNTs, the isolation process of a given nanotube is rather difficult. So far, electrochemical studies involve ensembles of CNTs with mixed diameters and therefore a mixture of DOS distribution fingerprints and rate constants. Only an averaged correlation can thus be obtained between DOS and electrochemical reactivity. The same averaged electrochemical characteristics are provided by MWNT electrodes since they are formed with graphene sheets of different structures and with averaged rate constants.

We have mentioned the chemical anisotropy characteristic of graphitic materials, which is also present in their electronic properties. For instance, it is well known that in the layered structure of HOPG, the electronic conductivity in the plane parallel to the graphene layers (basal plane) is about four orders of magnitude lower than in the perpendicular one (edge plane) [1]. The basal plane of HOPG is atomically ordered, with higher electronic resistance and is chemically more inert than edge-plane HOPG. Such anisotropy also influences the electrochemical behavior inducing an electrochemical anisotropy. It has been demonstrated that in graphite, the basal plane exhibits slow electron-transfer kinetics, whereas the reactive edge sites increase the electron-transfer rate. For instance, McCreery and coworkers have reported a k_o for a $Fe(CN)_6{}^{3-/4-}$ redox system smaller than 10^{-6} cm/s in the case of basal HOPG and around 0.06–0.10 cm/s in the case of edge HOPG [1]. The same electrochemical anisotropy has been attributed to CNTs. The open ends of carbon nanotubes have been likened to the edge planes of HOPG, whereas the tube walls are suggested to have similar electrochemical properties to those of basal HOPG [3, 7, 8, 45, 46]. It has also been demonstrated that defective sites (either in the form of edge sites or other type of defects) can even be counted on individual single CNTs by selective electrochemical metal deposition on such defective points at very low overpotentials. These findings only show the increased electrochemical reactivity of such defective sites that can be discriminated when working with small electrochemical driving forces [47].

Electrochemical experiments with carbon nanotube electrodes showed enhanced electron-transfer reactivity (increased redox currents and reduced peak separations in the voltammetry that enables lower detection limits and enhanced sensitivity) compared to other electrode materials for a variety of systems [48–54]. These features have impelled some research groups to label CNTs as electrocatalytical materials. However, Compton and coworkers have further investigated and compared the electrochemical response of CNT-modified electrodes with edge-plane graphite substrates for different redox systems (NADH, catecholamines, etc.) [3, 7, 8, 55–57]. Figure 3.6 shows the typical electrochemical response that was found when comparing CNT-modified electrodes, edge-plane and basal-plane pyrolytic graphite electrodes. Basal pyrolytic graphite exhibits higher peak separations (which depends on the surface edge-defect density) and consequently lower electron-transfer rates [7]. However, edge-plane pyrolytic graphite electrodes and carbon-nanotube-modified substrates show smaller and similar peak separation corresponding to fast electron-transfer kinetics. Such a finding only demystified the claim that CNTs provide novel electrochemical attributes such as those electrocatalytical effects [3, 7, 8, 10]. Indeed, CNTs can exhibit electrocatalytic effects but in the same way as can be found on edge pyrolytic graphite systems. This only reinforces the idea that the edge-plane-like sites (like the ones at the open ends of nanotubes) are the ones responsible for such electrocatalytic behavior. Thus, from

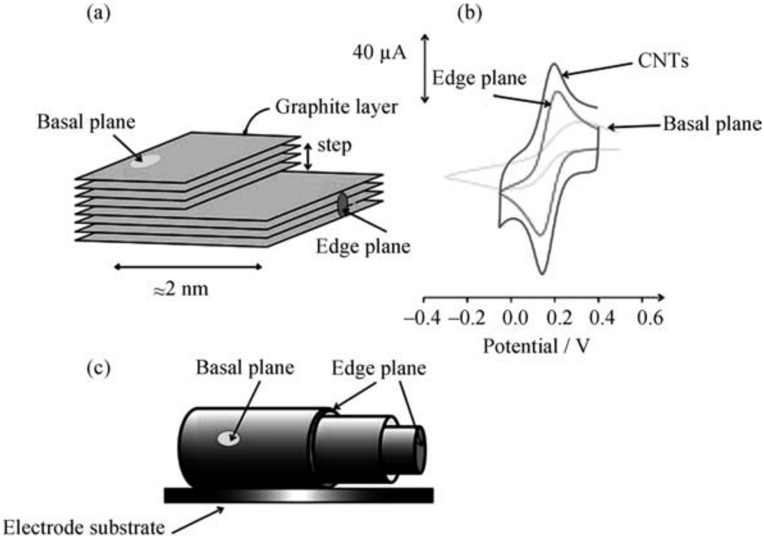

Figure 3.6 (a) Schematic representation of the layered structure of HOPG with the indication of the different edge and basal planes. (b) Voltammetric response of $Fe(CN)_6^{3-/4-}$ using basal-plane, edge-plane pyrolytic graphite and CNT electrodes. (c) Scheme of a MWNT on an electrode surface showing the edge plane and basal plane like sites. Reprinted with permission from Ref. [64]. Copyright, 2006, Wiley-VCH Verlag.

the electrochemical point of view, CNT systems have similar properties to edge-plane graphite, but the extra advantage comes from the nanometer size that can also be manipulated to design novel electrode architectures [10, 58] or for signal-amplification purposes [5, 9, 59]. Related to the latter issue, CNT systems exhibit a high effective surface area that is beneficial not only for enhancing electrochemical currents of diffusing electroactive species but also for allowing the load of high-density electrochemical active (bio)molecules that can improve electrochemical signals. Examples of the effect of such dimensional advantage can be found in the electrochemical investigation of DNA, where signal enhancement was achieved when using CNT-modified substrates compared to glassy carbon. It was proposed that CNTs could cause the double-helix DNA to unwrap, exposing the redox sites right next to the site of electron transfer [60]. Another example related to the fact that CNTs are versatile materials for the design of unusual electrode configurations can be provided by the SWNT-modified electrodes with the nanotubes disposed in an upright configuration, which, due to the nanometer size, they can establish excellent wiring to the redox center of metalloproteins favoring the direct electron-transfer process [45, 61]. More discussion about these issues can be found in the next sections.

It is important to point out that not all redox systems will exhibit electrocatalytic activity when probed on high-density edge CNT electrodes or edge pyrolytic graphite. Such phenomenon depends on the particular mechanism of the redox system [2]. It is important to recall that among the redox species there are some of them whose electrochemical behavior only depends on the carbon DOS but keep insensitive to the surface structure/morphology or chemistry [1, 2]. This is the case of many outer sphere redox species like $Ru(NH_3)_6^{2+/3+}$ or ferrocene. Normally, electrocatalytic effects are relevant on redox systems that involve specific chemical interactions with the electrodes and are very dependent on the surface structure and surface oxygen functionalities [1, 2]. In general, the examples mentioned before, on which an electrocatalytical behavior was observed, correlated with redox species that are very sensitive to the surface characteristics such as NADH, O_2, catecholamines, $Fe(CN)_6^{3-/4-}$. Moreover, at this point it is important to recall the relevance of surface oxygen functionalities on electrocatalysis processes. It was mentioned before that edge defect sites or unsatisfied valence are prone to react with oxygen and water. Such moieties can play an important role in electrocatalytical processes by enhancing the electron-transfer kinetics and also the adsorption. Some investigations in $Fe(CN)_6^{3-/4-}$ redox systems with CNTs have reported controversial results in the literature [62, 63]. McCreery and coworkers have found that the $Fe(CN)_6^{3-/4-}$ redox couple is sensitive to carbon surface structure but insensitive to carbon surface oxides [1, 2]. However, when such investigations were extended to CNTs, Gooding and coworkers [63] and other groups [4, 6] have found that oxygen functionalities in SWNTs increased the charge-transfer kinetics of the $Fe(CN)_6^{3-/4-}$ redox system. For a more detailed discussion of the effect of redox systems on carbon electrodes, the reader is referred to the nice work of McCreery and coworkers ([1, 2] and references therein).

It is important to clarify that there have been, in the literature, some examples of electrochemical processes on CNT-modified electrodes on which an apparent electrocatalytic process associated to the CNTs seems to take place (that is from the edge-plane-like sites) where in fact that was not the case. An example is the apparent electrocatalytic oxidation of hydrazine at MWNT electrodes [64, 65]. Such electrochemical behavior has been demonstrated to be a consequence of iron impurities contained in the CNTs that were responsible for the observed electrocatalytic effects (Figure 3.7). Therefore, caution is needed when reporting catalytic effects of CNTs under a given redox system and a careful comparison with, for instance, edge HOPG is mandatory to make sure that the CNTs are the responsible for the electrochemical enhancement.

Another relevant factor affecting the electrochemical performance of carbon nanotubes is adsorption. As was pointed out, CNTs exhibit high specific surface area that can develop high polarizability and additionally oxygen functionalities that can contribute with permanent dipoles [2]. Both effects can induce dipole interactions with adsorbates and favor the adsorption, which can be assisted by other interactions such as hydrophobic ones. Adsorbates can strongly alter the electron-transfer rates and the electrocatalytical activity. Positive effects can be found with the adsorption of some metalloproteins on CNTs that facilitates the electron exchange between the redox core and the carbon electrode and allows electrocatalytic activity to be monitored. Negative aspects are found when impurities are adsorbed on CNT substrates decreasing dramatically the electrochemical performance of the electrodes. In that case, activation procedures have been developed for removing such impurities. More precisely, surface preparation, as briefly discussed later on, is very important for the electrochemical performance on CNT electrodes.

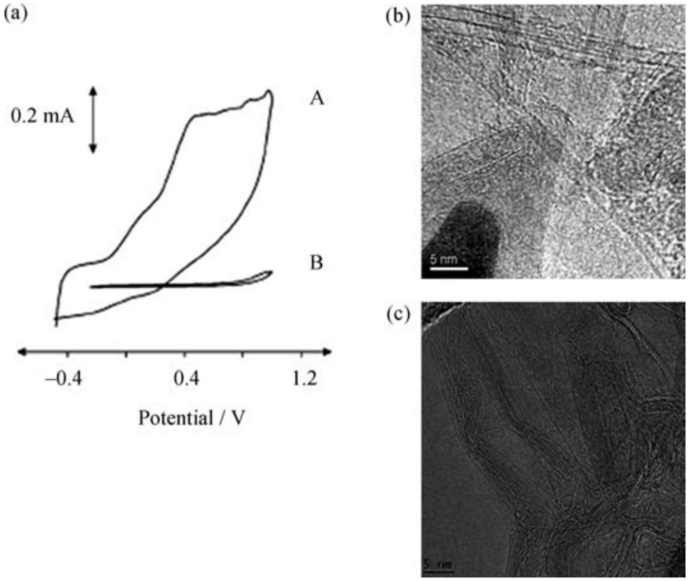

Figure 3.7 (a) Voltammetric response of (A) bamboo MWNTs and (B) high-purity catalyst free MWNTs in a solution containing 1 mM hydrazine in PBS. (b) Typical transmission electron image of MWNTs in which an iron metal particle sheathed by graphene layers is observed. Such impurities can lead to misinterpretations in the electrochemical CNT response, (c) transmission electron image of high-purity catalyst-free MWNTs that were used for acquiring the electrochemical response of curve (B). Figures 3.7(a) and (c) have been reprinted with permission from Ref. [65]. Copyright, 2007, American Chemical Society.

To summarize, one can say that the electrochemical performance of CNT electrodes is correlated to the DOS of the CNT electrode with energies close to the redox formal potential of the solution species. The electron transfer and adsorption reactivity of CNT electrodes is remarkably dependent on the density of edge sites/defects that are the more reactive sites for that process, increasing considerably the electron-transfer rate. Additionally, surface oxygen functionalities can exert a big influence on the electrode kinetics. However, not all redox systems respond in the same way to the surface characteristics or can have electrocatalytical activity. This is very dependent on their own redox mechanism. Moreover, the high surface area and the nanometer size are the key factors in the electrochemical performance of the carbon nanotubes.

3.3
Towards the Design of CNT-Modified Electrodes

3.3.1
Synthesis of CNTs

Even though an overwhelming number of CNT applications is currently being pursued, there is a long list of unsolved fundamental issues in the carbon-nanotube growth mechanism that make CNT production with defined characteristics and properties rather challenging. For instance, one unfulfilled aspiration is the control over nanotube chirality, diameter and lengths. Such lack of control added to the difficulties in CNT purification and processing are responsible for the high dispersion of results and performance of CNT devices. That is a very crucial point in the carbon nanotube research and a lot of effort should be invested in trying to settle such fundamental and very important issues.

Carbon nanotubes can be produced mainly by three different methods: electric arc discharge, laser ablation [66] and chemical vapor deposition (CVD) [67]. Arc-discharge and laser ablation rely on the condensation of carbon atoms generated from evaporation of solid carbon sources. These methods have the disadvantages of high operating temperatures, close to the melting temperature of graphite, together with the production of highly entangled CNT bundles that are difficult to purify, manipulate and assemble for building addressable structures. However, both methods provide high-quality CNTs with very few defects. The third method, based on CVD, operates at considerably lower temperatures with the handicap of bringing about more defective CNTs than in the case of the other methodologies. However, CVD has the advantage that CNTs can be grown directly on a substrate or wafer, thus facilitating device integration. In this case, the formation of tubes occurs as a result of thermal decomposition of a liquid- or gas-phase carbon source on a catalyst surface (typically Fe, Co or Ni nanoparticles). The growing interest in the CVD process lies in the greater possibilities of this method for successful synthesis of individual SWNTs and also aligned SWNTs or MWNTs with more controllable diameter and length. The growth direction of nanotubes can be controlled by the gas flow or by applying electric fields (plasma-enhanced CVD) [67]. Controlling CNT growth with CVD yields more organized CNT that can be readily integrated into addressable structures for fundamental characterization and potential applications.

3.3.2
CNT Purification Methods

As a result of CNT synthesis, catalyst metal nanoparticles (iron, cobalt, nickel) together with amorphous carbon and fullerenes are unavoidably present in the CNT soot.

As mentioned before, the lack of a good purification protocol can also constitute an important issue that hampers the applications. Therefore, an exhaustive pretreatment or purification process is required. Usually, purification consists of multistep purification procedures. Amorphous carbon removal can be achieved by heating the CNT material in air at temperatures below the CNT decomposition. Additionally, chemical treatments that can oxidize and dissolve the catalyst particles and the amorphous carbon can be performed. Many of these procedures rely on the use of either concentrated HNO_3 reflux with H_2SO_4 or HCl, or hydrogen peroxide reflux [68, 69]. Such treatments can eliminate a large amount of residual metal particles and other impurities. However, and even after prolonged washing treatments, metal catalyst can be still detected on CNT samples [70, 71]. The difficulties in removing the catalyst have been ascribed to the fact that in some cases the particles are sheathed and protected by graphene sheets. As mentioned before, Compton and coworkers have reported that such metal impurities on CNT can cause electrocatalysis on some electroactive species, as in the case of the hydrazine oxidation [64, 65]. They observed such behavior even though a superwashing purification procedure on the CNT was performed where it is assumed that at this stage the metal particles are passivated with graphitic layers. Figure 3.7 shows the electrochemical response of hydrazine on purified CNTs but still with some metal impurities present and on CNTs that were synthesized via a free-catalyst method. The figure clearly shows the electrocatalytic activity provided by the graphene-sheathed metal impurities. In that case, the hydrazine is not in close contact with the metal impurity, so it is not fully clear how the metal electrocatalysis is taken place. One plausible explanation may be related with the possibility that the metal impurity might induce changes in the electronic band structure of the CNT by adding additional energy states that might enhance the electron-transfer kinetics. Therefore, when probing a redox system using a CNT electrode, caution has to be taken in order to interpret the electrochemical results and a thorough characterization of the purified samples is mandatory in order to evaluate to what extent metal impurities influence the electrochemical performance.

3.3.3
Chemical and Biochemical Functionalization

The chemical and biochemical modification of CNTs possesses special interest because it opens the door to the achievement of novel hybrid systems for functional devices by combining the unique properties of CNTs with those resulting from functionalization, with for instance complexing agents, fluorescent and electroactive groups, (bio)catalysts, or biomolecules, (proteins, carbohydrates, nucleic acids, etc.). Chemical modification turns out to be one of the key issues for the development of selective electrochemical (bio)sensors for (bio)recognition or catalyst materials to be used in energy-storage devices. Moreover, chemical modification also helps to overcome one of the drawbacks for CNT applications that is the difficulty of dispersing them in solvents, especially in aqueous media. As-produced CNTs are tightly bundled in ropes (through Van der Waals interactions) that make them insoluble in aqueous and organic solvents, thus compromising their processability. Additionally, and taking into account the lack of control over CNT size and chirality during synthesis, chemical modification is becoming a very useful tool for post-produced CNT sorting.

The chemical modification of CNTs can be endohedral (inside the cavity of the tube) or exohedral [42]. There are some examples in the literature that have demonstrated the filling of CNTs with fullerenes, biomolecules (proteins, DNA), metals and oxides that have been driven inside by capillary pressure [39, 42, 72–78]. However, in this section we will focus on exohedral functionalization, taking place just at the external walls of the tubes. Both covalent (chemical-bond formation) and noncovalent (physiadsorption) functionlizations can be carried out. In the following subsections we will briefly discuss some selected examples dealing with both types of modifications.

For electrochemical devices, such functionalization schemes can be performed either before or after the CNTs are assembled on the electrodes.

3.3.3.1 Covalent Modification

As mentioned before, the CNT ends (either capped or as open edge ends) are chemically more reactive than the CNT walls. When the ends are open, the unsatisfied valence bonds become very reactive in the presence of water or oxygen and normally they are found enriched in oxygenated functionalities. Additionally, the capped ends can be opened and enriched with oxygenated species by oxidizing treatments with chemical agents (i.e. HNO_3), oxygen plasma or electrochemical anodization. These treatments can also introduce oxidized points in the sidewalls [42]. Among the oxygenated functionalities, one of special interest is the carboxylic group. These $-COOH$ residues constitute useful sites for further chemical functionalization through amide or ester bonds. The scheme in Figure 3.8 shows the covalent bonding of primary amine molecules through amide bonds facilitated by the carbodiimide chemistry which is aided by activated reagents such as N-hydroxysuccinimide (NHS) and dicyclohexylcarbodiimide (DCC) for organic solvents or EDAC (1-ethyl-3(3Dymethyl amino propyl carbodiimide hydrochloride) and sulfo NHS (N-hydroxysulfo-succinimide) for aqueous coupling [16, 25, 37, 44]. Amines can also be coupled to carboxyl groups activated with $SOCl_{2.}$ Ester linkages taken place by reacting the carboxyl -residues with alcohol functionalities are also shown in Figure 3.8 [25, 44]. The amide formation is being widely used for the anchoring of proteins, amine-terminated oligonucleotides, ion receptors, gold nanoparticles functionalized with aminethiols, polycationic electrolytes such as poly(ethyleneimine), and so on.

On the other hand, and as discussed before, the chemical reactivity of CNT sidewalls increases with the tube curvature (i.e. decrease of the tube diameter), due to the increase of the pyramidalization angle and greater strain energy per atom [37, 38]. Such pyramidalization of the CNT atoms causes the exohedral lobes of the orbitals to be larger than their endohedral counterparts. The reactivity of the surface is thus enhanced by the pronounced exposure of the hybrid orbitals from the exterior, which favors the orbital overlap with incoming reactants [38].

Accordingly, many reactions can be performed on the sidewalls of the CNTs, such as halogenation, hydrogenation, radical, electrophilic and nucleophilic additions, and so on [25, 37, 39, 42–44]. Exhaustively explored examples are the nitrene cycloaddition, the 1,3-dipolar cycloaddition reaction (with azomethinylides), radical additions using diazonium salts or radical addition of aromatic/phenyl primary amines. The aryl diazonium reduction can be performed by electrochemical means by forming a phenyl radical (by the extrusion of N_2) that couples to a double bond [44]. Similarly, electrochemical oxidation of aromatic or aliphatic primary amines yields an amine radical that can be added to the double bond on the carbon surface. The direct covalent attachment of functional moieties to the sidewalls strongly enhances the solubility of the nanotubes in solvents and can also be tailored for different

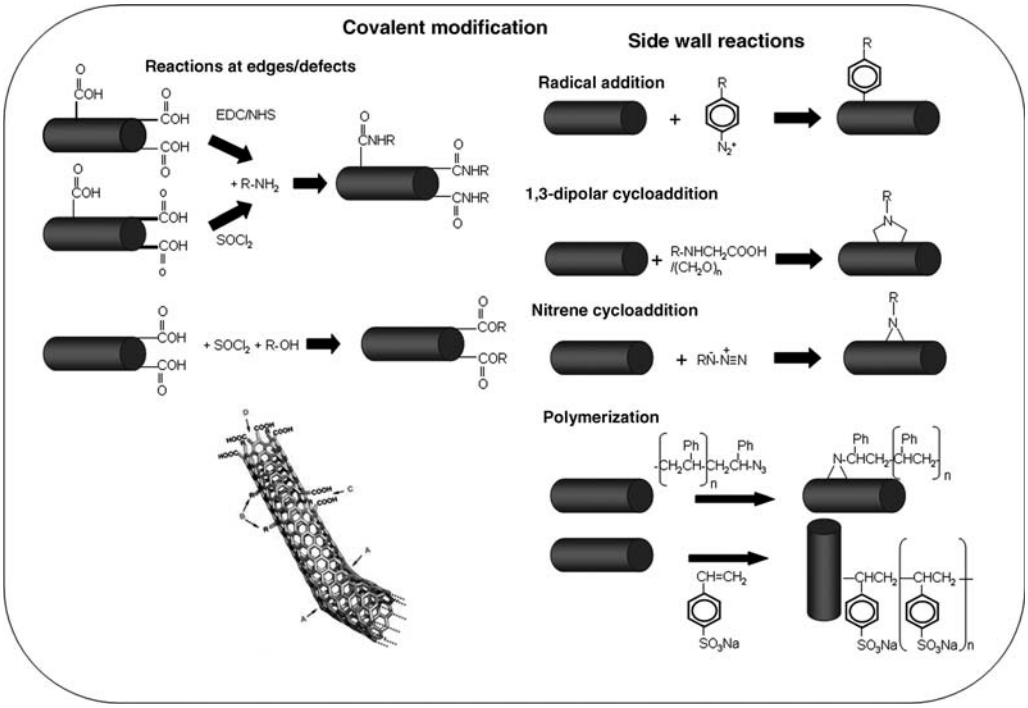

Figure 3.8 Scheme showing the more common covalent reactions at the CNT edge/defects and at the CNT sidewalls. The figure also shows the typical defects in a SWNT: (a) five- or seven-membered rings in the C network, instead of the normal six-membered ring, leads to a bend in the tube, (b) sp^3-hybridized defects (R=H and OH), (c) carbon network damaged by oxidative conditions, which leaves a hole lined with −COOH groups, and (d) open end of the SWNT, terminated with oxygenated species such as −COOH groups. The last figure has been reprinted with permission from Ref. [42]. Copyright, 2002, Wiley-VCH Verlag.

applications (for instance, in medical chemistry, solar energy conversion, and selective recognition of chemical species) [44].

The covalent reaction of CNTs with polymers is another important example because the long polymer chains also help to dissolve the tubes in a wide range of solvents (organic or aqueous ones). There are two main methodologies for the covalent attachment of polymeric substances to the surface of nanotubes, which are defined as “grafting to” and “grafting from” methods [44]. The former relies on the synthesis of a polymer with a specific molecular weight. Subsequently, this polymer chain is attached to the graphitic surface of CNT (i.e. polystyrene coupling). The ‘grafting from’ method is based on the covalent immobilization of the polymer precursors on the surface of the nanotubes and subsequent propagation of the polymerization in the presence of monomeric species. Examples of the latter procedure comprise the *in-situ* polymerization of polyvinylpyridine, polystyrenesulfonate, poly(methyl methacrylate), polyaniline, and so on [44]. Electrochemistry can also be used for polymerization via the formation of radical organic species by electron transfer between the CNT and the monomer. With such polymer coatings, the surface properties of the CNTs can be tailored from highly polar to hydrophobic.

3.3.3.2 **Noncovalent Modification**

Covalent modification yields a very stable and effective derivatization. However, some drawbacks can emerge when pursuing applications, especially with SWNTs. A high density of reactive sites or covalently functionalized points can lead to a loss of the CNT conjugation network with the consequent degradation of the CNT mechanical and electronic properties.

The large aromatic and hydrophobic character of CNTs make them ideal surfaces for noncovalent interaction with molecules via Van der Waals, π-stacking or hydrophobic forces [39, 44].

There are many examples in the literature of the noncovalent binding of amphiphilic agents on CNTs that have promoted CNT disentanglement and made them water soluble and biocompatible. Examples of such agents are some organic ionic surfactants such as sodium dodecyl sulfate or dodecylbenzene sulfonate. Other examples include polyaromatic compounds such as pyrenes with hydrophilic functional groups, proteins or polymers (polyethyleneglycol, triton, tween 20, polyvinylpyrrolidine, polystyrene sulfonate, DNA, RNA, polysaccharides, etc.) that coat or wrap the nanotube in such a way that the more hydrophobic part interacts with the CNT surface, whereas the hydrophilic region faces the aqueous medium. An illustration is depicted in Figure 3.9. Some of these polymers have also been used as blocking agents of nonspecific binding of proteins in the development of biosensors (PEG, tween 20, triton-100).

A variety of these physisorbed molecules were used as anchor points for covalent immobilization in a so-called hybrid approach [16]. That is the case of bifunctional pyrenes (i.e. 1-pyrenebutanoic acid succinimidyl ester, pyrene maleimide) or polymers with terminal amine/carboxylic groups that have been used to covalently immobilize proteins, functionalized oligonucleotides, and so on, (Figure 3.9) [43, 44].

3.3.3.3 **Chemical Modification for CNT Sorting**

As already pointed out, chemical modification is currently being used for CNT sorting. The separation of semiconducting and metallic nanotubes is crucial for many applications, such as those based on field effect transistor devices. Dielectrophoresis based on inducing a dipole moment on CNT has been used for this purpose [79]; different migrations can be obtained depending on whether the CNT is metallic or semiconductor. However, CNTs can also be separated by chemical means. For instance, it has been found that octadecylamine (ODA) selectively stabilizes semiconductor nanotubes [80]. Another important example of chiral selectivity in CNT functionalization is the case of diazonium salts [81, 82]. These reagents form a covalent aryl bond only with metallic carbon nanotubes, leading to the exclusion of semiconducting nanotubes. The selective reactivity was attributed to the availability of electrons near the Fermi level to stabilize a charge-transfer transition state preceding bond formation with the diazonium salt. Raman spectroscopy is an ideal technique for probing these selective interactions. Similarly, the preferential charge-transfer complex formation of bromine with metallic CNTs allowed their separation

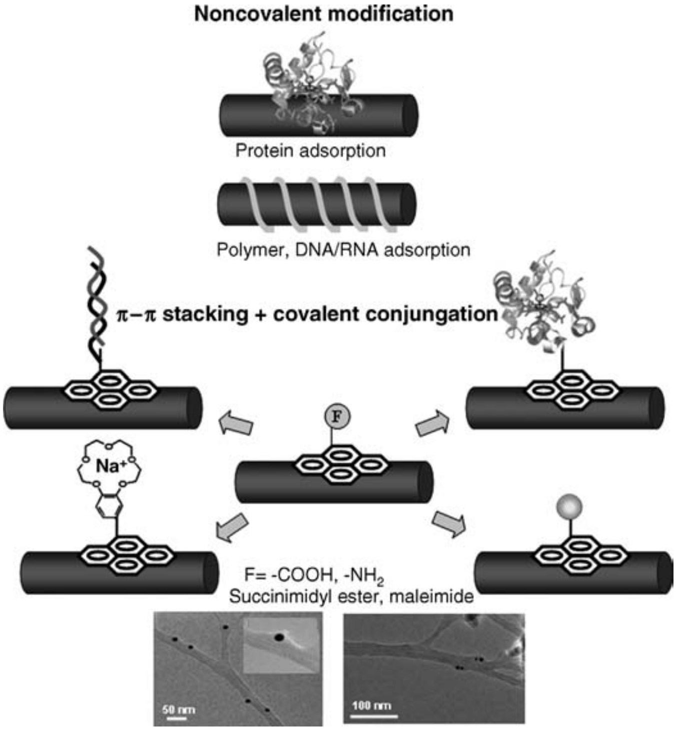

Figure 3.9 Schematic representation of the typical noncovalent CNT functionalizations and the hybrid approach by using pyrene linkers. The figure also shows transmission electron images of SWNT modified with streptavidin labeled with 10 nm gold nanoparticles that were covalently coupled to pyrene linkers that were stacked on the CNT surface (a). Their biorecognition with biotin, also labeled with 5-nm gold nanoparticles, is observed in (b) by the appearance of paired nanoparticles. Before the incubation with biotin, the streptavidin-modified SWNTs were passivated with polyethylenglycol (PEG) to avoid nonspecific adsorption of the biotin.

from semiconducting CNTs [83]. Other examples are free-base porphyrins that have been shown to specifically bind to semiconducting SWNTs [84]. The mechanism of the porphyrin-selective binding has not yet been fully understood, but a speculation has been made that the semiconducting SWNT is like a conjugated macromolecule with the nanotube surface properties similar to those found in radical ion pairs, thus providing interactions with the free-base porphyrin molecules. Wrapping SWNTs with single-stranded DNA was found to be sequence dependent. The electrostatics of the DNA/SWNT hybrid depends on the tube diameter and electronic properties, enabling nanotube separation by anion-exchange chromatography [85].

Separation of SWNTs based on chirality and diameter with surfactants has also been evidenced by density-gradient ultracentrifugation [86]. Finally, a recent study has demonstrated the separation of semiconducting nanotubes from metallic ones by chemical interaction of the former with attached amine-terminated silane molecules assembled on a silicon wafer. In a separate experiment, metallic nanotubes were also shown to bind selectively with phenyl-terminated silane molecules on the SiO_2 surface [87].

3.3.3.4 Chemical Doping, Intercalation and Artificial Defects

CNTs can be easily doped by noncovalent means via molecular adsorption, an aspect that has been considerably exploited to develop ultrasensitive field effect transistor sensors [88–91]. However, substitutional doping with B and N to confer p and n character to the CNTs has also been carried out [92]. Such doped systems can be more susceptible to react with donors or acceptors molecules (depending on the doping) allowing the chemically reactivity to increase.

Intercalation of species into the CNT structure has also been performed. For instance, the intercalation of lithium in CNTs [93, 94] is one attractive topic due to the potential applications in electrochemical energy storage in lithium batteries. Edge-plane defects turn out to be very important for such processes [95].

Carbon nanotubes inevitably contain defects, whose extent depends on the fabrication method but also on the CNT post-treatments. As already seen, oxidizing treatments, such as acid, plasma or electrochemical, can introduce defects that play an important role in the electrochemical performance of CNT electrodes. For instance, Collins and coworkers have published an interesting way to introduce very controlled functionalization points or defects on individual SWNTs by electrochemical means [96]. Other methodologies to introduce artificial defects comprise argon, hydrogen and electron irradiation. Under this context, a number of recent works have appeared with the goal of tailoring the electrochemical behavior of CNT surfaces by the controlled introduction of defects [97, 98].

3.3.4
CNT Deposition on Electrode Surfaces

In order to guarantee an efficient performance of the CNT-based electrochemical devices, attention has to be paid not only to CNT synthesis and purification but also to the way that the CNT electrode is built up. There have been many studies in the literature dealing with CNT dispersions either on conducting substrates or forming composites. In this subsection we will address the different carbon-nanotube deposition techniques and carbon-nanotube arrangements on different electrode surfaces.

We will discuss, on the one hand, the spaghetti-like CNT electrodes on conductive surfaces or randomly dispersed in a polymer matrix; and on the other hand, CNT arrays grown *in situ* on substrates with large-scale control of location and orientation. Finally, individual CNT electrodes will be briefly discussed. Figure 3.10 illustrates these different CNT electrode arrangements.

3.3.4.1 Randomly Dispersed CNTs

CNTs tend to aggregate in all kinds of aqueous and organic solutions due to the Van der Waals forces between them. This brings difficulties in making homogeneous CNT surfaces and constitutes a drawback for applications. Current studies on CNT

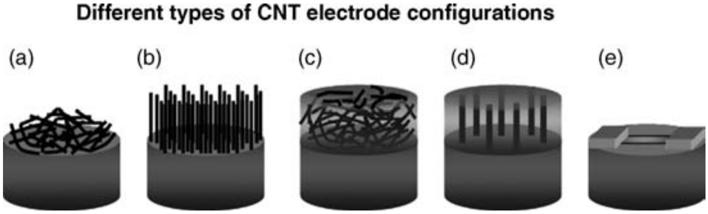

Figure 3.10 Illustration of different CNT electrode configurations: (a) randomly dispersed on a surface, (b) vertically aligned CNTs, (c) randomly dispersed CNT composites, (d) oriented CNTs embedded in a polymer matrix, (e) individual CNT electrode.

electrodes have shown a significant dispersion in the results. One of the major discrepancies can be attributed to the different configurations into which CNTs are assembled. Most of the electrochemical studies reported in the literature deal with CNTs randomly dispersed onto a substrate electrode or by confining the CNTs on a substrate with polymers. These kind of configurations can be a simple methodology for practical electrochemical studies but it turns out to be not very suitable for fundamental electrochemical studies since the random configuration of the CNTs onto the electrodes essentially causes difficulties in determining the contributions of the ends and the sidewall of the nanotubes to the electrochemical properties of the CNTs.

CNT conductive surface modification Both SWNTs and MWNTs can be deposited directly from a CNT dispersion as a random network or thin film on conventional electrodes. From the point of view of their construction such electrodes are very easy to prepare but they may suffer from mechanical instability, thus limiting their application.

A typical electrode substrate for building up nonoriented CNT films is glassy carbon. The modification of glassy carbon is currently done by casting drops of purified CNTs dispersed either in organic or aqueous solvents and allowing the electrode to dry [99–101]. Glassy carbon provides a hydrophobic surface that considerably stabilizes the CNT films. Another carbon substrate widely employed by Compton and coworkers is the basal plane pyrolytic graphite [3, 7, 8]. In this case, carbon nanotubes were abrasively immobilized onto basal pyrolytic graphite electrodes by gently rubbing the electrode surface with a fine-quality filter paper containing CNTs.

An important number of publications have recognized the differences in the electrochemical reactivity between the CNT-modified electrodes and the control electrodes (glassy carbon or basal pyrolytic graphite treated in the same way but without CNTs) that is attributed to the high specific surface area of the CNTs and to the differences in their surface chemistries (higher density of electroactive reactive sites given by defects or edges) [3, 7, 8, 54, 99, 100]. As mentioned previously, Compton and coworkers have clearly pointed out the key role of CNT edges and showed that CNTs were no more electrocatalytic than the edge planes of pyrolytic

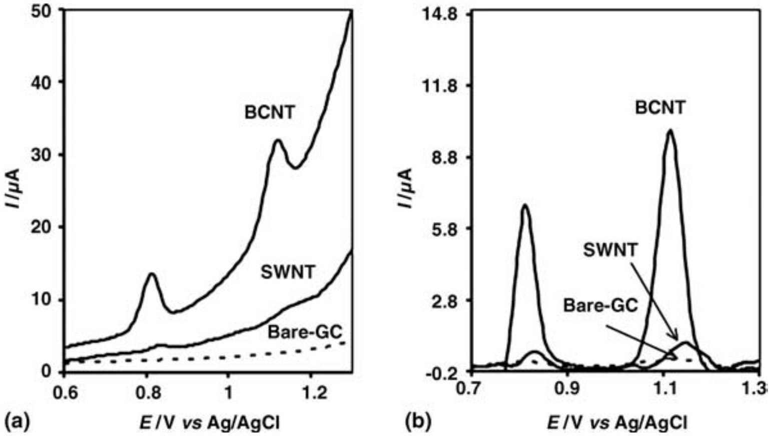

Figure 3.11 Differential pulse voltammograms (DPVs) for guanine at bare glassy carbon, SWNT modified glassy carbon and bamboo-modified glassy carbon. DNA conc, 0.4 mg mL^{-1}, (b) the corresponding DPV plots observed in (a) but with background subtraction. The signal generated from the bamboo CNTs is much higher than the signal generated from bare or SWNT-modified glassy carbon. Notice the appearance of the guanine peak for bare glassy carbon after background subtraction. Reprinted with permission from Ref. [101]. Copyright, 2005, Elsevier.

graphite [3, 7, 8]. The electrochemical importance of the edge planes has also been supported by Gooding and coworkers. They have shown evidence of the improved electrochemical reactivity of bamboo-like CNTs dispersed on glassy carbon as compared to SWNT-modified electrodes by probing the oxidation of guanine and adenine bases (Figure 3.11) [101].

However, in some cases and even more when the CNT layer is too thin, the underlying glassy carbon or basal pyrolytic graphite electrodes have been found to give some interferences in the electrochemical response. An illustrative example is shown in Figure 3.12 [56]. On the other hand, very thick 3D CNT films can contribute with large capacitive background currents due to the large surface area that can hamper electroanalytical applications, as often occur when using the highly porous bucky paper [102, 103]. In such CNT papers, formed basically by filtration of purified SWNTs, a small faradaic signal can be lost in the high capacitive currents. However, high CNT surface area is beneficial for energy storage or electrochemical actuator applications.

Gold or Pt electrodes have also been used as conducting supports for developing CNT-modified electrodes. Although an enhanced electrochemical response can be evidenced, the CNT films (when casting from a CNT dispersion) are not very stable on such hydrophilic surfaces and tend to be removed in contact with aqueous media, a problem that can be solved by covalent CNT attachment to the gold surface. Gooding and coworkers have also used randomly dispersed CNT-modified gold electrodes to show the importance of the density of active sites by using electrodes modified with different CNT lengths [63]. They found that the shorter the nanotubes were, the more rapid was the electron-transfer kinetics of the nanotube-modified electrode because of the greater contribution of the ends. In such studies they also claimed the

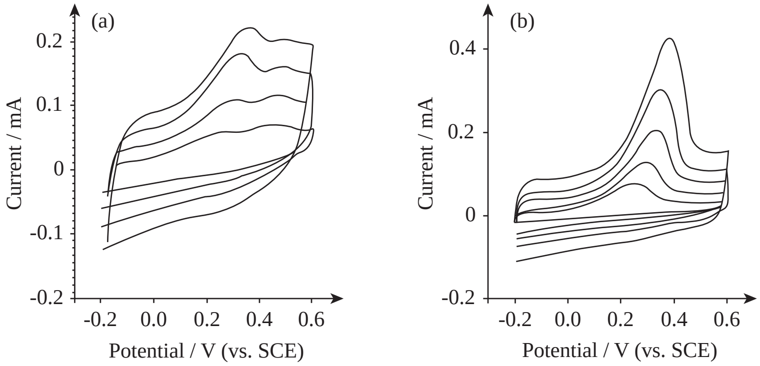

Figure 3.12 Cyclic voltammetric response of (a) abrasively modified MWNT basal pyrolytic graphite (bppg) and (b) film modified MWNTs on bppg electrodes in a pH 7.4 phosphate buffer solution containing 1.2 mM NADH. All scans are 25, 50, 75, 100 and 150 mV/s. The interference response of the bppg by the appearance of a second peak at higher anodic potentials can be observed in (a). Reprinted with permission from Ref. [56]. Copyright, 2005, The Royal Society of Chemistry.

importance of oxygenated species at the CNT edges for facilitating the electron-transfer process. Indium tin oxide (ITO) has also been used as supporting electrode for CNT dispersion [104]. Such modified substrates combine the low background current of the ITO with the enhanced electrochemical properties of the CNTs. At the same time ITO is a very interesting CNT electrode support due to its optical transparency that can be exploited for undertaking electrochemical/optical studies.

CNT randomly dispersed composites Many soft and rigid composites of carbon nanotubes have been reported [17]. The first carbon-nanotube-modified electrode was made from a carbon-nanotube paste using bromoform as an organic binder (though other binders are currently used for the paste formation, i.e. mineral oil) [105]. In this first application, the electrochemistry of dopamine was proved and a reversible behavior was found to occur at low potentials with rates of electron transfer much faster than those observed for graphite electrodes. Carbon-nanotube paste electrodes share the advantages of the classical carbon paste electrode (CPE) such as the feasibility to incorporate different substances, low background current, chemical inertness and an easy renewal nature [106, 107]. The added value with CNTs comes from the enhancement of the electron-transfer reactions due to the already discussed mechanisms.

Nafion, an insulator perfluorinated ionomer, has also been successfully used for preparing CNT-based electrodes [108, 109]. It results in a good material for confining CNTs on an electrode substrate and also has capabilities of CNT solubilization and ion-exchange properties.

Other nanocomposite CNT electrodes have been reported by mixing CNTs with granular Teflon [48], chistosan [110], polystyrene [111], polysulfone [112] and epoxy [103, 113] or by incorporating them into a silicate gel matrix [13, 114].

Composites with certain structural organization have been developed by approaching the self-assembly concept [13]. Electrostatic matching can be used to coat CNTs with layers of oppositely charged polyelectrolytes. Accordingly, the fabrication of CNT-based films using the layer-by-layer method (LBL) has gained interest because of its simplicity and the wide choice of materials. For example, multilayer films of MWNTs have been homogenously and stably assembled on glassy carbon using the LBL method based on electrostatic interaction between negatively charged MWNTs and positively charged chitosan [115].

Apart from the insulating polymeric matrices, conductive polymers such as polypyrrole and polyaniline have been used as nanocomposite electrodes by chemical or electrochemical polymerization [13, 17, 116, 117]. Such materials provide high conductivity and stability. However, the use of insulating polymers can be more advantageous than the conductive polymers when employed in cyclic voltammetry. This is because the former electrodes exhibit a more discernible response for the redox species from the low-charging faradaic current, compared with the latter.

CNTs–nanoparticles composites have also been exploited for electrochemical sensing applications [17, 118, 119]. Incorporation of metal and oxide nanoparticles has been demonstrated to enhance the electrocatalytical efficiency. A wide range of particles have been used (Pt, Pd, Co, FeCo alloy, Co, Cu, Ag, Cu) and in some cases such CNT/nanoparticles have been combined together with charged polymers [17].

Recently, the electrochemical performance of different rigid carbon-nanotube/epoxy composites was characterized. In particular, the electrochemical behavior of composites made of bamboo-like, single- and multiwalled carbon nanotubes of different diameters was studied, and compared with reference materials such as analog graphite composites and HOPG (basal and edge) as illustrated in Figure 3.13a [103]. The composites were prepared with the same weight ratio. The analysis was focused on the electron-transfer rate constants and charge-transfer resistances determined by cyclic voltammetry and impedance spectroscopy. The results suggested that the density of edges is the main parameter controlling the good electrochemical performance of the composite transducers. Specifically, a clear trend was found in these composites: the smaller the CNT diameter (i.e. higher density of CNTs in the composite and hence greater density of edge sites) the higher the rate-transfer constant, the higher the peak current and the smaller the charge resistance. In fact, the bamboo-like CNT composites were the ones showing the fastest electron-transfer rate and the smallest charge resistance due to their intrinsically high density of graphitic edges (Figure 3.13b). The electrochemical performance of the CNT composites was better than that of the graphite composite and lay between the basal and edge HOPG, but closer to the edge one in response. Figure 3.13c shows the electron-transfer rates calculated from voltammetry. A remarkable characteristic of the CNT composites was a good signal-to-noise ratio (sensitivity) due to relatively low background currents provided by the epoxy matrix [103].

Among soft organic matrices for electrochemical applications, polysulfone (PSf) appears as a suitable and not very exploited candidate with very attractive properties including a remarkable stability at high temperatures and extreme pH conditions [112]. Also recognized was the flexibility of such composites, the good adhesion with the carbon material and the versatility and easiness for a wide range of (bio)molecule trapping using a simple phase-inversion process for its fabrication. These CNT/PSf

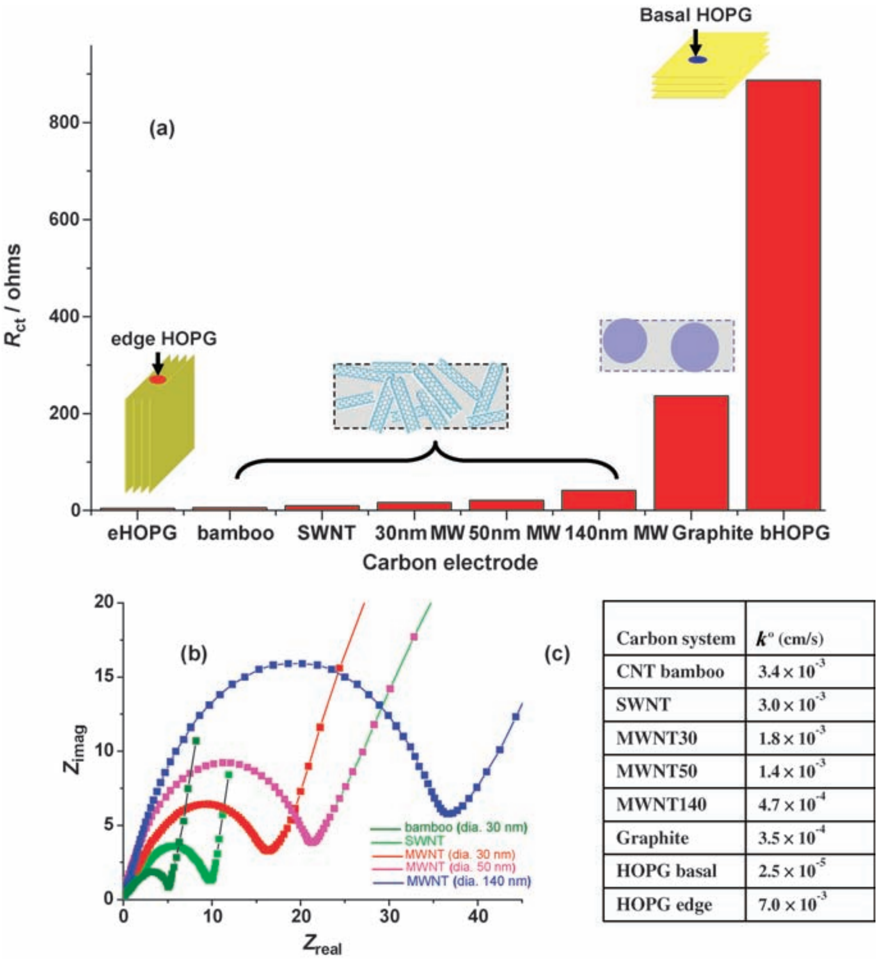

Carbon system	k^o (cm/s)
CNT bamboo	3.4×10^{-3}
SWNT	3.0×10^{-3}
MWNT30	1.8×10^{-3}
MWNT50	1.4×10^{-3}
MWNT140	4.7×10^{-4}
Graphite	3.5×10^{-4}
HOPG basal	2.5×10^{-5}
HOPG edge	7.0×10^{-3}

Figure 3.13 (a) Values of charge-transfer resistance of different systems based on carbon, using the redox probe $Fe(CN)_6^{3-/4-}$. (b) Nyquist plot of different carbon nanotube composites in the presence of the redox couple. (c) Table with the electron-transfer rate constants calculated from cyclic voltammetry data by using Nicholson method. Adapted with permission from Ref. [103]. Copyright, 2008, Elsevier.

nanocomposites constitute a very promising material for electrochemical and electroanalytical purposes with an enhanced electrochemical response as compared to that of its homologue graphite/PSf. It has been observed that carbon nanotubes are wrapped by the polymer resulting in a network with a remarkable specific surface area, which facilitates (bio)molecule trapping and stabilization [120]. Raman spectroscopy studies evidenced a higher density of structural defects as compared to the analog graphite composite, which can also enhance the electrochemical performance [120]. These nanocomposites have been recognized for their practical use as good candidates for screen-printed electrodes in (bio)analysis assays.

Summarizing, one can conclude that irrespective of the nature and the way in which the composite is built up, these matrices are important for providing robustness to the CNT platform and at the same time for facilitating the component trapping that is quite advantageous for many applications such as biosensing.

3.3.4.2 **Oriented CNT Electrodes**

For a thorough understanding of the fundamental CNT electrochemistry, many applications require well-organized and oriented carbon-nanotube arrays. For instance, the upright CNT configurations can provide a high density of oriented electroreactive edges facilitating, on the one hand, the electron-transfer process, and on the other hand, the covalent linkage of molecules. There are two major approaches for obtaining oriented CNTs: by self-assembly procedures, and by *in-situ* CVD growth of aligned CNTs with plasma enhancement. A schematic representation of such procedures is depicted in Figure 3.14.

Oriented CNT self-assembly route The self-assembly approach relies on the alignment of short SWNTs that were cut by oxidative treatments and ultrasonication [43, 45, 58, 61, 63, 121–126]. The main issue to control is the length of the cut CNT that should be quite homogeneous for guaranteeing a well-ordered assembly.

Many groups have reported the assembly of shortened SWNTs in an orthogonal orientation on a gold electrode via surface reactions (thiolation and carbodiimide chemistry as shown in Figure 3.14) [45, 58, 63, 122–124]. Such chemically assembled SWNTs can work as nanoelectrode arrays. Gooding and coworkers compared the electrochemical performance of the upright CNT arrangement with respect to randomly dispersed nanotubes on a cysteamine-modified gold electrode in the presence of $Fe(CN)_6{}^{3-/4}$. They found peak-to-peak potential separations of 105 mV for the randomly dispersed SWNTs, whereas the peak separation for the aligned SWNTs was about 72 mV. This difference revealed that the aligned SWNTs show better electrochemical properties than those randomly dispersed, as shown in

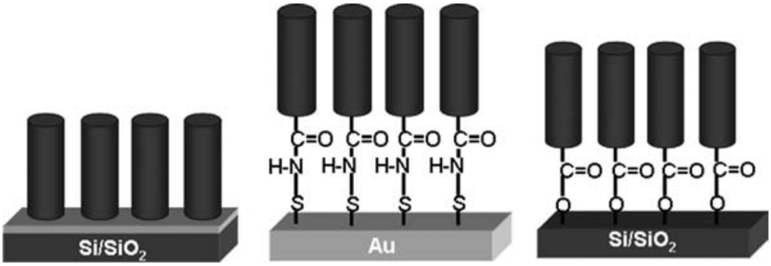

Figure 3.14 Different configurations of vertically aligned CNTs either by *in-situ* growth of CNTs from plasma enhanced CVD or CNT self-assembly through surface reactions on gold or silicon substrates.

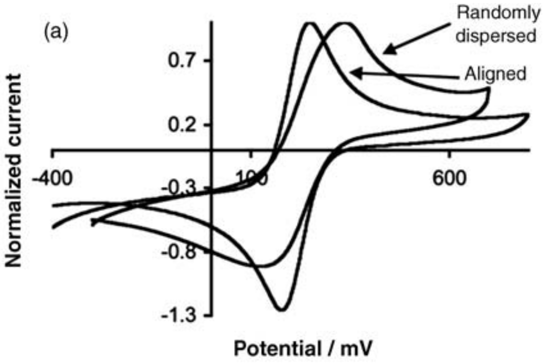

(b)

Electrochemical parameters for Fc-NH_2 attached onto gold modified with aligned SWNTs (a) or randomly dispersed SWNTs (b)

Electrode	Mean length (nm)	k_{app} (s^{-1})
6 h cut[a]	257 (+161,-109)	459±132
6 h cut[b]	257 (+57,-30)	12±8

Figure 3.15 (a) Cyclic voltammetry of SWNT-modified electrodes where the tubes were cut for 2 h and either randomly dispersed or vertically aligned. CVs are recorded relative to an Ag/AgCl reference electrode in 1 mM $K_3Fe(CN)_6$ in a background electrolyte of 0.05 M KH_2PO_4 and 0.05 M KCl at pH 7.0 at 100 mV/s. The y-axis shows the current normalized to the anodic peak current. Reprinted with permission from Ref. [63]. Copyright, 2005, The Royal Society of Chemistry. (b) Table showing the transfer-rate constants for aligned or randomly dispersed CNTs functionalized with ferrocene groups. The nanotubes were subjected to 6 h of cutting time in both cases. Adapted from Ref. [124] with permission. Copyright, 2007, Elsevier.

Figure 3.15 [63]. The table in Figure 3.15 also shows enhanced electron transfer rates for ferrocene attatched on aligned SWNTs as compared to ferrocene attatched on randomly dispersed SWNTs [124]. Moreover, such vertically aligned SWNTs act as molecular wires that allow efficient electrical communication between the underlying electrode and the redox enzymes [45, 123, 127].

Other groups have achieved CNT forest assemblies by electrostatic SWNT–COO^-/Fe^{3+} interactions also starting with shortened CNTs. The assembly process involves sequential substrate dipping in dilute Nafion and aqueous $FeCl_3$ solutions followed by DMF-assisted precipitation of the nafion-adsorbed Fe^{3+} to produce thin FeO(OH)/FeOCl nanocrystals. Subsequent immersion into a DMF disperse nanotube suspension produces the forest assembly that is driven by acid–base neutralization [12, 61, 121].

The silicon substrate constitutes a very interesting support for facilitating the integration in microelectronic devices. The electrochemical and electroanalytical fields can gain remarkable benefits from the silicon-based miniaturization devices, especially if arrays of metal electrodes can be fabricated. An understanding of the electrochemical properties of CNTs directly attached to silicon is thus essential for their potential application in developing silicon-based electrochemical or (bio)electrochemical sensors and ultra-microelectrode arrays. Therefore, following the same idea reported for SWNT assemblies oriented through surface reactions, some groups have reported new approaches for organizing vertically aligned shortened SWNTs onto highly doped silicon surfaces. [125, 126]. The ordered CNT assembly was made by the surface condensation reaction with hydroxyl-terminated silicon, or with ethyl undeconate monolayers (Figure 3.14) [125, 126]. A good electrochemical reversibility and enhanced conductivity was found in the case of the SWNTs–SiO_2 structure. Such electrode configurations hold promise for the fabrication and development of silicon-based electrochemical and (bio)electrochemical sensors, solar cells and nanoelectronic devices.

***In-situ* growth of oriented CNT films** In this approach, aligned CNTs are grown directly onto an electrode surface (i.e. Si coated with a Cr film) by using plasma-enhanced CVD [4, 6, 102, 128]. Meyyappan and coworkers have exploited such methodology and have developed vertical 3D CNT ensembles with different CNT density embedded or not in an insulating matrix (SiO_2) [4, 6, 102]. The different steps for achieving a passivated CNT ensemble are illustrated in Figure 3.16. As already mentioned, these upright CNT configurations can enhance the electron-transfer kinetics and also the

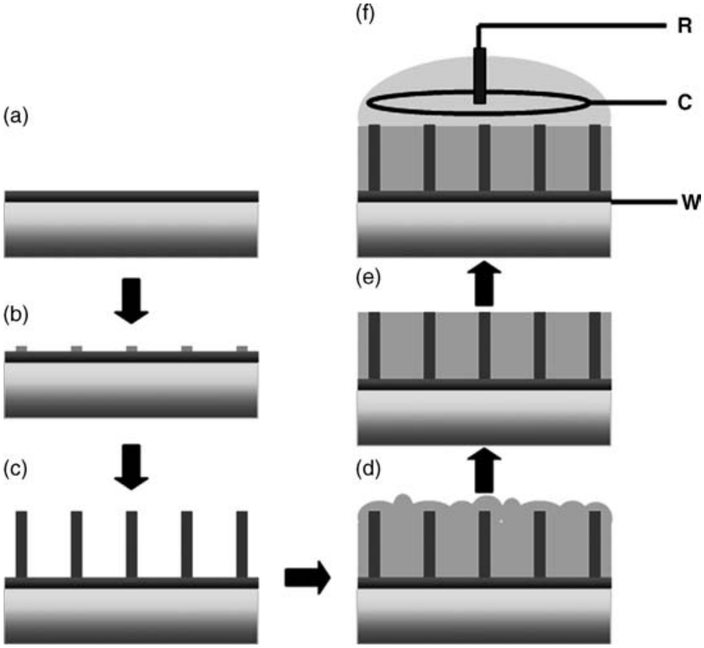

Figure 3.16 Different steps in the fabrication of MWNT nanoelectrode arrays. (a) metal film deposition, (b) catalyst deposition, (c) plasma-enhanced chemical vapor deposition for CNT growth, (d) dielectric encapsulation with SiO_2, (e) planarization with a chemical mechanical polishing to expose the ends of the carbon nanotubes, (f) electrochemical characterization. Readapted from Ref. [6].

chemical reactivity for covalent molecule anchorage. However, these arrays can provide more benefits from the electroanalytical point of view if the geometrical disposition of the CNTs can be controlled in order to make them act as nanoelectrode arrays [4, 6]. As is well known, nanoelectrode arrays exhibit unusual electrochemical properties that stem from non-planar radial diffusion of the electroactive species. Under this regime, the mass-transfer rate significantly increases and a steady-state current is rapidly reached that is directly proportional to analyte concentration. This makes the nanoelectrode exhibit a very fast response, very high signal/noise ratio (faradaic current/nonfaradaic charging current that can be improved by insulating the sidewalls of the CNTs), and consequently very low limits of detection, all these properties being highly desired in amperometric sensors. In order to guarantee the key factor, which is the radial diffusion, the diffusion layers of neighboring electrodes should not overlap and this can be accomplished by controlling the interspacing between the nanoelectrodes.

Li *et al*. have developed nanoelectrodes based on MWNT arrays on metal films embedded in a SiO_2 matrix with only the very end exposed at the surface [4, 6]. The size and the spatial distribution of MWNTs could be precisely controlled to ensure that each one behaves as an independent nanoelectrode. The spacing among individual nanoelectrodes was sufficiently larger than the diameter of the nanotubes to prevent the overlap of diffusion layers from the neighboring electrodes. The authors could vary the density of CNT nanoelectrodes from 10^6 to 2×10^9 electrodes cm^{-2}. Figure 3.17 shows different density CNT arrays and their corresponding electrochemical response. They confirmed that high-density electrodes behave very differently from those with lower densities. At high densities of CNTs, the electrochemical response was dominated by a planar diffusion transport evidenced by a common peak shape in the cyclic voltammetry; whereas at low densities of CNTs, the electrochemical response was basically sigmoidal, which is typical of radial diffusion mass transport. Thus, low-density MWNT nanoelectrode arrays displayed the desired independent nanoelectrode behavior showing diffusion-limited steady-sate currents in cyclic voltammetry over a wide range of scan rates. This configuration is very promising for developing ultrasensitive electrochemical sensors.

3.3.4.3 **Individual CNT Electrodes**

As already mentioned, nanoelectrodes yield high current densities at the electrode surface, which is very beneficial for electroanalysis studies and also for the study of fast heterogeneous electron-transfer kinetics. Moreover, they can also be exploited to develop electrochemical nanotools for biophysical applications including, for instance, probing biological membrane functions or the activity of single electroactive molecules (enzymes). The possibilities that CNTs bring for manipulation allow the fabrication of individual CNT nanoelectrodes, which is of remarkable importance since they represent geometrical well-defined nanoscale systems and avoid the limitations in the interpretation of electrochemical data. Lemay and coworkers have explored the use of individual single-walled carbon nanotubes as electrodes [129]. A scheme of the nanoelectrode device fabrication is shown in Figure 3.18. The unique structural and electronic properties of a SWNT render it an ideal candidate to act as a model carbon nanoelectrode for electrochemistry. It was

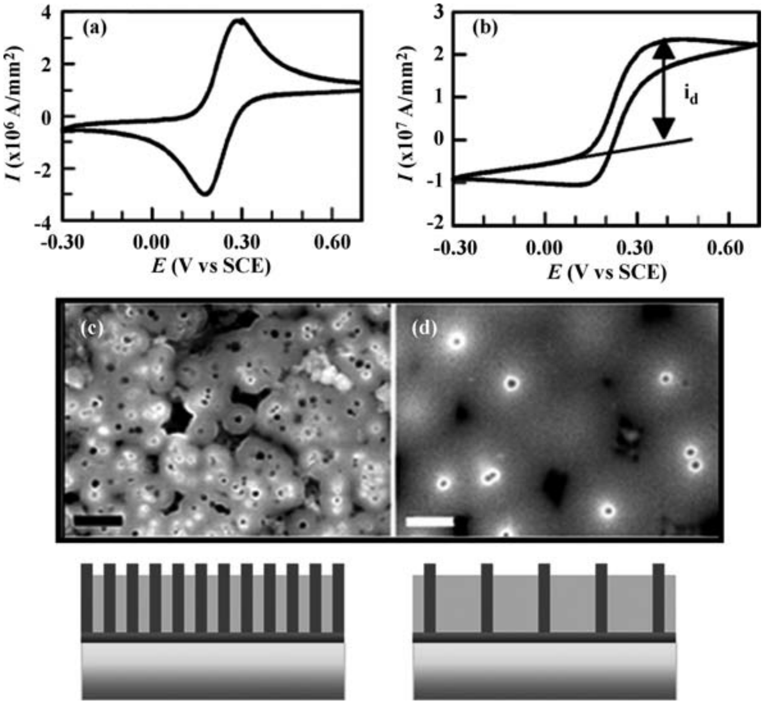

Figure 3.17 (a) and (b) CV measurements in 1 mM of $Fe(CN)_6^{3-/4-}$ and 1 M KCl with the high-density MWNT nanoelectrode array (2×10^9 electrodes/cm^2) and low density one (with about 7×10^7 electrodes/cm^2), respectively. (c) and (d) show the scanning electron images for the high and low density arrays. Readapted from Ref. [4] with permission. Copyright, 2004, RSC.

found that metallic and semiconducting SWNTs yielded similar steady-state voltammetric curves with very high electron-transfer rates at the SWNT sidewall (Figure 3.18) [129]. Such individual and well-defined nanoelectrodes are very promising since they can be additionally used to resolve electrochemically the semiconducting or metallic SWNT band structure and its distinct van Hove singularities, in a manner analogous to scanning tunneling spectroscopy. Consequently, SWNTs of different structure will yield different rate constants due to structure-dependent variations in the DOS that could be tracked.

Other individual CNT electrodes have been achieved by mounting them on scanning probe tips or on Pt wires and then passivating the walls with polymers to restrict the electrochemical response to the end of the carbon nanotube [130–132]. In all cases, a sigmoidal voltammetric response, characteristic of steady-state radial diffusion, was found [131, 132]. Such an individual nanoelectrode configuration, which can be coupled with scanning probe techniques, holds promise for applications in scanning electrochemical microscopy and electrochemical analysis of biological materials on surfaces with nanometric spatial control.

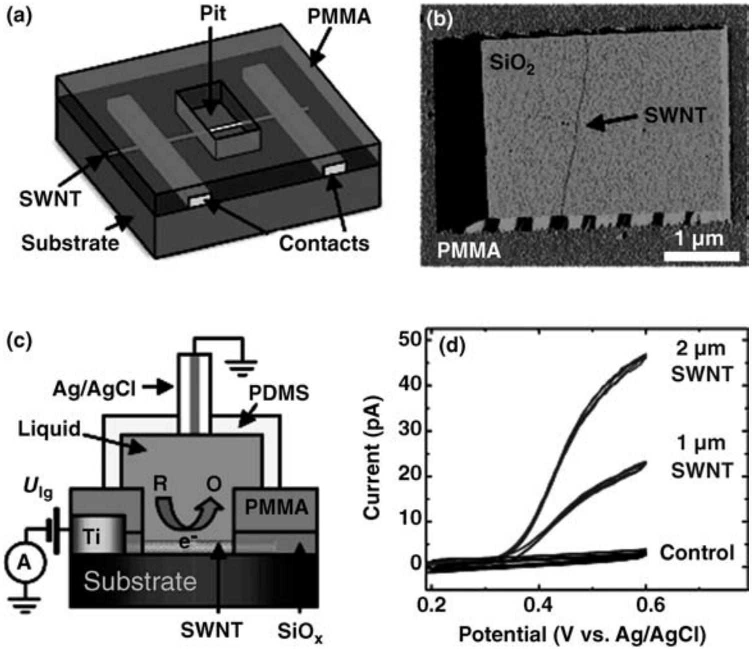

Figure 3.18 (a) Scheme of the individual SWNT electrode device. SWNTs are grown on Si/SiO$_2$ wafers and contacted by Ti leads. A layer of SiOx and PMMA is used as an insulating layer, in which windows are opened to selectively expose the SWNTs. (b) AFM-image of the SWNT in the PMMA window. (c) Low-current measurement setup. The SWNT is exposed to a solution containing a redox-active species. (d) Sampled current voltammograms measured from two metallic SWNT devices (1 μm and 2 μm exposed) and a control device exposed to an aqueous 1.2 mM FcTMA+ solution. The control device consists of a pit located near the leads but without a SWNT. Reprinted with permission from Ref. [129]. Copyright, 2005, American Chemical Society.

3.3.5
CNT-Modified Electrode Pretreatments

After the assemblage of CNTs, surface treatments can be pursued for many purposes. On the one hand, they can help to remove impurities. On the other hand, surface treatments can help to provide functionalities (such as the oxygenated moieties) for further molecule anchorage, to change the surface hydrophobic properties or to modify electrode kinetics. Different treatments can be performed such as vacuum and heat treatments or carbon electrode activation (surface cleaning, laser activation, electrochemical pretreatment, etc.) [1, 2, 133]. For instance, Wang and coworkers have reported a dramatic improvement in the electrochemical reactivity of CNT films produced by arc-discharge. The pretreatment effects were illustrated using NADH, ascorbic acid, hydrazine and hydrogen-peroxide model redox systems. Subjecting the CNT electrode to anodic potentials around 1.5 V vs. Ag/AgCl for 3 min was enough to improve the electron-transfer

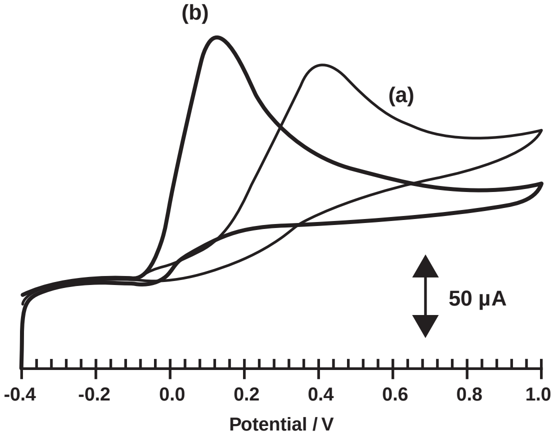

Figure 3.19 Cyclic voltammogram obtained with an arc-CNT-modified electrode in the presence of 5 mM ascorbic acid, (a) before and (b) after electrochemical activation at 1.5 V for 3 min in PBS solution, scan rate 100 mV/s. Adapted with permission from Ref. [133]. Copyright, 2005, Elesevier.

characteristics. The authors claimed that the anodic preanodization effectively 'breaks' the basal-plane end caps of arc–CNT, thereby exposing the electrochemically active edge-plane defects. The extent to which the anodic pretreatment affects the electrochemical behavior is dependent on the mechanism of the specific redox process [133]. Figure 3.19 shows the electrochemical signal improvement of the ascorbic acid after electrochemical activation [133].

3.4
Electrochemical Applications of CNT Electrodes

3.4.1
Biosensors

One of the cornerstones of CNT applications in electrochemistry lies in the development of (bio)sensors. Through this chapter we have pointed out the outstanding electrochemical properties of CNTs as a consequence of their electronic band structure and their richness in surface structure and chemistry. As mentioned before, CNTs have revealed, in many cases, electrocatalytical properties accompanied by enhanced electron-transfer rates, increased signal currents and decreased overpotentials. Although these properties have been demonstrated to be not so different from those corresponding to edge HOPG, the main advantage in the use of electrochemical CNT devices comes from their nanometer size, their high surface area and their versatility to tailor the CNT surfaces in different geometrical arrangements in order to expose the more electroactive sites and facilitate the electron exchange. Another advantage comes from their chemical anisotropy and their interesting covalent/noncovalent chemical functionalization possibilities, many of them facilitated by their curved surface, which can be used for selective chemical modification in the development of electrochemical biosensors.

3.4.1.1 Enzymatic and Redox Protein Biosensors

Electron transfer in biological systems is a very interesting topic not only because fundamental studies of such processes can help to unravel basic mechanisms in Nature's machinery, but also because such processes can be mimicked and exploited to develop sensors, bioreactors or novel fuel cells. In the electroanalytical field, there is an important interest in studying electron transfer between a redox biomolecule and an electrode for amperometric (bio)sensors. Such sensors are based on the ability of an enzyme to transduce the turnover with its corresponding substrate into a detectable, reliable and quantifiable current. One of the main goals in electroanalysis and mainly in enzymatic sensors is to achieve direct electron transfer between the protein redox center and the transducer, keeping at the same time its bioactivity [5, 12, 13, 17, 43, 58, 134]. Thus, the electrode itself can replace physiological partners or natural electron acceptors, providing the driving force to energize the reaction and a sensor to measure the response. For instance, in the case of glucose oxidase (GOx), which catalyses the reaction glucose + $O_2 \rightarrow$ glucolactone + H_2O_2, with oxygen acting as its natural electron acceptor to regenerate the enzyme, the electrode can take the role of its natural partner oxygen.

A direct electron transfer warrants an efficient transduction of the enzymatic recognition of a target analyte and avoids the use of mediators or low molecular weight relays [43]. However, such a goal is rather difficult to achieve since proteins, when adsorbed on electrode surfaces, undergo denaturation with the consequent loss of their electrochemical activity and bioactivity. Moreover, some enzymes contain the redox-active center buried deep inside the protein. This makes it generally difficult to obtain direct electron exchange between the protein and electrode surfaces so that mediators are needed to obtain an electrochemical response. Therefore, electrode materials with suitable physicochemical properties and enzyme-immobilization methods are important for obtaining the direct electron transfer and preserving their bioactivities. CNTs seem to be an ideal material to immobilize proteins and promote direct electron transfer without the need for mediators and without losing the bioactivity of the biomolecules [5, 12, 13, 17, 43]. Moreover, CNTs have been shown to promote a dramatic decrease in the overpotential of some important species (H_2O_2, NADH) involved in electrocatalytic enzymatic reactions such as oxidases or dehydrogenases [5]. For instance, the bioactivity of a CNT electrode modified with GOx can be monitored by the reduction or oxidation of H_2O_2. The detection of H_2O_2 has been carried out at such low overpotentials that interferences with other analytes can be minimized [106, 108]. All these features have greatly enhanced the development of enzymatic biosensors. Indeed, GOx represents a very interesting model system. It is known to have the redox-active center (flavin adenine dinucleotide, FAD) deep inside the peptide environment. Many nanotube-modified electrodes have been

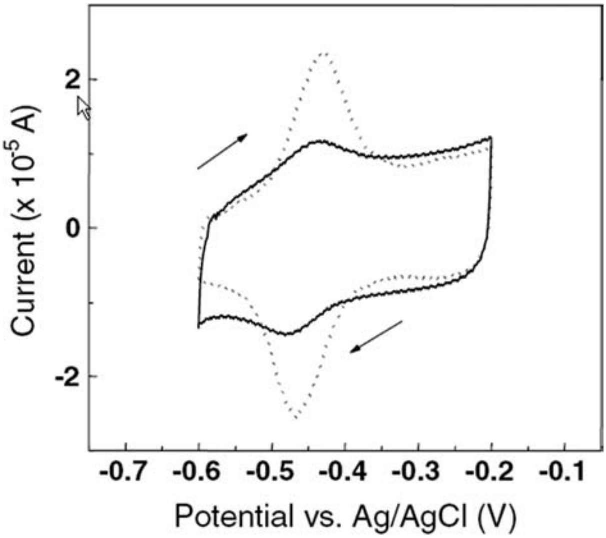

Figure 3.20 Cyclic voltammogram of GOx/SWNT/glassy carbon in pH 7.0 phosphate buffer/0.1 M KCl (solid curve); FAD/SWNT/glassy carbon in pH 7.0 phosphate buffer/0.1 M KCl (dotted curve). Scan rate: 50 mV/s. Reprinted with permission from Ref. [135]. Copyright, 2002, Institute of Physics publishing.

shown to exhibit direct electron transfer to glucose oxidase and at the same time preserve its bioactivity. Giuseppi-Elie *et al.* were the first to report direct electron exchange between adsorbed GOx and FAD onto unoriented SWNT mats [135]. Figure 3.20 shows the cyclic voltammogram for GOx/CNT where the two reversible peaks are related to the direct electron exchange between the FAD and the underlying CNT electrode. The direct electron transfer was attributed to the nanotubes being able to penetrate the protein and get close to the FAD center due to their nanometric size. Since then, many strategies have been pursued for modifying CNT electrodes with GOx, such as the immobilization of GOx on aligned CNT [123, 127], on random CNT network cast on glassy carbon or gold electrodes [135], enzyme immobilization in carbon nanotube pastes [106], in CNT/Teflon or CNT/epoxy composites [48, 136], enzyme entrapment in CNT modified with Nafion [137], chitosan [138], conductive polymers [139], or in a layer-by-layer assembly with charged polymers [140] and metal nanoparticles [141]. In the upright CNT configuration, different approaches have been used, including immobilization of GOx on aligned MWNTs grown by CVD on platinum substrates, [142]; on a CNT array fabricated by using an anodized aluminum oxide nanopore template [143]; covalently assembled on the edges of aligned low-density CNTs grown by CVD and embedded in an epoxy resin [128]; or covalently immobilized on aligned CNTs assembled on gold electrodes [123, 127]. An especially interesting system is the GOx/aligned CNT/gold electrodes that were fabricated either by the covalent attachment of the wild GOx onto the aligned CNTs assembled on the gold electrodes or by covalent attachment of the FAD group to the ends of the

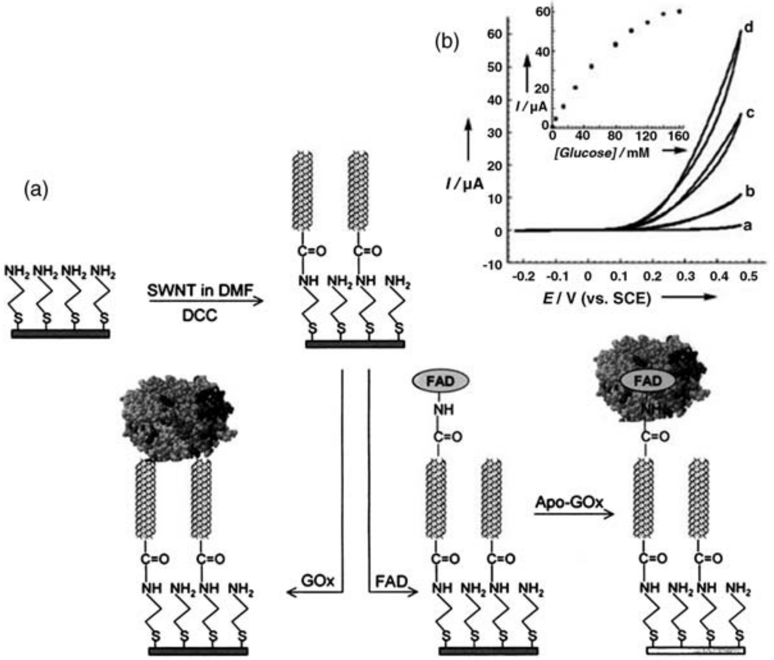

Figure 3.21 (a) Schematic procedure for the modification of a self-assembled monolayer gold electrode with aligned carbon nanotubes and their subsequent modification to allow direct electron transfer to glucose oxidase. In one case the GOx is covalently attached to the CNT assembly and in the other case the FAD center is first immobilized and then the apoenzyme is reconstituted around the FAD center. Reprinted with permission from Ref. [58]. Copyright, 2005, Elsevier. (b) Cyclic voltammograms corresponding to the electrocatalyzed oxidation of different concentrations of glucose by the GOx reconstituted on the 25-nm long FAD-functionalized CNTs assembly: (a) 0 mm glucose. (b) 20 mm glucose, (c) 60 mm glucose, (d) 160 mm glucose. Data recorded in phosphate buffer, 0.1 m, pH 7.4, scan rate 5 mV/s. Inset: calibration curve corresponding to the amperometric responses of the reconstituted GOx/CNTs (25 nm) electrode (at $E = 0.45$ V) in the presence of different concentrations of glucose. Adapted with permission from Ref. [123]. Copyright, 2004, Wiley-VCH Verlag.

tubes with the consequent reconstitution of the apo-enzyme around the FAD group (Figure 3.21) [123, 127]. From the last two approaches for the GOx immobilization, the latter exhibited the highest electron-transfer constant ($k = 0.3\ \mathrm{s}^{-1}$ for the native GOx immobilized on the aligned CNTs and $k = 9\ \mathrm{s}^{-1}$ for the reconstituted GOx on the same aligned CNT electrodes) [127]. Willner and coworkers observed that the reconstitution of the apo-GOx on the functionalized electrode had an enzyme turnover rate of about $4100\ \mathrm{s}^{-1}$, which is about sixfold higher than the turnover rate of electrons from the active site of native GOx to its natural oxygen electron acceptor ($700\ \mathrm{s}^{-1}$) [123]. They also found a dependence of the electron-transfer rate constant on the length of the SWNTs and ascribed this dependence to the defect sites introduced into the SWNTs that act as a local barrier to charge transport [123].

The use of aligned CNTs seems to be quite advantageous since the more electroactive ends of the nanotubes are readily accessible to species in solution. Moreover, the rigidity of the tubes allows them to be plugged into the biomolecules, which enables direct electrical connection to the active center of the enzyme and fast kinetics.

Direct electron transfer has also been achieved with many metalloproteins such as cytochrome C, horseradish peroxidase, microperoxidase (MP-11), myoglobin, hemoglobin, catalase, azurin, and so on, immobilized on different CNT-modified electrodes [45, 61, 144–153].

The electrochemical performance of a typical metalloprotein on CNT electrodes is discussed below taking as an example the small water-soluble myoglobin (Mb). This protein has a hemin core capable of redox activity and its natural task consists in binding and storing oxygen in the cells. Therefore, that protein exhibits high sensitivity towards oxygen but also to other analytes such H_2O_2 or NO [145–151]. It is generally difficult for Mb to transfer electrons to a conventional electrode, but this process can be enhanced when immobilized on adequate or modified metal substrates. CNT electrodes have once again demonstrated their performance as suitable electrode materials for such protein and promoted applications as potential (bio) sensors of oxygen or hydrogen peroxide or as reduction catalysts in batteries and fuel-cell systems. Taking advantage of the CNT benefits, such as electrode substrates for (bio)sensing, some groups have already started to investigate the physisorbed Mb response on randomly dispersed carbon-nanotube-modified substrates [145–150]. In all cases, direct electron exchange between Mb and CNT was observed in a quasi-reversible heme Fe(III)/Fe(II) voltammetry response. Very few studies have addressed the use of forest carbon nanotubes [61], which is known to be more beneficial from the electrochemical sensing point of view. The electrochemical performance of Mb covalently attached to different carbon electrodes (forest-like CNTs, randomly dispersed CNTs in epoxy composites, and graphite epoxy composites) has been established by focusing on the electrocatalytical response to oxygen and hydrogen peroxide [154, 155]. It was found that Mb-modified forest CNTs were the electrodes that offered the optimum conditions for a direct and fast electron exchange, with the highest sensitivity in a very wide analyte concentration range and with very low detection limits (Figure 3.22). The enhanced response of these electrodes was again attributed to the CNT orientation that provides, on the one hand, a facilitated framework for the protein covalent attachment without compromising the bioactivity, and on the other hand a high density of fast electron-exchange CNT edges [154, 155].

3.4.1.2 CNT/DNA and Genosensors

The modification of CNTs with nucleic acids constitutes a very promising area for the development of devices for genosensing, gene therapy, drug discovery and delivery, and so on. A genosensor consists in the immobilization of specific oligonucleotides that can detect targeted complementary DNA sequences under hybridization. The application of CNTs in electrochemical DNA biosensors is quite promising for many reasons: CNTs constitute novel platforms for DNA immobilization with important electrochemical transducing properties and high specific surface area that can increase not only the attached DNA amount but also concentrate a great number of enzymes or electroactive nanoparticles to amplify DNA hybridization [5, 12].

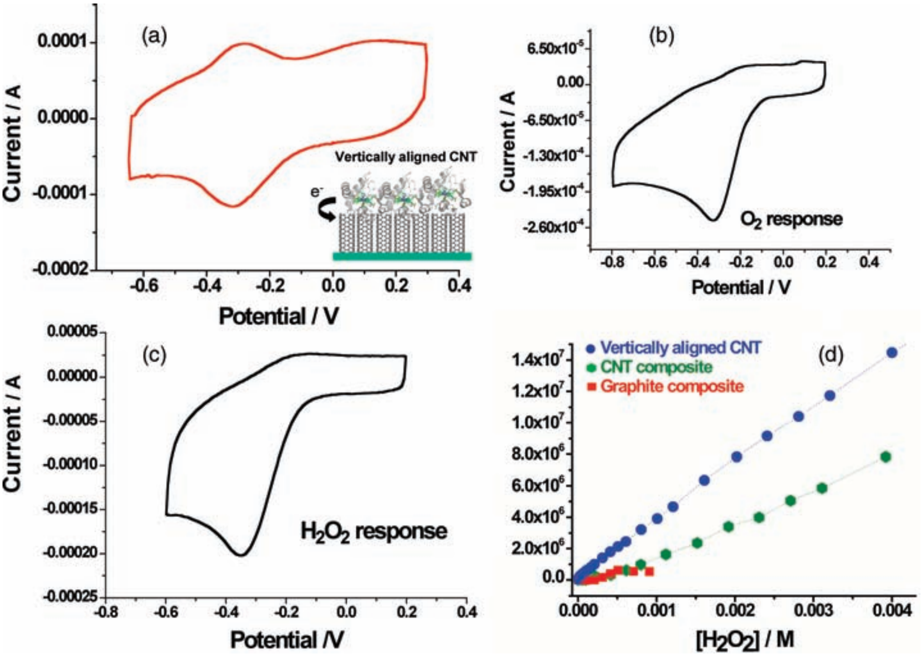

Figure 3.22 (a) Cyclic voltammogram of myoglobin covalently attached to a CNT forest in PBS solution under nitrogen atmosphere. The reversible redox behavior of the iron redox center is observed. (b) and (c) electrocatalytic response of Myoglobin/CNT forest electrode to oxygen and peroxide respectively; (d) Current-density change normalized with respect to the protein coverage as a function of H_2O_2 concentration for different myoglobin-modified carbon electrodes: forest CNT, randomly dispersed CNT in an epoxy composite and randomly dispersed graphite in an epoxy composite.

In order to prepare electroanalytical devices based on hybridization recognition, the first critical issue to face is related to the immobilization procedures on the surface of the transducer. It is important to guarantee a good orientation of the bases of the DNA probe on the CNT interface in order to get efficiency in the hybridization with the target DNA. The more basic approaches for DNA immobilization on CNTs are the physisorbed (multisite attachment) or the covalent anchoring (single-point linkage). In the latter case, typical covalent schemes are provided by the conjugation of DNA terminal functional groups with functional groups in the CNT surface via the carbodiimide chemistry, streptavidin/biotin interactions, and so on. In general, DNA is physisorbed on CNTs by wrapping the tube, with the bases (apolar region of the molecule) in close contact with the hydrophobic walls of CNT, whereas the phosphate backbone faces the solution [144, 156]. Such orientation of the adsorbed DNA is not so favorable for the surface hybridization, indicating that for a more appropriate biofunctionalization, hydrophobic interactions need to be minimized. Therefore, when genosensors based on physical adsorption of oligonucleotides are considered, chemical modification of the CNT surface (by promoting hydrophilic interactions) is more convenient to increase the efficiency of the hybridization detection. On the other hand, single-point attachment of the DNA turns out to be a more flexible configuration that enhances hybridization kinetics. Apart from these basic routes of DNA functionalization, many related approaches have been performed. Below, we will discuss some illustrative examples of electrochemically based DNA sensors. Again, the direct (label-free) electrochemical detection of DNA by the reduction of the DNA bases (mainly guanine) is of considerable interest, though the indirect detection methods of DNA hybridization by using hybridization indicators, including intercalators and labels are very popular and in some cases mandatory [157]. Label-free electrical-detection protocols are desirable since they greatly simplify DNA hybridization assays as they offer an instantaneous detection of the duplex. However, such detection requires a physisorbed multisite attachment as immobilization technique. Generally, when directly biosensing DNA, the guanine in single-stranded DNA probe (ssDNA) is often replaced by inosine in order to reduce the background signal interference derived from ssDNA probe and consequently increase the hybridization signal derived from the double-stranded DNA helix [157].

Wang and coworkers have achieved label-free detection of DNA hybridization on MWNT electrodes. They found enhanced electrochemical response of guanine at carbon-nanotube-modified glassy carbon electrodes as compared to other carbon electrodes [158]. The amplified guanine signal was exploited not only for label-free detection of DNA hybridization but also for trace measurements of nucleic acids (Figure 3.23). Such an enhanced guanine signal was attributed to a CNT-induced interfacial accumulation (due to its large surface area/volume ratio) rather than to an electrocatalytic reaction [158, 159]. A similar enhancement of the guanine and adenine DNA response was also reported by other groups at MWNT paste electrodes, SWNT-coated glassy carbon electrodes, and so on [60, 160]. Gooding and coworkers have demonstrated the advantages of using bamboo-like nanotubes for electrochemical biosensor applications compared with SWNTs by analyzing the label-free oxidation of guanine and adenine bases of surface-adsorbed DNA [101]. Having in mind that bamboo-like multiwalled carbon nanotubes provide more edge planes of graphene than SWNT, they found that bamboo-like nanotubes have superior electrochemical performance over SWNT due to the following aspects: (a) with the electroactive species in solution, peak separation of oxidation and reduction waves showed faster electron transfer on bamboo nanotubes and (b) greater number of electroactive sites along the walls of the bamboo tubes resulted in larger current signals and broader dynamic range for oxidation of DNA bases.

DNA sensors have been also developed on aligned CNTs. For instance, Dai and coworkers have reported a simple, but effective, method for preparing aligned carbon nanotube/gold–DNA sensors by covalently coupling DNA probes on both the tip ends and walls of plasma-activated aligned carbon nanotubes [161]. The probe DNA was targeted with a ferrocene-labelled complementary oligonucleotide to yield a reversible electrochemical response of the redox ferrocene label as hybridization signal that was observed by cyclic voltammetry. An enhanced electrochemical signal was provided by the high surface area of the CNT-modified electrode. The

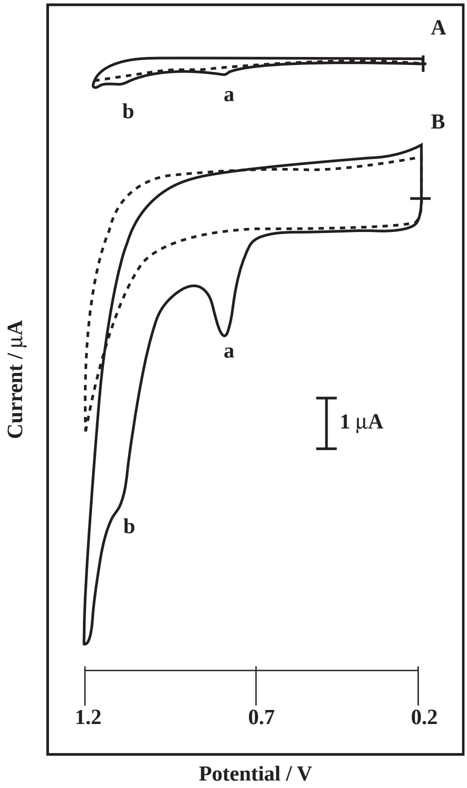

Figure 3.23 Cyclic voltammogram for a single-stranded DNA solution at the bare (A) and CNT (B) glassy carbon electrodes. Accumulation, 1 min at 0.2 V. Scan rate, 50 mV/s. Measurements performed in 0.5 M acetate buffer (pH 5.9). Reprinted with permission from Ref. [158]. Copyright, 2003, The Royal Society of Chemistry.

nanotube–DNA electrochemical sensors thus produced were highly sensitive and selective even in the absence of any electron mediator.

Meyyapan and coworkers reported a nanoelectrode array based on vertically aligned MWNTs embedded in SiO_2 for ultrasensititve DNA detection [162, 163]. The DNA probe was covalently immobilized through carbodiimide chemistry to the open ends of insulated aligned MWNT electrodes. In principle, the anodic current of the guanine oxidation could be used as the sensing signal. However, that signal was very low due to the limited number of guanine bases on the surface. Therefore, an electrocatalytic mechanism using $Ru(bpy)_3{}^{2+}$ mediators to amplify the guanine oxidation was developed. Sensitivity was dramatically increased by lowering the nanotube density and the hybridization of subattomole DNA targets was detected.

CNTs can also be used as hybridization indicators with amplifying properties as demonstrated by Wang and coworkers [164–166]. They showed that CNTs can play a dual amplification role in both the recognition and transduction events, namely as carriers for numerous enzyme tags and for accumulating the product of the enzymatic reaction (Figure 3.24). These novel support and preconcentration functions of CNTs reflect their large specific surface area and have been illustrated, for instance, by using the alkaline phosphatase (ALP) enzyme tracer [164, 165]. Signal amplification was even increased by loading enzyme multilayers on the CNT templates by electrostatic layer-by-layer self-assembly [165]. Such coupling of several CNT-derived amplification processes leads to extraordinary low detection limits in the attomolar range. A similar loading effect has been also demonstrated with quantum dots as electroactive labels for DNA hybridization detection by using stripping voltammetry [166].

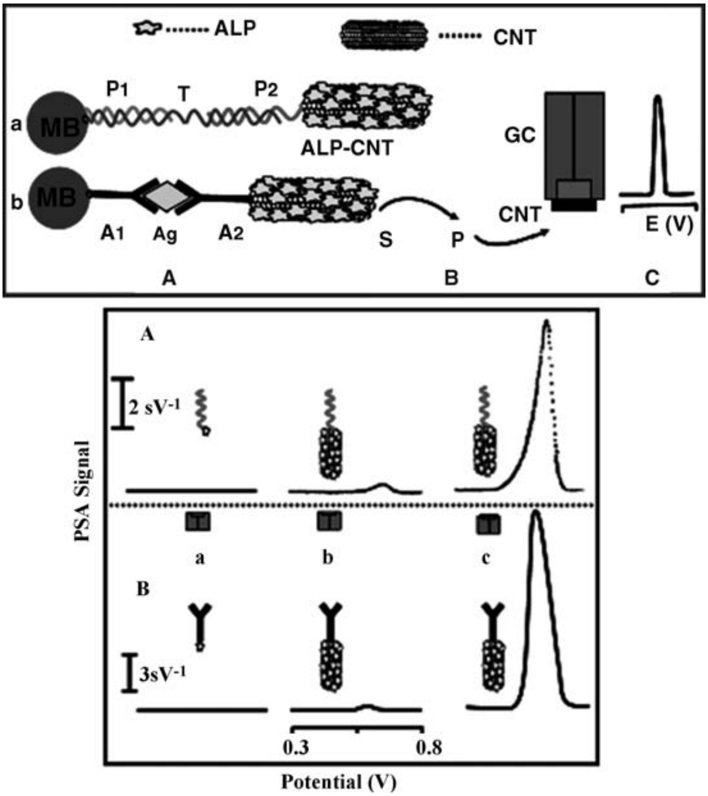

Figure 3.24 Schematic representation of the analytical protocol: (A) Capture of the ALP-loaded CNT tags to streptavidin-modified magnetic beads by a sandwich DNA hybridization (a) or Ab-Ag-Ab interaction (b). (B) Enzymatic reaction. (C) Electrochemical detection of the product of the enzymatic reaction at the CNT-modified glassy carbon electrode; MB, Magnetic beads; P, DNA probe 1; T, DNA target; P2, DNA probe 2; Ab1, first antibody; Ag, antigen; Ab2, secondary antibody; S and P, substrate and product, respectively, of the enzymatic reaction; GC, glassy carbon electrode; CNT, carbon nanotube layer. Plots below: chronopotentiometric signals for target oligonucleotide (A) and IgG (B) using the glassy carbon (GC) transducer and (a) a single ALP tag and (b) CNT-loaded with multiple ALP tags; (c) same as (b) but using the CNT-modified GC electrode. Reprinted with permission from Ref. [164]. Copyright, 2004, American Chemical Society.

3.4.1.3 **Immunosensors**

CNTs also have promising applications in the immunosensing field and many examples of such sensor devices can be found in the literature. For example, immunosensors with an electrochemiluminescence readout signal have been designed using CNTs as support of the immunorecognition systems [167].

Recently, some papers have started to highlight the performance of PSf-(bio) composites-CNT as electrode material for electrochemical immunosensing [112]. The authors have highlighted the attractive combination of PSf/CNT plus disposable screen-printed electrodes for monitoring the enzymatic activity of horseradish peroxidase and the RIgG inmunosensor response. In both cases an enhanced electroanalytical response was demonstrated in comparison with standard graphite/PSf composites.

Vertically aligned arrays of SWNT forests have been developed for amperometric enzyme (HRP)-linked inmunoassays of proteins by Rusling and coworkers [168]. The forests were self-assembled from oxidatively shortened SWNTs onto Nafion/iron oxide-coated pyrolytic graphite electrodes. The SWNT immunosensor was designed to detect biotin. Antibiotin antibody was strongly adsorbed to the SWNT forests. The initial study pointed out the importance of decreasing the nonspecific binding and of using mediators to obtain optimal sensitivity. While mediator-free electron-transfer detection of the HRP label was possible, only a fraction of the HRPs attached to biotin communicated with the SWNT forest, compromising sensitivity. This was understandable because the antibiotin antibody was placed between biotin-HRP and the nanotube. This brings a distance in the range of 5–20 nm between the nanotube ends and HRP that impedes electrochemical communication. Using hydroquinone as a soluble mediator, the detection limit for horseradish peroxidase-labeled biotin was 2.5 nM. Unlabeled biotin was detected in a competitive approach with a detection limit of 16 μM. They also reported improved detection limits and sensitivity for unmediated catalysis of H_2O_2 reduction by HRP bound to SWNTs resulting from denser and more defect-free SWNT forests made with aged nanotube dispersions in DMF. Moreover, by attaching antibodies to the ends of SWNT forests again with HRP labels, they obtained excellent sensitivity in sandwich immunoassays for the protein human serum albumin with detection limits of 75 nM without mediators and 1 nM with mediators.

Following the same protocol as in the case of hybridization amplification, enzymes generating electrochemically detectable products have also been used as amplifying labels for antigen/antibody recognition by Wang and coworkers [164]. Similarly, functionalized CNTs have been used as carriers of multiple enzyme labels for electrochemical immunosensing as shown schematically in Figure 3.24. In a similar context, Rusling and coworkers described the combination of electrochemical immunosensors using SWNT forest platforms with multilabel secondary antibody–nanotube bioconjugates for highly sensitive detection of a cancer biomarker in serum and tissue lysates [169]. Greatly amplified sensitivity was attained by using bioconjugates featuring horseradish peroxidase (HRP) labels and secondary antibodies (Ab2) linked to carbon nanotubes at high HRP/Ab2 ratio. This approach provided a detection limit of 4 pg mL^{-1} (100 amol mL^{-1}), for prostate-specific antigen (PSA) (Figure 3.25). These easily fabricated SWNT immunosensors show excellent promise for clinical screening of cancer biomarkers and point-of-care diagnostics [169].

3.4.2
Electrochemical Actuators

Many applications rely on the direct conversion of electrical energy to mechanical energy through a material response. The more common materials for electromechanical actuators are represented by ferroelectric and electrostrictive materials. However, applications are restricted by the maximum allowable operation temperature, the need for high voltages, and limitations on the work density per cycle [170]. Conducting polymer actuators based on electrochemical dopant intercalation represent another alternative. Faradaic processes for these battery-like devices involve solid-state dopant diffusion and structural changes that limit rate, life cycle, and energy-conversion efficiencies [170]. CNTs appear as a new class of electromechanical actuators that generate higher stresses than natural muscle and higher strains than high-modulus ferroelectrics. Like natural muscles, the macroscopic actuators are assemblies of billions of individual nanoscale actuators. The first CNT actuator developed was a SWNT buckypaper that produced elongation/contraction because of the change in dimensions of the nanotube in the covalently bonded direction caused by charge injection with an applied electric potential (electrochemical doping). The proposed actuation mechanism was based on a quantum-chemical expansion due to electrochemical double-layer charging without the requirement of ion intercalation, which limits the life and rate of faradaic conducting polymer actuators [170]. Unlike conventional ferroelectric actuators, low operating voltages of a few volts generate large actuator strains. Moreover, a surprising giant actuator response was obtained during electrochemically cycling CNT sheets at high redox potentials in aqueous NaCl or acid electrolytes [171]. A pnemumatic mechanism for the giant actuation was suggested with gas evolution at such extreme potentials, which induces gas containment voids in the CNT sheets. Other CNT actuators have been reported, examples of them are those based on bucky gels [172] which are built-in ionic-liquid components operating in air without external electrolytes, those based on CNT epoxy composites [173] or those based on vertically aligned MWNT towers [174]. Despite these advances, there are still many challenges to develop tailored practical devices mainly because of the uncontrollable properties of nanotube buckypaper and polymer nanocomposite actuators.

3.4.3
Electrochemical Energy-Harvesting Devices

Carbon nanotubes can be employed either as electrode materials or conductive fillers for the active materials in various electrochemical energy-storage systems [20]. For energy generation and storage, nanotubes hold promise as supercapacitors,

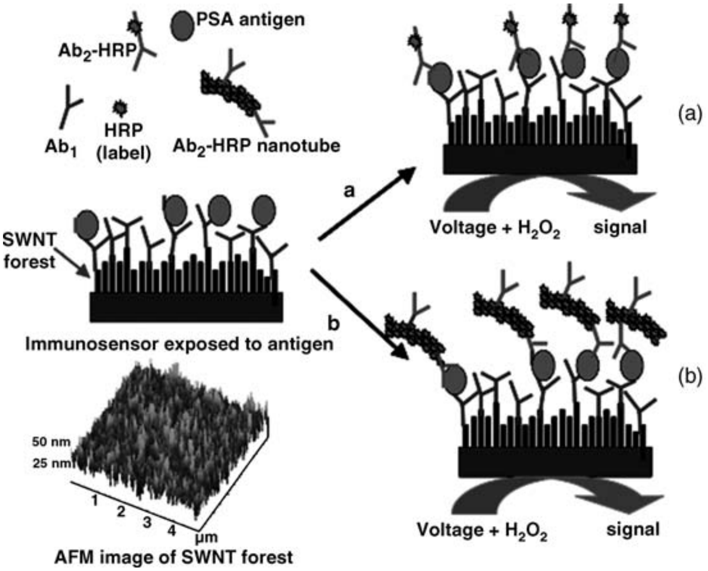

Figure 3.25 Scheme of a SWNT immunosensor using secondary antibody labeled with HRP enzyme. HRP catalyses H_2O_2 and generates electrons that can be amperometrically detected. (a) Treatment with a conventional HRP-labeled secondary antibody providing one label per binding event and (b) treatment with an HRP-CNT labeled secondary antibody for signal amplification with numerous enzyme levels per binding event. AFM image of the nanotube forest immunosensor. Reprinted with permission from Ref. [169]. Copyright, 2006, American Chemical Society.

Li-ion batteries (LIBs), solar cells and fuel cells due to their high specific surface area and mesoporous character [20].

Lithium battery research comprises an area of great interest for applications driven by their high demand in the world market. Intensive research is still focused on the optimization of anodic electrodes for increasing the perfomance of the batteries. The electrodes of LIBs are based on intercalation materials, among which lithium ions are transferred through the electrocatalytic medium during charge and discharge [175]. The cathodic electrode is normally made of lamellar oxides (LixMO2) while carbon has been used for the anodic electrode. A great amount of research has been focused on the role of carbon as anodic electrode material for lithium-ion batteries because of its excellent intercalation properties and safety over lithium metal. In the case of graphite anodes, lithium penetrates between the graphene layers through the intercalation process with charge transfer to carbon. It is important that such ion insertion and extraction on the anode proceeds very close to the potential of metallic lithium, allowing the lithium-ion battery to discharge at high and almost constant values of voltage [175, 176]. Nevertheless, it is important to point out that part of the lithium involved in the so-called solid electrolyte interphase (SEI) is not recovered in the electrolyte during deintercalation, giving rise to a noticeable irreversible capacity. Therefore, for such batteries, anodic electrodes with high reversible capacity at a potential close to metallic lithium and a moderate irreversibility are required [175, 176]. Due to their graphitized structure with internal channels and large surface area, carbon nanotubes have been proposed as a potential substitute for the traditional graphite for lithium intercalation. It was speculated that a higher lithium capacity may be obtained with carbon nanotubes if all the interstitial sites are accessible for lithium intercalation. Indeed, it has been possible to obtain very high reversible capacities in CNT systems [177], which can even be increased with CNT pretreatments (up to 1000 mAh/g) with ball milling [178, 179] and chemical etching [180–182] that increase lithium diffusion into the interior or inner cores of CNTs).

However, there are still some drawbacks in the use of CNT that need to be solved for practical applications. Not only large reversible capacities but also large irreversible capacities have been reported on CNTs [179, 183]. Such irreversible capacity together with the lack of voltage plateau during lithium extraction (hysteresis) limits the use of nanotubes as electrode material in LIBs. However, an active study (based on CNT treatments, surface modification, use of CNT nanocomposite matrices, etc.) is being carried out in order to overcome such difficulties [184].

Due to the open network of mesopores formed by the entanglement of nanotubes, the high density of graphene layers and consequently an easily accessible electrode/electrolyte interface, nanotubes are quite adapted for supercapacitors [175, 185]. Supercapacitors are based on the electrical double layer that is formed due to the electrostatic attraction between the ions and the charged surfaces of the electrodes together with additional faradaic pseudocapacitance reactions (mainly coming from redox activity of surface moieties). These systems have been extensively and actively investigated because they are able to store and deliver energy rapidly and efficiently for a long life cycle via a simple charge-separation process. In addition, their wide range of power capability makes it possible to hybridize them with other energy-storage devices, such as batteries and fuel cells.

In this context, supercapacitors with carbon-nanotube electrodes have been evaluated to increase their energy density [185]. For example, a SWNT electrode exhibited the maximum reported capacitance of about 180 F/g and a power density in the range of 6.5–7 Wh/kg. Many research studies are trying to increase the efficiency of such capacitors by adding stable pseudoeffects, for example, additional oxygenated functionalization of CNT, conducting polymers or other electroactive species deposited on the nanotubes [185]. Chemically modified MWNTs are also used as a conductive filler for porous carbon materials for high-power supercapacitors [186]. However, there is still an important search for new or optimized carbon, materials especially with well-controlled nanostructure and surface functionality in order to improve the storage capacity and the cyclability of the power supply.

Among solar cells, the silicon-based photovoltaic ones are the only ones that have reached solar-energy conversion efficiencies of >25% [20]. However, this technology requires environmentally hazardous processing and has proven to be too expensive to replace nonrenewable energy sources for widespread application. A different option is to use organic thin films of conjugated polymers, which, although having relatively low conversion efficiencies (<5%), would be lower in cost compared to silicon-based technologies [20]. Conjugated polymers are able to absorb a photon and generate an exciton that can dissociate into an electron–hole pair under the strong electric field found at polymer/metal interfaces. The most efficient design for organic solar cells uses a bulk heterojunction composite of a conjugated polymer with nanoscale electron acceptors forming a percolating network through the thin film. This maximizes the interfacial area between the metal filler material and the polymer, which promotes charge separation and allows conduction of the electrons through the percolating network to be collected at the electrode [20]. Carbon nanotubes can be a good material for forming bulk heterojunctions in organic solar cells [187–189]. Their high aspect ratio allows formation of a percolating network of nanotubes at low doping levels in a polymer composite. As one-dimensional nanostructures, nanotubes are also ideal for electron transport as they exhibit quasiballistic features.

Carbon nanotubes have been used in different conjugated polymer matrices with improvement in charge separation and transport [189–191]. The efficiencies of these devices have not reached those of the silicon technology but CNT enhancement is promising for long-term development. The incorporation of dyes and nanoparticle hybrids in the CNT network is a promising approach in the goal of increasing energy-conversion efficiencies [20, 192].

CNTs also represent promising candidates in the field of fuel-cell systems as supporting materials for Pt catalysts [20, 193–195]. Very promising performance is expected for MWNTs with high reactive edge densities that can provide a support to anchor homogeneously distributed small-sized Pt catalysts [20]. CNTs also hold promise as electrodes for the development of biofuel cells provided their high surface area, their possibility to be assembled in a 3D configuration, their suitable platform for entrapment of biomolecules without loss of the bioactivity, and their excellent electrochemical properties for establishing direct and fast electron exchange with proteins and enzymes. All these factors are desired requirements for a good performance in fuel cells [196].

3.5
Conclusions and Future Prospects

Without doubt, the advent of carbon nanotubes has opened up innovative perspectives for research and development of carbon electrodes. In this chapter, we have attempted to highlight the electrochemical properties of carbon nanotubes by rooting them mainly on their structural, electronic and chemical properties. If chirality of SWNTs could be controlled, it would be possible to probe electrochemically the unique electronic properties of the tubes with their corresponding unique DOS distribution and establish direct correlations between electronic structure and electrochemistry. However, so far, most of their electrochemical applications are based on ensembles of CNTs (MWNTs or SWNTs) in thin films supported on conductive surfaces or composites. Such ensembles, not so well defined from the structural point of view, contain a mixture of tubes with different diameters and DOS distribution and exhibit basically an averaged metallic behavior with averaged electron-transfer rates. Nevertheless, some generalizations can be made from the behavior of such averaged CNT systems.

Due to their structure, CNTs show a remarkable richness in their surface chemistry. CNTs show chemical and electrochemical anisotropy, with the edges being more chemically and electrochemically reactive, while the walls exhibit a more inert behavior. Therefore, a high density of CNT edges or defects is expected to increase the electrochemical performance of the electrodes. Due to their high surface area they show an increased current signal but also important electrocatalytical properties reflected in an increased electron-transfer kinetics, in a similar way as that found on edge pyrolytic graphite. Moreover, oxygenated surface functionalities can increase even further the electrochemical performance, depending on the redox system. However, caution in attributing such properties to different redox systems has to be taken, due to the presence of metal impurities from the CNT growth procedure that might bring about misinterpretations.

All these properties have revolutionized the electrochemical applications, but perhaps, the nanometer size and high aspect ratio of the carbon nanotubes are the distinct features that have contributed more to innovative electrochemical applications and to establish the differences with respect to other carbon materials. Thanks to this, novel electrode architectures have been accomplished, though this field is far from being fully exploited. Such electrode configurations can be tailored, according to electrochemical applications, from individual CNT nanoscale devices to massive ones. For instance, an upright configuration of CNTs, with the more electrochemical reactive sites facing towards the analytes can greatly improve the sensitivity and detection limits in biosensors. In this context, the use of vertically aligned CNT nanoelectrode arrays can increase even further the detection to the range of few molecules. Additionally, they can act as molecular wires where electroactive biomolecules can be plugged at their ends, thus facilitating the direct electron transfer. Alternatively, and following the continuous search of ultrasensitive electrochemical detectors, CNTs can be used as specific biorecognition indicators profiting from their high surface area available for loading electroactive markers that can amplify biorecongition events. On the other hand, the design of 3D CNT ensembles with high surface area and mesoporous character can yield large double layer capacitances, or provide suitable electrode frameworks for ion intercalation or catalyst entrapment/deposition, all being important for the development of electromechanical systems or electrochemical energy-storage systems.

However, behind the promising electrochemical devices, there are still many fundamental issues that affect the electrochemical response and that are poorly controlled. Such issues can be found right from the first steps of CNT growth, purification, separation, and so on. For instance, there are many unsettled issues in the fundamental CNT growth mechanism, hence CNT growth with controlled length, diameter and chirality is still not possible. Other difficulties comprise the removal of metal impurities from the tubes, the lack of practical techniques for CNT separation according to their chiralities and hence electronic properties, the control of defects/

surface oxides in CNTs, the difficulties in CNT solvent dispersion, difficulties in CNT electrode designs, and so on.

Advances in such issues could further improve nanotube uniformity, decrease the dispersion in the results of different research groups, improve the device efficiency and also provide further insights into fundamental electrochemical questions.

References

1 McCreery, R.L. (1991) in *Carbon Electrodes: Structural Effects on Electron Transfer Kinetics in Electroanalytical Chemistry* (ed. A.J. Bard), Vol. 17, Dekker, New York.

2 McCreery, R.L. (2008) *Chemical Reviews*, **108**, 2646.

3 Moore, R.R., Banks, C.E. and Compton, R.G. (2004) *Analytical Chemistry*, **76**, 2677.

4 Koehne, J., Li, J., Cassell, A.M., Chen, H., Ye, Q., Ng, H.T., Han, J. and Meyyappan, M. (2004) *Journal of Materials Chemistry*, **14**, 676.

5 Wang, J. (2005) *Electroanalysis*, **17**, 7.

6 Li, J., Koehne, J.E., Cassell, A.M., Chen, H., Ng, H.T., Ye, Q., Fan, W., Han, J. and Meyyappan, M. (2005) *Electroanalysis*, **17**, 15.

7 Banks, C.E., Davis, T.J., Wildgoose, G.G. and Compton, R.G. (2005) *Chemical Communications*, 829.

8 Banks, C.E. and Compton, R.G. (2006) *Analyst*, **131**, 15.

9 Merkoci, A. (2006) *Microchimica Acta*, **152**, 157.

10 Wildgoose, G.G., Banks, C.E., Leventis, H.C. and Compton, R.G. (2006) *Microchimica Acta*, **152**, 187.

11 Pumera, M., Sánchez, S., Ichinose, I. and Tang, J. (2007) *Sensors and Actuators B*, **123**, 1195.

12 Kim, S.N., Rusling, J.F. and Papadimitrakopoulos, F. (2007) *Advanced Materials*, **19**, 3214.

13 Gong, K., Yan, Y., Zhang, M., Su, L., Xiong, S. and Mao, L. (2005) *Analytical Sciences*, **21**, 1383.

14 Yun, Y., Dong, Z., Shanov, V., Heineman, W.R., Bhattacharya, A., Conforti, L., Narayan, R.K., Ball, W.S. and Schulz, M.J. (2007) *Nanotoday*, **2**, 30.

15 Bertoncello, P., Edgeworth, J.P., Macpherson, J.V. and Unwin, P.R. (2007) *Journal of the American Chemical Society*, **129**, 10982.

16 Yang, W., Thordarson, P., Gooding, J.J., Ringer, S.P. and Braet, F. (2007) *Nanotechnology*, **18**, 1.

17 Agüí, L., Yáñez-Sedeño, P. and Pingarrón, J.M. (2008) *Analytica Chimica Acta*, **622**, 11.

18 Kavan, L. and Dunsch, L. (2008) in *Carbon Nanotubes, Topics in Applied Physics 111* (eds A. Jorio, G. Dresselhaus and M.S. Dresselhaus), Springer-Verlag, Berlin Heidelberg, p. 567.

19 Dumitrescu, I., Unwin, P.R., Wilson, N.R. and Macpherson, J.V. (2008) *Analytical Chemistry*, **80**, 3598.

20 Endo, M., Strano, M.S. and Ajayan, P.M. (2008) in *Carbon Nanotubes, Topics in Applied Physics 111* (eds A. Jorio, G. Dresselhaus and M.S. Dresselhaus), Springer-Verlag, Berlin Heidelberg, p. 13.

21 Saito, R., Dresselhaus, G. and Dresselhaus, M.S. (1998) *Physical Properties of Carbon Nanotubes*, Imperial College Press, London.

22 Louie, S.G. (2001) in *Electronic Properties, Junctions and Defects of Carbon Nanotubes, Topics in Applied Physics 80* (eds M.S. Dresselhaus, G. Dresselhaus and P.H. Avouris Springer-Verlag, Berlin Heidelberg, p. 113.

23 Ouyang, M., Huang, J. and Lieber, C.M. (2002) *Accounts of Chemical Research*, **35**, 1018.

24 Avouris, Ph. (2002) *Accounts of Chemical Research*, **35**, 1026.

25 Balasubramanian, K. and Burghard, M. (2005) *Small*, **1**, 180.

26 Wildoer, J.W.G., Venema, L.C., Rinzler, A.G., Smalley, R.E. and Dekker, C. (1998) *Nature*, **391**, 59.

27 Odom, T.W., Huang, J.L., Kim, P. and Lieber, C.M. (1998) *Nature*, **391**, 62.

28 Krstic, V., Roth, S. and Burghard, M. (2000) *Physical Review B-Condensed Matter*, **62**, R16353.

29 Kong, J., Yenilmez, E., Tombler, T.W., Kim, W., Dai, H.J., Laughlin, R.B., Liu, L., Jayanthi, C.S. and Wu, S.Y. (2001) *Physical Review Letters*, **87**, 106801.

30 Heinze, S., Tersoff, J., Martel, R., Derycke, V., Appenzeller, J. and Avouris, P. (2002) *Physical Review Letters*, **89**, 106801.

31 Saito, R., Fujita, M., Dresselhaus, G. and Dresselhaus, M.S. (1992) *Applied Physics Letters*, **60**, 2204.

32 Dresselhaus, M.S., Dresselhaus, G. and Saito, R. (1992) *Solid State Commun*, **84**, 201.

33 Heller, I., Kong, J., Williams, K.A., Dekker, C. and Lemay, S.G. (2006) *Journal of the American Chemical Society*, **128**, 7358.

34 Hamon, M.A., Itkis, M.E., Niyogi, S., Alvaraez, T., Kuper, C., Menon, M. and Haddon, R.C. (2001) *Journal of the American Chemical Society*, **123**, 11292.

35 Han, J. (2005) in *Structures and Properties of Carbon Nanotubes, Carbon Nanotubes: Science and Applications* (ed. M. Meyyappan), CRC Press, London, p. 1.

36 Srivastava, D. (2005) in *Computational Nanotechnolgy of Carbon Nanotubes. Carbon Nanotubes: Science and Applications* (ed. M. Meyyappan) CRC Press, London, p. 25.

37 Niyogi, S., Hamon, M.A., Hu, H., Zhao, B., Browmik, P., Sen, R., Itkis, M.E. and Haddon, R.C. (2002) *Accounts of Chemical Research*, **35**, 1105.

38 Chen, Z., Thiel, W. and Hirsch, A. (2003) *ChemPhysChem*, **95**.

39 Burghard, M. (2005) *Surface Science Reports*, **58**, 1.

40 Gülseren, O., Yildirim, Y. and Ciraci, S. (2001) *Physical Review Letters*, **87**, 116802.

41 Gruneis, A., Esplandiu, M.J., García-Sánchez, D. and Bachtold, A. (2007) *Nano Letters*, **7**, 3766.

42 Hirsch, A. (2002) *Angewandte Chemie-International Edition*, **41**, 1853.

43 Katz, E. and Willner, I. (2004) *ChemPhysChem;* **5**, 1084.

44 tasis, D., Tagmatarchis, N., Bianco, A. and Prato, M. (2006) *Chemical Reviews*, **106**, 1105.

45 Gooding, J.J., Wibowo, R., Liu, J., Yang, W., Losic, D., Orbons, S., Mearns, F.J., Shapter, J.G. and Hibbert, D.B. (2003) *Journal of the American Chemical Society*, **125**, 9006.

46 Nugent, J.M., Santhanam, K.S.V., Rubio, A. and Ajayan, P.M. (2001) *Nano Letters*, **1**, 87.

47 Fan, Y., Goldsmith, B.R. and Collins, P.G. (2005) *Nature Materials*, **4**, 906.

48 Wang, J. and Musameh, M. (2003) *Analytical Chemistry*, **75**, 2075.

49 Wang, J., Li, M., Shi, Z., Li, N. and Gu, Z. (2001) *Electrochimica Acta*, **47**, 651.

50 Wu, F.H., Zhao, G.C. and Wei, X.W. (2002) *Electrochemistry Communications*, **4**, 690.

51 Zhao, Y.D., Zhang, W.D., Chen, H. and Luo, Q.M. (2003) *Sensors and Actuators, B*, **92**, 279.

52 Wang, J., Li, M., Shi, Z., Li, N. and Gu, Z. (2002) *Electroanalysis*, **14**, 225.

53 Wang, Z., Wang, Y. and Luo, G. (2003) *Electroanalysis*, **15**, 1129.

54 Musameh, M., Wang, J., Merkoci, A. and Lin, Y. (2002) *Electrochemistry Communications*, **4**, 743.

55 Banks, C.E., Moore, R.R., Davies, T.J. and Compton, R.G. (2004) *Chemical Communications*, 1804.

56 Banks, C.E. and Compton, R.G. (2005) *Analyst*, **130**, 1232.

57 Banks, C.E. and Compton, R.G. (2005) *Analytical Sciences*, **21**, 1263.

58 Gooding, J.J. (2005) *Electrochimica Acta*, **50**, 3049.

59 He, P., Xu, Y. and Fang, Y. (2006) *Microchimica Acta*, **152**, 175.

60 Wang, J., Li, M., Shi, Z., Li, N. and Gu, Z. (2004) *Electroanalysis*, **16**, 140.

61 Yu, X., Chattopadhyay, D., Galeska, I., Papadimitrakopoulos, F. and Rusling, J.F. (2003) *Electrochemistry Communications*, **5**, 408.

62 Banks, C.E., Ji, X., Crossley, A. and Compton, R.G. (2006) *Electroanalysis*, **18**, 2137.

63 Chou, A., Boecking, T., Singh, N.K. and Gooding, J.J. (2005) *Chemical Communications*, 842.

64 Banks, C.E., Crossley, A., Salter, C., Wilkins, S.J. and Compton, R.G. (2006) *Angewandte Chemie-International Edition*, **45**, 2533.

65 Jones, C.P., Jurkschat, K., Crossley, A. and Compton, R.G. (2007) *Langmuir*, **23**, 9501.

66 Moravsky, A.P., Wexler, E.M. and Loutfy, R.O. (2005) in *Growth of Carbon Nanotubes by Arc Discharge and Laser Ablation, Carbon Nanotubes: Science and Applications* (ed. M. Meyyappan), CRC Press, London, p. 65.

67 Meyyappan, M. (2005) in *Growth: CVD and PECVD, Carbon Nanotubes: Science and Applications* (ed. M. Meyyappan), CRC Press, London, p. 99.

68 Zhou, O., Shimoda, H., Gao, B., Oh, D., Fleming, L. and Yue, G. (2002) *Accounts of Chemical Research*, **35**, 1045.

69 Andrews, R., Jacques, D., Qian, D. and Rantell, T. (2002) *Accounts of Chemical Research*, **35**, 1008.

70 Jurkschat, K., Ji, X., Crossley, A., Compton, R.G. and Banks, C.E. (2007) *Analyst*, **132**, 21.

71 Pumera, M. (2007) *Langmuir*, **23**, 6453.

72 Han, W., Fan, S., Li, Q. and Hu, Y. (1997) *Science*, **277**, 1287.

73 Sloan, J., Hammer, J., Zwiefka-Sibley, M. and Green, M.L.H. (1998) *Chemical Communications*, 347.

74 Dujardin, E., Ebbesen, T.W., Krishnan, A. and Treacy, M.M.J. (1999) *Advanced Materials*, **10**, 1472.

75 Matsui, K., Pradhan, B.K., Kyotani, T. and Tomita, A. (2001) *The Journal of Physical Chemistry B*, **105**, 5682.

76 Govindaraj, A., Satishkumar, B.C., Nath, M. and Rao, C.N.R. (2000) *Chemistry of Materials*, **12**, 202.

77 Wilson, M. and Madden, P.A. (2001) *Journal of the American Chemical Society*, **123**, 2101.

78 Smith, B.W., Monthioux, M. and Luzzi, D.E. (1999) *Chemical Physics Letters*, **315**, 31.

79 Krupke, R., Hennrich, F., Löhneysen, H. v. and Kappes, M.M. (2003) *Science*, **301**, 344.

80 Chattopadhyay, D., Galeska, I. and Papadimitrakopoulos, F. (2003) *Journal of the American Chemical Society*, **125**, 3370.

81 Strano, M.S., Dyke, C.A., Usrey, M.L., Barone, P.W., Allen, M.J., Shan, H., Kittrell, C., Hauge, R.H., Tour, J.M. and Smalley, R.E. (2003) *Science*, **301**, 1519.

82 Strano, M.S. (2003) *Journal of the American Chemical Society*, **125**, 16148.

83 Li, H., Zhou, B., Lin, Y., Gu, L., Wang, W., Fernando, K.A.S., Kumar, S., Allard, L.F. and Sun, Y.-P. (2004) *Journal of the American Chemical Society*, **126**, 1014.

84 Chen, Z., Du, X., Du, M.-H., Rancken, C.D., Cheng, H.-P. and Rinzler, A.G. (2003) *Nano Letters*, **3**, 1245.

85 Zheng, M., Jagota, A., Strano, M.S., Santos, A.P., Barone, P., Chou, S.G., Diner, B.A., Dresselhaus, M.S., Mclean, R.S., Onoa, G.B., Samsonidze, G.G., Semke, E.D., Usrey, M. and Walls, D.J. (2003) *Science*, **302**, 1545.

86 Arnold, M.S., Stupp, S.I. and Hersam, M.C. (2005) *Nano Letters*, **5**, 713.

87 LeMieux, M.C., Roberts, M., Barman, S., Jin, Y.W., Kim, J.J.M. and Bao, Z. (2008) *Science*, **321**, 101.

88 Kong, J., Franklin, N.R., Zhou, C.W., Chapline, M.G., Peng, S., Cho, K. and Dai, H. (2000) *Science*, **287**, 622.

89 Bradley, K., Gabriel, J.C.P., Star, A. and Grüner, G. (2003) *Applied Physics Letters*, **83**, 3821.

90 Kong, J. and Dai, H.J. (2001) *The Journal of Physical Chemistry B*, **105**, 2890.

91 Takenobu, T., Takano, T., Shiraishi, M., Murakami, Y., Ata, M., Kataura, H., Achiba, Y. and Iwasa, Y. (2003) *Nature Materials*, **2**, 683.

92 Golberg, D., Bando, Y., Bourgeois, L., Kurashima, K. and Sato, T. (2000) *Carbon*, **38**, 2017.

93 Petit, P., Mathis, C., Journet, C. and Bernier, P. (1999) *Chemical Physics Letters*, **305**, 370.

94 Duclaux, L. (2002) *Carbon*, **40**, 1751.

95 Shimoda, H., Gao, B., Tang, X.P., Kleinhammes, A., Fleming, L., Wu, Y. and Zhou, O. (2002) *Physical Review Letters*, **88**, 015502.

96 Goldsmith, B.R., Coroneus, J.G., Khalap, V.R., Kane, A.A., Weiss, G.A. and Collins, P.G. (2007) *Science*, **315**, 77.

97 Nichols, J.A., Saito, H., Deck, C. and Bandaru, P.R. (2007) *Journal of Applied Physics*, **102**, 064306.

98 Nichols, J.A., Saito, H., Hoefer, M. and Bandaru, P.R. (2008) *Electrochemical and Solid State Letters*, **11**, K35.

99 Wang, J.X., Li, M.X., Shi, Z.J., Li, N.Q. and Gu, Z.N. (2002) *Analytical Chemistry*, **74**, 1992.

100 Lawrence, N.S., Deo, R.P. and Wang, J. (2005) *Electroanalysis*, **17**, 65.

101 Heng, L.Y., Chou, A., Yu, J., Chen, Y. and Gooding, J.J. (2005) *Electrochemistry Communications*, **7**, 1457.

102 Li, J., Cassell, A., Delzeit, L., Han, J. and Meyyappan, M. (2002) *The Journal of Physical Chemistry B*, **106**, 9299.

103 Pacios, M., del Valle, M., Bartrolí, J. and Esplandiu, M.J. (2008) *Journal of Electroanalytical Chemistry*, **619–620**, 117.

104 Aziz, Md.A., Park, S., Jon, S. and Yang, H. (2007) *Chemical Communications*, 2610.

105 Britto, P.J., Santhanam, K.S.V. and Ajayan, P.M. (1996) *Bioelectrochem Bioenergy*, **41**, 121.

106 Rubianes, M.D. and Rivas, G.A. (2003) *Electrochemistry Communications*, **5**, 689.

107 Valentini, F., Amine, A., Orlanducci, S., Terranova, M.L. and Palleschi, G. (2003) *Analytical Chemistry*, **75**, 5413.

108 Wang, J., Musameh, M. and Lin, Y. (2003) *Journal of the American Chemical Society*, **125**, 2408.

109 Gong, K., Dong, Y., Xiong, S., Chen, Y. and Mao, L. (2004) *Biosensors and Bioelectronics*, **20**, 253.

110 Zhang, M., Smith, A. and Gorski, W. (2004) *Analytical Chemistry*, **76**, 5045.

111 Mendoza, E., Orozco, J., Jimenez-Jorquera, C., González-Guerrero, A.B., Calle, A., Lechuga, L.M. and Fernández-Sánchez, C. (2008) *Nanotechnology*, **19**, 075102.

112 Sánchez, S., Pumera, M., Cabruja, E. and Fábregas, E. (2007) *Biosensors and Bioelectronics*, **23**, 332.

113 Pumera, M., Merkoci, A. and Alegret, S. (2006) *Sensors and Actuators B*, **113**, 617.

114 Gavalas, V.G., Law, S.A., Ball, J.C., Andrews, R. and Bachas, L.G. (2004) *Analytical Biochemistry*, **329**, 247.

115 Zhai, X., Wei, W., Zeng, J., Gong, S. and Yin, J. (2006) *Microchimica Acta*, **154**, 315.

116 Huang, J., Li, X., Xu, J. and Li, H. (2003) *Carbon*, **41**, 2731.

117 Guo, M., Chen, J., Li, J., Tao, B. and Yao, S. (2004) *Analytica Chimica Acta*, **532**, 71.

118 Lin, X. and Li, Y. (2006) *Biosensors and Bioelectronics*, **22**, 253.

119 Liu, H., Wang, G., Chen, D., Zhang, W., Li, C. and Fang, B. (2008) *Sensors and Actuators B*, **128**, 414.

120 Sánchez, S., Fábregas, E., Pumera, M. and Esplandiu, M.J. (2008) submitted.

121 Chattopadhyay, D., Galeska, I. and Papadimitrakopoulos, F. (2001) *Journal of the American Chemical Society*, **123**, 9451.

122 Diao, P., Liu, Z., Wu, B., Nan, X., Zhang, J. and Wei, Z. (2002) *ChemPhysChem*, **3**, 898.

123 Patolsky, F., Weizmann, Y. and Willner, I. (2004) *Angewandte Chemie International Edition*, **43**, 2113.

124 Gooding, J.J., Chou, A., Liu, J., Losic, D., Shapter, J.G. and Hibbert, D.B. (2007) *Electrochemistry Communications*, **9**, 1677.

125 Yu, J., Losic, D., Marshall, M., Böcking, T., Gooding, J.J. and Shapter, J.G. (2006) *Soft Matter*, **2**, 1081.

126 Scott Flavel, B., Yu, J., Shapter, J.G. and Quinton, J.S. (2007) *Journal of Materials Chemistry*, **17**, 4757.

127 Liu, J., Chou, A., Rahmat, W., Paddon-Row, M. and Gooding, J.J. (2005) *Electroanalysis*, **17**, 38.

128 Lin, Y., Lu, F., Tu, Y. and Ren, Z. (2004) *Nano Letters*, **2**, 191.

129 Heller, I., Kong, J., Heering, H.A., Williams, K.A., Lemay, S.G. and Dekker, C. (2005) *Nano Letters*, **5**, 137.

130 Esplandiu, M.J., Bittner, V.G., Giapis, K.P. and Collier, C.P. (2004) *Nano Letters*, **4**, 1873.

131 Burt, D.P., Wilson, N.R., Weaver, J.M.R., Dobson, P.S. and Macpherson, J.V. (2005) *Nano Letters*, **5**, 639.

132 Campbell, J.K., Sun, L. and Crooks, R.M. (1999) *Journal of the American Chemical Society*, **121**, 3779.

133 Musameh, M., Lawrence, N.S. and Wang, J. (2005) *Electrochemistry Communications*, **7**, 14.

134 Yin, Y., Lü, Y. and Cai, C. (2005) *Sensors*, **5**, 220.

135 Giuseppi-Elie, Lei, C., and Baughman, R.H. (2002) *Nanotechnology*, **13**, 559.

136 Pérez, B., Pumera, M., Del Valle, M., Merkoci, A. and Alegret, S. (2005) *Journal of Nanoscience and Nanotechnology*, **5**, 1694.

137 Cai, C. and Chen, J. (2004) *Analytical Biochemistry*, **332**, 75.

138 Liu, Y., Wang, M., Zhao, F., Xu, Z. and Dong, S. (2005) *Biosensors and Bioelectronics*, **21**, 984.

139 Gao, M., Dai, L. and Wallace, G.G. (2003) *Electroanalysis*, **15**, 1089.

140 Liu, G. and Lin, Y. (2006) *Electrochemistry Communications*, **8**, 251.

141 Kang, X., Mai, Z., Zou, X., Cai, P. and Mo, J. (2007) *Analytical Biochemistry*, **369**, 71.

142 Sotiropoilou, S. and Chaniotakis, N.A. (2003) *Analytical and Bioanalytical Chemistry*, **375**, 103.

143 Whitey, G.D., Lazareck, A.D., Tzolov, M.B., Yin, A., Aich, P., Yeh, J.I. and Xu, J.M. (2006) *Biosensors and Bioelectronics*, **21**, 1560.

144 Wang, L., Wang, J. and Zhou, F. (2004) *Electroanalysis*, **16**, 627.

145 Li, Y., Lin, X. and Jiang, C. (2006) *Electroanalysis*, **18**, 2085.

146 Zhao, L., Liu, H. and Hu, N. (2006) *Journal of Colloid and Interface Science*, **296**, 204.

147 Du, P., Liu, S., Wu, P. and Cai, C. (2007) *Electrochimica Acta*, **52**, 6534.

148 Zhang, L., Zhao, G., Wei, X. and Yang, Z. (2005) *Electroanalysis*, **17**, 630.

149 Zhang, L., Zhao, G., Wei, X. and Yang, Z. (2004) *Chemistry Letters*, **33**, 86.

150 Zhao, G., Zhang, L., Wei, X. and Yang, Z. (2003) *Electrochemistry Communications*, **5**, 825.

151 Zhao, G., Yin, Z., Zhang, L. and Wei, X. (2005) *Electrochemistry Communications*, **7**, 256.

152 Yin Wu, Y., Lü, P., Du, Y., Shi, Y., P. and Cai, C. (2007) *Journal of Solid State Electrochemistry*, **11**, 390.

153 Wang, J., Li, M., Shi, Z., Li, N. and Gu, Z. (2002) *Analytical Chemistry*, **74**, 1993.

154 Esplandiu, M.J., Pacios, M., Cyganek, L., Bartroli, J. and del Valle, M. (2008) submitted.

155 Pacios, M., del Valle, M., Bartroli, J. and Esplandiu, M.J. (2008) Journal of Nanoscience and Nanotechnology, in press.

156 Carot, M., Fiorito, P., Torressi, R.M., García, C., Esplandiu, M.J. and Giacomelli, C. (2008) submitted.

157 He, P., Xu, Y. and Fang, Y. (2006) *Microchimica Acta*, **152**, 175.

158 Wang, J., Kawde, A.N. and Musameh, M. (2003) *Analyst*, **128**, 912.

159 Wang, J., Li, M., Shi, Z., Li, N. and Gu, Z. (2004) *Electroanalysis*, **16**, 140.

160 Pedano, M. and Rivas, G.A. (2004) *Electrochemistry Communications*, **6**, 10.

161 He, P. and Dai, L. (2004) *Chemical Communications*, 348.

162 Li, J., Ng, H.T., Cassell, A., Fan, W., Chen, H., Ye, Q., Koehne, J., Han, J. and Meyyappan, M.M. (2003) *Nano Letters*, **3**, 597.

163 Koehne, J., Chen, H., Li, J., Cassell, A.M., Ye, Q., Ng, H.T., Han, J. and Meyyappan, M. (2003) *Nanotechnology*, **14**, 1239.

164 Wang, J., Liu, G. and Jan, M.R. (2004) *Journal of the American Chemical Society*, **126**, 3010.

165 Munge, B., Liu, G., Collins, G. and Wang, J. (2005) *Analytical Chemistry*, **77**, 4662.

166 Wang, J., Liu, G., Jan, R. and Zhu, Q. (2003) *Electrochemistry Communications*, **5**, 1000.

167 Wohlstadter, J.N., Wilbur, J.L., Sigal, G.B., Biebuyck, H.A., Billadeau, M.A., Dong, L.W., Fischer, A.B., Gudibande, S.R., Jamieson, S.H., Renten, J.H., Leginus, J., Leland, J.K., Massey, R.J. and Wohlstadter, S.J. (2003) *Advanced Materials*, **15**, 1184.

168 Yu, X., Kim, S.N., Papadimitrakopoulos, F. and Rusling, J.F. (2005) *Molecular BioSystems*, **1**, 70.

169 Yu, X., Munge, B., Patel, V., Jensen, G., Bhirde, A., Gong, J.D., Kim, S.N., Gillespie, J., Gutkind, J.S., Papadimitrakopoulos, F. and Rusling, J.F. (2006) *Journal of the American Chemical Society*, **128**, 11200.

170 Baughman, R.H., Cui, C., Zakhidov, A.A., Iqbal, Z., Barisci, J.N., Spinks, G.M., Wallace, G.G., Mazzoldi, A., de Rossi, D., Rinzler, A.G., Jaschinsli, O., Roth, S. and Kertesz, M. (1999) *Science*, **284**, 1340.

171 Spinks, G.M., Wallace, G.G., Fifield, L.S., Dalton, L.R., Mazzoldi, A., de Rossi, D., Khayrullin, I.I. and Baughman, R.H. (2002) *Advanced Materials*, **14**, 1728.

172 Fukushima, T., Asaka, K., Kosaka, A. and Aida, T. (2005) *Angewandte Chemie-International Edition*, **44**, 2410.

173 Yun, Y., Shanov, V., Schulz, M.J., Narasimhadevara, S., Subramaniam, S., Hurd, D. and Boerio, F.J. (2005) *Smart Materials & Structures*, **14**, 1526.

174 Yun, Y., Shanov, V., Tu, Y., Schulz, M.J., Yarmolenko, S., Neralla, S., Sankar, J. and Subramaniam, S. (2006) *Nano Letters*, **6**, 689.

175 Frackowiak, E. and Béguin, F. (2002) *Carbon*, **40**, 1775.

176 Leroux, F., Metenier, K., Gautier, S., Frackowiak, E., Bonnamy, S. and Beguin, F. (1999) *Journal of Power Sources*, **81**, 317.

177 Gao, B., Kleinhammes, A., Tang, X.P., Bower, C., Fleming, L., Wu, Y. and Zhou, O. (1999) *Chemical Physics Letters*, **307**, 153.

178 Eom, J.Y., Kim, D.Y. and Kwon, H.S. (2006) *Journal of Power Sources*, **157**, 507.

179 Gao, B., Bower, C., Lorentzen, J.D., Fleming, L., Kleinhammes, A., Tang, X.P., McNeil, L.E., Wu, Y. and Zhou, O. (2000) *Chemical Physics Letters*, **327**, 69.

180 Mi, C.H., Cao, G.S. and Zhao, X.B. (2004) *Journal of Electroanalytical Chemistry*, **562**, 217.

181 Shimoda, H., Gao, B., Tang, X.P., Kleinhammes, A., Fleming, L., Wu, Y. and Zhou, O. (2002) *Physica B*, **323**, 133.

182 Wu, Y.P., Jiang, C., Wan, C. and Holze, R. (2003) *Electrochimica Acta*, **48**, 867.

183 Sato, M., Noguchi, A., Demachi, N., Oki, N. and Endo, M. (1994) *Science*, **264**, 556.

184 Pushparaj, V.L., Manikoth, S.M., Kumar, A., Murugesan, S., Ci, L., Vajtai, R., Linhardt, R.J., Nalamasu, O. and Ajayan, P.M. (2007) *Proceedings of the National Academy of Sciences of the United States of America*, **104**, 13574.

185 Pandolfo, A.G. and Hollenkamp, A.F. (2006) *Journal of Power Sources*, **157**, 11.

186 Kim, Y.J., Kim, Y.A., Chino, T., Suezaki, H., Endo, M. and Dresselhaus, M.S. (2006) *Small*, **2**, 339.

187 Landi, B.J., Castro, S.L., Ruf, H.J., Evans, C.M., Bailey, S.G. and Raffaelle, R.P. (2005) *Solar Energy Materials and Solar Cells*, **87**, 733.

188 Kymakis, E. and Amaratunga, G.A.J. (2006) *Journal of Applied Physics*, **99**, 084302.

189 Xu, Z.H., Wu, Y., Hu, B., Ivanov, I.N. and Geohegan, D.B. (2005) *Applied Physics Letters*, **87**, 263118.

190 Rahman, G.M.A., Guldi, D.M., Cagnoli, R., Mucci, A., Schenetti, L., Vaccari, L. and Prato, M. (2005) *Journal of the American Chemical Society*, **127**, 10051.

191 Miller, A.J., Hatton, R.A. and Silva, S.R.P. (2006) *Applied Physics Letters*, **89**, 133117.

192 Bhattacharyya, S., Kymakis, E. and Amaratunga, G.A.J. (2004) *Chemistry of Materials*, **16**, 4819.

193 Britto, P.J., Santhanam, K.S.V., Rubio, A., Alonso, A. and Ajayan, P.M. (1999) *Advanced Materials*, **11**, 154.

194 Che, G., Lakshmi, B.B., Fisher, E.R. and Martin, C.R. (1999) *Nature*, **393**, 346.

195 Wu, G. and Xu, B. (2007) *Journal of Power Sources*, **174**, 148.

196 Minteer, S.D., Liaw, B.Y. and Cooney, M.J. (2007) *Current Opinion in Biotechnology*, **18**, 228.

4

Electrochemistry of Electroactive Surface-Immobilized Nanoparticles

Daniel A. Buttry

4.1

Introduction

The lure of new physical phenomena and new patterns of chemical reactivity has driven a tremendous surge in the study of nanoscale materials. This activity spans many areas of chemistry. In the specific field of electrochemistry, much of the activity has focused on several areas: (a) electrocatalysis with nanoparticles (NPs) of metals supported on various substrates, for example, fuel-cell catalysts comprising Pt or Ag NPs supported on carbon [1, 2], (b) the fundamental electrochemical behavior of NPs of noble metals, for example, quantized double-layer charging of thiol-capped Au NPs [3–5], (c) the electrochemical and photoelectrochemical behavior of semiconductor NPs [4, 6–8], and (d) biosensor applications of nanoparticles [9, 10]. These topics have received much attention, and relatively recent reviews of these areas are cited. Considerably less has been reported on the fundamental electrochemical behavior of electroactive NPs that do not fall within these categories. In particular, work is only beginning in the area of the electrochemistry of discrete, electroactive NPs. That is the topic of this review, which discusses the synthesis, interfacial immobilization and electrochemical behavior of electroactive NPs. The review is not intended to be an exhaustive treatment of the area, but rather to give a flavor of the types of systems that have been examined and the types of phenomena that can influence the electrochemical behavior of electroactive NPs.

Examples of electroactive NP materials discussed in the review include TiO_2, MnO_2, iron oxides, other metal oxides, hydroxides and oxyhydroxides and Prussian Blue. We use the term 'electroactive NPs' to refer to the faradaic electroactivity in such materials and to distinguish them from NPs comprised of metals (such as Au, Ag, Pt, Co, etc.) or semiconductors (such as CdS, CdSe, etc.). This distinction is based on the ability of many electroactive NPs to undergo faradaic oxidation or reduction of all of the metal (redox) centers in the NP. This is in contrast to the behavior of many metal and semiconductor NPs for which oxidation or reduction is fundamentally an interfacial, double-layer process. This definition is somewhat arbitrary, since the smallest metal and semiconductor NPs behave molecularly, blurring the distinction between faradaic reactivity and double layer charging. Nevertheless, it is a useful categorization, especially given the growing number of studies that focus on charge-storage applications of electroactive NPs of the types described here, and the fact that such applications benefit by having all the redox centers in a NP fully electroactive.

This review focuses on nanoparticles, namely objects that are roughly spherical. We use the commonly accepted definition for nanoscale objects of having a dimension below 100 nm, and so identify nanoparticles as objects with a diameter of 100 nm or smaller. The review does not focus on larger aspect ratio nanoscale materials such as nanotubes and nanorods, though they are mentioned in some cases.

Both capped and uncapped NPs are discussed. Capping refers to the (often strong, or even irreversible) adsorption of a passivating agent onto the surface of a NP. Examples of capped NPs include SnO_2 NPs capped with 3-phosphonopropionic acid via strong adsorption of the phosphonate group at the oxide surface [11], trioctylphosphine (TOP) or trioctylphosphine oxide (TOPO) capped CdS NPs [12, 13], or thiol-capped Au NPs, often called monolayer-protected clusters (MPCs) [5]. Many capped NPs are neutral species that are soluble in low dielectric constant solvents. However, it is possible to cap NPs with capping agents that bear pendant charged groups, rendering them soluble in aqueous solutions and other high dielectric constant solvents [5]. Examples of uncapped NPs include nanoparticulate metal-oxide colloids, such as the negatively charged MnO_2 NPs studied by Suib and coworkers [14]. These two types of materials, capped and uncapped NPs, exhibit different behavior by virtue of their very different surface energies. Capped NPs tend to have very low surface energies, which prevents irreversible aggregation [5]. Thus, they often can be precipitated and stored as solids, and then redissolved at a later time in an appropriate solvent. In contrast, the uncapped systems often have intrinsically high surface energies. This allows for very strong interparticle interactions that can lead to irreversible aggregation [15]. So, while colloidal solutions of uncapped, charged NPs may be stable for prolonged periods, once the NPs are allowed to aggregate it is typically not possible to redissolve them. This type of behavior influences the methods that can be used to immobilize them, as described further below.

In keeping with the theme of this Volume, we discuss electroactive NPs that have been immobilized at electrode surfaces, either in monolayer or multilayer formats. As will be seen below, immobilization can be done in a variety of ways, using simple adsorption, dip coating, film casting, spraying, electrodeposition, electrophoretic deposition, or layer-by-layer (LbL) film growth methods. In all cases, our primary focus is on NPs that are synthesized as discrete entities and then immobilized in some fashion at electrode surfaces. We explicitly do not discuss nanostructured electrode materials, which is a large area that has attracted considerable recent activity because of the potential of such materials in battery, capacitor and fuel-cell applications [16, 17]. While such materials are interesting in their own right, their behavior is sometimes different from that of electroactive NPs. For example, in many cases they behave as bulk materials with very large surface areas rather than as discrete nanoparticles.

As mentioned above, the electroactive NPs discussed here differ from typical semiconductor NPs or capped noble-metal NPs (e.g., Au-monolayer-protected clusters) in an important way. Specifically, the reduction or oxidation of the metal centers in electroactive NPs typically is accompanied by ion insertion or expulsion in order to achieve charge compensation. An example is the reduction of Mn(IV) centers in MnO_2 NPs to give Mn(III) with the simultaneous insertion of Li^+ or other cationic species from the supporting electrolyte [18]. This ability to achieve charge compensation throughout the NP allows for the transfer of many more electrons than is typical for semiconductor or noble-metal NPs. In fact, provided that ionic compensation may be achieved, electroactive NPs are generally capable of reduction or oxidation of each and every metal center in the NP via a faradaic process. In contrast, electron transfer to capped noble-metal NPs and many semiconductor NPs is fundamentally a double-layer charging process, except for the smallest of such NPs, which behave molecularly. For the larger metal and semiconductor NPs, charge compensation typically is achieved by creation of a double layer around the NP, much like the ionic atmosphere around ionic species in electrolyte solutions. Interestingly, this also may be an important charge-compensation mechanism for the smallest electroactive NPs, which should be able to achieve charge compensation either by ion insertion/expulsion or formation of double layers around the NPs. The ability to achieve charge compensation via external counterions may provide some advantages in terms of the rates at which electron transfers to and from small electroactive NPs may occur, since diffusion of the charge-compensating ions within the (solid) NP material, which is often rather slow, need not occur.

As mentioned, the possibility for complete reduction of the metal centers in electroactive NPs is in contrast to the behavior common for capped noble-metal NPs or semiconductor NPs, such as CdS, which are often reduced or oxidized by numbers of electrons considerably smaller than the number of metal centers in the NP. For example, 11 nm Ag NPs, which accommodate charge via bulk-like (i.e. continuous) double-layer charging, can accept approximately 1600 electrons over a 1 V potential excursion [5, 19]. But, this number of electrons is far below the number of Ag atoms in the NP, which can be estimated at about 50 000 using simple geometric arguments. Similarly, well-characterized capped Au NPs with 140 Au atoms in their core and diameters of 1.6 nm exhibit quantized double-layer charging and accommodate only 8 electrons over a 1 V potential excursion [5]. Again, the number of charges accommodated is far below the number of metal atoms in the core. Semiconductor NPs are similar in this way to noble-metal NPs. In many cases, semiconductor NPs have been observed to accommodate only one or a few electronic charges over quite large potential excursions [6]. This is in part due to their large bandgaps. Further, for some semiconductor NPs, charge injection leads to chemical decomposition. This important difference between (faradaically) electroactive NPs and the semiconductor and noble-metal NPs described above makes electroactive NPs of particular interest for charge-storage applications, such as batteries [20].

4.2
Synthetic Approaches and Characterization

In many cases, the electroactive NPs of interest here can be considered to be colloidal materials. Thus, many of the approaches to their synthesis rely on reaction types and conditions that can be found in the early colloid literature. For example, over one and a half decades ago Matijević summarized a large body of work on methods for producing uniformly sized, micrometer to submicrometer diameter inorganic particles using aqueous-solution methods [21]. Presaging more recent studies of core–shell nanoparticles, he also described several approaches for producing both coated and hollow particles. Common synthetic routes to inorganic particles include hydrolysis of soluble precursors and thermal decomposition of precursors, both of which can give colloidal solutions of NPs [21]. Hydrolytic methods are often used to produce metal oxides, hydroxides or oxyhydroxides, while thermal decomposition of metal complexes is often used to produce oxides. Direct precipitation also can be used, for example, to produce metal phosphates [22]. Another common synthetic route takes advantage of redox reactions of metal precursors that produce insoluble oxidation states. An example is the controlled reduction of MnO_4^- with butanol to give negatively charged MnO_2 nanoparticle colloids [14]. These colloid methods rely on the production of charged particles that are stabilized toward aggregation by like charges. As will be seen below, these charges also can be used in immobilization schemes, such as layer-by-layer film formation in which electrostatic forces between oppositely charged NPs and polymers are used to form and stabilize the films. When NP synthesis is carried out near room temperature, it is possible to produce (metastable) phases that are different from those obtained via high-temperature processes. For example, MnO_4^- reduction as described above produces a layered, birnessite-like MnO_2 structure, while higher-temperature routes to MnO_2 often produce spinel-like structures [14].

Electrochemical processes also can be used to deposit NPs directly onto electrode surfaces [23]. For example, MoO_3 NP deposits on highly oriented pyrolytic graphite (HOPG) surfaces have been prepared by electrodeposition of Mo metal followed by air oxidation to give NPs or nanowires of MoO_3 [24, 25]. Also, controlled electrochemical reduction of MnO_4^- was shown to produce MnO_2 NPs that coalesced into nanowires as additional material was electrodeposited [26]. In such cases, control of the nucleation and growth of the initially deposited nuclei is critical to control the size of the deposited NPs. Electrodeposition into templates also has been used to prepare electrode surfaces decorated with nanoscale electroactive materials [27]. However, this method has mostly been used to prepare high aspect ratio nanotubes or nanorods, which are not a subject for this review.

Solvothermal methods have also been used for synthesis of electroactive NPs [28, 29]. In this approach, high-temperature reaction conditions are employed, usually above the boiling temperature of the solvent. When done in water, the process is referred to as hydrothermal synthesis. In water, the method often employs surfactants, so that surfactant assemblies can serve as templates for the resulting nanoscale materials. These syntheses take advantage of the higher solubilities and reactivities for most reagents at elevated temperatures. An interesting variation on these methods involves the use of microwave reactors, which facilitate the rapid achievement of high temperatures [30]. This offers good control over nucleation and growth processes, giving excellent control over particle size and dispersity. Many different types of materials have been prepared in this way, including nanoparticles, nanotubes, nanorods, and so on. For example, nanoscale manganese oxides and oxyhydroxides have been prepared using such approaches [31].

Many different high-temperature syntheses have been developed based on thermal decomposition of precursors, often organometallic compounds. These methods can be used to produce solutions of NPs that are encapsulated by organic capping agents and, therefore, are soluble in organic solvents. In contrast to the colloidal NPs described above, these capped NPs typically are not charged. These high-temperature methods can give exquisite control over size, shape and composition. Several reviews give lucid descriptions of the key issues that control these properties [12, 13, 32]. Two of these reviews focus on synthesis of semiconductor NPs, such as CdS and CdSe [12, 13], while the third focuses on magnetic NPs, such as iron and cobalt oxides [32]. While these reviews do not explicitly discuss electroactive NPs, the general approaches they describe for synthesizing metal-containing NPs via high-temperature routes are relevant to the present case. All of the synthetic schemes discussed above may be adapted to produce core–shell or other more exotic materials, such as NPs with branched structures. Figure 4.1 gives an example of the production of iron-oxide NPs using two different thermal decomposition routes [32].

Sonochemical routes also have been used to produce electroactive NPs. For example, metal hydroxides containing Ni(II), Co(II) and mixtures of both have been prepared from the appropriate metal nitrate salts using ammonium hydroxide as the hydrolytic agent [33, 34]. This route produces metal-hydroxide NPs with diameters in the range of 2–10 nm. This method has been extensively applied in the synthesis of a wide variety of materials, including nanomaterials [35].

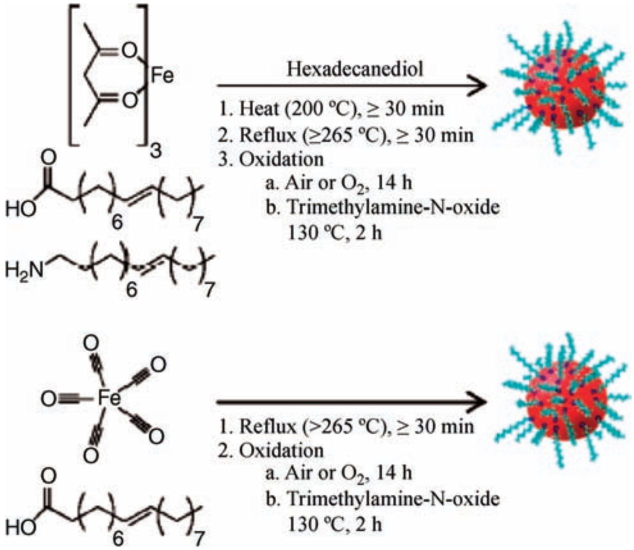

Figure 4.1 Synthetic scheme for production of iron-oxide NPs using a thermal-decomposition route. From reference [32] with permission.

One often desires knowledge of both the average size and the size dispersity of the NPs produced from the synthetic methods described above. Several different types of tools are used for this purpose, including ultraviolet-visible spectroscopy, dynamic light scattering, X-ray diffraction and electron microscopy. A recent review on iron-oxide NPs gives brief discussions of these [36]. Optical spectroscopic methods are very commonly used to assist in size determination of metal and semiconductor NPs, because the electronic states involved in the optical transitions are delocalized enough to 'sense' the boundaries of the NP. For example, the absorption associated with the bandgap in semiconductor NPs undergoes a blueshift with decreasing NP diameter, which can be used to accurately obtain the average diameter [12]. Similar effects are observed in the emission spectra of semiconducting NPs. Metal NPs often have plasmon resonances in the ultraviolet or visible regions whose energy or intensity correlate with size, except for the smallest of such particles that typically do not exhibit plasmon absorptions [3]. For the metal-oxide NPs discussed here, optical absorption processes do not always provide such direct information on size. While some metal-oxide NPs do exhibit a size-dependent shift in optical absorptions, many do not. For example, colloidal semiconducting MnO_2 NPs with a layered structure exhibit a blueshifted absorption with decreasing diameter that correlates with size [14]. In contrast, the optical transitions for some metal-oxide, hydroxide or oxyhydroxides NPs are highly localized, leading to optical transitions that do not provide information on size [32]. Thus, in many cases, other techniques must be used. X-ray diffraction peak widths and dynamic light scattering have been employed, both of which provide size information that is averaged over the entire sample population [36]. Electron microscopies provide perhaps the best information on size [37]. Scanning electron microscopy, especially with field emission sources, offers high enough resolution to give images of NPs with diameters approaching the 10s of nm range, and is being used increasingly to characterize NPs at surfaces [38]. Transmission electron microscopy (TEM) provides perhaps the ultimate in high-resolution imaging, and has been very widely used to obtain size information on NPs. However, because TEM images cover only a very small portion of a given sample, it is important to observe many areas in a given sample and use a statistical representation of the data (e.g., a size histogram) to report size information. There are limitations to the use of high-resolution electron microscopies. For example, it has been shown recently that overexposure to the electron beam can cause evolution of the structures of nanoparticles during TEM imaging, causing solid NPs to evolve into hollow spheres [39]. Thus, care must be taken in using such techniques.

4.3
Immobilization Schemes

Several approaches have been described for the immobilization of NPs at electrode surfaces. The simplest is direct adsorption of the NP from solution onto an electrode surface. This method takes advantage of favorable electrostatic interactions between the surface and the NPs. This has been used, for example, to immobilize TiO_2 NPs

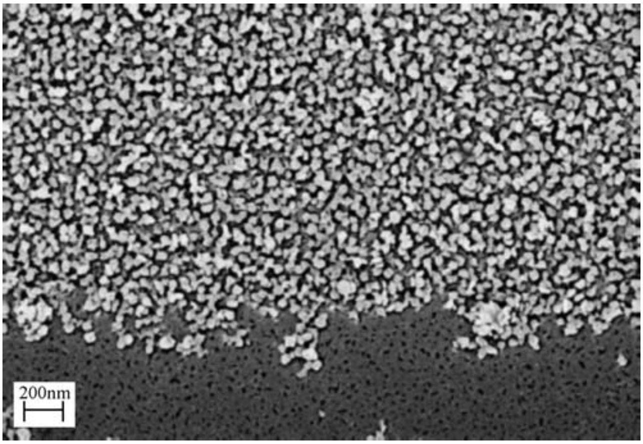

Figure 4.2 Field emission SEM image of a monolayer of TiO_2 NPs adsorbed onto a highly polished boron-doped diamond electrode. From reference [38] with permission.

onto boron-doped diamond (BDD) electrodes [38]. In this case, the positively charged TiO_2 NPs were adsorbed at a negatively charged BDD electrode. Figure 4.2 shows a field emission SEM image of the TiO_2 monolayer obtained in this way. The same group has used a dip-coating/evaporation method to deposit TiC NPs from methanol solutions onto ITO electrodes [40]. In another example of using favorable electrostatic interactions between the surface and the NPs, Liu *et al*. immobilized Prussian Blue NPs at gold electrode surfaces by using cysteine anchors [41]. They first treated the Au surface with cysteine, which produces a self-assembled monolayer with amine groups oriented away from the surface. This surface was then immersed in a solution containing a Prussian Blue NP colloid that caused immobilization of the PB NPs at the surface. In this case immobilization probably occurs by virtue of favorable electrostatic interactions between the negatively charged PB NPs and the protonated, positively charged amine groups at the surface. Films of NPs also can be applied using a spraying processes, sometimes followed by heat treatment [42, 43]. For all of the cases described above, one might expect that the high surface energies of the uncapped NPs drive strong attachment to the surface and/or aggregation of the NPs once in the interfacial assembly. This may be responsible for the strong, irreversible adsorption of TiO_2 NPs onto BDD electrodes [38]. Thus, even though the NPs may initially bear like charges, leading to repulsive interparticle interactions, the contact that occurs between the surface and the NPs or between the NPs themselves during film formation may lead to irreversible immobilization.

For cases in which the NPs are not soluble in the supporting electrolyte in which they will be examined, it is possible to solvent-cast a thin film of the NPs on the electrode surface followed by evaporation [44] or to directly apply an insoluble gel containing the NPs [45]. In a related approach, films of anionic Prussian Blue NPs that had been synthesized in a solution containing chitosan (a cationic glucosamine polymer) were drop-cast onto glassy carbon surfaces, giving very stable immobilization [46]. Bard's group has used an experimental protocol in which core–shell Ag/Ag_2O NPs were mixed into a solution with conductive graphite powder and Nafion. This solution was then cast onto a gold electrode for examination of the electrochemical behavior of the Ag/Ag_2O NPs [47]. Finally, NPs can be mixed directly into carbon paste or similar formulations and then used to make paste electrodes. Similarly, simple mechanical immobilization of electroactive NPs by pressing onto the surface of paraffin-impregnated graphite electrodes has been described [48].

As mentioned above, electrodeposition can be used to synthesize electroactive NPs. This method also can serve as a means to immobilize the NPs at an electrode surface. Penner's group has pioneered in this area [23]. They have used both metal deposition followed by oxidation [24] and electrochemically induced changes in oxidation states [26] to produce metal-oxide deposits on graphite surfaces. In the latter case, they electrochemically reduced MnO_4^- at graphite surfaces to produce MnO_2 NPs, but did not explore the electrochemical behavior of the deposits. Another novel approach involves the electrophoretic deposition of electroactive NPs [49–51]. For example, WO_3 NPs were deposited onto fluorine-doped SnO_2 (FTO) surfaces from methanol solutions using a two-electrode arrangement with a relatively high voltage (300 V) between the electrodes [49, 50]. Film thicknesses up to 1 micrometer were produced. Also, diamond NPs were electrophoretically deposited onto Si substrates, producing films with thicknesses between 1 and 10 micrometers [51]. The electrophoretic deposition method relies on the particles having a net surface charge, as do many of the approaches described here. Thus, the application of large voltage differences (up to several hundred volts) between two electrodes in a solution containing the charged NPs can drive their immobilization at an oppositely charged electrode. Such deposits are likely to be quite stable toward dissolution because of the high surface energies expected for uncapped NPs.

One of the most common methods for NP immobilization at electrode surfaces is the layer-by-layer (LbL) method [52]. The LbL approach takes advantage of attractive electrostatic interactions between two film components to build up layers by alternate exposures of an initially charged substrate to solutions of each of the components. For example, Figure 4.3 shows a typical sequence used to produce a LbL film comprised of alternating layers of a cationic polyelectrolyte and anionic NPs. As will be seen below, this is a common approach for immobilizing electroactive NPs at electrode surfaces. In this example, one begins with a surface that has a net, fixed charge. This might be achieved by exposure of an indium-doped tin oxide (ITO) electrode to a solution of aqueous base, giving a negatively charged surface via deprotonation of surface hydroxyl groups [53]. This is followed by immersion in a solution containing a cationic polyelectrolyte, such as poly(diallyldimethylammonium) hydrochloride (PDDA), which functions as a polymeric binder. After rinsing in pure water, the PDDA-coated ITO substrate is then exposed to a solution containing a colloid of a negatively charged electroactive NP, again followed by rinsing. This produces a surface coated with a bilayer of PDDA and the NP, indicated by ITO/PDDA/NP. This procedure can be repeated many times to build up on the surface a film comprised of multiple bilayers of PDDA and the NP. This is typically designated as $ITO/(PDDA/NP)_n$, where n is the number of bilayers. Such films are usually

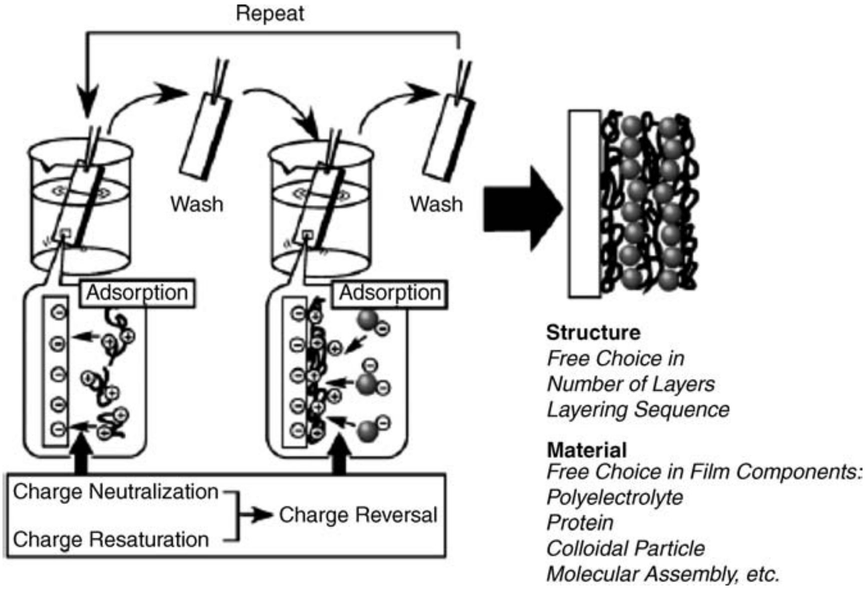

Figure 4.3 Outline of LbL assembly through electrostatic interactions. From reference [52] with permission.

terminated with a layer of the polymeric binder that serves to stabilize the final layer of NPs. This film would then be designated as ITO/(PDDA/NP)$_n$/PDDA. The procedure used to produce such films implies that the films may be layered, and therefore fairly well organized. However, some evidence suggests that these types of polymer/NP films are less organized than the 'fuzzy' nanocomposite polymer/polymer LbL films originally described by Decher [54]. A consequence of this is the limited number of electroactive bilayers that can be effectively built on a substrate. Thus, typically one finds polymer/NP LbL films with between one and 30 bilayers. For thicker films, repeated cycling through the film growth steps often does not lead to additional film growth or electroactivity, presumably because of the progressively disorganized nature of the film structure as the film thickness increases. Many variations on this simple LbL scheme have been described, in which different types of polymers and/or different types of NPs are used in the same film [52, 55]. Thus, the approach allows considerable flexibility in film design and function [52]. Further, newer approaches are being envisioned in which interactions other than electrostatic forces are used to build up the assembly [55]. For example, hydrogen bonding and covalent-bond formation are now being used in LbL film formation. The inherent ease and flexibility of the LbL method have caused it to be widely used as an immobilization strategy for examining the electrochemistry of NPs at modified electrode surfaces.

The nature of the LbL film structure puts the NPs into close proximity to one another. Thus, for cases in which the NPs are electroactive, charge propagation through the films seems most likely to occur by electron exchange, first between the electrode and the layer of NPs closest to the electrode surface and then by electron exchange between the NPs in the film. This mechanism has been described for thiol-capped Au NPs in LbL films [5]. This allows electron propagation through the bulk of the film. However, there may be limits to this charge propagation, especially for thicker LbL films. For example, Torresi and coworkers described LbL films comprised of PDDA and MnO_2 NPs in which charge propagation became ineffective beyond about 12 bilayers [18]. Note also that for NPs with high surface energies, incorporation into a LbL film may cause the NPs to form strong, even covalent, interparticle contacts. In such cases, it may not be appropriate to view electron propagation through the film as arising from electron exchange between isolated, discrete NPs.

We turn now to discussion of the specific types of electroactive NPs that have been described. The NPs are grouped according to the composition of the electroactive NP rather than the method of immobilization. In most cases, metal-oxide/hydroxide/oxyhydroxides materials are grouped together using a formulation such as 'MO_x', to indicate the different compositions and redox states of the metals that may be described.

4.4
Metal Oxides

4.4.1
TiO_x

Pletcher's group at Southampton was one of the first to examine the electrochemistry of films prepared from initially discrete metal-oxide nanoparticles [43, 56]. They prepared films of 21 nm diameter TiO_2 from Degussa by spraying solutions of the TiO_2 NPs onto a Ti wire followed by heat treating. SEM revealed a high surface area deposit. There was no clear evidence for discrete 21 nm building blocks in the film, suggesting extensive sintering during the heat treatment. They examined the voltammetry in aqueous 1.0 M NaOH and observed a reversible set of peaks centered at −0.96 V vs. SCE. These were attributed to reduction of Ti(IV) to Ti(III). However, the charge for this reduction was far too small to derive from all of the Ti(IV) centers in the film. In fact, it was too small even to arise from the interfacial Ti(IV) sites, based on a geometrical estimate of the film surface area. Interestingly, they observed an increase in the charge for this interfacial redox process when the electrodes were cycled over the Ti(IV)/Ti(III) wave in the presence of $Fe(CN)_6{}^{3-}$. They attributed this increase in charge to an increase in surface caused by corrosion during the cycling experiment. In a companion study they deposited Pt particles on these surfaces and examined the electrocatalytic oxidation of H_2, CO and methanol [56].

Marken and coworkers examined TiO_2 NPs in various types of interfacial assemblies [38, 40, 57, 58]. In their first study, commercially available 6-nm diameter TiO_2 NPs were directly adsorbed onto polished boron-doped diamond electrodes from acidic aqueous solutions containing the TiO_2 sol [38]. Using field emission SEM and STM, they observed relatively uniform adsorption of the TiO_2 NPs and small aggregates (<40 nm) onto the BDD surface (Figure 4.2). Voltammetric experiments were done in aqueous phosphate buffer and in $NaClO_4$ containing various amounts of $HClO_4$. In phosphate buffer, two redox processes were observed in the range -1.0 to -1.5 V vs. SCE. By using $NaClO_4/HClO_4$ mixtures to study their dependence on the H^+ concentration, these were both assigned to reduction of Ti(IV) to Ti(III), with the first reduction occurring at near-surface sites and the second (more negative) reduction occurring at deeper sites within the NPs. The charge for the reduction at both sites was consistent with reduction of roughly one third of the Ti(IV) sites in the NPs. This is one of a few examples in which the electrochemical responses of sites at the surface and within a NP appear to have been electrochemically distinguishable.

In a second study, Marken, Mortimer and coworkers examined the electrochemical behavior of TiC/TiO_2 core shell NPs [40]. First, they deposited 20–30-nm diameter TiC NPs from a methanol suspension onto an ITO surface using an emersion/drying technique. This produced a layer of firmly attached TiC NPs. The process could be repeated to give a multilayer deposit, as monitored using a quartz crystal microbalance (QCM) system. The electrochemical response of the TiC film showed a large, irreversible anodic process at $+1.0$ V that was attributed to oxidation of TiC to TiO_2 in a thin layer on the surface of the NP. Thus, the electrochemical process produced a TiC/TiO_2 core–shell structure for the NPs in the film. They also demonstrated that similar core–shell structures could be produced using thermal treatments. These core–shell NP films were shown to be electrocatalytically active toward hydroquinone, ascorbic acid and dopamine oxidation. These properties were attributed to good electrochemical activity for the TiO_2 component and good electronic conductivity for the TiC component, showing a synergistic combination of the TiC and TiO_2 properties.

Marken and coworkers also examined LbL films comprised of 6 nm TiO_2 NPs and Nafion, a perfluorosulfonated polymer [57]. They alternately deposited 6-nm diameter positively charged TiO_2 NPs and Nafion on ITO electrodes, which was monitored using QCM, atomic force microscopy (AFM) and electron microscopy. Deposition led to aggregation and the production of a mesoporous structure. The electrochemical properties of the films were examined in 0.1 M KCl, revealing a reversible reduction process that occurred between -0.7 V and -1.0 V vs. SCE. This is due to the same Ti(IV) reduction described above [38]. The charge for this process scales with LbL film thickness (i.e. number of layers) as shown in Figure 4.4. The electrochemical responses of several cation redox couples were examined in these films, including $Ru(NH_3)_6{}^{3+}$, diheptylviologen and a cationic ferrocene derivative. It was determined that, for redox couples with reduction potentials near the Ti(IV) reduction, charge conduction through the film to the couple can occur by direct electron propagation through the TiO_2 NPs. On the other hand, for redox couples with reduction potentials far from the Ti(IV) reduction, electron propagation through the film to deliver charge to the redox couple was attributed to electron hopping between redox couples incorporated (concentrated) within the film.

Marken's group also prepared LbL films from combinations of positively charged 6-nm diameter TiO_2 NPs and negatively charged 20 nm diameter Au NPs, using an approach in which the polymeric binder for the LbL structure was alternated between

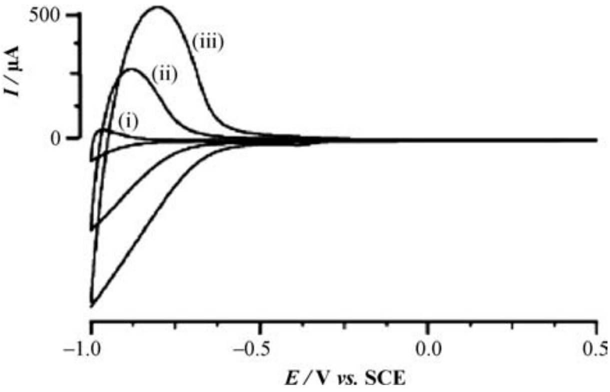

Figure 4.4 Cyclic voltammogram for the reduction and reoxidation of 6 nm TiO_2 NPs immobilized in LbL films with Nafion. Scan rate, 100 mV s^{-1}. Electrolyte 0.1 M KCl. (i) 2 layers TiO_2, (ii) 10 layers TiO_2, (iii) 20 layers TiO_2. From reference [57] with permission.

Nafion and PDDA [58]. Thermal treatment of the resulting films gave a mesoporous TiO_2 matrix with Au NPs embedded within and dispersed on top of the TiO_2 matrix. Only about 10% of the Au surface area was electrochemically active, suggesting that a large fraction of the Au NPs was not well connected to the underlying electrode surface. These mesoporous deposits were shown to be effective electrocatalysts for NO and nitrite oxidation.

4.4.2
MnO_x

Manganese-oxide materials have been studied by several groups. These materials are of interest for several reasons. First, there is considerable interest in the Mn(IV)/Mn(III) redox couple for energy storage, both in battery and ultracapacitor applications [59, 60]. Second, MnO_2 is known to be quite a good electrocatalyst for O_2 and H_2O_2 reduction, as well as for the disproportionation of hydrogen peroxide, all in aqueous base [61]. Thus, several of the studies below focus on these two aspects of the behavior of manganese oxide.

Lvov *et al.* [53] prepared LbL films using anionic MnO_2 NPs prepared according to the method pioneered by Suib's group [14]. These LbL films were prepared by alternate exposure to MnO_2 and PDDA or to MnO_2 and myoglobin, which was cationic under the conditions of the LbL film assembly. This was the first example of LbL films containing electroactive NPs and electroactive proteins. Film growth was monitored using optical absorption and QCM methods. Interestingly, LbL films comprised of MnO_2 and PDDA exhibited no obvious electrochemical response over the range 0.1 to −0.7 V vs. SCE. This is in contrast to results from other studies in which MnO_2 NPs were examined in nonaqueous media (see below). However, LbL films containing both MnO_2 NPs and myoglobin gave very well-defined Fe(III)/Fe(II) redox responses for the heme groups in the myoglobin. These films were shown to have good behavior for electrocatalytic reduction of O_2.

Wang *et al.* examined the electrochemical behavior of MnO_2 in LbL films prepared from exfoliated nanosheets of MnO_2 [62]. Solutions containing the nanosheets were prepared by exfoliation of MnO_2 NPs with diameters in the range of 100 to 300 nm. These were then used with either PDDA or poly(ethyleneimine) (PEI) to prepare LbL films containing the MnO_2 nanosheets. The electrochemical behavior of a single bilayer of ITO/PEI/MnO_2 was examined in 0.1 M $LiClO_4$ in propylene carbonate. A chemically reversible reduction was observed at -0.6 V vs. Ag/Ag^+, which was attributed to the Mn(IV)/Mn(III) redox process. Geometric arguments were used to suggest that all of the Mn centers in the single bilayer LbL film were electroactive.

Torresi's group has examined the electrochemical behavior of MnO_2 NPs in LbL films in room-temperature ionic liquids (RTILs) [18]. They prepared LbL films on ITO using alternating layers of anionic 5–20 nm diameter MnO_2 NPs and PDDA. A field emission SEM of such a 10-bilayer film is shown in Figure 4.5. Film growth was monitored using UV-visible spectroscopy, AFM and QCM methods. The LbL films were then examined in RTILs comprised of 1-butyl-2,3-dimethyl-imidazolium (BMMI) bis(trifluoromethanesulfonyl)imide (TFSI), as well as BMMITFSI that also contained small amounts of LiTFSI. In BMMITFSI, the LbL film exhibited a small reversible reduction/oxidation attributed to the Mn(IV)/Mn(III) redox couple. Addition of LiTFSI to the ionic liquid resulted in a dramatic increase in the magnitude of the Mn(IV)/Mn(III) redox wave, showing that the electrochemistry of the Mn centers in the NPs is inhibited unless Li^+ is available for insertion to achieve charge compensation within the NPs. This may suggest that the electrochemical response in the absence of Li^+ is due to interfacial Mn sites that can achieve charge

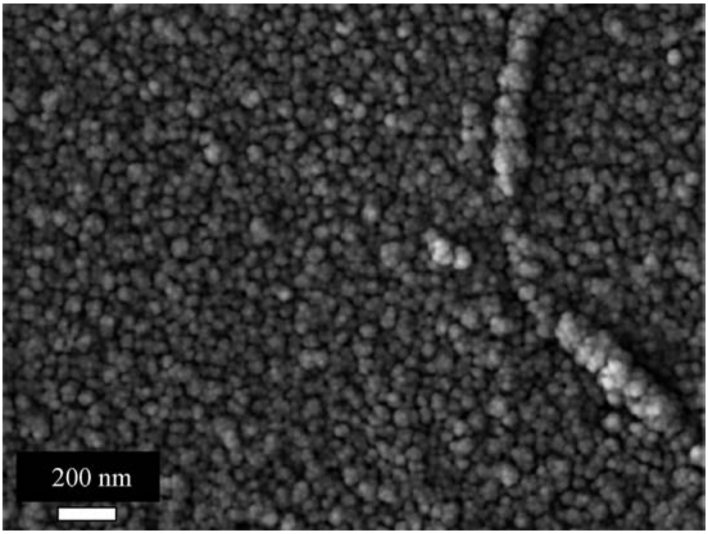

Figure 4.5 FEG-SEM image corresponding to the surface LBL film of 10 deposited bilayers. From reference [18] with permission.

compensation using counterions outside of the NP, while the larger response in the presence of Li^+ may be due to the Mn centers in the interior of the NP that require cation insertion to achieve charge compensation. Comparison of the experimental charge with the number of Mn centers in the LbL film revealed that, even with Li^+ present, only half of the Mn centers are electroactive, in contrast to the results reported by Wang *et al.* above [62]. This was attributed to poor swelling of the layered MnO_2 NPs in the ionic liquid and/or to low mobility of Li^+ in the RTIL. They also used *in-situ* electrochemical QCM measurements to monitor the charge compensation in the films during the Mn-based redox process in a Li^+-containing RTIL. The data showed that both anions and cations are transported during the redox process, suggesting that Li^+ transport is not sufficiently fast for it to dominate the charge-compensation process.

The studies discussed above used LbL methods to immobilize MnO_2 NPs at electrode surfaces to explore their electrocatalytic and charge storage characteristics. Another approach that has been used involves the electrochemical deposition of manganese-oxide NPs directly onto electrode materials, or onto materials that are later immobilized at electrode surfaces. For example, Roche *et al.* used a chemical deposition method in which $MnSO_4$ was reacted with $KMnO_4$ (both in solution) in the presence of a very high surface area (about 1000 m^2/g) carbon-support material to deposit MnO_x NPs on the C support [63]. The material is designated as MnO_x/C to indicate uncertainty regarding its exact composition and chemical state. TEM was used to characterize the C-supported NP material, revealing an average diameter for the MnO_x NPs of 3.4–4.2 nm. In addition, Ni-doped and Mg-doped MnO_x also were prepared using the same approach, except with the addition of $Ni(NO_3)_2{\cdot}6H_2O$ or $Mg(NO_3)_2{\cdot}6H_2O$ to the $MnSO_4$ solution prior to addition of the $KMnO_4$. These materials are designated as Me-MnO_x/C. The doped Me-MnO_x NPs were slightly larger, with diameters ranging from 4.3–6 nm. These materials were then immobilized on a glassy-carbon electrode from a solution containing the polymeric, film-forming binder poly(tetrafluoroethylene) (PTFE). The electrochemical activity of the MnO_x/C and Me-MnO_x/C NPs toward dioxygen reduction was examined in aqueous base. They observed a four-electron reduction with electrocatalytic activity rivaling that of the benchmark ETEK/Pt NP catalyst for the Ni-doped material. They suggested that the combination of very high surface areas of both the C support and the MnO_x electrocatalyst provides a situation in which the catalytic intermediates are trapped at or near the NP surface, so the four-electron reduction of O_2 can occur. This is one of only a few studies that used a detailed mechanistic assessment to understand the very high catalytic activity available from nanoscale metal-oxide materials.

Ohsaka's group has extensively examined the electrochemical behavior of both chemically and electrochemically deposited MnO_2, both as discrete NPs and as nanostructured interfacial materials [61, 64–81]. We focus here on two of their studies that exemplify the electrocatalytic nature of these nanoscale materials. In the first effort, El-Deab and Ohsaka explored the electrocatalytic behavior of MnOOH nanorods that had been electrodeposited onto Pt electrodes by oxidation of Mn(II) in an aqueous solution of manganese acetate [76]. The nanorods had average diameters of 20 nm and aspect ratios of 45 (i.e. average lengths of 900 nm) and covered nearly the entire surface of the underlying Pt electrode substrate. The electrocatalytic behavior of these derivatized surfaces was then examined in O_2-saturated 0.1 M KOH. They observed a significant shift of the reduction potential for O_2 on the modified surface compared to the control bare Pt surface, demonstrating enhanced catalytic activity for the modified surface. X-ray photoelectron spectroscopy was used to demonstrate that the origin of the enhanced activity was not due to a change in the electronic structure of the underlying Pt substrate. Rather, the enhanced activity was speculated to be due to a change in the orientation for the adsorbed O_2 on the MnO_2/Pt surface compared to that on a bare Pt surface. They argued that the different orientation caused a change in the pre-exponential factor for the rate constant governing the reduction process, leading to an enhanced rate. This is one of the few examples in which the nanoscale composite character of a metal-oxide electrocatalyst has been invoked to explain a significant change in its electrocatalytic activity.

El-Deab and Ohsaka also explored the unique behavior of a binary MnO_2 nanorod/Au NP electrocatalyst toward the electroreduction of O_2 in aqueous base [67]. In that study, they used electrochemical methods to deposit either MnO_2 nanorods (via Mn (II) oxidation), Au NPs and nanoclusters (via $AuCl_4^-$ reduction) or both onto glassy-carbon electrodes. For the mixed-deposit case, the sequence of the deposition was explored, that is, MnO_2 was deposited first in one case, while Au was deposited first in the other. They also examined the dependence of the electrocatalytic activity on the loadings of the two components. The MnO_2 deposition conditions gave spiked clusters of MnO_2 nanorods with diameters in the 100 nm range. The Au-deposition conditions gave Au NPs with average diameters of about 50 nm, as well as small aggregates of these NPs. The results showed that the catalyst prepared by first depositing MnO_2 nanorods, followed by deposition of Au NPs gave the best performance of all the catalysts explored. This catalyst showed a four-electron reduction of O_2 with a rate comparable to that observed at a benchmark bare Pt catalyst. The apparent four-electron reduction of O_2 was attributed to a mechanism in which O_2 is first reduced to hydrogen peroxide via a two-electron pathway at the Au NPs. Then, a rapid disproportionation of hydrogen peroxide occurs at the MnO_2 nanomaterial. The combined effect of these two processes provides an overall apparent four-electron reduction at attractively positive potentials.

Manganese-oxide nanoparticles also have been examined with regard to their potential use in ultracapacitor applications. For example, Hu and coworkers used hydrothermal synthesis to prepare nanoscale Mn_3O_4 and MnOOH from aqueous solutions containing 20 mM $Mn(CH_3COO)_2{\cdot}4H_2O$ via chemical oxidation [31]. In one case, dissolved O_2 was used as the oxidant. The limited availability of O_2 in the solution and the consequent simultaneous presence of Mn(II) and Mn(III) gave Mn_3O_4 (hausmanite) nanocrystals with either a cubic or rhombohedral structure. TEM images showed these nanocrystals to have average diameters of about 100 nm. In contrast, when $S_2O_8^{2-}$ was used as the chemical oxidant, the complete oxidation of Mn(II) to Mn(III) led to the production of MnOOH nanorods, with diameters of about 100 nm and lengths of several micrometers. Modified electrodes were prepared by drop-coating solutions of either Mn_3O_4 or MnOOH onto graphite electrodes,

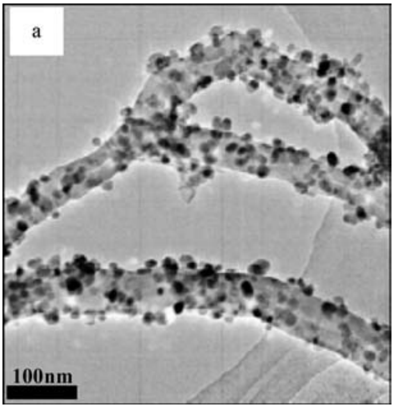

Figure 4.6 TEM showing Mn_3O_4 NPs on MWNT. From reference [82], with permission.

evaporating the solvent, and then coating a film of PTFE on top of the oxide coatings. This latter procedure was used to stabilize the films toward loss from the surface. To evaluate their capacitance, modified electrodes with the two materials were then cycled between 0.0 and 1.0 V at 25 mV s^{-1} for 1500 cycles in 1.0 M Na_2SO_4. The MnOOH material showed quite poor capacitance. However, the capacitance of the Mn_3O_4 material increased with cycling, finally reaching a stable value of 170 F g^{-1}.

Liu and coworkers also examined ultracapacitor behavior for Mn_3O_4 [82]. They used an approach similar to that employed by Hu, oxidizing Mn(II) with O_2 in the presence of multiwalled carbon nanotubes (MWNT). This produced 4–10 nm diameter Mn_3O_4 NPs that were relatively uniformly distributed on the surfaces of the MWNTs, as shown in Figure 4.6. Glassy-carbon electrodes were modified with the Mn_3O_4/MWNT material by preparing a dispersion in DMF and drop-casting a film onto the surface. The capacitance behavior of these materials was examined by cycling between 0.0 and 0.7 V vs. Hg/Hg_2Cl_2 in 2 M KCl. Scan rate studies showed a capacitance as high as 420 F g^{-1} at a scan rate of 5 mV s^{-1}. Repeated cycling showed a fairly stable response up to 400 cycles. The relatively high capacitance of the Mn_3O_4 phase was attributed to a redox pseudocapacitance in which reduction of Mn centers in the material is accompanied by proton injection, and vice versa. The relatively poor electronic conductivity of the Mn_3O_4 was thought to be compensated for by its immobilization on MWNTs, suggesting that such nanocomposite materials may prove useful in this and other areas.

4.4.3
FeO_x

In one of the early studies of the electrochemistry of discrete electroactive NPs, Marken's group examined iron-oxide NPs. In their first exploration of this area they prepared α-Fe_2O_3 using an aqueous hydrolysis route [83]. This produced 4–5 nm diameter cationically charged NPs of α-Fe_2O_3 which contained about 2500 Fe centers per NP. Immobilization was achieved by direct adsorption onto cleaned ITO electrodes, which was shown to be a superior substrate compared to Au, glassy C and Pt, presumably because of the possibility of using electrostatic interactions as part of the immobilization process. Cyclic voltammetry was used to examine the redox behavior of these NPs in aqueous solutions. Examination as a function of pH revealed that at lower pH values the reduction of these NPs led to reductive dissolution of the NPs via production of soluble Fe(II). Similarly, reduction of the α-Fe_2O_3 NPs in the presence of EDTA in solution also led to rapid reductive dissolution. At higher pH values, the electrochemical response of the material was more stable toward repeated cycling, but was complicated by the possibility of multiple iron-oxide phases being present. They also used ultrasound to convectively deliver the iron-oxide NPs to electrodes in order to detect their voltammetry directly. This was done to circumvent the rather low diffusion coefficient of $8.5 \times 10^{-7}\,\mathrm{cm^2\,s^{-1}}$ for the NPs [83]. These experiments were somewhat complicated by the adsorption of the NPs on the electrode. However, conditions were obtained in which adsorption did not unduly obscure the voltammetry of the NPs. While they were able to observe convectively enhanced voltammetry of dissolved NPs using this approach, they found that the effective n-value for reduction of the NPs was about 1, meaning that the NPs were reduced by just one electron each in spite of the presence of about 2500 Fe centers per NP. There are several possible explanations for this, including a poor electron-transfer rate between the NPs and the surface, an inability for charge compensating ion insertion into the bulk of the NPs and some form of aggregation in solution that precluded the effective delivery of discrete NPs to the surface.

In an interesting extension of the work described above, the same group also compared the electrochemistry of 8 nm diameter hydrous ferric oxide (HFO) NPs with that of the iron-oxide cores in the iron-storage protein ferritin [84]. The voltammetry was examined in aqueous phosphate buffer, which complicated the situation by allowing the formation of $FePO_4$. Thus, during the first reduction for both types of NPs (i.e. the HFO NPs and the ferritin iron-oxide cores) the first process was reductive dissolution of the iron-oxide phase. Scan reversal then led to Fe(II) oxidation to Fe(III), giving $FePO_4$ which formed by reaction of the electrochemically produced Fe(III) with HPO_4^{2-} in the phosphate buffer. The behavior of the HFO NPs and the iron-oxide cores in ferritin was nearly identical, suggesting that the ferritin iron-oxide cores were able to achieve facile electrochemical communication with the electrode even in the presence of the protein coat.

4.4.4
NiO_x and CoO_x

Sonochemical methods have been used by the Córdoba de Torresi group to prepare $Ni(OH)_2$, $Co(OH)_2$ and mixed Ni/Co hydroxide NPs [33, 34]. For the sonochemical synthesis, the appropriate metal nitrate was mixed with ammonium hydroxide solutions and then sonochemically irradiated for various times. This produced about 5-nm diameter metal-hydroxide NPs that were then immobilized at ITO surfaces using a LbL approach with poly(allylamine) hydrochloride (PAH). In one study, the electrochromic behavior of the LbL deposits was compared with that of bulk deposits of the same material [34]. The results showed that for both $Ni(OH)_2$ and $Co(OH)_2$, the nanoparticulate material gave superior electrochromic efficiency (i.e. absorbance change per unit charge) compared to bulk electrodeposits of the same materials. They also showed slightly faster coloration and decoloration compared to the bulk materials. The feasibility of a simple LbL approach to a two-color electrochromic structure was also demonstrated. In a second study, 5-nm diameter NPs of a novel $Ni_{0.8}Co_{0.2}(OH)_2$ mixed material were prepared using a similar sonochemical method [33]. These were immobilized using a LbL protocol with PDDA as the cationic, polymeric binder. The mixed material was shown to be a better catalyst for urea oxidation than either of the parent, single-metal materials. It was also shown to be about ten times more active than the bulk electrodeposited material, presumably due to the much larger surface area.

Hydrothermal methods also were used to prepare irregularly shaped, discrete nanoscale materials of α-$Ni(OH)_2$ using urea as the hydrolytic agent [48]. These materials were incorporated into paraffin impregnated graphite (PIGE) electrodes and examined electrochemically for their charge-storage characteristics. While they did exhibit a Ni(II)/Ni(III) redox couple, the thermodynamically unstable α phase was observed to reorganize to the more stable β phase during repeated cycling.

4.5
Other Metal Oxides and Metal Sulfides

Bard and coworkers reported an interesting study of the electrochemical behavior of core–shell Ag/Ag_2O NPs [47]. They used aerobic heat treatments to oxidize commercially available Ag NPs with diameters under 100 nm. If conditions were properly controlled, they showed that surface oxidation of the Ag NPs could be achieved, producing core–shell Ag/Ag_2O NPs. These were then incorporated into film-casting gels that also contained graphite (for enhanced conduction) and Nafion (for film stability). Using these gels, the core–shell NPs were immobilized at gold electrodes for examination using cyclic voltammetric methods. They showed that reduction of the Ag_2O could be used to assay the amount of silver oxide in the shell part of the core–shell NP. Combined with the charge for subsequently oxidizing all of the silver (i.e. both the original core component and the silver metal produced reducing the Ag_2O shell), this provided a method to quantitatively measure the amounts of both the core and shell components.

Yuan and coworkers reported the incorporation of 1–3-nm diameter CuO NPs directly into cast Nafion films [85]. In their experiments the Nafion films were cast onto Pt electrodes and the CuO NPs incorporated by simple soaking, suggesting that the CuO NPs were cationic under the conditions of preparation. Voltammetric investigations showed a clear Cu(II)/Cu(I) redox process at about −0.3 V vs. SCE. A second process at −0.8 V was assigned to the Cu(I)/Cu redox process. However, the appropriate controls were not shown, and it is not clear whether this second process might be attributed to hydrogen adsorption on the underlying Pt electrode. The Cu(II)/Cu(I) redox couple was shown to be a good electrocatalyst for hydrogen-peroxide reduction.

McKenzie and Marken examined the electrochemical behavior of hydrous RuO_x NPs immobilized onto boron-doped diamond electrodes [86]. Both small (1–2 nm diameter) and large (8–14 nm diameter) NPs were prepared. Just as for the TiO_2 NPs discussed in an earlier section, these hydrous RuO_x NPs adsorb readily and irreversibly onto BDD electrodes, giving roughly monolayer coverage. Cyclic voltammetric investigation revealed a prominent redox process at $+0.82$ V vs. SCE at pH 7 that was attributed to the Ru(III)/Ru(IV) redox process. The Nernstian pH dependence of the redox wave was consistent with a $1e^-/1H^+$ redox process, suggesting proton insertion into the NP during reduction and vice versa. Both types of NPs were shown to be good electrocatalysts for the hydrogen-evolution reaction, with the smaller NPs being more active.

Fujishima and coworkers reported a method to electrochemically deposit IrO_x NPs at BDD electrodes [87]. The deposition process was based on preparation of a solution containing hydrolysis products of $IrCl_6^{3-}$ and oxalate, followed by anodic electrodeposition of IrO_x from this solution onto an anodically pretreated BDD electrode. They showed that for conditions under which only limited deposition was allowed to occur it was possible to deposit about 30 nm diameter IrO_x NPs that were relatively homogeneously distributed across the surface. They examined these deposits for hydrogen-peroxide oxidation and observed significant oxidative current at potentials as low as $+0.35$ V at pH 7.

In an effort directed at electrochromic applications, Dillon and coworkers developed a novel electrophoretic deposition method to immobilize nanoparticles of WO_3 at fluorine-doped SnO_2 (FTO) electrodes [49, 50]. The NPs were prepared using a chemical vapor deposition process that had been previously described, giving nanorods with lengths and widths in the 10–100 nm range. Electrophoretic deposition was achieved by applying a large voltage difference (300 V) between the FTO working electrode and the counter electrode. Electrochemical studies of the WO_3 NPs revealed that they had far superior charge capacities per unit mass than either amorphous or crystalline materials. Further, they were much more stable toward repetitive cycling. The electrochromic efficiencies were better than those of the amorphous and crystalline comparator materials when the WO_3 was prepared under oxygen-deficient conditions.

Rao, Jayalakshmi and coworkers have prepared NPs of SnO, SnS and ZnS in order to study their capacitance behavior [88–90]. The metal oxide and metal sulfide NPs were prepared using hydrothermal methods. After immobilization in PIGE electrodes, their electrochemical properties were examined. Capacitance values in the 4–15 $F\,g^{-1}$ were reported for SnS. Comparable values were reported for ZnS.

4.6
Prussian Blue and Its Derivatives

Prussian Blue (PB) has been known for many decades, originally because of its wide use as a pigment and later because of its interesting redox properties [91]. PB is comprised of Fe(II) and Fe(III) centers, CN^- ligands and K^+ counterions. It has a

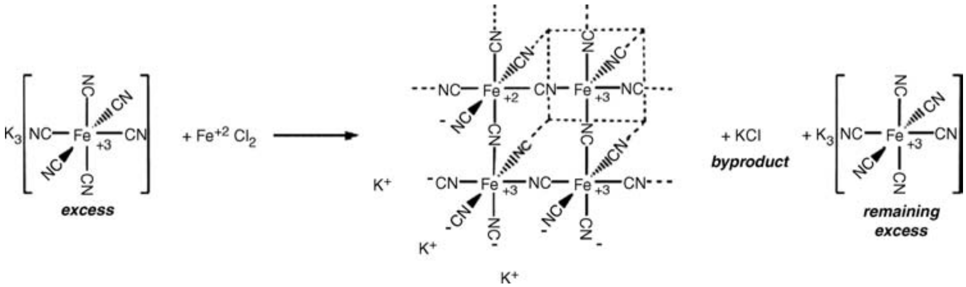

Figure 4.7 Synthetic scheme for synthesis of colloidally stabilized PB NPs. From reference [92] with permission.

face-centered cubic structure in which the transition metals are bound at opposite ends of CN^- bridging ligands and the K^+ ions occupy the cubic voids [91]. When prepared as a nanoparticulate colloidal material, the ability of the K^+ counterions to dissociate from the NPs can lead to a net negative charge on the NP, as shown in Figure 4.7 [92]. This stabilizes the PB NPs against aggregation. The parent material, PB, is formed by reaction of $K_3Fe(CN)_6$ with a soluble source of Fe(II) (often $FeCl_2$) to give $KFe^{III}[Fe^{II}(CN)_6]$, an insoluble 3-dimensional solid. Other derivatives also can be formed by reaction of ferricyanide or ferrocyanide with different metal cations. In spite of a deceptively simple structure and composition, PB and its derivatives exhibit a complex set of properties. This is because the material can exist in multiple redox states and because the electron-transfer processes to reach some of these redox states require simultaneous transport of charge-compensating counterions into or out of the cubic lattice. For example, reduction of Prussian Blue to give Prussian White (PW) typically occurs between 0.0 and 0.2 V vs. SCE in aqueous solutions containing K^+ counterions [91, 93]. This reduction is accompanied by the insertion of charge-compensating cations into the cubic lattice, as shown in the following equation.

$$\underset{\text{Prussian Blue}}{KFe^{III}[Fe^{II}(CN)_6] + 1\,e^- + 1\,K^+} \quad \leftrightarrow \quad \underset{\text{Prussian White}}{K_2Fe^{II}[Fe^{II}(CN)_6]} \tag{4.1}$$

PB also can be oxidized to give first a green material, Berlin Green (BG), in the partially oxidized state, and then finally a yellow material, Prussian Yellow (PY), in the fully oxidized state. This oxidation typically occurs between 0.8 and 1.0 V vs. SCE. The complete oxidation of Prussian Blue to Prussian Yellow is shown in the following equation.

$$\underset{\text{Prussian Blue}}{KFe^{III}[Fe^{II}(CN)_6]} \quad \leftrightarrow \quad \underset{\text{Prussian Yellow}}{Fe^{III}[Fe^{III}(CN)_6] + 1\,e^- + 1\,K^+} \tag{4.2}$$

In aqueous solutions containing K^+ counterions this oxidation typically occurs near 0.8 V vs. SCE. Other counterions besides K^+ may be incorporated into PB and its derivatives, changing the energetics of the various redox transitions. The ability to reversibly oxidize or reduce all of a given type of metal center in PB and its derivatives endows PB with behavior similar to that described above for many other electroactive NPs.

PB and its derivatives are of interest for a variety of reasons, the most important of which is its electrochromism [93]. In addition, it is an electrocatalyst for several different types of substrates, notably hydrogen peroxide, as will be seen below. Synthesis of nanoparticles of Prussian Blue is relatively straightforward. It relies on many of the principles of colloid chemistry, and produces ionically stabilized colloidal solutions (Figure 4.7). As a consequence, the electrochemical behavior of PB NPs has been examined by several groups. In this section, we discuss the behavior of PB NPs immobilized at electrodes.

Chen and coworkers were the first to describe the electrochemical behavior of PB NPs [41]. They prepared solutions of PB NPs by reaction of Fe(III) with $Fe(CN)_6{}^{3-}$ in the presence of H_2O_2, giving 30–50-nm diameter NPs. These were then immobilized at cysteine-modified Au electrodes with pendant amine groups by prolonged (10 h) exposure of the modified electrode to a solution of the NPs. This produced a monolayer of immobilized NPs that was subsequently examined using cyclic voltammetry. Interestingly, they observed two redox processes near 0.25 V vs. SCE rather than the single process typically observed. One of the peaks exhibited a dependence of current on scan rate (linear plot of I vs. $\nu^{1/2}$) consistent with diffusion, while the other had behavior consistent with a surface process (linear plot of I vs. ν^1). Thus, they attributed the latter to a redox process of Fe sites at the surface of the PB NPs and the former to Fe sites within the interior of the NPs. However, this appears unlikely since the ratio of the charges they observed is far larger than the ratio of surface to bulk Fe sites in a 30–50-nm diameter NP. Nevertheless, they were the first to propose different behavior for surface and bulk redox sites in PB NPs.

Hammond's group has investigated several aspects of the behavior of PB NPs, including electrochromism [92], multicolor electrochromism in LbL nanocomposite films comprised of PB NPs and polyaniline [94], and controlled-release processes from LbL films containing PB NPs [95]. They described a simple synthetic route to negatively charged PB NPs in which a fivefold excess of $Fe(CN)_6{}^{3-}$ is reacted with a soluble Fe(II) reagent (Figure 4.7). This gives deep blue, stable solutions of PB NPs with diameters ranging from 1–15 nm and an average diameter of 4–5 nm. These negatively charged PB NPs were then assembled into LbL films using PEI as the cationic polymeric binder. As seen in Figure 4.8, two redox processes are observed for these films, one at about 0.1 V and another at about 0.9 V. Starting from negative potentials, the first corresponds to a colorless (PW) to cyan (PB) transition. The second corresponds to a transition from cyan (PB) through green (BG, produced midway through the wave) to yellow (PY, produced past the wave). Because the Prussian Yellow state is neutral, the ionic stabilization of the LbL films was removed, thus inducing dissolution while in this redox state. The electrochromic behavior of the PB/PEI LbL films showed them to switch with speeds comparable to those for bulk PB films and to have electrochromic efficiencies that were substantially superior. This group also investigated multicolor electrochromic films comprised of LbL nanocomposites of cationic poly(aniline) and anionic PB NPs [94]. They showed that the PANI/PB nanocomposite undergoes an uncolored to green to blue transition over the potential range from −0.2 to 0.6 V vs. SCE. The film switching rates were very good, presumably due to the nanoscale PB materials used and the

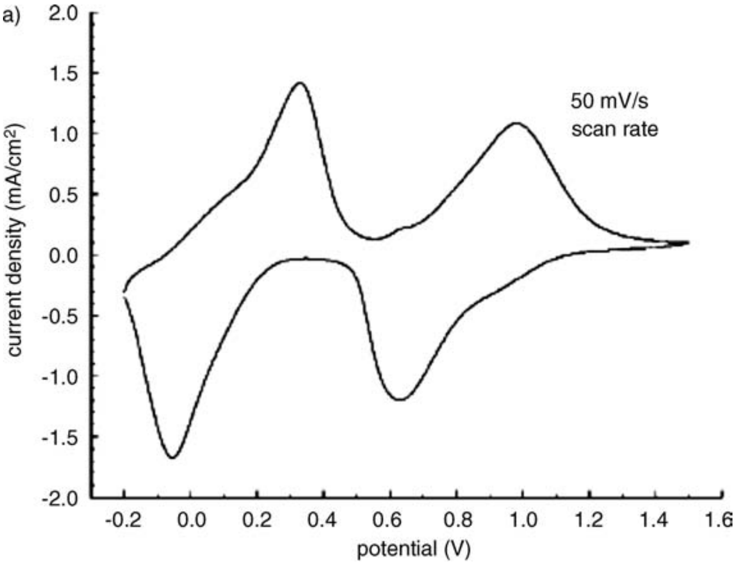

Figure 4.8 Cyclic voltammetry of a 50-layer film of PEI/PB. From reference [95] with permission.

excellent electronic and ionic conductivity of the cationic PANI binder. The oxidative dissolution behavior described above for PB/PEI LbL films formed the basis for more recent work by that group on the use of such films in controlled-release applications [95]. In that study they demonstrated multiple, controlled-release events for an anionic radiolabeled model compound, ^{14}C-dextran sulfate, from LbL films containing PB NPs by oxidizing the films to the PY (neutral) form. Thus, they demonstrated the feasibility of 'pharmacy-on-a-chip' applications based on electrochemically controlled film dissolution.

Córdoba de Torresi and coworkers reported a sonochemical synthesis of 10-nm diameter nanoparticles of copper hexacyanoferrate (CuPB), the copper Prussian Blue derivative, for the purposes of examining their electrochromic behavior [96]. The CuPB NPs were prepared by sonicating a solution containing $CuCl_2$ and $K_3Fe(CN)_6$. These CuPB NPs were incorporated into LbL films on ITO electrodes using poly (allylamine) hydrochloride (PAH) as the cationic polymeric binder, giving a brownish film. Cyclic voltammetric examination revealed a single redox process at $+0.8$ V that produced an orange film according to the redox process shown in Equation 4.3. Note that $2e^-$ and $2K^+$ are shown to balance the redox process according to the commonly used formula unit for CuPB, as shown [97].

$$K_2Cu_3^{II}[Fe^{II}(CN)_6]_2 \leftrightarrow Cu_3^{II}[Fe^{III}(CN)_6] + 2e^- + 2K^+ \tag{4.3}$$

UV-visible studies were done that showed that the switching times and stability toward multiple cycling was excellent for this material. In the context of the reports by Hammond discussed above, it is interesting that the oxidation process described in Equation 4.3 did not lead to film dissolution, since the net charge of the formula unit for CuPB in its oxidized form should (at least formally) be zero. This suggests that the

CuPB NPs produced by the sonochemical process may have an excess of negative charge above that available by K^+ dissociation.

Several groups have used PB NPs for electrocatalytic applications. Xian *et al.* synthesized PB NPs in the presence of poly(vinylpyrrolidone) (PVP), thus producing PVP-encapsulated PB NPs [98]. They showed that manipulation of the ratios of the reagents used in the synthesis allowed for production of NPs with diameters between 8 and 18 nm. Glassy-carbon electrodes were modified with these NPs by drop-casting the PVP/PB NP solution onto GC followed by application of a Nafion film to stabilize the film. They observed multiple redox processes for these PB NPs over a potential range in which one normally observes only the Prussian White/Prussian Blue process, but did not attempt to assign the multiple processes. The PB NPs were shown to serve as electrocatalysts for the reduction of the heme groups in hemoglobin.

Zhao *et al.* prepared magnetite (Fe_3O_4) nanoparticles modified with electroactive Prussian Blue [44]. These modified NPs were drop-cast onto glassy-carbon electrodes. They observed the redox processes commonly observed for PB (similar to that seen in Figure 4.8), and also demonstrated that the Prussian White material produced by PB reduction at 0.2 V served as an electrocatalyst for H_2O_2 reduction. They also prepared LbL films in which PB NPs and glucose oxidase were alternated between PDDA layers [99]. These were demonstrated to act as electrocatalysts for H_2O_2 reduction. Based on the ability to sense the product of the enzymatic reaction, these structures were shown to act as glucose sensors.

Phani and coworkers developed a novel method to prepare core–shell Au/PB nanoparticles on glassy-carbon electrodes [100]. In their approach, gold NPs were electrodeposited onto glassy-carbon electrodes. These electrodes were then cycled in solutions containing $Fe(CN)_6{}^{3-}$ under conditions in which the Au NPs would undergo gold-oxide formation and stripping. When done in an unbuffered aqueous solution, the decrease in interfacial pH caused by gold-oxide formation was proposed to cause decomposition of $Fe(CN)_6{}^{3-}$, ultimately leading to deposition of PB on the previously formed Au NPs. These novel nanocomposites were demonstrated to serve as effective electrocatalysts for H_2O_2 reduction.

In a similar study, Xia and coworkers examined the electrocatalytic behavior of core–shell Au/PB NPs toward H_2O_2 reduction [101]. These workers prepared 12-nm diameter Au NPs using a well-known route in which $AuCl_4{}^-$ is reduced by citrate. They then generated PB in a solution of these Au NPs, producing 30–60 nm diameter core–shell Au/PB NPs, designated as PB@Au. They modified ITO electrodes using this material in two ways. In one approach, they formed LbL films of the type $ITO/(PAH/PB@Au)_n$ using a standard LbL protocol. In a second approach, they sonicated solutions containing both PAH and PB@Au and then drop-cast films from this solution directly onto ITO electrodes. Both films showed the expected PB/PW redox couple between 0.0 and 0.2 V vs. SCE. Examination of the electrocatalytic activity of these films toward H_2O_2 reduction showed that the PW form of the LbL film was effective as an electrocatalyst for this reaction.

Li and coworkers used LbL techniques to immobilize 10–15-nm diameter PB NPs at ITO electrodes where positively charged polyoxocations of Al_{13} Keggin ions were used as the cationic binder for the LbL structure [102]. These novel films were shown to exhibit normal, stable redox transitions for PB, as exhibited by two waves at 0.2 V and 0.9 V vs. SCE for the PW/PB and PB/PY redox processes, respectively. The PW form of the LbL films was shown to be an effective electrocatalyst for H_2O_2 reduction.

Niu and coworkers prepared LbL films comprised of PB NPs and a novel polyelectrolyte-functionalized ionic liquid (PFIL) [103]. The PFIL was based on a PEI backbone with a covalently attached imidazolium group. They compared LbL films comprised of ITO/$(PFIL/PB)_{10}$ and ITO/$(PDDA/PB)_{10}$ with respect to the charge for the PB redox processes and the ability of the PB NPs in the films to electrocatalyze the reduction of H_2O_2. Both the charge for the PB reduction in the LbL films and the electrocatalytic currents for H_2O_2 reduction were larger for the ITO/$(PFIL/PB)_{10}$ film than for the ITO/$(PDDA/PB)_{10}$. They speculated that this may be due to an increased quantity of PB in the PFIL-based film.

Mao and coworkers reported a novel synthesis of 20-nm diameter PB NPs in a 1-n-butyl-3-methylimidazolium hexafluorophosphate ([Bmim][PF6]) ionic liquid [45]. The PB NPs were synthesized using a sonochemical approach from $FeCl_2$ and $K_3Fe(CN)_6$ precursors. The resulting PB NP solution in [Bmim][PF_6] was mixed with 5,10,15,20-tetrakis (4-methoxyphenyl) 21H, 23H porphine cobalt(II) (CoP) and multiwalled carbon nanotubes. This produced a black gel that was subsequently coated onto glassy-carbon electrodes. These coated electrodes were then examined as to their electrocatalytic reactivity toward O_2 reduction. The strategy behind the work was to use the CoP component to electrocatalyze the two-electron reduction of O_2 to H_2O_2, and then to use the PB NP component to reduce the resulting H_2O_2 to water. Rotating ring disk experiments demonstrated that this novel composite catalyst did, indeed, catalyze the overall four-electron reduction of O_2. However, the potential at which the process occurred was not as attractive as it would be for a direct four-electron reduction, as expected for a sequential process.

Li and coworkers reported a synthetic approach to PB NPs in which $Fe(CN)_6{}^{3-}$ was first electrostatically bound to chitosan (a natural, polycationic glucosamine polymer) in solution, followed by addition of Fe(II) to the vigorously stirred chitosan-$Fe(CN)_6{}^{3-}$ solution [46]. This produced chitosan-capped PB NPs that were very stable toward aggregation. They showed that the diameter of the PB NPs could be controlled through the ratio of chitosan to the iron-containing reagents in the synthetic mixture. As expected, higher chitosan concentrations produced smaller NPs, with the range of diameters being 5–20 nm. Thin films of the chitosan-capped PB NPs were drop-cast onto glassy-carbon electrodes for electrochemical examination. Two redox waves were observed at 0.2 V and 0.9 V vs. SCE for the PW/PB and PB/PY redox processes, respectively. These films were shown to be modestly active toward electrocatalysis of H_2O_2 reduction.

4.7
Concluding Remarks

The work described above constitutes the beginning of a new area in which the faradaic electrochemistry of discrete, electroactive nanoparticles is explored, both from a fundamental standpoint and for various types of applications. Overall, the types of phenomena that distinguish the behavior of NPs from their bulk-material counterparts are (1) the possibility of observing a significant fraction of the redox process for a given NP to originate from interfacial redox sites (which may have intrinsically faster electron transfer and ionic compensation processes), (2) the possibility of shorter times required for charge-compensating ions to access all of the electroactive sites in the NP, (3) the significantly enhanced surface areas of NPs, which allow for more entry points for these same ions, as well as providing more active sites for cases in which surface structures on the NPs are involved in electrocatalytic processes. While the phenomenological observations of faster redox processes for electroactive NPs compared to bulk materials and higher electrocatalytic activity described above can certainly be explained on the basis of these types of phenomena, much work remains to characterize and more fully exploit these phenomena.

Acknowledgment

This effort was supported by the National Science Foundation under Grant No. 0313661.

References

1 Raimondi, F., Scherer, G.G., Koetz, R. and Wokaun, A. (2005) *Angewandte Chemie-International Edition*, **44**, 2190.

2 Wieckowski, A. (2003) *Electrochemistry (Tokyo, Japan)*, **71**, 206.

3 Daniel, M.C. and Astruc, D. (2004) *Chemical Reviews*, **104**, 293.

4 Riley, D.J. (2002) *Current Opinion in Colloid & Interface Science*, **7**, 186.

5 Murray, R.W. (2008) *Chemical Reviews*, **108**, 2688.

6 Bard, A.J., Ding, Z. and Myung, N. (2005) Structure and Bonding Springer (Berlin, Germany), *Semiconductor Nanocrystals and Silicate Nanoparticles*, vol. **118**, 1.

7 Chen, S.W. (2007) *Journal of Materials Chemistry*, **17**, 4115.

8 Guyot-Sionnest, P. (2008) *Microchimica Acta*, **160**, 309.

9 Pingarron, J.M., Yanez-Sedeno, P. and Gonzalez-Cortes, A. (2008) *Electrochimica Acta*, **53**, 5848.

10 Grieshaber, D., Mackenzie, R., Voros, J. and Reimhult, E. (2008) *Sensors*, **8**, 1400.

11 Holland, G.P., Sharma, R., Agola, J.O., Amin, S., Solomon, V.C., Singh, P., Buttry, D.A. and Yarger, J.L. (2007) *Chemistry of Materials*, **19**, 2519.

12 Trindade, T., O'brien, P. and Pickett, N.L. (2001) *Chemistry of Materials*, **13**, 3843.

13 Yin, Y. and Alivisatos, A.P. (2005) *Nature (London)*, **437**, 664.

14 Brock, S.L., Sanabria, M., Suib, S.L., Urban, V., Thiyagarajan, P. and Potter, D.I. (1999) *The Journal of Physical Chemistry B*, **103**, 7416.

15 He, Y.T., Wan, J.M. and Tokunaga, T. (2008) *Journal of Nanoparticle Research*, **10**, 321.

16 Long, J.W. and Rolison, D.R. (2007) *Accounts of Chemical Research*, **40**, 854.

17 Arico, A.S., Bruce, P., Scrosati, B., Tarascon, J.M. and Van Schalkwijk, W. (2005) *Nature Materials*, **4**, 366.

18 Benedetti, T.M., Bazito, F.F.C., Ponzio, E.A. and Torresi, R.M. (2008) *Langmuir*, **24**, 3602.

19 Ung, T., Giersig, M., Dunstan, D. and Mulvaney, P. (1997) *Langmuir*, **13**, 1773.

20 Bazito, F.F.C. and Torresi, R.M. (2006) *Journal of the Brazilian Chemical Society*, **17**, 627.

21 Matijevic, E. (1993) *Chemistry of Materials*, **5**, 412.

22 Kandori, K., Kuwae, T. and Ishikawa, T. (2006) *Journal of Colloid and Interface Science*, **300**, 225.

23 Penner, R.M. (2000) *Accounts of Chemical Research*, **33**, 78.

24 Zach, M.P., Inazu, K., Ng, K.H., Hemminger, J.C. and Penner, R.M. (2002) *Chemistry of Materials*, **14**, 3206.

25 Zach, M.P., Ng, K.H. and Penner, R.M. (2000) *Science*, **290**, 2120.

26 Li, Q.G., Olson, J.B. and Penner, R.M. (2004) *Chemistry of Materials*, **16**, 3402.

27 Sides, C.R., Li, N.C., Patrissi, C.J., Scrosati, B. and Martin, C.R. (2002) *MRS Bulletin*, **27**, 604.

28 Mao, Y., Park, T.J., Zhang, F., Zhou, H. and Wong, S.S. (2007) *Small*, **3**, 1122.

29 Byrappa, K. and Adschiri, T. (2007) *Progress in Crystal Growth and Characterization of Materials*, **53**, 117.

30 Lu, Q.Y., Gao, F. and Komarneni, S. (2004) *Journal of Materials Research*, **19**, 1649.

31 Hu, C.C., Wu, Y.T. and Chang, K.H. (2008) *Chemistry of Materials*, **20**, 2890.

32 Latham, A.H. and Williams, M.E. (2008) *Accounts of Chemical Research*, **41**, 411.

33 Vidotti, M., Silva, M.R., Salvador, R.P., Cordoba De Torresi, S.I. and Dall'antonia, L.H. (2008) *Electrochimica Acta*, **53**, 4030.

34 Vidotti, M., Van Greco, C., Ponzio, E.A. and Cordoba De Torresi, S.I. (2006) *Electrochemistry Communications*, **8**, 554.

35 Suslick, K.S. and Price, G.J. (1999) *Annual Review of Materials Science*, **29**, 295.

36 Laurent, S., Forge, D., Port, M., Roch, A., Robic, C., Elst, L.V. and Muller, R.N. (2008) *Chemical Reviews*, **108**, 2064.

37 Wang, Z.L. (2003) *Advanced Materials*, **15**, 1497.

38 Marken, F., Bhambra, A.S., Kim, D.-H., Mortimer, R.J. and Stott, S.J. (2004) *Electrochemistry Communications*, **6**, 1153.

39 Latham, A.H., Wilson, M.J., Schiffer, P. and Williams, M.E. (2006) *Journal of the American Chemical Society*, **128**, 12632.

40 Stott, S.J., Mortimer, R.J., Dann, S.E., Oyama, M. and Marken, F. (2006) *Physical Chemistry Chemical Physics*, **8**, 5437.

41 Liu, S.-Q., Xu, J.-J. and Chen, H.-Y. (2002) *Electrochemistry Communications*, **4**, 421.

42 Cheng, K.-C., Chen, F.-R. and Kai, J.-J. (2007) *Electrochimica Acta*, **52**, 3330.

43 Hayden, B.E., Malevich, D.V. and Pletcher, D. (2001) *Electrochemistry Communications*, **3**, 390.

44 Zhao, G., Feng, J.-J., Zhang, Q.-L., Li, S.-P. and Chen, H.-Y. (2005) *Chemistry of Materials*, **17**, 3154.

45 Yu, P., Yan, J., Zhao, H., Su, L., Zhang, J. and Mao, L. (2008) *The Journal of Physical Chemistry C*, **112**, 2177.

46 Zhang, Q., Zhang, L. and Li, J. (2008) *Electrochimica Acta*, **53**, 3050.

47 Ghilane, J., Fan, F.-R.F., Bard, A.J. and Dunwoody, N. (2007) *Nano Letters*, **7**, 1406.

48 Jayalakshmi, M., Venugopal, N., Reddy, B.R. and Rao, M.M. (2005) *Journal of Power Sources*, **150**, 272.

49 Deshpande, R., Lee, S.H., Mahan, A.H., Parilla, P.A., Jones, K.M., Norman, A.G., To, B., Blackburn, J.L., Mitra, S. and Dillon, A.C. (2007) *Solid State Ionics*, **178**, 895.

50 Lee, S.-H., Deshpande, R., Parilla, P.A., Jones, K.M., To, B., Mahan, A.H. and Dillon, A.C. (2006) *Advanced Materials (Weinheim, Federal Republic of, Germany)*, **18**, 763.

51 Riveros, L.L., Tryk, D.A. and Cabrera, C.R. (2005) *Reviews on Advanced Materials Science*, **10**, 256.

52 Ariga, K., Hill, J.P. and Ji, Q.M. (2007) *Physical Chemistry Chemical Physics*, **9**, 2319.

53 Lvov, Y., Munge, B., Giraldo, O., Ichinose, I., Suib, S.L. and Rusling, J.F. (2000) *Langmuir*, **16**, 8850.

54 Decher, G. (1997) *Science*, **277**, 1232.

55 Quinn, J.F., Johnston, A.P.R., Such, G.K., Zelikin, A.N. and Caruso, F. (2007) *Chemical Society Reviews*, **36**, 707.

56 Hayden, B.E., Malevich, D.V. and Pletcher, D. (2001) *Electrochemistry Communications*, **3**, 395.

57 Milsom, E.V., Novak, J., Green, S.J., Zhang, X.H., Stott, S.J., Mortimer, R.J., Edler, K. and Marken, F. (2007) *Journal of Solid State Electrochemistry*, **11**, 1109.

58 Milsom, E.V., Novak, J., Oyama, M. and Marken, F. (2007) *Electrochemistry Communications*, **9**, 436.

59 Athouel, L., Moser, F., Dugas, R., Crosnier, O., Belanger, D. and Brousse, T. (2008) *The Journal of Physical Chemistry C*, **112**, 7270.

60 Whittingham, M.S. (2004) *Chemical Reviews*, **104**, 4271.

61 Mao, L.Q., Zhang, D., Sotomura, T., Nakatsu, K., Koshiba, N. and Ohsaka, T. (2003) *Electrochimica Acta*, **48**, 1015.

62 Wang, L.Z., Omomo, Y., Sakai, N., Fukuda, K., Nakai, I., Ebina, Y., Takada, K., Watanabe, M. and Sasaki, T. (2003) *Chemistry of Materials*, **15**, 2873.

63 Roche, I., Chainet, E., Chatenet, M. and Vondrak, J. (2007) *The Journal of Physical Chemistry C*, **111**, 1434.

64 Ohsaka, T., Mao, L.Q., Arihara, K. and Sotomura, T. (2004) *Electrochemistry Communications*, **6**, 273.

65 Zhang, D., Chi, D.H., Okajima, T. and Ohsaka, T. (2007) *Electrochimica Acta*, **52**, 5400.

66 Zhang, D., Sotomura, T. and Ohsaka, T. (2006) *Chemistry Letters*, **35**, 520.

67 El-Deab, M.S. and Ohsaka, T. (2007) *Electrochimica Acta*, **52**, 2166.

68 Ohsaka, T. and El-Deab, M.S. (2007) *Electrochemistry*, **75**, 858.

69 Mohammad, A.M., Awad, M.I., El-Deab, M.S., Okajima, T. and Ohsaka, T. (2008) *Electrochimica Acta*, **53**, 4351.

70 El-Deab, M.S. and Ohsaka, T. (2006) *Journal of The Electrochemical Society*, **153**, A1365.

71 Arihara, K., Mao, L.Q., Liddell, P.A., Marino-Ochoa, E., Moore, A.L., Imase, T., Zhang, D., Sotomura, T. and Ohsaka, T. (2004) *Journal of The Electrochemical Society*, **151**, A2047.

72 Mao, L.Q., Sotomura, T., Nakatsu, K., Koshiba, N., Zhang, D. and Ohsaka, T. (2002) *Journal of The Electrochemical Society*, **149**, A504.

73 Tian, Y., Mao, L.Q., Okajima, T. and Ohsaka, T. (2004) *Analytical Chemistry*, **76**, 4162.

74 El-Deab, M.S. and Ohsaka, T. (2008) *Journal of The Electrochemical Society*, **155**, D14.

75 El-Deab, M.S., Awad, M.I., Mohammad, A.M. and Ohsaka, T. (2007) *Electrochemistry Communications*, **9**, 2082.

76 El-Deab, M.S. and Ohsaka, T. (2006) *Angewandte Chemie-International Edition*, **45**, 5963.

77 El-Deab, M.S. and Ohsaka, T. (2006) *Angewandte Chemie-International Edition*, **45**, 5963.

78 El-Deab, M.S., Sotomura, T. and Ohsaka, T. (2005) *Journal of The Electrochemical Society*, **152**, C730.

79 El-Deab, M.S., Othman, S.H., Okajima, T. and Ohsaka, T. (2008) *Journal of Applied Electrochemistry*, **38**, 1445.

80 Mao, L.Q., Arihara, K., Sotomura, T. and Ohsaka, T. (2004) *Electrochimica Acta*, **49**, 2515.

81 Mao, L.Q., Arihara, K., Sotomura, T. and Ohsaka, T. (2003) *Chemical Communications*, **2818**.

82 An, G.M., Yu, P., Xiao, M.J., Liu, Z.M., Miao, Z.J., Ding, K.L. and Mao, L.Q. (2008) *Nanotechnology*, **19**, 275709.

83 Mckenzie, K.J. and Marken, F. (2001) *Pure and Applied Chemistry*, **73**, 1885.

84 Marken, F., Patel, D., Madden, C.E., Millward, R.C. and Fletcher, S. (2002) *New Journal of Chemistry*, **26**, 259.

85 Miao, X.M., Yuan, R., Chai, Y.Q., Shi, Y.T. and Yuan, Y.Y. (2006) *Journal of Electroanalytical Chemistry*, **612**, 157.

86 Mckenzie, K.J. and Marken, F. (2002) *Electrochem Solid-State Lett*, **5**, E47.

87 Terashima, C., Rao, T.N., Sarada, B.V., Spataru, N. and Fujishima, A. (2003) *Journal of Electroanalytical Chemistry*, **544**, 65.

88 Jayalakshmi, M., Mohan Rao, M. and Choudary, B.M. (2004) *Electrochemistry Communications*, **6**, 1119.

89 Jayalakshmi, M. and Rao, M.M. (2006) *Journal of Power Sources*, **157**, 624.

90 Rao, M.M., Jayalaksmi, M., Reddy, B.R., Madhavendra, S.S. and Kantam, M.L. (2005) *Chemistry Letters*, **34**, 712.

91 Itaya, K., Uchida, I. and Neff, V.D. (1986) *Accounts of Chemical Research*, **19**, 162.

92 Delongchamp, D.M. and Hammond, P.T. (2004) *Advanced Functional Materials*, **14**, 224.

93 Mortimer, R.J. (1997) *Chemical Society Reviews*, **26**, 147.

94 Delongchamp, D.M. and Hammond, P.T. (2004) *Chemistry of Materials*, **16**, 4799.

95 Wood, K.C., Zacharia, N.S., Schmidt, D.J., Wrightman, S.N., Andaya, B.J. and Hammond, P.T. (2008) *Proceedings of the National Academy of Sciences*, **105**, 2280.

96 Baioni, A.P., Vidotti, M., Fiorito, P.A., Ponzio, E.A. and Cordoba De Torresi, S.I. (2007) *Langmuir*, **23**, 6796.

97 Detacconi, N.R., Rajeshwar, K. and Lezna, R.O. (2003) *Chemistry of Materials*, **15**, 3046.

98 Xian, Y., Zhou, Y., Xian, Y., Zhou, L., Wang, H. and Jin, L. (2005) *Analytica Chimica Acta*, **546**, 139.

99 Zhao, W., Xu, J.-J., Shi, C.-G. and Chen, H.-Y. (2005) *Langmuir*, **21**, 9630.

100 Kumar, S.S., Joseph, J. and Phani, K.L. (2007) *Chemistry of Materials*, **19**, 4722.

101 Qiu, J.-D., Peng, H.-Z., Liang, R.-P., Li, J. and Xia, X.-H. (2007) *Langmuir*, **23**, 2133.

102 Wang, G., Zhou, J. and Li, J. (2007) *Biosensors & Bioelectronics*, **22**, 2921.

103 Li, F., Shan, C., Bu, X., Shen, Y., Yang, G. and Niu, L. (2008) *Journal of Electroanalytical Chemistry*, **616**, 1.

5

Structure, Electrochemistry and Applications of Self-Assembled Monolayers of Thiols

Manfred Buck

5.1

Introduction

With reports on 'a useful technique for preparing supported, oriented monolayers' by Nuzzo and Allara in 1983 [1] and the modification of a gold surface by a bis(bipyridyl) disulfide to study the redox chemistry of cytochrome C [2] organosulfur compounds were introduced as a new class of self-assembling monolayers (SAMs, see Figure 5.1) in addition to carboxylic acids and silanes already studied [3, 4]. Together with gold as a convenient, easy to handle substrate material [5], unprecedented opportunities opened up for tailoring interfacial properties such as wetting and adhesion, charge transfer, and chemical functionality.

The tremendous success of these systems derives from a combination of factors that are, firstly, the flexibility in molecular structures enabling control at the molecular level, secondly, the usually straightforward preparation from solution and, thirdly, the possibility to produce multicomponent SAMs consisting of either a random mixture of molecular species or well-defined patterns with dimensions ranging from the macroscopic to the nanoscopic length scale [5–8]. The different segments of a SAM-forming molecule (see Figure 5.1a), encompassing a head group for bonding to the substrate, a tail group providing chemical functionality and the so-called spacer as a thickness- and structure-defining linker between the other two segments, allow for a diversity of properties that results in a broad range of applications in sensors, microfluidics, tribology and, as the focus of this chapter, electrochemistry. However, their potential for technological applications is not the only reason why these SAMs have seen a mushrooming interest over the past 15 years. It is also their role as model systems afforded by their adjustable properties that allow systematic variations of parameters and, therefore, the unraveling of details of interfacial forces [9], solvent effects [10], protein resistance [11] or charge transfer [12, 13], to name a few examples.

With respect to the latter it was realized not long after the introduction of organosulfur SAMs that they represent ideal model systems to study interfacial

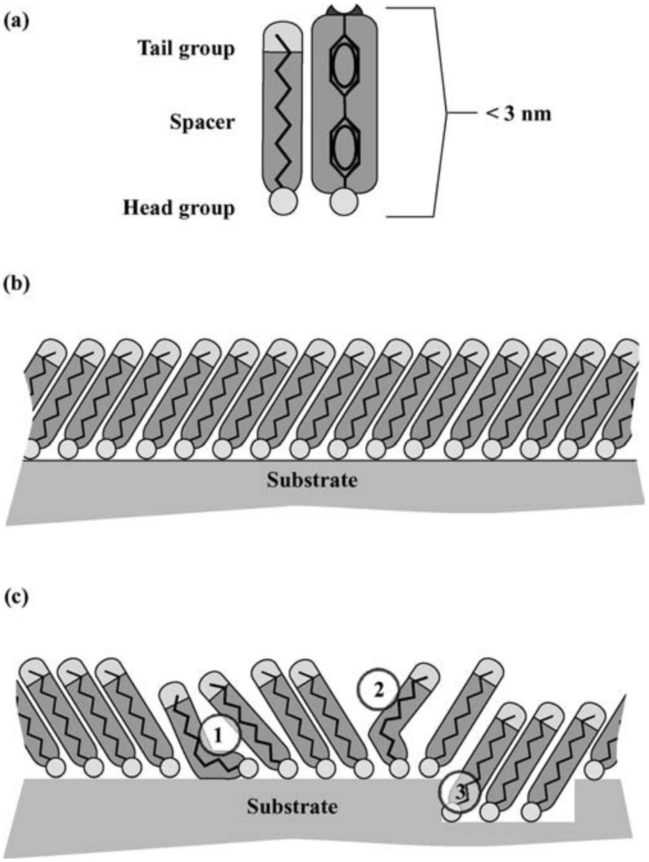

Figure 5.1 Illustration of (a) molecular architecture of a SAM-forming molecule, (b) an idealized SAM and (c) a more realistic description with molecular defects (1), domain boundaries (2) and substrate topography such as steps (3).

phenomena in electrochemistry, that is, heterogeneous charge transfer and double-layer phenomena [12, 14–18]. However, besides the fundamental studies there have always been major activities to harness SAMs for a variety of applications ranging from corrosion inhibition [19, 20] to electroanalysis [21, 22]. The technological aspect of SAMs is also underlying the selection of the topics discussed in the present review. Discussion of the material has, on the one hand, been motivated by the potential the author sees in the combination of SAMs and electrochemistry for the field of nanotechnology and, on the other hand, the knowledge about factors determining structure and properties of SAMs, required to achieve control on the ultrasmall length scale through a precise design. There will be a focus on two particular aspects of SAMs related to electrochemistry, namely the use of thiol-based SAMs as templates to control electrochemical metal deposition and potential-controlled modification of SAMs. While these two topics are complementary in the sense that one deals with

SAMs controlling electrochemistry, whereas the reverse holds for the other one, both topics are inseparably intertwined as exemplified by the underpotential deposition of metal on SAM-modified electrodes where patterned SAMs allow localization of metal UPD, which in turn affects the monolayer.

Given the tremendous development of SAMs over the past two decades it is clear that this chapter is able to cover only a fraction of the spectrum of topics related to the combination of SAMs and electrochemistry. For a comprehensive picture the reader is referred to a number of additional review articles, one of which is the excellent and extensive account of organized monolayers on electrodes by Finklea [23]. Besides this one, which comprehensively covers the literature up to the mid-1990s, other more focused reviews are available that address various developments over the past decade in areas of sensor development and electroanalytical applications [22, 24–28] and electrochemical metal deposition on SAM-modified electrodes [29, 30].

As far as SAM-controlled electrochemical metal deposition is concerned, substantial interest derives from microelectronics with its need to control the generation of interconnects and, thus, to understand the influence of organic layers on the metal nucleation and growth. However, the scope of this topic reaches well beyond that, as illustrated by the substantial range of potential applications where small-scaled metal structures are of crucial importance, for example in electrochemical [31] and optical [32] sensing, molecular electronics [33], for plasmonics [34], or as metamaterials [35].

The possibilities afforded by SAM-controlled electrochemical metal deposition were already demonstrated some time ago by Sondag-Huethorst *et al.* [36] who used patterned SAMs as templates to deposit metal structures with line widths below 100 nm. While this initial work illustrated the potential of SAM-controlled deposition on the nanometer scale further activities towards technological exploitation have been surprisingly moderate and mostly concerned with basic studies on metal deposition on uniform, alkane thiol-based SAMs [37–40] that have been extended in more recent years to aromatic thiols [41–43]. A major reason for the slow development of this area is that electrochemical metal deposition with, in principle, the advantage of better control via the electrochemical potential compared to nonelectrochemical methods such as electroless metal deposition or evaporation, is quite critical in conjunction with SAMs. Relying on their ability to act as barriers for charge transfer and particle diffusion, the minimization of defects in and control of the structural quality of SAMs are key to their performance and set the limits for their nanotechnological applications.

For advanced electrochemical applications of SAMs in this area, their design is, therefore, a key issue. While SAMs are often perceived to form easily well-defined structures, a closer look into the literature reveals that thiol SAMs, in fact, very often lack the structural quality anticipated. Contrasting their ease of preparation, organosulfur SAMs represent systems whose structure is determined by a complex interplay of interactions and if those are not properly taken into account, a SAM of limited structural quality and performance will result. To optimize SAMs for electrochemical applications and to exploit their properties for electrochemical nanotechnology it is, therefore, crucial to identify the factors controlling their structure. For this reason we start with an account of the structural aspects of SAMs.

5.2
Structural Aspects of Thiol-Like SAMs

The formation, structure and properties of thiol SAMs have been discussed in great detail in a number of extensive review articles [5, 8, 44]. Therefore, starting from some basic aspects only a few more recent developments are discussed in the following that have been selected with applications of SAMs for electrochemical metal deposition in mind. The discussion is focused on Au(1 1 1) since the vast majority of studies has been done on this surface. Therefore, knowledge about formation and structure of SAMs on Au(1 1 1) is much more detailed than on any other substrate, thus, allowing for an indepth discussion. Gold, in general, has been the substrate of choice for various reasons (e.g., cleanliness, easy availability as films) not only in electrochemical but also in the other countless studies of thiol-based SAMs [5]. Evaporated gold films are commonly used where the polycrystalline Au layer either exhibits a pronounced (1 1 1) texture (e.g., Au on Si, glass) or consists of epitaxially oriented (1 1 1) crystallites (Au/mica). Since the (1 1 1)-oriented surface is the most relevant one, it has also been the dominating one in studies on single crystals. Investigations of SAM on other low-index surfaces are scarce, in general, and electrochemical studies of SAMs on Au (1 1 0) [45, 46] or Au(1 0 0) [47–49], in particular. Similarly, other metal substrates such as Ag, Pd, Pt, Cu have also been studied comparatively little [5].

SAMs, in general, and thiol SAMs, in particular, are very often perceived as systems that easily form layers of high structural quality and this view is reflected in oversimplifying cartoons where a SAM is represented by a two-dimensional crystalline arrangement of molecules on a surface, similar to the one depicted in Figure 5.1b. For some systems one can get quite close to this ideal picture, as seen from Figure 5.2a, however, the more common case exemplified by Figure 5.2b is quite different. While

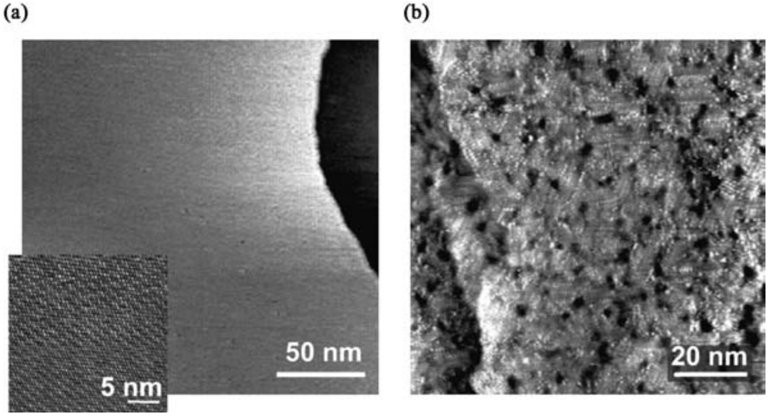

Figure 5.2 STM images of thiols SAM on Au/mica illustrating the range of structural qualities. (a) high-quality SAM of dodecane thiol prepared from a solution of dodecane thiocyanate [111] and a low-quality aromatic SAM of methylbiphenyl butane thiol (MBP4) (b) [90].

it will depend on the particular application to what extent deviations from structural perfection, as shown in Figure 5.1c, compromise the performance of a SAM, electrochemical applications are particularly sensitive to structural irregularities such as molecular defects, domain boundaries or even larger defects such as pin holes, as discussed in more detail in Section 5.4.3. For nanotechnological applications of SAMs the exact control of their structure becomes an increasingly pressing issue as a factor limiting the accessible length scale.

Aiming for an exact design, that is, the ability to precisely predict structure and properties of a SAM for a given molecule–substrate combination, the understanding of the determining factors has gradually improved over the years and some design principles have emerged. However, there is still a substantial empirical component involved due to the fact that a SAM is determined by a complex interplay of factors, some of which are illustrated in Figure 5.3. There is the chemisorption of the thiol that is the energetically biggest contribution to a SAM (160–200 kJ/mole for thiols on Au [5, 44]) and, thus, a major driving force for self-assembly by maximizing coverage. Another factor refers to intermolecular interactions that, depending on the type of molecule, comprise stabilizing noncovalent interactions such as van der Waals in alkane thiols [4], hydrogen bonds [50–52], π–π or π–H interactions [53–56]. However,

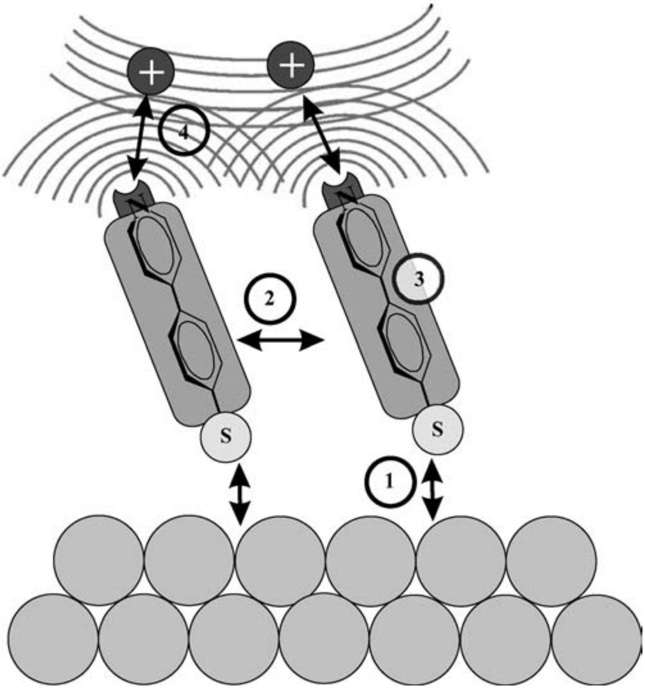

Figure 5.3 (a) Structure-determining factors in SAMs. Chemisorption of molecule onto substrate (1), intermolecular interactions (2) intramolecular conformational degrees of freedom (3) and interactions of SAM with the environment (4).

in the case of dipolar molecules a possible counteracting repulsive contribution can be introduced due to the alignment of molecules. The same holds if there are directional forces through preferential interactions between tail groups that are in conflict with the preferential packing of the spacer. While one is tempted to regard the structure of a SAM as static, the interaction of the monolayer with its environment can be an important factor and, thus, exert a significant influence onto the structure of a monolayer. This comprises conformational changes of the molecules caused by their interaction with a solvent [10, 57], and structural transitions mediated by interaction with ionic [58] or atomic species [59].

With regard to electrochemical applications the electric field across the SAM is another source of structural influence, as demonstrated by the potential-dependent switching behavior of a carboxy-terminated thiol SAM [60] and the structural transitions observed in SAMs upon variation of the potential [48, 58, 61, 62]. From this brief noncomprehensive account of SAM-determining factors, some of which are in conflict with each other (*vide infra*), it can be easily imagined that accurate prediction of a SAM structure can be a challenge. Several structures of similar energy might even exist, which means that an observed SAM structure does not necessarily reflect the thermodynamically most stable state but is determined by kinetic factors. This is illustrated by the archetypical system of simple alkane thiols where a variety of slightly different structures have been identified [63, 64] with one evolving only over a long period of time [65]. A pronounced case of polymorphism has been observed for MBPm SAMs ($CH_3(C_6H_4)_2$-$(CH_2)_mSH$) on Au(1 1 1) if $m =$ even [66–68]. The existence of different structures energetically very close is also consistent with the difference in structure seen between SAMs formed from mercaptopyridine and dithiodipyridine. Contrasting the general belief derived from studies in nonelectrochemical environment that thiols and disulfides yield identical SAMs, different structures were observed for the two pyridine compounds in H_2SO_4 and a potential range negative of a phase transition [69].

Among the factors crucial for a SAM structure, the thiol–substrate bond has been a subject of particular controversy over more than 15 years. It is worth discussing the SAM/substrate interface in some detail since it is important not only for understanding SAM structures in general but also for electrochemical metal deposition when metal is intercalated at the SAM/Au interface (Section 5.4.3). As indicated above we limit the discussion to SAMs on Au(1 1 1) as this is the interface where theoretical and experimental work is sufficiently detailed to allow for a discussion at the atomic level.

Based on initial models that assumed that thiols are chemisorbed as a thiolate species into threefold hollow sites of an essentially bulk-terminated Au(1 1 1) surface, others followed suggesting different adsorption sites [70–72], but recent experiments have provided indirect and direct evidence that the gold surface undergoes significant restructuring upon SAM formation. From experiments involving a number of techniques such as STM, photoelectron diffraction and X-ray diffraction [73–78] it was concluded that gold adatoms are involved. Studies on different systems and under different conditions, that is, alkane thiols of different chain length and different preparation conditions/temperatures, suggested gold adatoms either located in

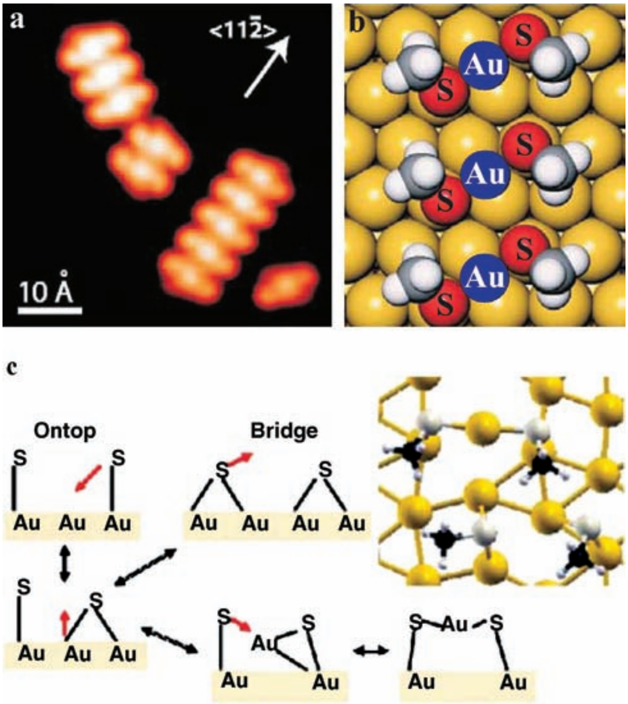

Figure 5.4 STM image and models of CH_3S on Au(1 1 1). (a) STM micrograph of stacks of CH_3S-Au-SCH_3 on Au(1 1 1) recorded at $T = 5$ K. Structure was obtained by dissociating adsorbed CH_3SSCH_3 at 300 K. (b) Model of proposed structure with gold adatoms labelled as Au. (c) Structures of CH_3S obtained by MD simulations. At 300 K, structure with molecules at on-top sites evolves into bridged species and a CH_3S–Au–SCH_3 configuration. Ball and stick model shows structure obtained after quenching a 600 K MD simulation. Reproduced with permission from Refs. [73] (a, b) and [75] (c).

between two thiolate species [73, 77] or, as part of a gold thiolate species, in between the molecule and the Au surface [79]. This confirmed theoretical work that predicted that a more open Au surface with vacancies is energetically more favorable for thiol bonding compared to a bulk-terminated one [80]. Low-temperature STM experiments on dimethyldisulfide (DMDS, H_3CSSCH_3) evidenced that Au adatoms are located between two methylthiolate moieties (Figures 5.4a and b) Interestingly, a combination of experiment and calculations on methylthiolate on gold found a coexistence of structures [75] with thiolate species either in a bridge position or present as a CH_3S-Au-SCH_3 complex with the sulfur atoms in on-top positions as illustrated in Figure 5.4c. Substantiating earlier conjectures [67, 81] the restructuring of the gold surface upon SAM formation might also explain some features of SAMs that have not been very satisfyingly explained in the past. One point is the formation of vacancy islands (VIs) that are monoatomic depressions in the gold substrate (seen as dark islands in Figure 5.2b) [82, 83]. While for preparation from solution, corrosion of the substrate could be a way for them to form [84], their occurrence under vacuum preparation requires a different explanation. Formation of an energetically favorable SAM/Au interface involving gold adatoms provides an explanation for the previously unresolved driving force for the 'ejection of extra Au adatoms' [85] in addition to the 4.4% of a gold monolayer released upon lifting of the herringbone reconstruction of a clean Au(1 1 1) surface. The observation of a coexistence of thiolate–Au structures, that is, different SAM/substrate interfacial structures that are energetically close [75], is also able to explain the dependence of VI formation on the type of molecule. Whereas VIs are observed for SAMs with the thiol group attached to an alkane chain, islands of monoatomic height of gold form for aromatic thiols [53, 86–89] and even both cases are observed for MBP1, depending on the preparation conditions [90]. It is noted that this interpretation is not in conflict with recent STM experiments that found essentially the same RS-Au-SR gold adatom structure for both an alkane thiol ($R=CH_3$) [73] and an aromatic thiol ($R=C_6H_5SH$) [77]. In contrast to complete SAMs, these experiments were performed at low thiol coverage where molecular packing effects are not important.

The possibility of a manifold of interfacial structures suggested from the work of Mazzarello *et al.* [75] and an energy gain associated with a restructuring of the interface [75, 78, 80] leads to another crucial aspect of the SAM/substrate interface, which is the bonding configuration of the sulfur. It is the C–S–substrate bond angle that is of particular interest here as it affects the molecular orientation and, thus, interferes with other factors influencing a SAM structure. Experiments on SAMs of a homologue series of ω-(4′-methylbiphenyl-4-yl)alkanethiols ($CH_3(C_6H_4)_2(CH_2)_mSH$, MBP*m*) revealed a decisive influence of the C–S–substrate bond angle on the SAM structure and properties. The architecture of these SAMs is depicted in Figure 5.5. They consist of a rigid biphenyl (BP) unit on top of an aliphatic chain that provides the link between thiol and BP moiety. Varying the number of methylene units between $m=0$ and 6, a pronounced odd–even effect was found, that is, packing density of the molecules and orientation of the BP moieties alternates upon variation of m between even and odd [90–92]. Importantly, this odd–even effect is inverted when going from Au(1 1 1) to Ag(1 1 1) that evidences a directional force of the head group [91]. Phenomenologically,

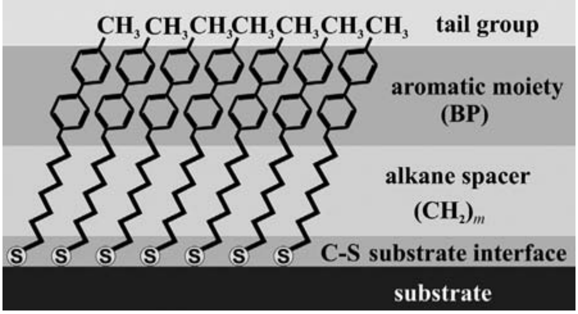

Figure 5.5 Architecture of a layered SAM consisting of a rigid biphenyl unit (BP) on top of an aliphatic spacer chain of m methylene units. The surface-terminating tail group can be either chemically inert (e.g., $X=CH_3$, H) or active (e.g., $X=CN$).

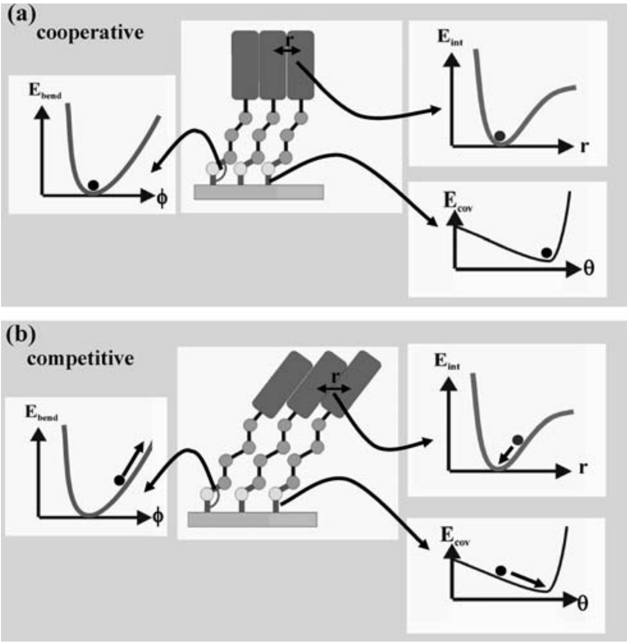

Figure 5.6 Factors determining a SAM structure illustrated by the mutual influence of coverage θ, C–S–substrate bond angle ϕ and intermolecular interactions represented by distance r and their dependencies on the molecular structure. For the different contributions the actual position of the system on the potential curves is indicated by solid circles. (a) Cooperative case. Molecular structure allows all contributions to adopt an energy minimum. (b) Competitive effect. Molecular structure is such that not all contributions can be optimized at the same time. SAM structure is a result of balance of partially opposing forces. For details see text.

the bonding geometry of the sulfur can be approximated by an sp^3 and sp-like hybridization on gold and silver, respectively, which results in very different C–S–metal bond angles on both substrates. Importantly, this change in hybridization occurs also for modification of the substrates by metal UPD as further outlined in Section 5.4.3 [93]. The consequences of a particular hybridization for the structure of a SAM are illustrated in Figure 5.6 for the example of MBPm monolayers on gold. For simplicity, a reduced set of three different contributions to the energetics of a SAM is shown, namely coverage θ, C$-$S$-$Au bond angle ϕ and intermolecular interactions reflected by their intermolecular distance r. The dependencies of the associated energies E_{cov}, E_{bend} and E_{int} on the respective parameters θ, ϕ, and r are schematically represented by the potential curves. The consequence of the directional force, arising from a preferred value of ϕ, is a pronounced difference between odd and even numbers of methylene units. For $m =$ odd (Figure 5.6a) all three factors contributing to the energy of the SAM act cooperatively, that is, can adopt a minimum in energy simultaneously, as indicated by the position of the solid circles on the potential curves, which means that one structure should be strongly preferred. For $m =$ even this is very different (Figure 5.6b). The optimum angle ϕ no longer allows for the molecules to pack densely, that is, the other two contributions are out of their energy minima. Conversely, a move of these energies towards the minimum forces the bending potential to higher values as indicated by the arrows. Due to this competition between factors, the system will minimize its energy by compromising between the different contributions. Consequently, such a SAM is in an energetically higher state compared to the $m =$ odd case, which is what has been found experimentally. Even-numbered MBPm SAMs on Au (1 1 1) are less stable than odd-numbered ones [94–96]. This simple model pinpoints the challenges one is faced with when aiming for a precise design of SAMs and makes it understandable that even apparently small changes in the molecular structure can strikingly alter structure and properties of a SAM. In general, one should expect a manifold of local minima that, depending on the details of the system, might result in closely related structures, as in the case of alkane thiols [63–65] or distinctly different ones as found for MBPm SAMs on Au(1 1 1) with $m =$ even [66–68]. The situation is exacerbated by additional factors that add to the complexity of the energy landscape of a SAM. Besides conformational degrees of freedom of the SAM molecules there is another one of crucial importance that is the mismatch between the lattices of SAM and substrate. In a simplifying picture where the bond strength between molecule and substrate is represented by a periodic potential whose periodicity is determined by the substrate, a mismatch between molecular and substrate lattices gives rise to stress[1] [98–100] as illustrated in Figure 5.7a that shows the side view of the SAM in the top row, a top view of the substrate (bulk terminated for simplicity) with the binding sites of the molecules indicated (second row) and the corrugation potential in the third row with the molecule–substrate interaction energy indicated by the solid circle. For a rigid molecule such as MBP0 with a minimum intermolecular distance larger than the periodicity of the corrugation potential an ordered arrangement of the molecules requires the adsorption sites to adopt energetically unfavorable positions. As a consequence, stress is built up that, for example, is released by defect formation in the film resulting in small domains and an overall poor crystallinity of a SAM. To avoid this, either SAM-like alkane thiols can be used where geometries seem to fit or sufficient degrees of freedom are available to accommodate lattice mismatch. This case is illustrated in Figure 5.7b, which is analogous to Figure 5.7a but now the molecule has sufficient conformational degrees of freedom. This reduces stress to an extent that a crystalline packing of the molecular moieties is possible over extended areas but the exact position of the sulfur should vary to some extent. The observation of contrast variations in STM images has been interpreted to arise from this [81]. It is stressed that the models depicted are rather simplistic and that a more realistic representation should take into account that the substrate is not bulk terminated. Examples of the effects just discussed are given in Figure 5.7c showing SAMs of MBP1 (left), MBP3 (middle) and MBP4. This series of molecules whose structures differ only in the number of methylene units but have the same rigid aromatic system, highlights that the design of a SAM requires the molecular structure to match the requirement of the substrate. MBP1, which lacks a clear order, is essentially equal to the case presented in

---

[1] In addition to the stress by lattice mismatch there are additional electrostatic effects arising from charge redistribution [97, 98].

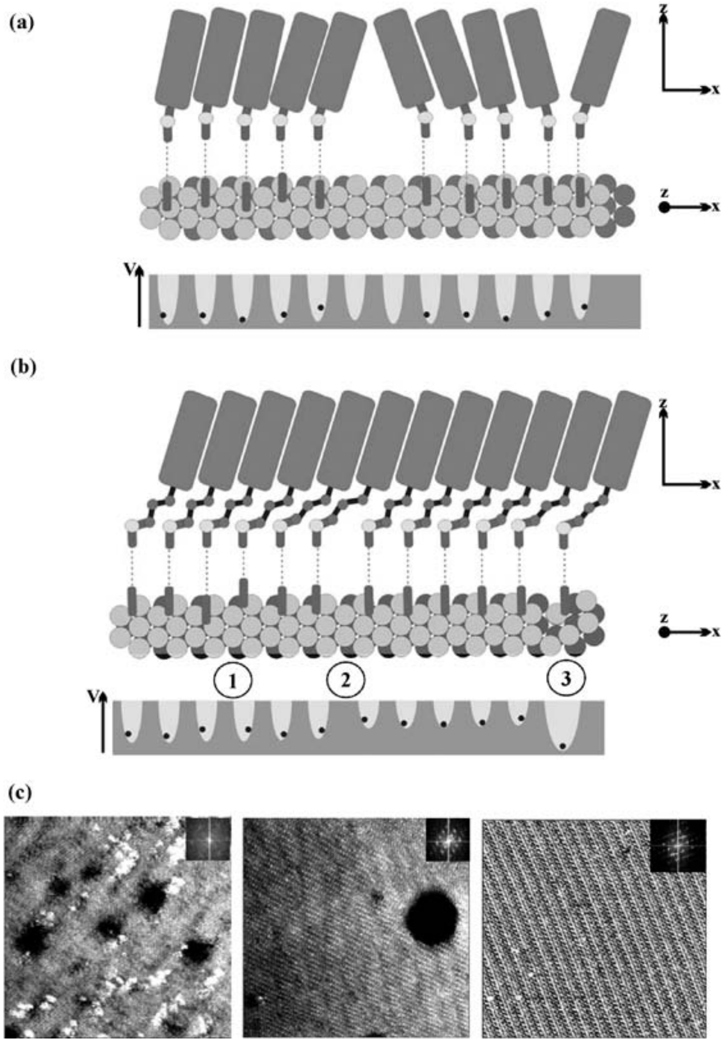

Figure 5.7 The role of stress caused by lattice mismatch between SAM and substrate illustrated in (a) and (b) by a cross-section of a SAM (*x*-*z* plane), indicated adsorption sides (*x*-*y* plane) and the molecule–substrate interaction potential *V*, where the solid circles indicate the energy of an adsorption site for a particular SAM molecule. (a) For rigid molecules, stress is mainly released by defect formation in SAM, which results in a layer of rather low crystallinity and small domains. (b) Molecules with sufficient conformational degrees of freedom allow accommodation of mismatch between packing of rigid moieties and substrate lattice. Different possibilities for mismatch accommodation are indicated. Slight displacement from most favorable adsorbate site (1), jump to different site (2), and restructuring of the interface (3). (c) STM images ($40 \times 40\,\text{nm}^2$) of SAMs of MBP1 (left), MBP3 (middle) and MBP4 (right) all on Au(1 1 1)/mica recorded in air. For details see text.

Figure 5.7a except that the occurrence of islands of monoatomic height of gold shows that the substrate also undergoes restructuring. It is noted that the influence of lattice mismatch can be dominating with standard procedures usually applied such as thermally promoted Ostwald ripening not improving a film structure. For the MBP3 SAM that has been prepared at an elevated temperature of 343 K one sees high molecular order but there are substantial contrast variations, most likely due to the reasons discussed for Figure 5.7b. Finally, MBP4 is an example where these contrast variations are absent and the crystallinity of the layer has become exceptionally high after the SAM has been thermally annealed at 423 K (note the difference in film quality to the SAM shown in Fig. 5.2b). SAMs of such low defect density might be valuable for electrochemical applications, in particular for those related to nanotechnology, where the control of defects is decisive.

The points discussed so far have been limited to forces and interactions present in the SAM and between SAM and substrate. An additional level of complexity is added when considering a liquid environment such as an electrolyte and the influence of the potential on the structure of a SAM, aspects of both have been studied relatively little. Solvent studies reported penetration of the solvent into alkane thiol-based SAMs causing molecular reorientation and conformational changes [10, 57, 101] and as a consequence a change in the blocking properties [102]. For alkane thiols SAMs the structural robustness varied with film thickness and a higher degree of solvent penetration was also found in electrochemical experiments [103]. Penetration of the solvent might not only affect the structure of the SAM, for example, impair their blocking properties, but might also affect charge transfer through weakening of the S–substrate bond [104]. For aqueous systems preferential adsorption of ionic species is another solvent effect as exemplified by the negative charging of methyl and ethylene-glycol-terminated alkane thiol SAMs by hydroxide ions [9]. For reactive SAMs charging by protonation/deprotonation can occur, again resulting in changes in the order of the SAM [105]. Adding to the influence the SAM exerts on the interfacial solvent structure such as change of solvent density [106], a charged SAM alters the system in different ways. The potential of zero charge (PZC) is shifted and the course of the potential is altered that in turn affects the double layer, the structure of the immediate SAM/electrolyte interface and possibly the SAM structure, all of which can be difficult to separate and that can make the behavior of the system dependent on the details of the experiment. An example is mercaptopyridine, for which only one structure is observed in aqueous Na_2SO_4 over the potential range investigated, whereas a structural transition occurs in H_2SO_4 [69]. This system also illustrates another point of importance when controlling electrochemical processes that is the potential dependence of the monolayer structure, also well known for other organic adsorbates [107, 108]. It will depend on the relative strength of interactions whether potential-induced phase transitions occur. For a short-chain thiol such as ethane thiol (MC2) on Au(1 1 1) where intermolecular interactions are quite weak [61], a structural transformation occurs whereas ω-(4′-methylbiphenyl-4-yl)ethane thiol (MBP2) with its rigid aromatic moiety does not exhibit any structural changes [43].

Up to now the discussion has focused on basic properties of SAMs inherent to the particular combination of SAM-forming molecule and substrate, as well as environmental conditions, that is, solvent and/or potential. The points outlined above even hold for an idealized system, that is, a SAM forming on perfectly flat substrate. Of course, a realistic picture has to include further structural details that are briefly addressed here because of their relevance for the electrochemical behavior of SAMs. Atomic steps, kinks, corners or dislocations in the substrate and even coarser-grained defects like grain boundaries for polycrystalline substrates, these substrate defects are mapped by the SAM that, therefore, will exhibit structural imperfections. The restructuring of the substrate during SAM formation, that is, creation of either VIs or adatom islands, increases the number of these defects. The structural perfection of a SAM is further limited by domain boundaries that, depending on the details of the SAM, such as molecular orientation (see Figure 5.1c), can be more or less disruptive. Related to defects in the molecular packing are kinetically trapped vacancies inside a SAM domain. These type of defects can at best be reduced to some extent but not eliminated. Since all these so-called intrinsic defects introduce discontinuities of varying degree in the layer they may compromise the properties of a SAM. Another type of defect defined as extrinsic arise from contaminations. Present either on the substrate prior to SAM formation, where they prohibit adsorption of SAM molecules, or being present as an impurity in the SAM solution they can generate significant defects in the SAM. Pin holes, that is, defects where the electrolyte comes in direct contact with the substrate or at least very close to it, can be ascribed to this type of defects. As has been discussed in the literature [23] and will be exemplified below (Section 5.4.3) the control of extrinsic defects is crucial and, in fact, can become the limiting factor for the performance of a SAM. Impurities in the molecular material are an issue whose importance depends on the details of the system. While it might not be a serious problem for strongly adsorbing molecules such as alkanethiols, careful purification is required for molecules that exhibit weaker interactions or exhibit a significantly slower adsorption kinetics than the impurity. A striking example of this is the SAM formation from organo thiocyanates that, upon cleavage of the S–CN bond, form layers chemically identical to those obtained by thiol adsorption. Originally, the thiocyanates were reported to form SAMs whose structural quality is inferior to ones formed by thiols [109, 110]. However, a striking improvement in film quality resulted when using carefully purified thiocyanates. The achievable SAM quality is at least as good as the best SAMs prepared from thiols [111]. In light of the fact that in chemical synthesis substances are rarely purified to a level higher than 99% this point has to be kept in mind when working with systems whose tolerance to contaminations is not clear and it is obvious that this point requires particular attention for electrochemical applications of SAMs, given the sensitivity of their electrochemical properties to the presence of defects.

5.3
Reductive Desorption of SAMs

Similar to other fundamental studies on SAMs, alkane thiols on Au(1 1 1) have also been prevailing in electrochemistry with, however, aromatic thiols receiving increased attention. A major topic has been formation and stability of SAMs and

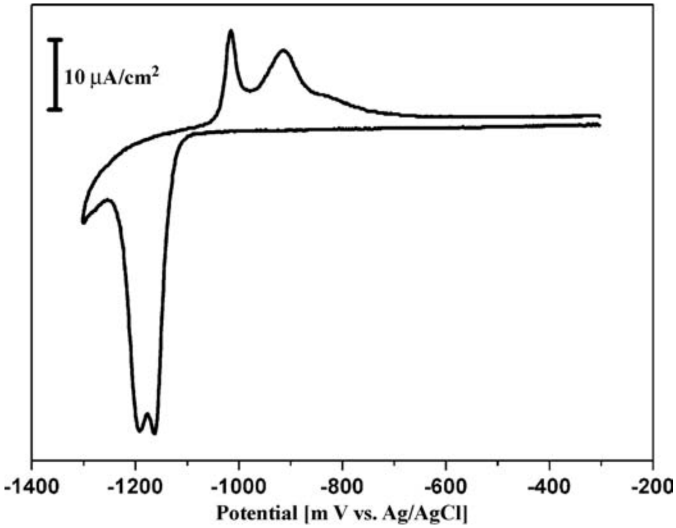

Figure 5.8 CV of a hexadecane thiol SAM on Au/mica recorded in 0.5 m KOH at a scan rate of 20 mV/s. KOH is used to shift the hydrogen-evolution reaction negative of the thiol desorption peak.

cyclic voltammetry is the most common means of investigation. Looking at a typical example of an alkane thiol SAM adsorbed on a Au(1 1 1) electrode (Figure 5.8), the cathodic scan is characterized by a pronounced feature that marks the reductive desorption (RD) of the molecules described by a one-electron transfer process ($RS + e^- \rightarrow RS^-$) to be discussed in more detail below. The anodic waves indicate oxidative readsorption. It is a general feature that the readsorption signal consists of at least two waves, which indicates a distinctly stepwise adsorption process. Since SAM formation is not within the focus of this chapter this is not discussed any further. For more information on this, the reader is referred to the literature that addresses the process for alkane thiols on different substrates such as Au [45, 112–115], Ag [115–119] or Hg [115, 120, 121]. We also refer to the literature for work on the oxidative desorption of thiols [47, 68, 115, 122–124] that, compared to the reductive desorption, is a much slower process involving transfer of electrons in several steps and that is less defined as gold oxidation occurs at the same time.

The reductive desorption of thiol SAMs has been studied in detail, mainly for analytical purposes since the desorption signal is sensitively dependent on the SAM structure and properties. However, RD as a way to manipulate SAMs also bears significant potential for applications, which is illustrated by the range of examples including selective desorption of one type of thiol from a binary SAM [125–127], electrochemical whittling, that is, controlled shrinking of features [128, 129], change in wetting properties [130] or the selective desorption from UPD-modified SAMs that will be addressed in Section 5.4.3. Another interesting application of reductive desorption is the generation of a composition gradient. In contrast to the normal case of a potential gradient along the surface normal, a potential difference was applied parallel to the surface. This resulted in stripping of the thiols only in areas of the substrate where the potential was sufficiently negative for RD. A transition region of the order of 200 μm formed between unmodified and stripped areas where thiol coverage continuously varied [131, 132].

Examining thiol desorption reveals that the position, shape and magnitude of the desorption wave depend on a number of mutually dependent factors such as the type of molecule, molecular packing, substrate structure and molecule–substrate bonding. For some of these factors the influence on the desorption signal is well understood, whereas for others assessment has been more difficult without a fully conclusive answer as yet, despite several investigations over the years. One of the obvious factors determining the desorption potential is the film thickness, which is attributed to an increase in the intermolecular interactions and resistance to ion penetration [23]. For alkane thiols there is a continuous negative shift in the desorption potential by 15–20 mV per CH_2 group [122, 133, 134]. This length dependence of the desorption signal has been exploited in the generation of heterogeneous SAMs [125]. From mixed SAMs consisting of phase-separated thiols such as hexadecane thiol (MC16) and mercaptopropionic acid (MPA) as long- and short-chain thiols, respectively, the shorter one was selectively desorbed by restricting the potential to values positive of the region where the long-chain thiol desorbs. Since the stability is affected by intermolecular interactions, a variation of the tail group also gives rise to differences in the desorption potential. This was exploited in a study of surface diffusion in mixed SAMs [126]. Starting from an artificially phase-separated SAM consisting of undecane thiol and mercaptoundecanoic acid where two desorption peaks are observed, the mixing of the molecules upon annealing in water reduced their splitting until only one peak remained, thus, indicating formation of a homogeneously mixed SAM. It is worth noting that the carboxy-terminated SAM is electrochemically less stable (desorption peak at -0.92 ± 0.01 V vs. Ag/AgCl) compared to the methyl terminated thiol SAM with the same number of carbon atoms (-1.01 ± 0.01 V). The difference in the desorption potentials for methyl- and carboxy-terminated thiol SAMs was also exploited in exchange studies where, starting from a homogeneous SAM exchange by exposure to a solution of the other type was followed via the shift of the desorption peak [135].

While alkane thiol SAMs exhibit a continuous shift with layer thickness, studies of a homologue series of MBPm thiols (see Fig. 5.5) revealed a pronounced difference in the desorption potential between $m =$ odd and $m =$ even as seen from Figure 5.9 [94]. This odd–even variation, which was confirmed in another study of this series [68], is a clear reflection of the difference in stability of these layers due to the cooperative and competitive way the energy-determining factors enter into the energy balance of the system, as outlined in Section 5.2. Interestingly, the shift in the desorption potential as a function of m is identical to alkane thiols for both sets of MBPm SAMs [94]. While this can be understood for $m =$ odd that exhibit the same packing density as alkane thiols [92, 136], it is somewhat unexpected that this value is also found for $m =$ even where the intermolecular interactions should be less due to the significantly lower packing density of the molecules. Presently, it is not clear whether the larger tilt angle of the aromatic units for $m =$ even results allows for an

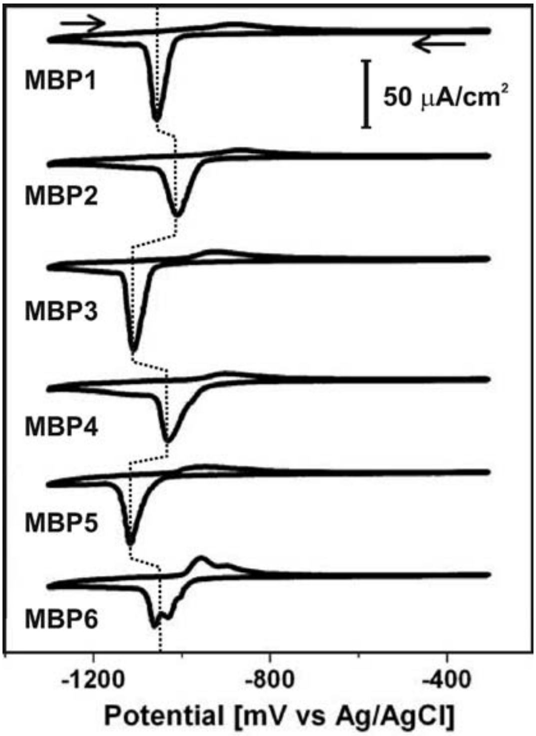

Figure 5.9 Cyclic voltammograms of MBPm SAMs on Au/mica recorded in 0.5 m KOH at a scan rate of 20 mV/s. The dotted line highlights the odd–even effect in the desorption peak. Arrows in MBP1 curve indicate CV scan direction. Samples were prepared at 295 K.

optimized interaction between the methylene spacer chains or whether it is a coincidence that the increased conformational degrees of freedom of the spacer chain reduces the strain on the interfacial bonding geometry and, thus, increases the stability of the SAM by the same value as a CH_2 group in alkane thiol SAMs.

Another obvious piece of information contained in the desorption signal is coverage, which can, in principle, be determined from the integrated charge of the desorption peak. However, a quantitative evaluation has several pitfalls. Firstly, caution is required as, depending on the length of the thiol, the desorption potential of the SAM might interfere with the hydrogen-evolution reaction, which adds a background to the desorption signal. This can be suppressed to some extent by measuring at high pH, typically above 13, but becomes increasingly critical for thiols longer than about 10 carbon atoms. Secondly, the faradaic current due to the charge transfer from the electrode to the sulfur is convoluted with the capacitive current arising from the different capacities of the SAM-covered electrode and the pure Au surface. Assuming a $\sqrt{3} \times \sqrt{3}$ structure for a simple alkane thiol SAM desorption corresponds to a faradaic charge of 74 $\mu C/cm^2$. The difference in capacity between

SAM-coated and clean substrates can easily reach $20\,\mu C/cm^2$, which means that a simple coverage calculation from charge associated with the desorption wave is flawed, as pointed out by Schneider and Buttry [137]. In this context it is worth noting that the difference in capacity between SAM-coated and clean electrodes is not only due to the introduction of a dielectric layer but depends also on the surface of the SAM and its interaction with the environment, that is, whether the surface exhibits some additional charges either due to ionic tail groups or due to specific interaction of the SAM with the electrolyte.

Even if taking a possible background from hydrogen evolution and capacitive charging into account [138] there is a third aspect, which is the neglect of the influence of the electrolyte. Instead of describing thiol desorption as a one-electron transfer process it should be treated as a substitution reaction with solvent (e.g. water) replacing the desorbing thiol according to

$$\mathrm{RS(ads)} + \mathrm{e}^- + x\mathrm{H_2O} \rightarrow \mathrm{RS^-(aq)} + x\mathrm{H_2O(ads)} \tag{5.1}$$

As a consequence, the measured charge number q_m is, in general, not an integer and can vary between 0 and 1 as a function of the applied potential, as discussed in detail by Laredo *et al.* [139]. Applying chronocoulometry they found that for an MC18 layer, which in this case was formed by a Langmuir–Blodgett transfer technique, the charge number per adsorbed molecule varies substantially with potential. At -1.0 V vs. SCE, that is, close to the desorption potential, the average value of q_m deviates only about 10% from -1. Towards more positive potentials $|q_m|$ gets substantially smaller, which, in particular, has to be kept in mind when comparing thiol SAMs that differ significantly in their desorption potentials. At potentials around -0.3 V where short-chain thiols in an acidic environment desorb [61, 140] the difference from the full electron charge can exceed 30%. A further point to note is that the value of q_m depends on the electrolyte used and in cases where specific adsorption occurs this has also to be considered in the thiol–electrolyte substitution reaction.

Beside stability and coverage, the third point concerned with the reductive desorption of thiol SAMs is the shape of the desorption signal. While a single peak is mostly observed both for aliphatic and aromatic thiols, which can exhibit some variation with respect to its symmetry, also a double-peak structure can occur depending on the experimental details. Exemplified by Figure 5.8, such a double-peak structure is observed at $\mathrm{pH} > 12$ for alkane thiols on Au(1 1 1) with the chain length exceeding 11 carbon atoms [114, 141–143]. However, this does not seem to persist since for MC22 a single peak is observed again [114]. So far this double-peak structure is known to occur for alkane thiols and the only other example reported is MBP6 [94] adsorbed on a Au/mica substrate. Interestingly, also for the MBPm series the double peak seems to disappear again since MBP12 exhibits only one peak [94]. It is worth noting that also for alkane thiols on Ag(1 1 1) a similar behavior is observed. Even though a double-peak feature could still be identified for MC9, the longest-chain thiol studied, the separation was clearly smaller compared to the shorter analogs [144]. The occurrence of the double-peak structure in the reductive desorption wave of alkane thiol SAMs has been the subject of some discussion. Originally, it was proposed to arise from differently sized SAM domains exhibiting different stability and/or different Au–sulfur binding modes. A different interpretation was suggested based on spectroelectrochemical studies using *in-situ* IR spectroscopy [142]. The presented model associates the first peak with a faradaic current due to the reduction of thiols and the second one with a capacitive current caused by a rearrangement of the molecules to micelles [145]. However, another study demonstrated that the occurrence of a double-peak structure is sensitively dependent on the nanoscopic substrate roughness [143] and vanishes if the step density is too high. Maintaining the separation into faradaic and capacitive currents, the difference between one peak and two peaks was explained as a kinetic effect with smaller domains on the more terraced surface rearranging quickly upon reductive desorption, whereas larger domains are more stable after desorption and, thus, exhibit a delayed micelle formation. This refined model has been challenged by another study on alkane thiol SAMs where reductive desorption was monitored by SHG *in situ* and in real time parallel to the CV [114]. Since SHG is specifically sensitive to the faradaic component in the desorption process by probing the S–Au bond, comparison of the desorption current with the SHG signal allows identification of faradaic and capacitive components. For all chain lengths, irrespective of whether the CV shows a single or double peak, no indication of a separation between capacitive and faradaic currents was found, at least up to the point where the coverage of chemisorbed thiols was below 0.1. To explain the double-peak structure a model developed for describing redox processes of surface-confined species was proposed [146–149]. Its essential point is that the shape of the desorption peak depends on the sign and relative strength of energies describing the pairwise interaction between the possible combinations of reduced and oxidized species. This appears consistent with the previously made observation that the exact shape of the desorption peak depends on the structural quality of the SAM [143].

While the desorption process has been mainly studied by electrochemical and spectroscopic techniques ECSTM has also been applied [150–153]. Desorption was reported to start at domain boundaries, missing rows or edges of VIs and to proceed domainwise [151]. VIs as a characteristic feature of SAM formation remained after desorption. A common feature in all experiments, irrespective of whether acidic or basic electrolytes were used, was the formation of larger aggregates. Even though their exact structure is not clear, this observation is consistent with the formation of physisorbed aggregates suggested by the spectroscopic investigations [142]. While STM provides a picture at the molecular level its time resolution is rather limited and, therefore, chronoamperometric measurements provide useful complementary information on the desorption kinetics. The current–time curves that have been recorded for a number of different thiol layers including alkane thiols of different chain length [154–156], mercaptopurine- [157] and biphenyl-based SAMs [68], exhibit a shape that is characteristic for a nucleation and growth mechanism. There is agreement that defects play a crucial role, which is reflected by the series of curves depicted in Figure 5.10. Increasing the time of thiol adsorption, the structural quality of the SAM improves, thus causing the maximum of the curve to shift significantly to longer times, in agreement with the shift of the peak potential to more negative values [158]. To describe the desorption process quantitatively, different models have been discussed invoking a nucleation and growth mechanism. Instantaneous and

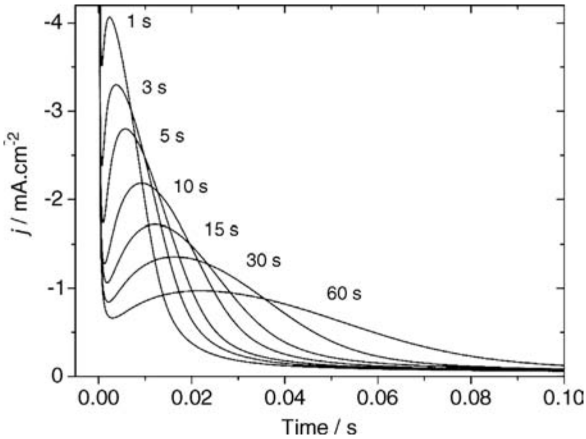

Figure 5.10 Current transients of the desorption of octadecane thiol from Au(1 1 1) recorded in 0.1 m KOH. The times indicate the time of formation at a potential of −0.2 V vs. SCE. To record the curves the potential was stepped to −1.31 V. Printed with permission from Ref. [158].

progressive nucleation, that is, fast and slow formation of etching centers according to the Avrami equations, were unable to explain the data, whereas incorporation of diffusion of the desorbed species was able to describe the experimental curves for shorter-chain thiols such as MC4 and MC9. [154–156] Depending on the type of thiol and the potential chosen, desorption of SAMs progressed from a mechanism dominated by a limited number of etching centers (at less negative potentials) to a homogeneous removal across the surface (more negative potentials). In an analogous study the aromatic MBPm SAMs were also investigated [68]. For MBP3 as an example of an $m =$ odd thiol the hole nucleation and growth mechanism also explained the data. For MBP4 as even-numbered thiol, the time-dependent current adopted a more complex shape with an additional term introducing a power-law dependence for the formation of active nuclei of desorption. To model the behavior of longer-chain alkanethiols such as MC18 that exhibit a poor solubility in aqueous alkaline solutions and for which diffusion into the bulk should, therefore, not play a significant role [159], different models were applied by Doneux *et al.* [158]. These models, proposed by Poelman *et al.* [160] and Mulder *et al.* [161], are based on order/disorder transitions and assume that, in contrast to the above modeling, mass transport and desorption is much faster than disordering and, thus, not rate limiting. Assuming simple geometries for the ordered SAM domains, that is, circles and squares, disordering/desorption starts at domain boundaries (line defects) and progresses by shrinking of the ordered areas. In addition to this shrinking the Mulder model also includes nucleation and growth of internal holes, similar to the models mentioned above. Since the key of both mechanisms is a shrinking of ordered islands it might not be too surprising that they describe the experimental data similarly well. Fits of the Poelman model to the different formation times were interpreted in terms of an increasing length of line defects for longer preparation times consistent with the physical picture that longer times yield larger domains due to Ostwald ripening. A third approach to model thiol desorption has been taken by Martin *et al.* [162] who applied Monte Carlo simulation. With the stripping probability of the adsorbed thiol molecule depending on several parameters, namely potential, intermolecular forces and substrate defects, they obtained a good correlation with experimental observations made in STM experiments such as delayed stripping at step edges and aggregate formation.

In contrast to the detailed work on the Au(1 1 1) surface, desorption studies from the other low-index surfaces are scarce with, for example, MC9 and MC4/8 on Au(1 1 0) [45, 46] and MC4 [47] on Au(1 0 0). Compared to Au(1 1 1) thiols are more stable on Au(1 1 0) as reflected by a negative shift of the desorption peak by 200–300 mV, which was explained by the difference in the pzc for both surfaces [46]. No obvious differences in the shape of the desorption peaks were found for Au(1 0 0) compared to Au(1 1 1). Interestingly, for MC4 a higher thiol coverage compared to both MC4 on the Au(1 1 1) and MC2 Au(1 0 0) was concluded from the desorption studies. For polycrystalline surfaces the desorption signal is more complicated with additional features, possibly due to the presence of different crystallographic domains [94, 163, 164].

With respect to desorption experiments on substrates other than Au, Cu [165], Ag [116, 117, 122, 134, 144], Ag-Au alloy [166], Zn [167], Pt [168], Pd [168] have been studied. Compared to Au, the desorption potentials of alkane thiols are significantly shifted towards more negative potentials for silver ($\Delta E = -0.23\,\mathrm{V}$) and copper ($\Delta E = -0.6\,\mathrm{V}$). No significant differences between the three metals were observed in the shift of the desorption potential as a function of the length of the carbon chain [165]. To pin down the desorption potential for copper substrates for which it is shifted into the HER region, a rotating disk-ring technique was applied. Using a bipotentiostat, thiols desorbed from a Cu disk are oxidatively readsorbed onto the Au electrode, which is held at a constant potential positive of that where thiols adsorb on Au. The potential sweeps of this experiment are shown in Figure 5.11. While the Cu disk only shows a monotonous increase in the cathodic current due to HER but does not exhibit any feature indicating thiol desorption (Figure 5.11a), the peak in current of the Au anode (Figure 5.11b) clearly indicates that thiol desorption from copper occurs and that it is just masked by HER. Note the differences between the current densities of the dominating HER for the copper electrode, reductive thiol desorption on a gold electrode (Figures 5.8 and 5.9) and oxidative thiol adsorption on the Au ring electrode. The significant increase in stability of thiol SAMs on Cu compared to Au is of interest for applications, as discussed in more detail in Section 5.4. With Au and Ag giving rise to distinctly different desorption potentials a study of an Ag-Au(1 1 1) alloy surface is interesting where the composition was varied from pure Au to pure Ag. Upon increase of the Ag concentration a peak at potentials negative of the one for Au emerged. Notably, the peak representative for Au disappeared already at a mole fraction of Ag of 0.5. Furthermore, the peak for a high Ag content alloy is at more negative potentials than for pure Ag. While the reasons for this remain elusive, one explanation given was that for the Au–Ag mixture more of the sulfur atoms can bind to sites of minimum energy as compared to the more densely packed SAM on Ag.

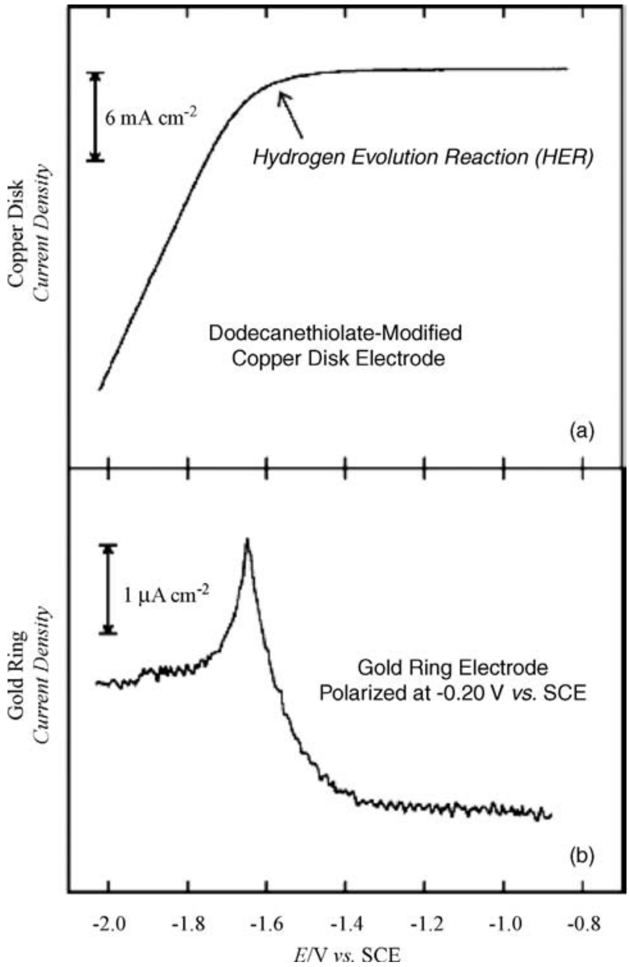

Figure 5.11 Desorption of a SAM of dodecanethiolate from a rotating Cu-disk electrode. (a) Current measured at the Cu electrode. (b) Current measured at a Au-ring electrode indicating oxidative adsorption of a thiol. Electrolyte: 0.1 NaOH + H_2O (5%) in methanol. Reproduced with permission from Ref. [165].

A case different from the ones discussed so far is desorption of alkane thiols from Pt, where a standard CV in KOH does not exhibit a reduction peak. Originally, it was suggested that thiol SAMs on Pt are more stable than on Au [169] the lack of a desorption wave was recently unravelled to be due to a much slower kinetics compared to Au. Applying a protocol that involves two steps, Williams and Gorman [168] showed that desorption indeed takes place and that thiol SAMs are slightly less stable on Pt compared to Au. In the first step thiols were desorbed by holding the potential at a constant value for a fixed period of time. The degree of desorption was then analyzed in a second separate experiment using ferricyanide as a redox probe and deriving the extent of thiol desorption from a change in the blocking behavior of the SAM through the magnitude of the current in the redox waves. Repeating this for a set of samples covering the relevant potential range enabled them to unravel the potential-dependent desorption. This work also showed that thiol desorption from Pd is rather different from Pt and Au since the desorption rates did not change as a function of chain length. Formation of a Pd–S interlayer was suggested to account for this [170].

5.4
Metal Deposition on SAM-Modified Electrodes

5.4.1
General Remarks

Electrochemical metal deposition on SAM-modified electrodes has been investigated for various reasons. Focusing on small molecules such as mercapto propionic acid [171] or sulfopropyl mercaptane/disulfide [172, 173], interest has been in their role as additives to influence growth of metal on metal in for example, copper electroplating [174, 175]. Furthermore, the passivating properties of SAMs in combination with control of interfacial energies has been exploited for the generation of metal structures either by use of SAM-covered substrates as mold [176] or patterned SAMs to localize and confine metal deposition [36, 96, 177, 178]. The molecules studied under this aspect are usually larger ones such as long-chain alkane thiols [176] or aromatic thiols [178]. A third type of activity aims for metal deposition on top of either aliphatic or aromatic SAMs, which is of interest for both the generation of low-dimensional metallic systems [179–181] or providing electrical contacts for use of molecular layers as active components in electronics devices [182].

Focusing on selected aspects, a few reviews have covered SAM-controlled electrometallization [29], [30, 183]. Reviewing work published over the past 15 years, the following sections summarize the current state-of-the-art and discuss the different routes currently pursued. For this purpose we first start with a brief account of metal deposition on a clean metal substrate [29]

$$\mathrm{Me}^{n+}(\mathrm{aq}) + n\mathrm{e}^- \rightarrow \mathrm{Me(s)} \tag{5.2}$$

to provide a basis for discussion of metal deposition on SAM-modified electrodes. The dependence of the equilibrium potential E_D for the metal/electrolyte interface on the concentration of the metal ion in solution is given by the Nernst equation

$$E_\mathrm{D} = E_0 + \frac{RT}{nF}\ln\frac{a_{\mathrm{Me}^{n+}}}{a_\mathrm{Me}} \tag{5.3}$$

with E_0 as the standard potential of metal redox couple $\mathrm{Me}^{n+}/\mathrm{Me}$, $a_{\mathrm{Me}^{n+}}$ as the activity of the ion in solution and a_Me that of the metal, which is unity for a pure phase. Deposition of metal starts at potentials negative of E_D and continues until the ion concentration has reached a value satisfying Equation 5.3 for a given deposition potential. In the potential range negative of E_D, the so-called region of overpotential deposition (OPD), bulk-metal deposition occurs. As described in detail in Refs. [184, 185] three types of growth modes are observed on substrates different from the deposited metal that are termed Volmer–Weber (three-dimensional), Frank-van de Merwe (layer-by-layer) and Stranski–Krastanov growth (initial layer-by-layer followed by three-dimensional growth). Very often, the potential where deposition starts is shifted to more negative values due to kinetic effects that occur if there are energetic barriers such as SAMs.

Beside OPD it is well known that metal deposition can also take place at potentials positive of E_D. For this reason called underpotential deposition (UPD) it is characterized by formation of just one or two layer(s) of metal. This happens when the free enthalpy of adsorption of a metal on a foreign substrate is larger than on a surface of the same metal [186]. This effect has been observed for a number of metals including Cu and Ag deposited on gold [187]. Maintaining the formalism of the Nernst equation, deposition in the UPD range means an activity of the deposited metal monolayer smaller than one [183].

As indicated, metal nucleation and growth is strongly affected upon modification of an electrode by a SAM. Phenomenologically, deposition is described to occur in three different ways [29] one of which is intercalation of the deposited metal at the SAM/substrate interface (Figure 5.12a). For a mono- or bilayer this is formally equivalent to UPD but like a surfactant a SAM might also float on top of the thicker growing deposit, thus, influencing the morphology of the deposit. Another process is illustrated in Figure 5.12b where the metal deposition also originates at the SAM/substrate interface but subsequently proceeds in a mushroom-like fashion. In contrast, the third way (Figure 5.12c) is characterized by nucleation on top of a SAM and further growth results in a metal–SAM–substrate sandwich structure. This possibility is intriguing since the electronic properties of low-dimensional metal deposits will be affected by the metal–SAM interaction. Given the flexibility in tailoring surface properties of SAMs, unprecedented ways of tuning metal properties can be envisaged. However, the other two pathways of metal deposition also bear significant potential for technological applications as their characteristics can be

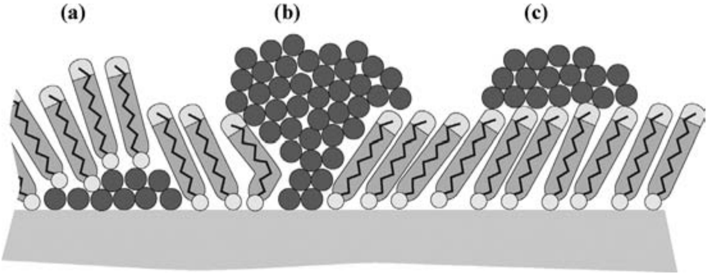

Figure 5.12 Possibilities to deposit metal onto a SAM-modified electrode. (a) intercalation of metal at the SAM/substrate interface. (b) deposition originating at the substrate with subsequent mushroom-like growth. (c) deposition on top of a SAM resulting in a metal–SAM–metal sandwich structure.

exploited for the generation of patterns and in the following sections all three variations will be addressed in some detail with a discussion of the underlying atomistic/molecular mechanisms where possible. One should, however, keep in mind that the data basis to date is still relatively patchy, that is, discussion is sometimes based on observations for a particular metal and a particular type of SAM and, therefore, caution might be required when generalizing things to other metals and SAMs and/or combinations of them.

With respect to systems, copper deposition has been studied most but a number of other metals including Ag, Pb, magnetic metals such as Co and Ni, metals of interest for catalysis such as Pt or Ru or even a CoNiFe alloy have been investigated. Notably, also some oxidic materials such as zirconia, copper zinc oxide have been deposited on SAM-modified or SAM-patterned metal substrates. As substrate, Au(1 1 1), both as single crystals and epitaxial films on mica, has been the most common choice. Nevertheless, Cu has also been used with the advantage that SAMs on this substrate are electrochemically more stable compared to gold (see Section 5.3). Reductive desorption of the SAM at more negative potentials allows a wider range of metals to be deposited. A compilation of systems studied is presented in Table 5.1, which contains all types of electrodeposition on SAM-modified electrodes, that is, UPD-like, mushroom-type bulk growth and on top deposition. Systems have been arranged according to the type of SAM with two main groups, aliphatic and aromatic ones and subgroups defined by the tail groups. For a given SAM system, the combination of metal substrate/deposited metal is listed and further details such as the type of deposition are provided in the following columns. From the table one can once more see that the majority of work is based on aliphatic SAMs. The more recent interest in the less well studied aromatic thiols arises from the emerging field of molecular electronics. For electrochemical metal deposition the use of aromatic-based thiols is of interest due to the higher charge-transfer rate in conjugated systems compared to aliphatic ones and the achievable structural perfection for some of the aromatic systems. In the following sections we will separately look at the different routes of metal deposition on SAM-modified electrodes.

5.4.2
On-Top Deposition

Investigations of metal deposition on top of a SAM have, in particular, been motivated by molecular electronics where metal–SAM–metal sandwich structures are, in principle, convenient systems to study charge transfer through molecular systems, issues related to contacts between molecules and metallic electrodes, and electronic functionality of molecular systems [33, 188]. The central problem in this area is to circumvent shortcircuiting between top and bottom electrodes or to avoid deposited metal becoming buried at the SAM/substrate interface right away. When thinking about strategies to get around this problem one has to bear in mind that a metal–SAM–metal sandwich is not a stable system. There is a substantial thermodynamic driving force for intercalation of the deposited metal at the SAM/substrate interface due to large differences in interfacial tensions between two metals, on the

Table 5.1 Compilation of thiol SAMs for which electrochemical metal deposition has been studied.

SAM		Substrate[a]	Deposited metal	Reference	Type of deposition[b]
Tail group	Spacer				Additional comments
Aliphatic thiols					
CH_3	1[c]	Au(1 1 1)	Cu	[29, 40, 210]	UPD, OPD
CH_3	2	Au(1 1 1)/mica	Cu	[203]	UPD
CH_3	5,7,9,11,13,15,17	Au(1 1 1)	Cu	[39, 183, 204, 212, 217, 234]	UPD, OPD
CH_3	5,15,17	Au(1 1 1)	Cu	[195]	UPD, OPD, temperature dependence (300–345 K)
CH_3	17	Au(1 1 1)	Cu	[213]	UPD, identification of SAM defects
CH_3	4,6,9,15	Au	Cu	[207]	OPD AFM
CH_3	2,3,11	Au(1 1 1)/glass Au NPs[d]	Ag	[245]	UPD, also by Q/QH_2[d]
CH_3	11,15,17,21	Au	Ag, Cu	[199, 201, 214, 246]	UPD prior to SAM formation
CH_3	2,5,9,11	Au(1 1 1)	Ag	[118, 119]	UPD prior to SAM formation
CH_3	9	Au(1 1 1)/mica	Ag, Cu	[219, 220]	UPD, selective thiol desorption
CH_3	3-10, 12-14	Au/glass	Ag, Cu, Hg, Bi	[93]	UPD prior to SAM formation, sp vs. sp^3 hybridization
CH_3	7,11, 17	Au/glass	Pb	[221, 247]	UPD prior to SAM formation
CH_3	11,17,21	Au	Cu	[37]	OPD, hemispherical particles
CH_3	2,7	Au/mica	Ag	[38]	UPD, reductive desorption
CH_3	1, 5, 17	Au(1 1 1)	Ag	[211]	UPD, OPD
CH_3	5	Au(1 1 1)	Pt	[180]	OPD
CH_3	2,7,15	Au(1 1 1)/mica	Tl, Pb, Ag, Cd, Cu, Bi	[202]	UPD, RD[d] Comparison of SAM stability
CH_3	17	Au	Ag, Cu	[248]	OPD, patterning, multicomponent features
CH_3	3,7,11	Au	Cu	[249]	OPD, patterning, microjet
CH_3	15	Au	Ag	[236]	OPD, patterning AFM nanoshaving
CH_3	17	Au	Co	[250]	OPD, patterning μCP[d]
CH_3	15,17,21	Au	Cu	[36, 96, 223, 239]	OPD, electron induced patterning

(*Continued*)

Table 5.1 (*Continued*)

SAM		Substrate[a]	Deposited metal	Reference	Type of deposition[b] Additional comments
Tail group	**Spacer**				
CH_3	11	Au	Rh	[233]	OPD
CH_3	11	Cu	Cu	[30, 176, 243, 251]	OPD, molding
CH_3	11	Cu	CoNiFe alloy	[244]	OPD, molding
CH_3	15	Cu/mica Cu/glass Au/glass	Ni	[177]	OPD, patterning, μCP, mechanical scribing
CH_3	11	Au	Cu	[252]	OPD, influence of bromide
OH		Au	Zirconia	[253]	
CH_3					
CH_3		Cu	Cu oxide	[30]	
CH_3		Cu	Zn oxide	[30]	
CH_3	15,17	Cu	Cu	[235]	Dissolution, patterning μCP
H	Adamantane thiol	Au(1 1 1)/mica	Cu	[231]	UPD on hybrid structure of hydrogen-bonded network and SAM
OCH3	11	Au	Ag, Cu	[199]	UPD prior to SAM adsorption
$(CF_3CF_2CH_2)$-O-	11	Au	Ag, Cu	[199]	UPD prior to SAM adsorption
COOH	1	Au	Cu	[254]	UPD
COOH	1	Au	Ag	[255]	OPD
COOH	1	Au	Pb	[256]	UPD
COOH	2	Au(1 1 1)	Cu, Ag	[171, 211]	UPD, OPD
COOH	10	Au/glass	Cu	[207]	OPD
COOH	10	Au		[199]	UPD prior to SAM adsorption
COOH	10	Au	Cu	[252]	OPD, influence of bromide
OH	2	Au(1 1 1)	Ag	[211]	UPD, OPD
OH	11	Au	Cu	[37]	OPD
OH	11	Au	Ag, Cu	[199]	UPD, prior to SAM adsorption
SH	6	Au(1 1 1)	Ag	[211]	UPD, OPD

SH	6	Au	Au	[180]	on-top deposition by complexation
SH	6	Au NPs	Cu, Ag, Pb, and Tl	[257]	UPD
CN	17	Au(1 1 1)	Ag	[211]	UPD, OPD
$(CH_3O)_3Si$	3	Ag	Tl, Pb, Cd	[258]	UPD
SO_3Na/H	2,3	Au	Cu, Pb	[172, 254, 256, 259–263]	UPD
SO_3Na	3,8	Cu	Cu	[174, 175, 264–267]	OPD, disulfide
FcCO[e]	10	Au		[199]	UPD, prior to SAM adsorption
Aromatic thiols					
	Pridine	Au(1 1 1)	Pd, Pt, Rh	[41, 179, 181, 196, 197, 268, 269]	On-top deposition by complexation
H	$-\phi-$[f]	Pt(1 1 1)	Au	[270]	UPD
H	$-\phi-\phi-$[f]	Au/Si	Cu, Co	[223, 239]	OPD, electron induced patterning
CH_3	$-\phi-$	Au/Si	Cu	[214]	UPD prior to SAM formation
CH_3	$-\phi-\phi-CH_2$	Au/Si	Cu	[96, 178]	OPD, patterning
	$-\phi-\phi-(CH_2)_{12}$				
CH_3	$-\phi-\phi-(CH_2)_2$	Au(1 1 1)/mica	Cu	[43]	UPD
OH	$-\phi-$	Au/Si	Cu	[214]	SAMs on UPD, effect of SAM on Cu-UPD oxide stripping studies
SH	$-\phi-$	Pt(1 1 1)	Au	[270]	UPD
CH_2SH	$-\phi-CH_2-$	Au(1 1 1)	Pt	[180, 198]	On-top deposition by complexation
	2-mercapto-benzothiazole	Au(1 1 1)	Cu	[271]	UPD, OPD
	2-mercapto-benzimidazole	Au(1 1 1)	Cu	[271]	UPD, OPD
	glutathione	Au	Cu	[272]	Ion gated UPD
	l-homo-cysteine	Au	Cu	[273]	Enantioselective Cu deposition

---

[a] If no crystallographic orientation is specified polycrystalline substrates such as nonepitaxial films or foils were used.

[b] Irrespective of deposition potential, intercalation of deposited metal at SAM/substrate interface and bulk growth are labelled as UPD and OPD, respectively.

[c] Number indicates length of alkane spacer chain.

[d] Q/QH_2: p-benzochinone/p-hydrochinone redox couple. NP: nanoparticle. RD: reductive deposition. μCP: microcontact printing.

[e] Fc = ferrocenyl.

[f] ϕ = phenyl, $\phi-\phi$ = biphenyl.

one hand, and a metal-organic interface on the other hand. Both electrochemical and nonelectrochemical methods have been attempted to tackle the problem, with varying degree of success. Electroless deposition, deposition of metallic nanoclusters and evaporation of metals have been pursued and substantial progress has been made in recent years but the success is critically dependent on the details of the system, that is, the combination of metal and molecule [182, 189]. For evaporated metals where the mechanisms have been studied in some detail the structural quality of the layer and tail-group functionality, that is, minimization of defects and the chemical interaction of the outer SAM surface with the metal are crucial factors to reduce penetration of the metal into the SAM [190, 191].

For electrochemical metal deposition onto SAMs, which offers some significant advantages compared to other deposition methods, such as a more precise control of the deposition process and precisely localized metalization by using patterned SAMs, the challenge of confining metal to on top of the monolayer is even more daunting than for the other deposition methods. To rationalize this we start from the model depicted in Figure 5.13a that shows both a region of a perfect SAM and different types of defects. The course of the potential and its change as a function of the electrode potential in the perfect region is schematically illustrated. It is noted that the potential can exhibit a distance dependence more complicated than indicated here. Its gradient need be neither constant nor exhibit the same sign across the layer due to intralayer dipoles origination from anisotropic charge distribution in the molecules.

Even though the exact ratio of the potential drop in the SAM and the double layer might vary somewhat with thickness of the organic layer, that is, decreases if the layer is thin such as, for example, at defects, most of the potential drop occurs within the SAM. A simple approximation is, therefore, to assume that the electrostatic potential of the metal ion does not change upon variation of the electrode potential. The change in the Gibbs free energy of the ion-reduction reaction is then given by $-F(\phi-\phi_0)$, with

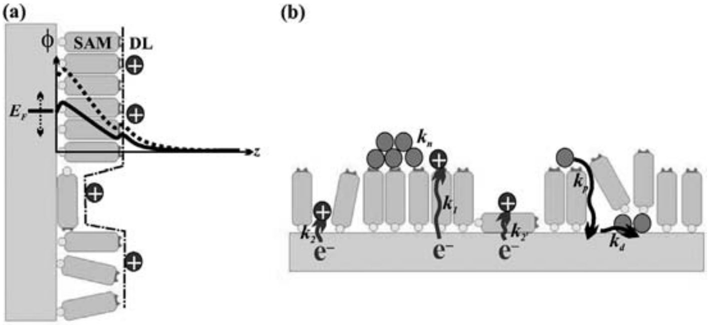

Figure 5.13 (a) Potential drop across a SAM and the adjacent double layer (DL) in a region free of defects shown in top part. Solid and dashed lines are two examples of different positions of the Fermi level E_F. Dash-dot line indicates the course of an equipotential line representing the potential at the outer surface of the SAM including defects. (b) Illustration of processes involved in electrochemical metal deposition. For details, see text.

ϕ_0 as the standard equilibrium potential of the reaction and the phenomenological Butler–Volmer equation can be applied [12]. The rate constant of reduction of a metal ion is, as described in more detail in Ref. [23], given by

$$k_t = \nu \int \rho(E) n(E) D_{\mathrm{Ox}}(E, \lambda, \eta) P(E, \eta) \mathrm{d}E \tag{5.4}$$

with ν as the frequency factor, density of electron donor and acceptor levels represented by $\rho(E)n(E)$ and $D_{\mathrm{Ox}}(E, \lambda, \eta)$ and the tunneling probability $P(E, \eta)$. These quantities are functions of the energy E (defined relative to the Fermi energy of the electrode), the reorganization energy of the metal ion and the overpotential η. The quantity of interest here is the tunneling probability

$$P(E, \eta) = C\mathrm{e}^{-\beta(E,\eta)z} \tag{5.5}$$

where the pre-exponential factor C and the tunneling parameter β depend on the details of the tunneling mechanism and the electronic structure of the SAM. From the exponential distance dependence of the tunneling probability it is clear that defects in the SAM are fatal as the metal ions can approach the electrode more closely compared to the regular SAM structure and, thus, make defect-mediated deposition much more likely. It is noted that since β depends on the electronic levels involved and the potential, values might be structure dependent, that is, are likely to be different at defects and ordered areas. Further deviations from the exponential dependence can arise from structural changes in the interfacial region of the electrolyte [192–194]. These effects originating from the mutual interactions between SAM and the electrolyte make the exact prediction of the distance dependence difficult. The extent to which these effects affect the metal deposition is poorly understood at present but as we will see below they have to be significant as even SAMs, which are expected to exhibit a rather poor blocking behavior, are surprisingly effective in slowing down deposition and suppressing formation of bulk metal.

The processes competing with metal deposition on top of a SAM are illustrated in Figure 5.13b. As is known from general nucleation theory [184, 185], the key point is that a metal nucleus on top of a SAM has to reach a critical size in order to become stable, which requires the rate of nucleation k_n to be high enough compared to the rates of competing processes. With discharge of metal ions preceding nucleation, a sufficiently high rate for tunneling through the SAM (k_1) is a prerequisite besides minimization of defects whose associated rates of metal discharge k_2 and $k_{2'}$ are much larger than k_1. Of course, defects are also detrimental to metal atoms diffusing on top of the SAM as they will penetrate the layer at a rate k_p and become unavailable due to intercalation by diffusion at the SAM/substrate interface reflected by rate k_d. It is noted that a defect does not imply a purely static one such as, for example, missing molecules or domain boundaries. New channels can either temporarily open up [191] or existing ones can change by thermal activation [195]. As a result of the metal penetration the bonding of the thiol is changed, which in turn affects the SAM structure as discussed above in Section 5.2. This can have an adverse effect on the blocking properties of the SAM, that is, might lower the barrier for penetration of either neutral atoms or ions. Another process to be addressed in more detail is the diffusion at the SAM/substrate interface described by the rate k_d, which is important in relation to defect-mediated bulk growth (Section 5.4.4) or control of UPD (Section 5.4.3).

From this brief account of processes one can imagine that confinement of metal deposition to on top of a SAM by a standard procedure, that is, deposition with metal ions present in the bulk electrolyte is a challenging task that requires a SAM of extremely high perfection and a structure that has to be very robust and must not exhibit changes as a function of the applied potential. Therefore, it might not be too surprising that, so far, attempts to metalize SAMs by such a standard electrochemical approach have not been successful.

In search of a solution to this problem a two-step procedure has been successfully demonstrated by Kolb and coworkers [41]. This scheme depicted in Figure 5.14a involves complexation as the first step. Carried out without potential control, the sample is immersed into a solution containing the metal ion, which results in formation of a layer of coordinated metal ions. In a second step, the sample is transferred to an electrochemical cell whose electrolyte, most importantly, is free of metal ions. Applying a cathodic potential the metal ions coordinated to the SAM are then reduced by electron tunneling across the layer. The substantially weaker interaction between the SAM and the neutral metal atoms allows them to diffuse across the surface and to nucleate to nanometer-sized metal clusters. The first demonstration of this concept used a SAM of mercaptopyridine (PyS) on Au(1 1 1) and Pd as metal [41]. Proof that metal was deposited on top of the SAM came from spectroscopic measurements (XPS, UPS) [41, 179]. The observation of a Coulomb barrier, which was reported in STM tunneling spectroscopy experiments and that is indicative of a double tunneling junction, corroborate the results [181]. The irreversible reduction of the coordinated metal ions in step 2 of the process is clearly seen in the CV (see Figure 5.14b) where the distinct cathodic wave indicating metal reduction is only seen in the first cycle (solid line) but not in the second one (dotted line). Depending on the experimental conditions the Pd coverage can be controlled, as illustrated by the STM images (Figure 5.14c) showing an almost continuous layer. Most interesting is the evolution of the electronic structure of the Pd deposit as a function of coverage, which was monitored by UPS (Figure 5.14d) and that revealed a size-induced metal to nonmetal transition. In comparison with bulk Pd a strongly reduced or even vanishing DOS at the Fermi energy is observed for the nearly closed monolayer or nanometer islands, respectively. A number of interesting questions and perspectives arise from these experiments. One intriguing point is that this scheme offers a wide range of control of electronic properties not only through the dimensions of the deposit but also via chemical effects. However, the extent to which the latter plays a role is not clear at present but a crucial influence can be concluded from DFT calculations that only gave agreement with the experimental data if a significant influence of the nitrogen of the pyridine moiety was taken into account [179]. Another point is that this scheme is strictly two-dimensional, that is, in contrast to other deposition methods where material is supplied through a bulk phase, it is confined to the outer surface of the SAM. In this context it is noteworthy that islands of monolayer height were reported for Pd [41, 179], which is unexpected

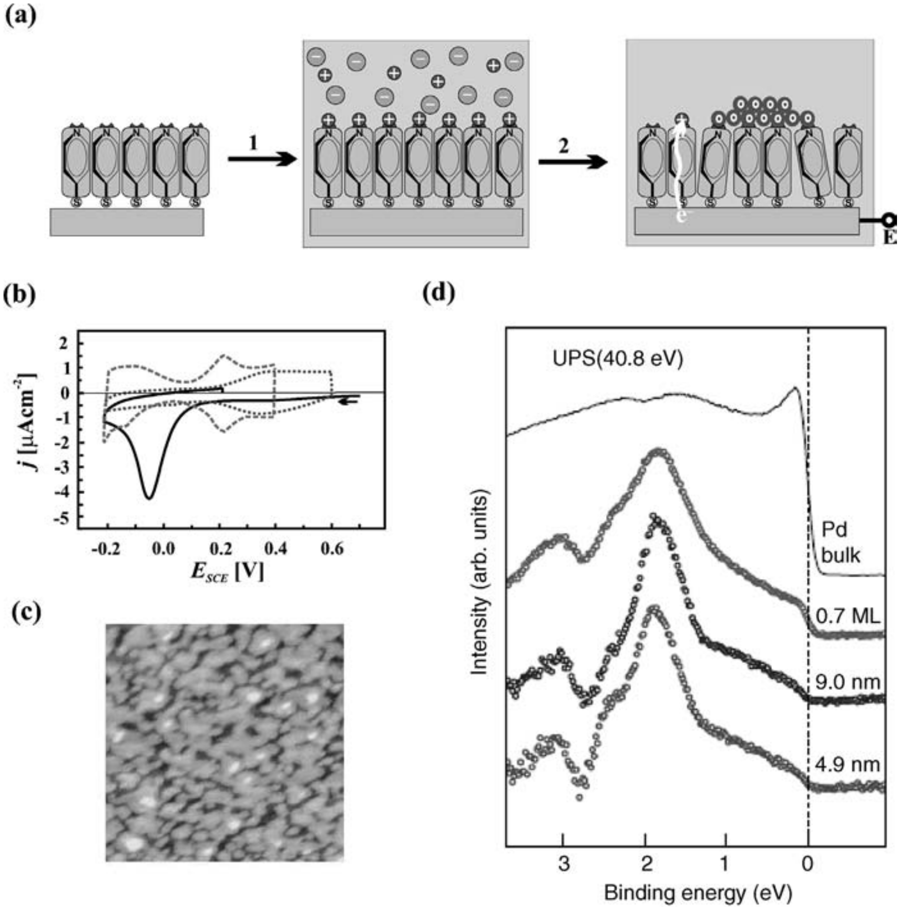

Figure 5.14 Electrochemical metal deposition on top of a mercaptopyridine (PyS) SAM. (a) Two-step scheme consisting of coordination of metal ions at the SAM surface (step 1) followed by an electrochemical reduction of the metal ions to form metal islands (step 2). (b) Cyclic voltammograms of a PyS SAM on Au (1 1 1) in 0.1 M H_2SO_4 reflecting step 2 after modification by exposure to a 0.1 M $PdSO_4$/ 0.1 M H_2SO_4 solution in step 1. The cathodic peak in the 1st cycle (solid line) indicates the reduction of the metal ions. The irreversibility of the deposition process is reflected by the 2nd cycle (dotted line) where the peak is absent. CV of Pd on Au is shown for comparison (dashed line). (c) STM image ($100 \times 100\,\mathrm{nm}^2$) of Pd islands on top of a PyS SAM. (d) Comparison of a series of UP spectra for different Pd coverages. The Fermi energy is at 0 eV. The curve labelled 0.7 ML corresponds to the Pd coverage depicted in (c). Adapted from Refs. [41, 179].

since, given the surface tension of metals, one should expect minimization of the metal surface area and, thus, formation of 3D clusters rather than an extended layer of monoatomic height. However, the exact behavior seems to depend on the details of the systems as seen from Pt deposition where, in contrast to the percolating Pd islands, isolated islands at high density are obtained [196]. It remains to be seen how important electronic and chemical effects are in determining the morphology and surface properties of these low-dimensional systems.

While the combination of currentless and electrodeposition has been reported for different metals such as Pd [41, 179], Pt [196] and Rh [197] on mercaptopyridine SAMs, the scheme has also been applied to thiol-terminated SAMs by Qu and Uosaki [180, 198]. Using dithiol SAMs of 1,4-benzenedimethanethiol ($HSCH_2C_6H_4CH_2SH$, BDMT) and hexanedithiol ($HS(CH_2)_6SH$, HDT) on Au(1 1 1), Pt and Au were deposited. Interestingly, by adsorbing another thiol, namely decane thiol, onto a deposited Au metal layer, a bilayer was formed, which also demonstrates the potential of this scheme for accessing the third dimension.

The appeal of the two-step scheme is that it provides a flexible access to the generation of metal–SAM–metal structures that are of great interest both from the fundamental and application point of view. Since the work performed so far strongly suggests that it is more widely applicable (different molecules, metals), it will be interesting to see how variation of tail-group functionality affects the metal deposits and in turn their electronic properties. The reported strong dependence of the density of states (DOS) on the size and/or morphology of the metal [179] gives a first glimpse of the potential of metallization of SAMs for tailoring electronic properties and applications for electronic or catalytic purposes can be easily envisaged. To develop this field further a better understanding of the interaction between metal and SAM and their mutual influence is required. An important point is the mismatch between lattices of the SAM and the deposited metal, which causes stress in both parts. As a result, both the electronic properties of the metal and the structure of the SAM are affected, the latter being schematically indicated in Figure 5.14a. In this context it is worth mentioning that the excellent order of the PyS SAM persists only for low metal coverage, that is, sufficiently large separation of the metal islands [196]. This pinpoints the issue of whether and how the structural integrity of the SAM can be maintained upon metal deposition. It is open at present as to what extent metal atoms diffusing at the SAM surface (k_p in Figure 5.13b) can penetrate the layer and become incorporated at the SAM/substrate interface, thus, affecting the structure and stability of the layer, or accumulate at the substrate to ultimately shortcircuit top and bottom metal, which would impair electronic applications. Another question that remains unanswered at this point is whether the structural quality of a SAM can be improved and the procedure be optimized to an extent that deposition can be restricted to on top of a SAM with metal ions present in the bulk electrolyte. This would enable the somewhat tedious procedure of repetitive cycling through the 2-step scheme to be circumvented.

5.4.3
Underpotential Deposition

Metal UPD at the SAM/substrate interface is of interest for several reasons. Firstly, from an application point of view as the intercalation of another metal alters the thiol–substrate bond and, thus, the stability of a SAM that can be exploited to generate heterogeneous and patterned SAMs, a point we will return to later. Secondly, the intercalation and alteration of the thiol–substrate bond changes the morphology of a

SAM (see Figure 5.12a) and affects the molecular orientation [43, 199, 200] that, in turn, can affect the overall blocking properties of a SAM. As a step preceding bulk growth it is, therefore, crucial to know the implications of UPD.

The change in stability by UPD was first reported by Jennings and Laibinis [199, 201] who found that alkane thiols adsorbed on Au(1 1 1) modified by Ag or Cu yield a significantly more stable SAM compared to one on clean gold. An improved thermal stability of *n*-docosanethiolate ($C_{22}H_{45}S$) on UPD-Ag/Au compared to clean Au was found that is reflected by a difference in the rate constants of desorption by about an order of magnitude when immersing the SAM into organic solvents at temperatures in the range of 343–378 K [201]. The electrochemical stability of SAMs is also affected by a UPD layer, as illustrated in Figure 5.15 for a series of metals that shows the reductive desorption (see Section 5.3) of a propane thiol SAM from Au/mica [202]. While for Tl, Pb, Cd and Bi there is no or only a marginal change, a substantial shift to negative potentials is observed for Ag and Cu, thus indicating a substantial increase in stability. The effect is more pronounced for Cu than for Ag. As a consequence, no RD peak of the thiol is observed in the case of Cu since it is shifted into the region of hydrogen evolution, like for a thiol SAM on bulk Cu where reductive desorption is monitored through oxidative readsorption on a second working electrode as shown in Figure 5.11. A few things on UPD on SAMs are noteworthy here. One is that improvement in stability is independent of whether thiol adsorption follows UPD [199, 201] or whether this sequence is reversed, that is, SAM formation first and then UPD [38, 202, 203]. However, despite showing the same trend one should not assume that the same structure of the SAM/substrate interface is obtained for both procedures. These points remain to be elucidated. Another interesting point is

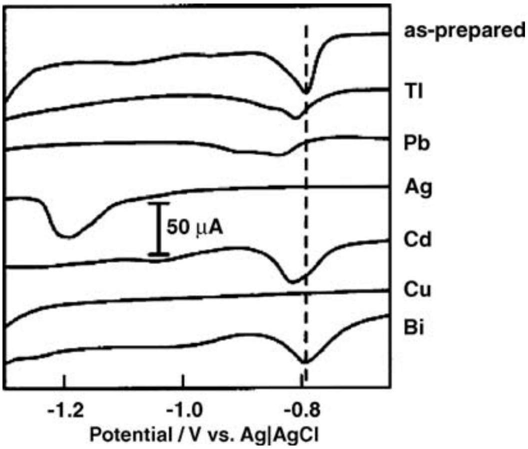

Figure 5.15 Stability change of a SAM of propane thiol on Au/mica by UPD of a series of metals. The linear sweep voltammograms were recorded in 0.5 M KOH at a scan rate of 0.1 V/s. The electrode area was 0.36 cm^2. In the case of Cu UPD no desorption is discernible since the stability is increased to such an extent that the desorption peak shifts negative beyond the range shown into the region of hydrogen evolution. Reproduced with permission from Ref. [202].

that, similar to bulk metal, UPD affects substantially the sulfur-bonding geometry as evidenced by the changes in the odd–even alternation of the orientation of methyl end group in alkane thiol SAMs [93].

Addressing the kinetics of UPD it is obvious from Figure 5.16, which compares CVs of Cu UPD of a bare gold electrode with SAM-coated ones, that the typical UPD features are completely quenched by SAMs [183]. However, even when a CV lacks any features indicating UPD this is by no means a sign that it does not occur. It is rather a question of time scale [40, 43, 204]. Therefore, caution is required when comparing results, in particular, if different techniques working on different time scales such a

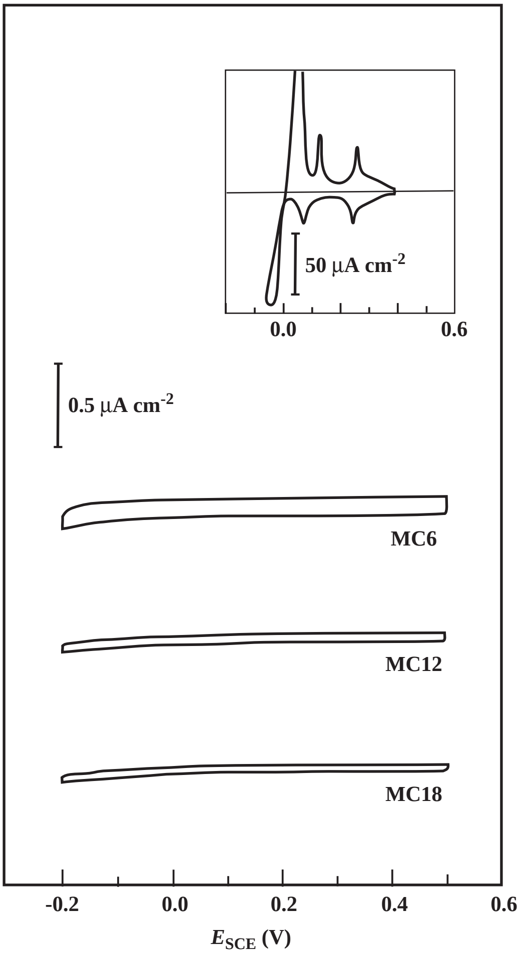

Figure 5.16 Cyclic voltammograms for the Cu deposition on alkane thiol-modified (CH_3 $(CH_2)_{m-1}$ SH, MC_m) Au(1 1 1) electrodes in 0.1 M H_2SO_4/1 mM $CuSO_4$. Scan rate: 10 mV/s. Inset shows CV for a bare Au(1 1 1) electrode for comparison. Reproduced with permission from Ref. [183].

STM and CVs are applied. This is exacerbated by the fact that the extent to which UPD features are suppressed in the CVs depends sensitively on the quality of the SAM. For such a pronounced quenching a good film quality is required, that is, a low defect density is required. To achieve this reproducibly is quite critical as has been pointed out in the literature [40, 183, 204–206]. Therefore, it is no surprise that substantial variations in the blocking properties reflected in the CVs have been observed [39, 183, 203, 207–209].

It might be helpful to clarify at this point the use of the term UPD layer in conjunction with SAM-modified electrodes. Firstly, describing deposition on clean metal substrates positive of the Nernst potential UPD is a term based on thermodynamics. However, for SAM-coated electrodes where processes can be greatly slowed down, processes restricted to the UPD region might require potentials well in the OPD region in order to proceed sufficiently fast. Secondly, use of this term does not imply that the metal layer deposited at the SAM/substrate interface is structurally identical to a normal UPD layer. On the contrary (and not surprisingly), the presence of the SAM makes it rather different as outlined below. This said, the term UPD is used here for any metal structure deposited at the SAM interface with a height of up to two layers of metal regardless of the actual potential applied.

To elucidate the mechanism of metal UPD, a number of studies on Cu and Ag UPD have been performed over the years comprising phenomenological, CV-based studies and microscopic investigations with STM both *ex situ* and *in situ* [38, 39, 42, 43, 202, 204, 210–214]. While some features, such as the formation of UPD islands, were commonly reported for various systems (different thiols and metals, that is, Ag and Cu) differing interpretations were given with respect to the details such as formation, extension or height, possibly due to the sometimes difficult interpretation of data that, furthermore, can vary with the details of the system and the experimental conditions applied. Some of the issues could be resolved in a recent study on high-quality aromatic SAMs where the UPD process could be extremely slowed down to allow time-resolved *in-situ* studies [43].

For a discussion of the mechanism of metal UPD on SAM-modified electrodes we turn to Figure 5.17, which illustrates four plausible mechanisms of UPD. If the layer has very poor blocking behavior a more or less uniform penetration might occur and the UPD should be completed within a short time (Figure 5.17a). The other mechanisms are based on a major defect at which UPD starts (Figure 5.17b). Since the presence of the UPD layer introduces height changes and, thus, a disruption of the SAM at the edge of the UPD island, one possible way of UPD growth is via ion penetration at the boundary of the UPD area (1 in Figure 5.17b). The other mechanism takes into account that the UPD island affects the structural integrity of the SAM structure caused by changes in the SAM–substrate bonding (2 in Figure 5.17b). As a consequence, the SAM becomes permeable and ions can penetrate to the electrode all across the UPD island. Either the ions or the reduced metal atoms can then diffuse to the edge of the UPD islands and intercalate in the native areas. The fourth possibility (3 in Figure 5.17b) is that the blocking properties of the SAM are not significantly affected by formation of the UPD layer. In this case the only channel is the supply of ions through the initial defect.

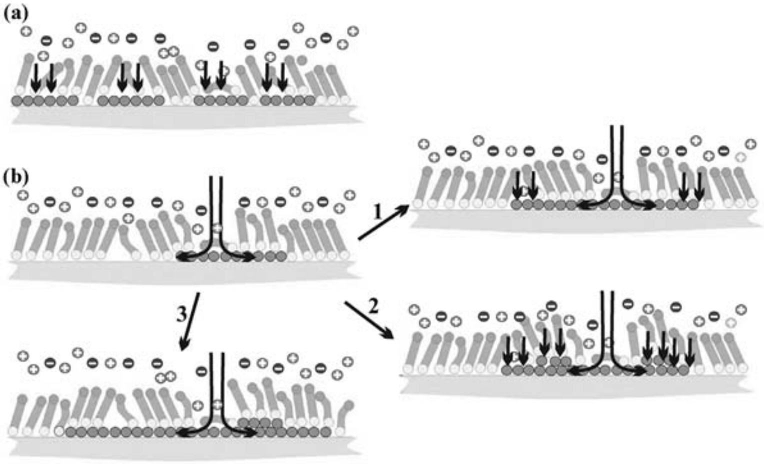

Figure 5.17 Illustration of different pathways for growth of a UPD layer on a SAM-modified electrode. (a) Uniform penetration across the whole SAM area, (b) deposition starting at a major defect with subsequent penetration at edge of UPD island (1), penetration through SAM across the whole UPD area due to the distortion of SAM structure by UPD (2) and growth of UPD island through initial defect only (3).

One can expect that the exact mechanism depends on the type of SAM. Furthermore, the various pathways for UPD might not only depend on the particular SAM system but also on the potential applied, since a SAM can undergo potential induced structural transitions as observed for ethane thiol (C_2H_5SH), for example [61, 210].

Two systems that illustrate the dependence of Cu-UPD on the type of SAM are shown in Figure 5.18. For an MC2 SAM a ramified growth can be observed (Figure 5.18a) [210]. Such a growth behavior of a UPD layer that was also reported for hexane thiol [204] points to a diffusion-limited growth caused by the slowing down of the growth kinetics due to the presence of thiols. For the other example depicted in Figure 5.18b, a SAM of MBP2, UPD is also strongly hindered. However, in this case circular Cu patches grow. A characteristic feature of this type of SAM is that the patches grow solely through ion penetration at the original defect and diffusion of metal at the SAM/substrate interface, that is, the third mechanism described in Figure 5.17b applies [43]. The initial defect being rate limiting, its dimension determines the rate at which a Cu UPD patch grows and, as a consequence, quite different temporal evolutions and sizes of the UPD patches result. The two examples illustrate the range of possibilities and represent clear-cut cases. In other cases, such as for Ag deposition on octane thiol [38], the data are less straightforward to interpret and either of the alternatives in Figure 5.17b might apply. In general, one can anticipate that it depends on the details of the system, such as robustness of a SAM to potential changes and the extent of structural modification by metal UPD which of the mechanisms is realized. To pin down the exact mechanism requires a rather detailed monitoring of UPD growth at high resolution, a requirement not always easy to meet.

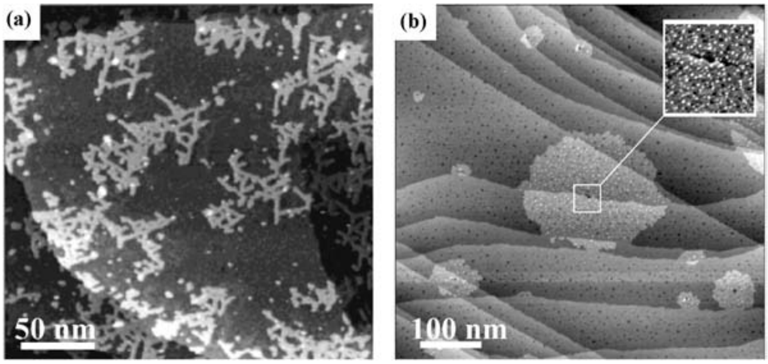

Figure 5.18 *In-situ* STM images recorded in $CuSO_4/H_2SO_4$ electrolyte of Cu UPD growth on Au(1 1 1) modified by two different types of thiols. (a) SAM of ethane thiol ($250 \times 250\,nm^2$) with a ramified structure and (b) SAM of MBP2 ($600 \times 600\,nm^2$) with circular copper patches [43]. Enlarged area reveals nanometer-sized islands protruding on patches. (a) Reproduced with permission from Ref [210].

In studies of metal UPD on SAMs, STM has been extremely valuable and provided new insights into the mechanisms down to the atomic length scale. However, data interpretation might be difficult as measured height changes induced by UPD cannot always be straightforwardly correlated to structural changes. This is illustrated in Figure 5.19, which compares Cu UPD on Au(1 1 1) coated with a SAM of either MC4 or MBP2 [200]. The topographic images show very similar UPD areas consisting of nanometer-sized islands on top of circular patches. This strongly suggests that the UPD process and the structure of the patches are very similar for MC4 and MBP2. However, a look at the height profiles reveals significant differences in the measured height of the UPD patches for the two thiols. With 2.35 Å as the internal reference value of the gold step [215, 216], a height of about 1 Å is measured for the alkane thiol, that is, substantially less than the step height for a metal monolayer, whereas for MBP2 a value around 2.3 Å is found [43], which is consistent with a metal step. The strong dependence of the patch height on the type of SAM is further evidenced by other SAMs. Another structural phase of MBP2, the so-called δ-phase, yields a value of 3.7 Å [43], whereas for MBP3 the patch can hardly be identified as its height is essentially zero [200]. The small value for alkane thiols, significantly less than a step of a metal layer might also explain the variations in the interpretation of UPD features given in the literature. Even though the nanoislands have been consistently observed for different SAMs and interpreted as islands of UPD metal [38, 42, 43, 200, 210, 217], different interpretations were given such as the nanoislands being an intermediate state of a metal monolayer at the SAM/substrate interface and growing bigger with time [38], forming behind a growth front and staying of fixed size [204] or emerging on top of a first layer [43, 211]. It is noted that the interpretation of the nanoislands in terms of a partially covered surface is incompatible with CVs monitoring the reductive desorption of thiols since the absence or strong shift of the original

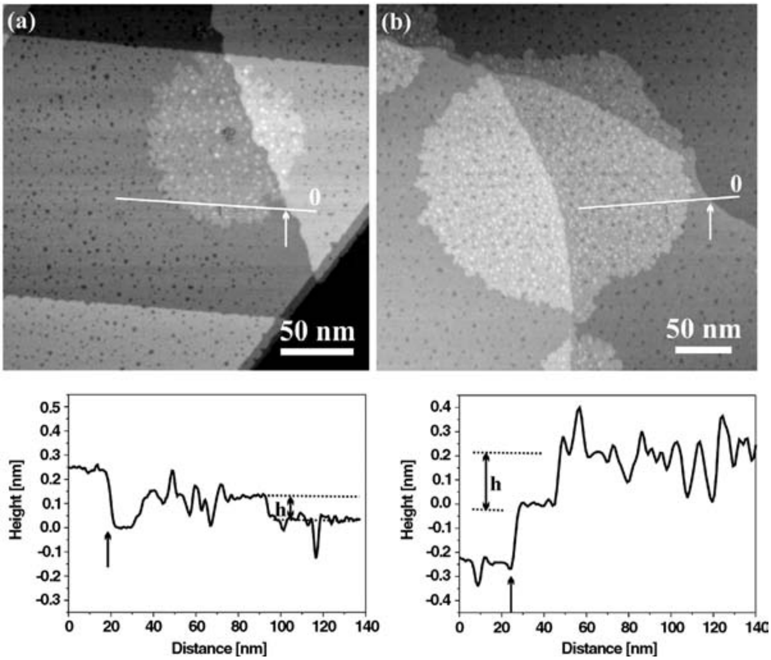

Figure 5.19 STM topographic images of patches of Cu UPD deposited on butane thiol (MC4) (a) and MBP2 (b) modified Au(1 1 1)/mica substrates together with height profiles along the lines shown. Arrows in image and height profile mark monoatomic gold steps, the steps of height *h* mark the height of the UPD patch that is about 1 Å and 2.3 Å for MC4 and MBP2, respectively. (a) Image recorded in air, $E_{\mathrm{tip}} = 0.25$ V. I = 50 pA. Deposition: 30 s at 100 mV vs Cu/Cu^{2+} from 5 mM $\mathrm{CuSO_4}$/50 mM $\mathrm{H_2SO_4}$. (b) ECSTM image, $E_{\mathrm{sample}} = 0.15$ V vs Cu/Cu^{2+}, $E_{\mathrm{tip}} = 0.33$ V, I = 40 pA. Electrolyte: 5 mM $\mathrm{CuSO_4}$/50 mM $\mathrm{H_2SO_4}$ [200].

desorption peak for Cu and Ag UPD reveals uniform deposition. From the studies of different types of SAMs, the picture emerges that the nanoislands represent a second UPD layer on top of a first one forming the patch. While the strong variation of the patch height is not clear at present, it strongly suggests that the interfacial structures are very dependent on the type of SAM, thus giving rise to different changes in geometry and electronic properties for the first layer. It is also not clear whether this first layer consists only of UPD metal or represents a mixture with Au atoms. The latter seems rather likely given the structure of the SAM/Au interface involving Au adatoms as discussed in Section 5.2 (Figure 5.4). Also, the mechanism of the nanoisland formation is not understood at present. Appearing always behind the edge of the UPD patch it is conceivable that metal UPD, causing a restructuring of the SAM, builds up stress, which could be released via this island formation. In this context it is also worth noting that the first layer is not smooth but appears significantly disrupted by holes with a typical depth in the range of a metal step.

Another common feature of metal UPD on SAM-modified electrodes is the pronounced suppression of nucleation that for bare Au occurs at steps unless the step density is very low [218]. Even though nucleation still occurs mostly at steps for

SAM-covered electrodes as seen from Figure 5.18b, the reason for this is quite different from the case of clean gold. Steps as such are not sufficient to cause nucleation, thus, evidencing that the distortion of the SAM structure caused by steps is not significant enough to allow metal UPD. Defects in the SAM have to be more substantial and contaminations present on the substrate prior to film formation are a major source for nucleation of UPD patches [43]. The fact that most of the islands nucleate at steps is, therefore, a secondary effect resulting from a preferential pinning of contaminations at steps. While the exact nature of these contaminations is not known at present a careful cleaning of the substrate can strongly reduce the size and density of the defects and, thus, minimize uncontrolled UPD, which is crucial for applications where patterned SAMs can be used to generate UPD patterns. In this context it is important to note that for SAMs of good structural quality other intrinsic defects such as domain boundaries or missing molecules are not sufficient to act as nucleation sites for metal UPD.

It is obvious that the change in stability upon UPD of Cu and Ag (Figure 5.15) can be harnessed for manipulation of SAMs, as demonstrated by the scheme of Figure 5.20a where nanopores were created in a sequence of steps involving UPD of both Ag and Cu as well as reductive desorption and adsorption of thiols [219, 220]. As evidenced by the STM image and the height profiles, nanopores on the order of 5–10 nm were formed. Since deposition of Ag UPD patches starts at defects of the SAM, the pores are randomly distributed. There are several interesting features in this scheme, one of which being that the average size of the nanopores can be controlled through the size of the Ag UPD patches, that is, deposition time of Ag. Another interesting aspect is that Ag seems to allow control of the deposition of Cu, which means that despite the fact that the Cu–thiol bond is stronger than the Ag–thiol bond as inferred from the reductive desorption (Figure 5.15), Cu does not seem to interfere with Ag, that is, Cu is deposited onto the areas where the SAM is directly adsorbed onto gold. Furthermore, the scheme promises flexibility with respect to the thiol combination as the initial SAM can be completely replaced.

In a scheme complementary to the one just presented where thiols are removed by reductive desorption of thiols, molecules can also be removed during stripping of a UPD layer. This was demonstrated by Shimazu *et al.* [221] where an alkane thiol SAM was deposited onto a Au(1 1 1) that had been modified with Pb. Oxidative stripping of the lead also caused thiols to be removed. The empty sites were then subsequently filled with mercaptopropionic acid (MPA). A remarkable result is that the binary SAMs exhibit only one desorption peak. From this it was concluded that a well-mixed layer forms that is very different from the mixed SAM obtained by adsorption from solution containing both types of thiols. In this case the layer exhibits single-component domains that are reflected by two desorption peaks.

The examples where UPD-induced stability changes of thiol SAMs are exploited to modify and manipulate SAMs down to the nanometer scale, indicate the potential of UPD for addressing the ultrasmall length scale. However, so far UPD-based modification on the small scale has only been achieved in a random fashion making use of the long-known fact that UPD originates at defects in SAMs [43, 222]. To take the UPD-based patterning of SAMs further for the controlled generation of

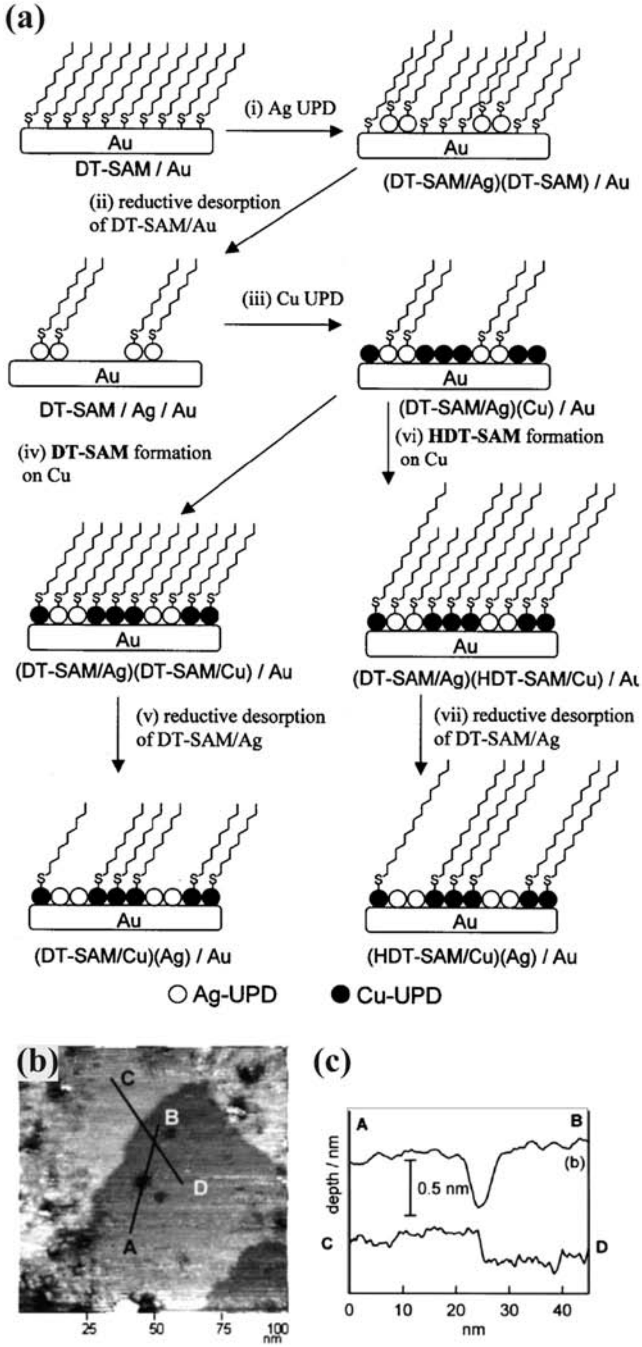

Figure 5.20 (a) Scheme of generation of mixed SAMs and nanopores using UPD of Ag and Cu. (b) STM image of a sample prepared by the sequence of steps i–v. (c) height profiles with lines A–B and C–D crossing a nanopore and a substrate step. Reproduced with permission from Ref. [220].

nanostructures, UPD has to be exactly defined with respect to its location and lateral dimension, which can be achieved by generating defects in SAMs in a controlled way. However, this also means that uncontrolled defects introduced during the formation of a SAM have to be minimized, that is, SAMs of very high structural quality are required. As mentioned above, for good-quality SAMs this type of defects have been shown to consist of extrinsic defects such as molecular impurities or contaminations on the substrate [43], whereas intrinsic defects such as domain boundaries or step edges in the substrate can be tolerated. Controlled local modification of SAMs on the small scale is easily done, for example, through degradation of the molecules by an electron beam [36, 223]. Other schemes of SAM modification rely on scanning probe techniques, such as SECM [224, 225], STM or AFM, which have been used in different ways [6, 7] including mechanical disruption of a SAM by AFM [226] (nanoshaving) or STM-induced removal of thiols by applying a voltage between tip and substrate above the damage threshold. It is noted that, depending on the conditions, an electrochemical process can underlie the latter [124, 227–229]. The latter was applied in the example given in Figure 5.21, which shows spatially controlled UPD of copper [230]. With the sample in air, an array of nanoscopic patches was produced first by pulsing an STM tip, which locally disrupts the SAM. Subsequently, UPD of Cu was accomplished in an electrochemical cell. The patches where the SAM was damaged act as nucleation centers, analogous to the case of a SAM with extrinsic defects (see Figure 5.18b). UPD appears as concentric protruding rings that grow in size as deposition time proceeds. For the image recorded after 12 min (Figure 5.21d) the characteristic nanoislands discussed above become discernible. It is worth mentioning that while UPD occurs easily in the damaged area there is still a high barrier against bulk-metal deposition. While the exact mechanism is not yet known, this indicates that the patches do not expose the clean substrate but thiols are still present, even though in the case shown the voltage of the patterning pulse was high enough to cause damage not only to the SAM but also to the underlying substrate. This is, for example, apparent from Figure 5.21c where the depressions seen inside a patch have a depth corresponding to a multiple of the height of a Au step. The example is also interesting from a technological point of view as it shows defined deposition in an area of rather high step density. It is, thus, another illustration that unavoidable intrinsic defects such as steps are not impeding the application of thiol SAMs for controlling electrochemical metal deposition on the nanometer scale.

While the spatially controlled Cu UPD just discussed takes the top-down approach, that is, it is based on small-scale patterns inscribed into initially uniform SAMs, a complementary approach was taken recently by generating patterned SAMs via molecular self-assembly. In this scheme a porous hydrogen-bonded network acts as template to direct thiol adsorption, as shown in Figure 5.22. Upon exposure of a PTCDI/melamine network on Au(1 1 1) to a thiol solution, the molecules adsorb into the pores, thus yielding an extended array of hexagonal SAM islands [231]. This solution-based approach not only provides rather straightforward access to the generation of precisely defined regular patterns on the sub-5 nm scale but also yields a SAM–network hybrid structure whose behavior towards UPD is quite different from a homogeneous SAM in several ways. Firstly, the presence of the network

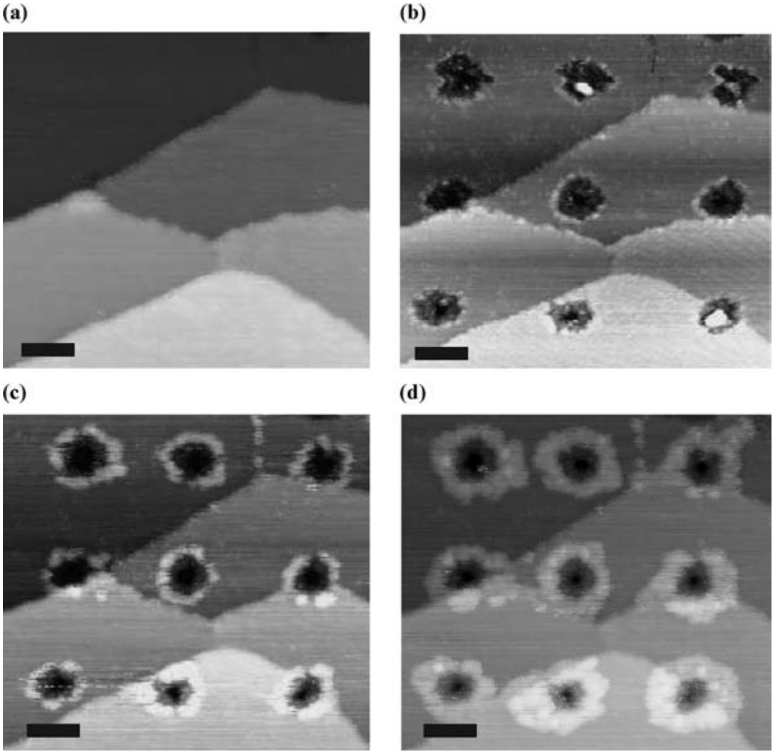

Figure 5.21 Cu UPD on a SAM patterned by an STM tip. (a) Native BP2 SAM on Au(1 1 1) and (b) array of nine patches generated by tip induced modification. A patch was generated by applying a voltage pulse of 3.5 V for 50 ms. Modification and imaging was done in air. (c, d) *In-situ* ECSTM images of Cu UPD at different stages. (c) was recorded immediately after start of UPD and (d) after 12 min. Scale bars are 20 nm [230].

makes the SAM very open and, thus, greatly facilitates Cu UPD. Deposition is accomplished within minutes compared to uniform SAMs where deposition can take hours under comparable conditions. Secondly, since the network acts like well-defined defects, deposition occurs uniformly across the whole pattern (Figure 5.22d). Thirdly, the UPD mechanism is also rather different, as inferred from comparison of Figure 5.18b with Figure 5.22c. In contrast to the uniform SAM where UPD copper spreads across the SAM/substrate interface by lateral diffusion over distances easily exceeding 100 nm, this is suppressed by the network. The presence of isolated, UPD-modified pores that are marked by the arrows Figure 5.22c, evidence that Cu UPD is accomplished via direct deposition into the cell and not by a surface diffusion mechanism [231, 232]. This is an interesting feature from the perspective of the application of Cu UPD on the nanoscale since the uncontrolled spreading at the interface in the case of the uniform SAM, which might become a factor limiting

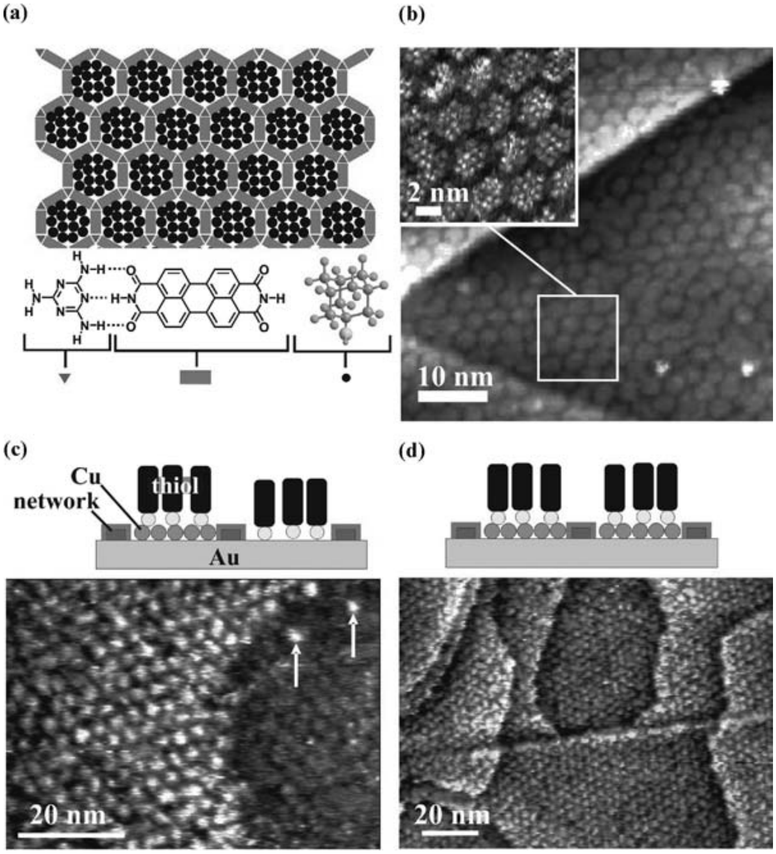

Figure 5.22 Cu UPD on a Au/mica substrate modified by a hybrid nanostructure consisting of a hydrogen-bonded network and a thiol SAM. (a) Cartoon of the hybrid structure and molecular structures of the components. The hydrogen-bonded network is composed of 1,3,5-triazine-2,4,6-triamine (melamine, triangles) and perylene-3,4,9,10-tetracarboxylic di-imide (PTCDI, rectangles) that interact via a triple hydrogen bond (dotted lines). Pores of the network are filled with adamantane thiol (circles). (b) STM images of network–SAM hybrid structure with inset showing the hexagonal thiol island at molecular resolution. (c, d) Schematic illustrations and STM images of Cu UPD on hybrid structure with partial and full UPD shown in (c) and (d), respectively. Arrows in (c) mark individual adamantane thiol islands modified by Cu UPD.

the ultimately achievable resolution, is eliminated by the presence of the supramolecular network.

5.4.4
Bulk-Metal Deposition

As indicated above, failure of depositing metal on top of a SAM directly from bulk solution results from the imperfections in SAMs that allow metal ions to penetrate, thus making reduction at the electrode much more likely due to the strong dependence of charge transfer on the tunneling distance (Equations 5.4 and 5.5). With defect-mediated deposition starting at the electrode surface, metal deposition is two-dimensional in the low-overpotential range as discussed in the previous section. Only at more negative potential does the transition to three-dimensional mushroom-like growth occur, as illustrated in Figure 5.12c, with the onset from 2D to 3D being strongly dependent on the details of the system. This type of growth has been observed for different systems such as Cu [37], Ag [209] and Rh [233] and the formation of hemispherical particles on top of the SAM seems to be a common feature [37, 233]. The overpotential required to initiate bulk growth is significant, even for the very short alkane thiols like ethane thiol [210]. For alkanethiols with more than five methylene units a two-dimensional growth was reported for potentials positive of $-200\,\mathrm{mV}$ (vs. $\mathrm{Cu/Cu^{2+}}$) [234] that changed into a 3D mode for more negative potentials. In general, the overpotential required for 3D growth scales with the thickness of the layer. For alkane thiols a shift of about $\sim$15–25 mV per $\mathrm{CH_2}$ unit has been observed [37, 178], even though no detailed measurements are available, that is, it is not clear whether this is a truly linear dependence and over what range of chain length this holds. The main effect of an increasing layer thickness can be assumed to arise from an increasing ability of the molecules to mask structural defects such as missing molecules or contaminations with the latter, as discussed in Section 5.4.3, playing a particularly important role. The resulting reduction in the rate of penetration of ions into the layer makes it increasingly difficult for a metal nucleus to reach the critical size and become thermodynamically stable, in particular as other processes compete such as the lateral diffusion at the SAM/substrate interface (Figures 5.17 and 5.18b). Another point is that the SAM should not be considered a static system and, therefore, a nucleus *in status nascendi* could be passivated due to the mobility of the thiol molecules that can be expected to become even more important in cases where the metal deposit binds more strongly to the thiol than the substrate metal. In general, the deposition current exhibits the characteristic shape of a nucleation and growth process, that is, a delayed maximum (similar to the curves depicted in Figure 5.10 for short times of SAM formation) but nucleation and growth morphology of metal deposits depend on the details of the experiment, that is, the type and structural quality of the SAM as well as the potential applied [207, 210, 234]. Lower overpotentials or current densities result in less dense nucleation and larger clusters, whereas high nucleation density and smoother deposits prevail at higher overpotential/current densities.

With respect to the influence of the end group no conclusive picture has emerged yet since only a few studies have been performed on rather different systems. The interpretation is also complicated by the fact that the change of the end group is not only affecting the interaction of the SAM with the metal ion/atom but can also affect the SAM structure. Therefore, the influence ranges from negligible ($\mathrm{CH_3}$ vs. OH [37, 209]) to distinctly different ($\mathrm{CH_3}$ vs. SH [209]). Detailed studies of the influence of the type of spacer on the deposition behavior are essentially lacking. One study comparing SAMs of alkane with MBPm thiols of similar length showed better passivation for the former [178].

Irrespective of the lack of detailed knowledge at present, one can imagine that the SAM-dependent conditions for bulk-metal deposition have potential for applications since SAMs can be patterned on length scales ranging from macroscopic dimensions to sub-20 nm [5, 8]. Patterning combines favorably with another property of SAMs, namely the tuning of interfacial energies and, thus, control of adhesion. All these aspects open up interesting opportunities for electrochemical generation of metal structures with SAM acting as templates in different ways.

There are several possibilities to exploit the inhibition of metal deposition by SAMs and the most obvious way is to selectively passivate an electrode surface by a SAM pattern and deposit metal on the SAM-free areas. On the scale of micrometers or slightly below one micrometer this is straightforwardly done by a stamping technique, called microcontact printing (μCP) [5]. A flexible polymeric stamp bearing the pattern is inked with a thiol and brought into contact with the substrate upon which the thiol transfers to the substrate in the areas defined by the pattern. For such a selectively passivated surface, electrochemical metal deposition takes place only in the uncoated areas [177]. In this context, a complementary procedure is worth mentioning where the blocking properties of a SAM are utilized to generate a relief in a metal substrate. An alkane thiol pattern on a copper substrate resulted in selective electrochemical dissolution of the metal only in the SAM-free areas [235].

Another related approach starts from a uniform SAM and contrast is achieved by selective modification of the SAM. Different methods can be applied based on, for example, mechanical scribing [177], AFM [236], photons [237, 238] or electrons [36, 223] and sub-100 nm features can be easily generated. For all these techniques SAMs act as positive resists, that is, the SAM is locally removed or chemically changed at least to an extent that its blocking properties are significantly reduced compared to the native SAM and, therefore, metal deposition takes place in the modified areas. In this context electron-beam lithography (EBL) is particularly interesting. Besides offering very high resolution down to the sub-20 nm range, both types of resists, that is, positive and negative, can be realized by proper choice of the type of molecule. Alkane thiols act as positive resists since degradation of the layer by the electron beam results in a loss of the blocking properties [36, 96, 223, 239]. In contrast, aromatic thiols exhibit negative-resist behavior with irradiated areas becoming more passivating than native ones [96, 223, 239]. This is due to crosslinking of the aromatic units [240], which reduces the size and number of defects acting as nucleation sites for metal deposition. A demonstration of this scheme is shown in Figure 5.23 where Cu was deposited onto an MBP12-modified electrode that was irradiated with electrons through a mask. The optical micrographs shown in Figure 5.23b evidence that extended structures can be deposited and the SEM image demonstrates the possibility to generate structures in the submicrometer range. However, the SEM image also highlights some of the issues that have to be addressed to make not only EBL patterned but any patterned SAM routinely applicable to metal deposition on a length scale well below 100 nm. There is, firstly, the need to further suppress deposition in passivating areas. Even though the overall passivation in the shown example of a crosslinked SAM is very good, growth of some isolated granules still occurs. Secondly, the location of nucleation sites has to be exactly controlled as

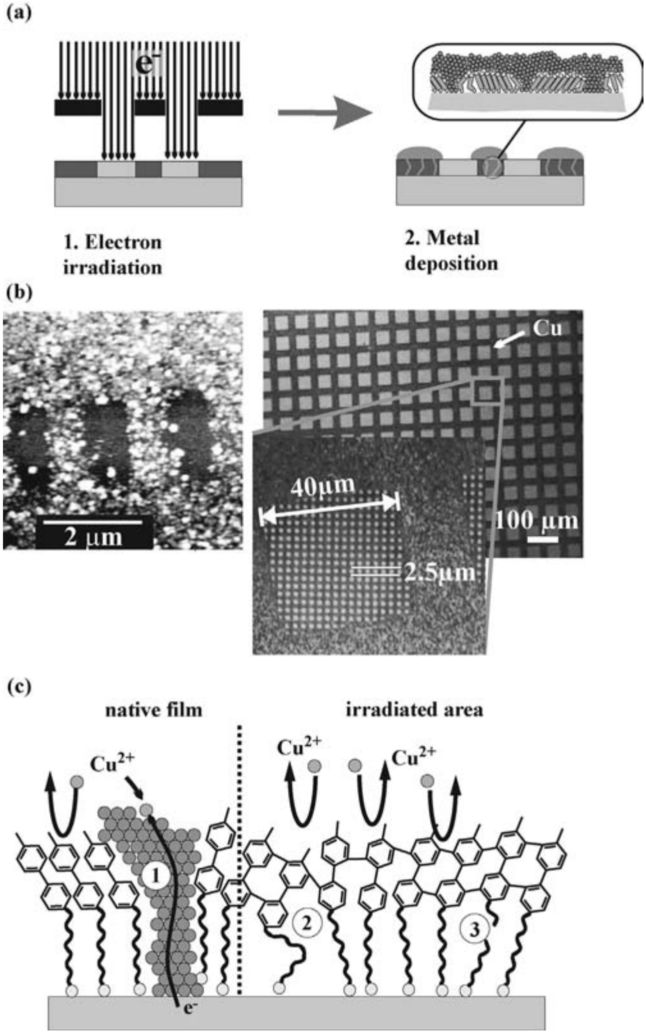

Figure 5.23 Electrochemical Cu deposition onto a SAM of MBP12 on Au. (a) Patterning scheme involving patterning by electron irradiation through a mask and subsequent localized electrochemical metal deposition. (b) optical micrographs (right) and SEM image (left) of deposited Cu patterns. (c) Illustration of the deposition process. Copper deposition in areas of the native SAM occurs at defects (1). Electron irradiation links the biphenyl moieties that can mask defects (2) or damage in the alkane chain caused by electron irradiation (3). After Ref. [96].

this will be a major factor in determining how small and well-defined any metal structure can be produced. Nucleation and growth at random defects on which bulk deposition has been relied on so far will not be sufficient. With respect to EBL it is noted that for alkanethiols, which act as a positive resist, degradation is hard to control exactly due to the chemical processes involved [241] leaving fragments on the surface whose structural details are not clear. From that perspective, aromatic thiols seem to be better suited as deposition is on areas of the native SAM with, hence, a well-defined structure. As far as defects in the passivating areas are concerned it remains to be clarified whether extrinsic contaminations are responsible, analogous to metal UPD discussed in Section 5.4.3, or whether this is a limitation intrinsic to the statistical nature of the crosslinking process.

An alternative to patterning methods that involve chemical reactions such as bond cleavage, crosslinking or oxidation processes, is the use of a binary SAM with one SAM being highly blocking and the other SAM allowing for metal deposition. This introduces quite some flexibility with regard to the freedom of choice of molecules. For the areas where metal deposition takes place, either poorly blocking SAMs resulting in a mushroom-type growth or complexing ones allowing metal deposition on top of the SAM can be used. While for a mere definition of areas of metal deposition, patterns consisting of crosslinked and native SAMs or a blocking/nonblocking combination of two types of molecules offer no advantage over patterns defined by a single-component SAM and areas of clean electrode surface, there is a decisive difference with respect to the adhesion of the deposited metal structure onto the electrode. On the SAM-coated electrode metal is deposited, as discussed, in a mushroom-like fashion by defect-mediated deposition and a continuous layer results upon further growth. As indicated in Figure 5.23a the deposited metal is only in contact with the electrode metal through the trunks of the mushroom, which means that the area of direct contact between substrate and deposit is greatly reduced compared to deposition on a clean metal surface. Since the interaction between metal and SAM is dominated by dispersion forces, adhesion is very poor compared to metal–metal interactions and the deposited metal can be easily lifted off. While electrochemical metal deposition on a weakly interacting substrate with subsequent transfer to an insulating substrate had been realized before [242], the nature of the substrate used and the underlying mechanism, that is, step decoration on graphite, restricted the process to the generation of nanowires. The limitation is lifted by use of SAMs that can act not only as templates to define arbitrarily shaped 2D patterns but can also be applied to nonflat geometries. The latter, pioneered by Schilardi *et al.* [176] and discussed in detail in Ref. [30], allows for a highly conformal reproduction of surface topographies. A master structure such as a grating, coated by an alkane thiol SAM, serves as a mold onto which metal is deposited in a mushroom-type fashion, yet in a highly conformal way. Due to the small effective area of direct contact between deposited metal and substrate the lift off is easily possible, thus, on the one hand, leaving the master behind for another replication cycle. The replica, on the other hand, can be used itself as a master and applying the same procedure to the replica, the shape of the original master is reproduced. Despite the simplicity of this process its precision is remarkable, as shown by the generation of an array of Cu dots from a Au master with an hexagonal arrangement of holes. The holes with a depth of about 3 nm and a diameter of $\sim$50 nm were well reproduced both with respect to the inplane and vertical dimensions. Two further points are also interesting for applications. One is that deposition was not restricted to metal but also successful deposition and lift off of semiconducting Cu_2O and ZnO structures were reported [30]. The other interesting point is the use of Cu as the material for the master substrate. Since, as discussed in Section 5.3, the higher stability of thiol SAMs extends the potential range to more negative values, less-noble metals can be deposited. Even an alloy, namely CoNiFe, was deposited [243, 244] which is appealing from the application point of view as this alloy is magnetic. The possibility to lift off the structure evidences that the thiol SAM is not desorbed reductively even at the negative potential required to deposit these metals. In contrast, use of a Au substrate with a more positive RD potential resulted in

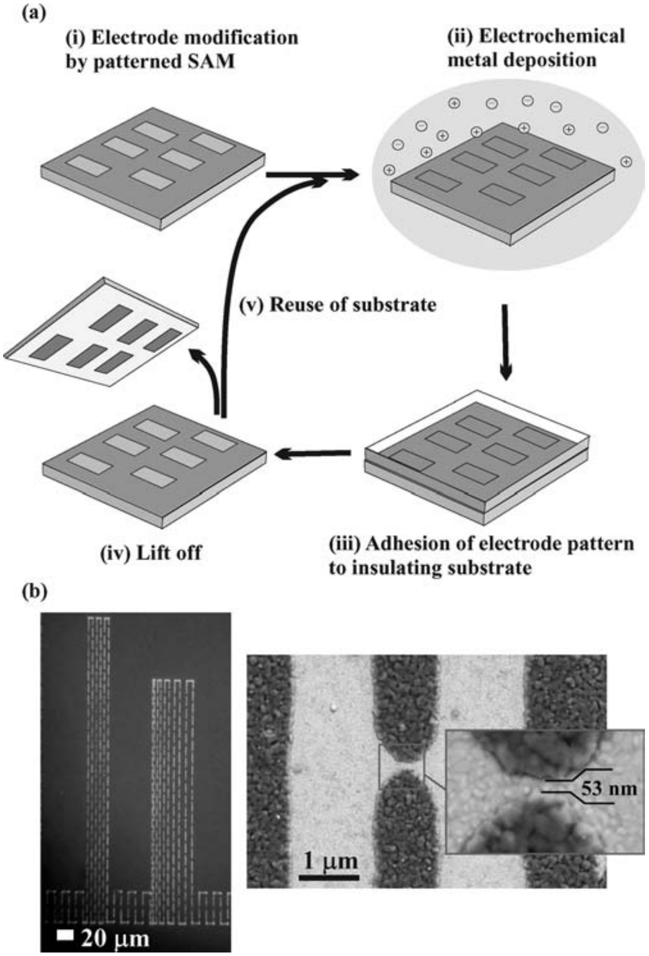

Figure 5.24 Template-directed metal deposition and lift-off scheme based on a SAM defining a pattern of blocking and nonblocking thiols. (a) illustration of the process starting with the generation of the master (i), metal deposition (ii), attachment of an insulating transferring substrate (iii) and subsequent lift off (iv). Provided that the SAM is sufficiently robust the original substrate can be repeatedly used for the deposition/lift-off cycle. (b) Optical micrograph (left) and SEM image (right) of Cu patterns generated by a binary SAM consisting of MBP1 and MC16. Optical micrograph shows a Cu structure on glass (step iv). The SEM image shows a sample after step (ii).

a well-adhering CoNiFe layer, thus indicating that the SAM was destroyed during deposition.

An extension of the scheme just described is to use binary SAMs that consist of blocking and non-blocking thiols and that bear a pattern defined by these two types of molecules. This enables the scheme depicted in Figure 5.24a. Starting with the preparation of a master bearing a SAM pattern (i), localized deposition is accomplished by the SAM acting as template (ii). After attachment of an insulating substrate (iii) and lift off (iv), the master can be reused (v). The advantage of the deposition/lift off cycle is obvious, both for uniform and patterned SAMs, since it is fast, simple and scalable due to the electrochemical process. Examples demonstrating the concept are seen in Figure 5.24b. The SEM image showing a gap of about 50 nm between Cu lines indicates that nanoscopic dimensions can be easily addressed. Envisaging the nanoscopic length scale there is another crucial point, which is the fact that the master can be reused. Therefore, the most sophisticated step in this scheme, that is, the generation of the master pattern has to be only done occasionally with the number of cycles possible depending on the robustness of the SAM. Since the patterning process becomes increasingly cumbersome due to the necessity of using serial techniques such as an electron beam or scanning probe techniques this aspect becomes increasingly attractive with shrinking dimensions. It has to be seen how far into the nanometer dimension this scheme can be developed that, again, will depend on how well nucleation can be controlled. Since for applications on the ultrasmall scale it is a central issue to control the points of nucleation, the scheme based on two intact layers appears of advantage over patterning involving chemical alteration of the SAM.

5.5
Summary and Outlook

Different aspects of thiol SAMs have been addressed in this chapter comprising the interplay of structure-determining factors, patterning and manipulation, and electrochemical metal deposition. With respect to the latter, two complementary facets have been highlighted that are modification of SAMs through metal UPD on the one hand and control of metal deposition by SAMs on the other hand. The unique features associated with an electrochemically controlled liquid/solid interface such as the precise control of conditions, reversibility, scalability and simplicity, together with the various possibilities to deposit metal on SAM-modified electrodes, that is, at the SAM/substrate interface, on top of a SAM and in a mushroom-like fashion, as summarized in Figure 5.12, open a number of exciting perspectives for developments related to nanotechnology. However, with studies of the underlying basic processes performed almost exclusively on uniform, single-component SAMs, binary heterogeneous SAMs with a random distribution of phases or patterned on a relative large length scale of typically micrometers or somewhat below, the key question is to what extent it is possible to exploit the combination of SAMs and electrochemistry for the nanoscale. A characteristic effect of shrinking dimensions, the breakdown of familiar concepts with the suddenly dominating role of processes that are of negligible influence on a larger scale, can safely be expected to become also a major issue for the combination of electrochemistry and SAMs. One example, which might serve as illustration of possible challenges ahead, is the patterned modification of a SAM by intercalation of a UPD metal layer. While this is relatively straightforwardly achieved on a length scale well above 10 nm, as illustrated by Figure 5.21 the situation for even smaller dimensions might be very different, as inferred from studies discussed in conjunction with Figure 5.18. Defects with dimensions of a few nm exhibit a drastically changed behavior compared to big defects as the associated UPD islands show an individual growth behavior and even a fluctuating behavior with respect to their growth rate. Therefore, reproducibility on the ultrasmall length scale requires further advancement of our understanding of the molecular processes involved, of which the dynamics of SAMs and its influence on electrochemical processes are of particular relevance. Similarly, extension of defect-mediated bulk-metal growth as discussed in Section 5.4.4 to the ultrasmall length scale will require a better understanding of the influence of SAM molecules on nucleation and growth of metal deposits. Another example refers to metal deposition on top of a SAM (Figure 5.14). This type of metal-organic interface offers unprecedented opportunities for tailoring properties of metal structures since for these low-dimensional metal structures the interaction with the environment, that is, the SAM, is of major influence on their electronic properties. Since this type of metallization involves nucleation and growth processes on a substrate that is very different in terms of structure and interactions compared to, for example, metal or inorganic insulating surfaces, further developments in this area will be determined by the understanding of the mutual influence of SAM and metal at the molecular level and by the precision at which these processes can be controlled. While these few examples illustrate that significant challenges lie ahead to harness the opportunities for nanotechnological applications afforded by the combination of SAMs and electrochemistry, the knowledge acquired up to now is solid enough to make it an endeavor well worth exploring further.

Acknowledgments

Support by EPSRC, Deutsche Forschungsgemeinschaft and The Leverhulme Trust is gratefully acknowledged. The author would also like to thank D. M. Kolb for helpful discussions and, in particular, former and present members of the author's group, P. Cyganik, R. Madueno, M. Räisänen, C. Shen, C. Silien and I. Thom for their invaluable contributions.

Appendix: List of abbreviations

AFM	Atomic force microscopy
BP	Biphenyl
CV	Cyclic voltammogram

DFT	Density functional theory
DMDS	Dimethyldisulfide, CH_3SSCH_3
DOS	Density of states
EBL	Electron beam lithography
ECSTM	Electrochemical scanning tunnelling microscopy
GXRD	Grazing incidence X-ray diffraction
HER	Hydrogen evolution reaction
MBPm	ω-(4′-methylbiphenyl-4-yl)alkanethiols, $CH_3(C_6H_4)_2$-$(CH_2)_mSH$
MCm	*n*-alkane thiols, $CH_3(CH_2)_{m-1}SH$
μCP	Micro contact printing
MD	Molecular dynamics
MPA	Mercaptopropionic acid, $HOOC(CH_2)_2SH$
MUA	Mercaptoundecanoic acid ($CH_3(CH_2)_{10}SH$)
NIXSW	Normal incidence X-ray standing wave
NP	Nanoparticle
OPD	Overpotential deposition
PED	Photoelectron diffraction
RD	Reductive desorption
PZC	Potential of zero charge
SAM	Self-assembled monolayer
SECM	Scanning electrochemical microscope
SEM	Scanning electron microscopy
SHG	Second harmonic generation
STM	Scanning tunneling microscopy
UPD	Underpotential deposition
UPS	Ultraviolet photoelectron spectroscopy
XPS	X-ray photoelectron spectroscopy
VI	Vacancy island

References

1 Nuzzo, R.G. and Allara, D.L. (1983) *Journal of the American Chemical Society*, **105**, 4481.

2 Taniguchi, I., Toyosawa, K., Yamaguchi, H. and Yasukouchi, K. (1982) *Journal of the Chemical Society. Chemical Communications*, 1032.

3 Sagiv, J. (1980) *Journal of the American Chemical Society*, **102**, 92.

4 Ulman, A. (1996) *Chemical Reviews*, **96**, 1533.

5 Love, J.C., Estroff, L.A., Kriebel, J.K., Nuzzo, R.G. and Whitesides, G.M. (2005) *Chemical Reviews*, **105**, 1103.

6 Liu, G.-Y., Xu, S. and Qian, Y. (2000) *Accounts of Chemical Research*, **33**, 457.

7 Kramer, S., Fuierer, R.R. and Gorman, C.B. (2003) *Chemical Reviews*, **103**, 4367.

8 Smith, R.K., Lewis, P.A. and Weiss, P.S. (2004) *Progress in Surface Science*, **75**, 1.

9 Dicke, C. and Hähner, G. (2002) *Journal of the American Chemical Society*, **124**, 12619.

10 Zolk, M., Eisert, F., Pipper, J., Herrwerth, S., Eck, W., Buck, M. and Grunze, M. (2000) *Langmuir*, **16**, 5849.

11 Herrwerth, S., Eck, W., Reinhardt, S. and Grunze, M. (2003) *Journal of the American Chemical Society*, **125**, 9359.

12 Miller, D.R.J., McLendon, G.L., Nozik, A.J., Schmickler, W. and Willig, F. (1995) *Surface Electron Transfer Processes*, VCH Publishers, Weinheim.

13 Adams, D.M., Brus, L., Chidsey, C.E.D., Creager, S., Creutz, C., Kagan, C.R., Kamat, P.V., Lieberman, M., Lindsay, S., Marcus, R.A., Metzger, R.M., Michel-Beyerle, M.E., Miller, J.R., Newton, M.D., Rolison, D.R., Sankey, O., Schanze, K.S., Yardley, J. and Zhu, X.Y. (2003) *The Journal of Physical Chemistry B*, **107**, 6668.

14 Porter, M.D., Bright, T.B., Allara, D.L. and Chidsey, C.E.D. (1987) *Journal of the American Chemical Society*, **109**, 3559.

15 Chidsey, C.E.D. (1991) *Science*, **251**, 919.

16 Becka, A.M. and Miller, C.J. (1992) *The Journal of Physical Chemistry*, **96**, 2657.

17 Miller, C. and Graetzel, M. (1991) *The Journal of Physical Chemistry*, **95**, 5225.

18 Miller, C., Cuendet, P. and Graetzel, M. (1991) *The Journal of Physical Chemistry*, **95**, 877.

19 Azzaroni, O., Cipollone, M., Vela, M.E. and Salvarezza, R.C. (2001) *Langmuir*, **17**, 1483.

20 Tremont, R. and Cabrera, C.R. (2002) *Journal of Applied Electrochemistry*, **32**, 783.

21 Burshtain, D., Wu, J., Melman, A., Mandler, D. and Scherson, D.A. (2004) *Langmuir*, **20**, 4498.

22 Mandler, D., Gal-Oz, R., Burshtain, D. and Turyan, I. (2003) in *Electrochemical Metal Speciation using Self-Assembled Monolayers* (eds D. Mandler, R. Gal-Oz, D. Burshtain and I. Turyan), E D P Sciences, Grenoble, France, p. 801.

23 Finklea, H.O. (1996) in *Electroanalytical Chemistry*, vol. 19 (eds A. Bard and I. Rubinstein), Marcel Dekker, New York, p. 109.

24 Kaifer, A.E. and Gomez-Kaifer, M. (1999) *Supramolecular Electrochemistry*, Wiley-VCH, Weinheim.

25 Mirsky, V.M. (2002) *Trac-Trends in Analytical Chemistry*, **21**, 439.

26 Gooding, J.J., Mearns, F., Yang, W.R. and Liu, J.Q. (2003) *Electroanalysis*, **15**, 81.

27 Chen, D. and Li, J. (2006) *Surface Science Reports*, **61**, 445.

28 Potyrailo, R.A. and Mirsky, V.M. (2008) *Chemical Reviews*, **108**, 770.

29 Schneeweiss, M.A., Hagenström, H., Esplandiu, M.J. and Kolb, D.M. (1999) *Applied Physics A–Materials Science & Processing*, **69**, 537.

30 Schilardi, P.L., Dip, P., Claro, P.C.D., Benitez, G.A., Fonticelli, M.H., Azzaroni, O. and Salvarezza, R.C. (2005) *Chemistry – A European Journal*, **12**, 38.

31 Salaun, P., Planer-Friedrich, B. and van den Berg, C.M.G. (2007) *Analytica Chimica Acta*, **585**, 312.

32 Anker, J.N., Hall, W.P., Lyandres, O., Shah, N.C., Zhao, J. and Van Duyne, R.P. (2008) *Nature Materials*, **7**, 442.

33 Cuniberti, G., Fagas, G. and Richter, K. (2005) in *Introducing Molecular Electronics*, Lecture notes in Physics Vol. 680 (eds G. Cuniberti, G. Fagas and K. Richter), Springer, Heidelberg.

34 Barnes, W.L., Dereux, A. and Ebbesen, T.W. (2003) *Nature*, **424**, 824.

35 Shalaev, V.M. (2007) *Nature Photonics*, **1**, 41.

36 Sondag-Huethorst, J.A.M., Vanhelleputte, H.R.J. and Fokkink, L.G.J. (1994) *Applied Physics Letters*, **64**, 285.

37 Sondag-Huethorst, J.A.M. and Fokkink, L.G.J. (1995) *Langmuir*, **11**, 4823.

38 Oyamatsu, D., Nishizawa, M., Kuwabata, S. and Yoneyama, H. (1998) *Langmuir*, **14**, 3298.

39 Cavalleri, O., Bittner, A.M., Kind, H. and Kern, K. (1999) *Zeitschrift Fur Physikalische Chemie-International Journal of Research in Physical Chemistry & Chemical Physics*, **208**, 107.

40 Hagenström, H., Schneeweiss, M.A. and Kolb, D.M. (1999) *Electrochimica Acta*, **45**, 1141.

41 Baunach, T., Ivanova, V., Kolb, D.M., Boyen, H.G., Ziemann, P., Buttner, M. and Oelhafen, P. (2004) *Advanced Materials*, **16**, 2024.

42 Baunach, T. and Kolb, D.M. (2002) *Analytical and Bioanalytical Chemistry*, **373**, 743.

43 Silien, C. and Buck, M. (2008) *The Journal of Physical Chemistry C*, **112**, 3881.

44 Schreiber, F. (2000) *Progress in Surface Science*, **65**, 151.

45 Yang, D.F., Wilde, C.P. and Morin, M. (1996) *Langmuir*, **12**, 6570.

46 Zhong, C.J., Zak, J. and Porter, M.D. (1997) *Journal of Electroanalytical Chemistry*, **421**, 9.

47 Loglio, F., Schweizer, M. and Kolb, D.M. (2003) *Langmuir*, **19**, 830.

48 Schweizer, M., Hagenström, H. and Kolb, D.M. (2001) *Surface Science*, **490**, L627.

49 Schweizer, M., Manolova, M. and Kolb, D.M. (2008) *Surface Science*, **602**, 3303.

50 Tamchang, S.W., Biebuyck, H.A., Whitesides, G.M., Jeon, N. and Nuzzo, R.G. (1995) *Langmuir*, **11**, 4371.

51 Lewis, P.A., Smith, R.K., Kelly, K.F., Bumm, L.A., Reed, S.M., Clegg, R.S., Gunderson, J.D., Hutchison, J.E. and Weiss, P.S. (2001) *The Journal of Physical Chemistry B*, **105**, 10630.

52 Valiokas, R., Ostblom, M., Svedhem, S., Svensson, S.C.T. and Liedberg, B. (2002) *The Journal of Physical Chemistry B*, **106**, 10401.

53 Dhirani, A.A., Zehner, R.W., Hsung, R.P., GuyotSionnest, P. and Sita, L.R. (1996) *Journal of the American Chemical Society*, **118**, 3319.

54 Dou, R.F., Ma, X.C., Xi, L., Yip, H.L., Wong, K.Y., Lau, W.M., Jia, J.F., Xue, Q.K., Yang, W.S., Ma, H. and Jen, A.K.Y. (2006) *Langmuir*, **22**, 3049.

55 Xu, Q.M., Ma, H., Yip, H. and Jen, A.K.Y. (2008) *Nanotechnology*, **19**, 135605.

56 Shen, C., Haryono, M., Grohmann, A., Buck, M., Weidner, T., Ballav, N. and Zharnikov, M. (2008) *Langmuir*, **24**, 12883.

57 Ong, T.H., Ward, R.N., Davies, P.B. and Bain, C.D. (1992) *Journal of the American Chemical Society*, **114**, 6243.

58 Baunach, T., Ivanova, V., Scherson, D.A. and Kolb, D.A. (2004) *Langmuir*, **20**, 2797.

59 Tai, Y., Shaporenko, A., Eck, W., Grunze, M. and Zharnikov, M. (2004) *Applied Physics Letters*, **85**, 6257.

60 Lahann, J., Mitragotri, S., Tran, T.N., Kaido, H., Sundaram, J., Choi, I.S., Hoffer, S., Somorjai, G.A. and Langer, R. (2003) *Science*, **299**, 371.

61 Hagenström, H., Schneeweiss, M.A. and Kolb, D.M. (1999) *Langmuir*, **15**, 2435.

62 Seo, K. and Borguet, E. (2007) *The Journal of Physical Chemistry C*, **111**, 6335.

63 Lüssem, B., Müller-Meskamp, L., Karthäuser, S. and Waser, R. (2005) *Langmuir*, **21**, 5256.

64 Müller-Meskamp, L., Lüssem, B., Karthäuser, S. and Waser, R. (2005) *The Journal of Physical Chemistry B*, **109**, 11424.

65 Noh, J. and Hara, M. (2002) *Langmuir*, **18**, 1953.

66 Cyganik, P., Buck, M., Strunskus, T., Shaporenko, A., Wilton-Ely, J.D.E.T., Zharnikov, M. and Wöll, C. (2006) *Journal of the American Chemical Society*, **128**, 13868.

67 Cyganik, P. and Buck, M. (2004) *Journal of the American Chemical Society*, **126**, 5960.

68 Aguilar-Sanchez, R., Su, G.J., Homberger, M., Simon, U. and Wandlowski, T. (2007) *The Journal of Physical Chemistry C*, **111**, 17409.

69 Zhou, W.P., Baunach, T., Ivanova, V. and Kolb, D.M. (2004) *Langmuir*, **20**, 4590.

70 Fenter, P., Schreiber, F., Berman, L., Scoles, G., Eisenberger, P. and Bedzyk, M.J. (1998) *Surface Science*, **413**, 213.

71 Kondoh, H., Iwasaki, M., Shimada, T., Amemiya, K., Yokoyama, T., Ohta, T., Shimomura, M. and Kono, S. (2003) *Physical Review Letters*, **90**, 066102/1.

72 Torrelles, X., Vericat, C., Vela, M.E., Fonticelli, M.H., Millone, M.A.D., Felici, R., Lee, T.L., Zegenhagen, J., Munoz, G., Martin-Gago, J.A. and Salvarezza, R.C. (2006) *The Journal of Physical Chemistry B*, **110**, 5586.

73 Maksymovych, P., Sorescu, D.C. and Yates, J.T. (2006) *Physical Review Letters*, **97**, 146103/1.

74 Yu, M., Bovet, N., Satterley, C.J., Bengio, S., Lovelock, K.R.J., Milligan, P.K., Jones, R.G., Woodruff, D.P. and Dhanak, V. (2006) *Physical Review Letters*, **97**, 166102.

75 Mazzarello, R., Cossaro, A., Verdini, A., Rousseau, R., Casalis, L., Danisman, M.F., Floreano, L., Scandolo, S., Morgante, A. and Scoles, G. (2007) *Physical Review Letters*, **98**, 016102.

76 Roper, M.G., Skegg, M.P., Fisher, C.J., Lee, J.J., Dhanak, V.R., Woodruff, D.P. and Jones, R.G. (2004) *Chemical Physics Letters*, **389**, 87.

77 Maksymovych, P. and Yates, J.T. (2008) *Journal of the American Chemical Society*, **130**, 7518.

78 Cossaro, A., Mazzarello, R., Rousseau, R., Casalis, L., Verdini, A., Kohlmeyer, A., Floreano, L., Scandolo, S., Morgante, A., Klein, M.L. and Scoles, G. (2008) *Science*, **321**, 943.

79 Woodruff, D.P. (2007) *Applied Surface Science*, **254**, 76.

80 Molina, L.M. and Hammer, B. (2002) *Chemical Physics Letters*, **360**, 264.

81 Cyganik, P., Buck, M., Wilton-Ely, J.D.E.T. and Wöll, C. (2005) *The Journal of Physical Chemistry B*, **109**, 10902.

82 Edinger, K., Gölzhäuser, A., Demota, K., Wöll, C. and Grunze, M. (1993) *Langmuir*, **9**, 4.

83 McDermott, C.A., McDermott, M.T., Green, J.B. and Porter, M.D. (1995) *The Journal of Physical Chemistry*, **99**, 13257.

84 Edinger, K., Grunze, M. and Wöll, C. *Berichte der Bunsen-Gesellschaft für Physikalische Chemie*, (1997) **101**, 1811.

85 Poirier, G.E. (1997) *Langmuir*, **13**, 2019.

86 Jin, Q., Rodriguez, J.A., Li, C.Z., Darici, Y. and Tao, N.J. (1999) *Surface Science*, **425**, 101.

87 Yang, G.H. and Liu, G.Y. (2003) *The Journal of Physical Chemistry B*, **107**, 8746.

88 Fuxen, C., Azzam, W., Arnold, R., Witte, G., Terfort, A. and Wöll, C. (2001) *Langmuir*, **17**, 3689.

89 Azzam, W., Fuxen, C., Birkner, A., Rong, H.T., Buck, M. and Wöll, C. (2003) *Langmuir*, **19**, 4958.

90 Cyganik, P., Buck, M., Azzam, W. and Wöll, C. (2004) *The Journal of Physical Chemistry B*, **108**, 4989.

91 Rong, H.T., Frey, S., Yang, Y.J., Zharnikov, M., Buck, M., Wühn, M., Wöll, C. and Helmchen, G. (2001) *Langmuir*, **17**, 1582.

92 Azzam, W., Cyganik, P., Witte, G., Buck, M. and Wöll, C. (2003) *Langmuir*, **19**, 8262.

93 Chen, I.W.P., Chen, C.C., Lin, S.Y. and Chen, C.H. (2004) *The Journal of Physical Chemistry B*, **108**, 17497.

94 Thom, I. and Buck, M. (2005) *Surface Science*, **581**, 33.

95 Long, Y.T., Rong, H.T., Buck, M. and Grunze, M. (2002) *Journal of Electroanalytical Chemistry*, **524**, 62.

96 Felgenhauer, T., Yan, C., Geyer, W., Rong, H.T., Gölzhäuser, A. and Buck, M. (2001) *Applied Physics Letters*, **79**, 3323.

97 Ibach, H. (1997) *Surface Science Reports*, **29**, 195.

98 Berger, R., Delamarche, E., Lang, H.P., Gerber, C., Gimzewski, J.K., Meyer, E. and Guntherodt, H.J. (1997) *Science*, **276**, 2021.

99 Berger, R., Delamarche, E., Lang, H.P., Gerber, C., Gimzewski, J.K., Meyer, E. and Guntherodt, H.J. (1998) *Applied Physics A–Materials Science & Processing*, **66**, S55.

100 Godin, M., Williams, P.J., Tabard-Cossa, V., Laroche, O., Beaulieu, L.Y., Lennox, R.B. and Grutter, P. (2004) *Langmuir*, **20**, 7090.

101 Skoda, M.W.A., Jacobs, R.M.J., Willis, J. and Schreiber, F. (2007) *Langmuir*, **23**, 970.

102 Sur, U.K. and Lakshminarayanan, V. (2001) *Journal of Electroanalytical Chemistry*, **516**, 31.

103 Anderson, M.R., Evaniak, M.N. and Zhang, M.H. (1996) *Langmuir*, **12**, 2327.

104 Long, D.P., Lazorcik, J.L., Mantooth, B.A., Moore, M.H., Ratner, M.A., Troisi, A., Yao, Y., Ciszek, J.W., Tour, J.M. and Shashidhar, R. (2006) *Nature Materials*, **5**, 901.

105 Methivier, C., Beccard, B. and Pradier, C.M. (2003) *Langmuir*, **19**, 8807.

106 Subramanian, S. and Sampath, S., (2007) *Journal of Colloid and Interface Science*, **313**, 64.

107 Mayer, D., Dretschkow, T., Ataka, K. and Wandlowski, T. (2002) *Journal of Electroanalytical Chemistry*, **524**, 20.

108 Su, G.J., Zhang, H.M., Wan, L.J., Bai, C.L. and Wandlowski, T. (2004) *The Journal of Physical Chemistry B*, **108**, 1931.

109 Ciszek, J.W., Stewart, M.P. and Tour, J.M. (2004) *Journal of the American Chemical Society*, **126**, 13172.

110 Dreesen, L., Volcke, C., Sartenaer, Y., Peremans, A., Thiry, P.A., Humbert, C., Grugier, J. and Marchand-Brynaert, J. (2006) *Surface Science*, **600**, 4052.

111 Shen, C., Buck, M., Wilton-Ely, J.D.E.T., Weidner, T. and Zharnikov, M. (2008) *Langmuir*, **24**, 6609.

112 Ma, F. and Lennox, R.B. (2000) *Langmuir*, **16**, 6188.

113 Byloos, M., Al-Maznai, H. and Morin, M. (2001) *The Journal of Physical Chemistry B*, **105**, 5900.

114 Thom, I. and Buck, M. (2008) *Zeitschrift Für Physikalische Chemie*, **222**, 739.

115 Cohen-Atiya, M. and Mandler, D. (2003) *Journal of Electroanalytical Chemistry*, **550**, 267.

116 Hatchett, D.W., Stevenson, K.J., Lacy, W.B., Harris, J.M. and White, H.S. (1997) *Journal of the American Chemical Society*, **119**, 6596.

117 Hatchett, D.W., Uibel, R.H., Stevenson, K.J., Harris, J.M. and White, H.S. (1998) *Journal of the American Chemical Society*, **120**, 1062.

118 Fonticelli, M., Azzaroni, O., Benitez, G., Martins, M.E., Carro, P. and Salvarezza, R.C. (2004) *The Journal of Physical Chemistry B*, **108**, 1898.

119 Fonticelli, M.H., Benitez, G., Carro, P., Azzaroni, O., Salvarezza, R.C., Gonzalez, S., Torres, D. and Illas, F. (2008) *The Journal of Physical Chemistry C*, **112**, 4557.

120 Stevenson, K.J., Mitchell, M. and White, H.S. (1998) *The Journal of Physical Chemistry B*, **102**, 1235.

121 Sumi, T. and Uosaki, K. (2004) *The Journal of Physical Chemistry B*, **108**, 6422.

122 Widrig, C.A., Chung, C. and Porter, M.D. (1991) *Journal of Electroanalytical Chemistry*, **310**, 335.

123 Yang, D.F., AlMaznai, H. and Morin, M. (1997) *The Journal of Physical Chemistry B*, **101**, 1158.

124 Gorman, C.B., Carroll, R.L., He, Y., Tian, F. and Fuierer, R. (2000) *Langmuir*, **16**, 6312.

125 Imabayashi, S., Hobara, D., Kakiuchi, T. and Knoll, W. (1997) *Langmuir*, **13**, 4502.

126 Imabayashi, S., Hobara, D. and Kakiuchi, T. (2001) *Langmuir*, **17**, 2560.

127 Satjapipat, M., Sanedrin, R. and Zhou, F.M. (2001) *Langmuir*, **17**, 7637.

128 Zhang, Y., Salaita, K., Lim, J.H. and Mirkin, C.A. (2002) *Nano Letters*, **2**, 1389.

129 Zhang, Y., Salaita, K., Lim, J.H., Lee, K.B. and Mirkin, C.A. (2004) *Langmuir*, **20**, 962.

130 Gorman, C.B., Biebuyck, H.A. and Whitesides, G.M. (1995) *Langmuir*, **11**, 2242.

131 Balss, K.M., Coleman, B.D., Lansford, C.H., Haasch, R.T. and Bohn, P.W. (2001) *The Journal of Physical Chemistry B*, **105**, 8970.

132 Plummer, S.T. and Bohn, P.W. (2002) *Langmuir*, **18**, 4142.

133 Imabayashi, S., Iida, M., Hobara, D., Feng, Z.Q., Niki, K. and Kakiuchi, T. (1997) *Journal of Electroanalytical Chemistry*, **428**, 33.

134 Azzaroni, O., Vela, M.E., Andreasen, G., Carro, P. and Salvarezza, R.C. (2002) *The Journal of Physical Chemistry B*, **106**, 12267.

135 Kim, Y.K., Koo, J.P. and Ha, J.S. (2005) *Thin Solid Films*, **479**, 277.

136 Cyganik, P., Buck, M., Strunskus, T., Shaporenko, A., Witte, G., Zharnikov, M. and Wöll, C. (2007) *The Journal of Physical Chemistry C*, **111**, 16909.

137 Schneider, T.W. and Buttry, D.A. (1993) *Journal of the American Chemical Society*, **115**, 12391.

138 Kawaguchi, T., Yasuda, H., Shimazu, K. and Porter, M.D. (2000) *Langmuir*, **16**, 9830.

139 Laredo, T., Leitch, J., Chen, M.H., Burgess, I.J., Dutcher, J.R. and Lipkowski, J. (2007) *Langmuir*, **23**, 6205.

140 Petri, M., Kolb, D.M., Memmert, U. and Meyer, H. (2003) *Electrochimica Acta*, **49**, 175.

141 Zhong, C.J. and Porter, M.D. (1997) *Journal of Electroanalytical Chemistry*, **425**, 147.

142 Byloos, M., Al-Maznai, H. and Morin, M. (1999) *The Journal of Physical Chemistry B*, **103**, 6554.

143 Wong, S.S. and Porter, M.D. (2000) *Journal of Electroanalytical Chemistry*, **485**, 135.

144 Mohtat, N., Byloos, M., Soucy, M., Morin, S. and Morin, M. (2000) *Journal of Electroanalytical Chemistry*, **484**, 120.

145 Kondo, T., Sumi, T. and Uosaki, K. (2002) *Journal of Electroanalytical Chemistry*, **538**, 59.

146 Calvente, J.J., Gil, M.L., Sanchez, M.D., Andreu, R. and de Pablos, F. (2000) *Electrochimica Acta*, **45**, 3087.

147 Honeychurch, M.J. and Rechnitz, G.A. (1998) *Electroanalysis*, **10**, 285.

148 Matsuda, H., Aoki, K. and Tokuda, K. (1987) *Journal of Electroanalytical Chemistry*, **217**, 15.

149 Matsuda, H., Aoki, K. and Tokuda, K. (1987) *Journal of Electroanalytical Chemistry*, **217**, 1.

150 Hobara, D., Miyake, O., Imabayashi, S., Niki, K. and Kakiuchi, T. (1998) *Langmuir*, **14**, 3590.

151 Wano, H. and Uosaki, K. (2001) *Langmuir*, **17**, 8224.

152 Vela, M.E., Martin, H., Vericat, C., Andreasen, G., Creus, A.H. and Salvarezza, R.C. (2000) *The Journal of Physical Chemistry B*, **104**, 11878.

153 Wano, H. and Uosaki, K. (2005) *Langmuir*, **21**, 4024.

154 Yang, D.F. and Morin, M. (1997) *Journal of Electroanalytical Chemistry*, **429**, 1.

155 Yang, D.F. and Morin, M. (1998) *Journal of Electroanalytical Chemistry*, **441**, 173.

156 Vinokurov, I.A., Morin, M. and Kankare, J. (2000) *The Journal of Physical Chemistry B*, **104**, 5790.

157 Madueno, R., Pineda, T., Sevilla, J.M. and Blazquez, M. (2005) *Journal of Electroanalytical Chemistry*, **576**, 197.

158 Doneux, T., Nichols, R.J. and Buess-Herman, C. (2008) *Journal of Electroanalytical Chemistry*, **621**, 267.

159 Pesika, N.S., Stebe, K.J. and Searson, P.C. (2006) *Langmuir*, **22**, 3474.

160 Poelman, M., Buess-Herman, C. and Badiali, J.P. (1999) *Langmuir*, **15**, 2194.

161 Mulder, W.H., Calvente, J.J. and Andreu, R. (2001) *Langmuir*, **17**, 3273.

162 Martin, H., Vericat, C., Andreasen, G., Vela, M.E. and Salvarezza, R.C. (2002) *Journal of Chemical Physics*, **117**, 2293.

163 Strutwolf, J. and O'Sullivan, C.K. (2007) *Electroanalysis*, **19**, 1467.

164 Shepherd, J.L., Kell, A., Chung, E., Sinclar, C.W., Workentin, M.S. and Bizzotto, D. (2004) *Journal of the American Chemical Society*, **126**, 8329.

165 Azzaroni, O., Vela, M.E., Fonticelli, M., Benitez, G., Carro, P., Blum, B. and Salvarezza, R.C. (2003) *The Journal of Physical Chemistry B*, **107**, 13446.

166 Kawasaki, M. and Iino, M. (2006) *The Journal of Physical Chemistry B*, **110**, 21124.

167 Zhang, H.P. and Baldelli, S. (2006) *The Journal of Physical Chemistry B*, **110**, 24062.

168 Williams, J.A. and Gorman, C.B. (2007) *The Journal of Physical Chemistry C*, **111**, 12804.

169 Yang, Y.C., Yen, Y.P., Yang, L.Y.O., Yau, S.L. and Itaya, K. (2004) *Langmuir*, **20**, 10030.

170 Love, J.C., Wolfe, D.B., Haasch, R., Chabinyc, M.L., Paul, K.E., Whitesides, G.M. and Nuzzo, R.G. (2003) *Journal of the American Chemical Society*, **125**, 2597.

171 Petri, M., Kolb, D.M., Memmert, U. and Meyer, H. (2003) *Electrochimica Acta*, **49**, 183.

172 Chen, H.M., Parulekar, S.J. and Zdunek, A. (2008) *Journal of the Electrochemical Society*, **155**, D349.

173 Dow, W.P. and Yen, M.Y. (2005) *Electrochemical and Solid State Letters*, **8**, C161.

174 Bozzini, B., D'Urzo, L., Romanello, V. and Mele, C. (2006) *Journal of the Electrochemical Society*, **153**, C254.

175 Jenq, S.N., Wan, C.C. and Wang, Y.Y. (2007) *Journal of Electroanalytical Chemistry*, **609**, 68.

176 Schilardi, P.L., Azzaroni, O. and Salvarezza, R.C. (2001) *Langmuir*, **17**, 2748.

177 Moffat, T.P. and Yang, H. (1995) *Journal of the Electrochemical Society*, **142**, L220.

178 Thom, I., Hähner, G. and Buck, M. (2005) *Applied Physics Letters*, **87**, 024101.

179 Boyen, H.G., Ziemann, P., Wiedwald, U., Ivanova, V., Kolb, D.M., Sakong, S., Gross, A., Romanyuk, A., Buttner, M. and Oelhafen, P. (2006) *Nature Materials*, **5**, 394.

180 Qu, D. and Uosaki, K. (2006) *The Journal of Physical Chemistry B*, **110**, 17570.

181 Shekhah, O., Busse, C., Bashir, A., Turcu, F., Yin, X., Cyganik, P., Birkner, A., Schuhmann, W. and Wöll, C. (2006) *Physical Chemistry Chemical Physics*, **8**, 3375.

182 Haick, H. and Cahen, D. (2008) *Progress in Surface Science*, **83**, 217.

183 Schneeweiss, M.A. and Kolb, D.M. (1999) *Physica Status Solidi A Applied Research*, **173**, 51.

184 Staikov, G. (2007) in *Electrocrystallisation in Nanotechnology* (ed. G. Staikov), Wiley-VCH, Weinheim.

185 Budevski, E., Staikov, G. and Lorenz, W.J. (1996) *Electrochemical Phase Formation and Growth*, VCH, Weinheim.

186 Kolb, D.M. (1978) in *Advances in Electrochemistry and Electrochemical Engineering*, Vol. 11 (eds H. Gerischer and C.W. Tobias), Wiley-Interscience, New York, p. 125.

187 Herrero, E., Buller, L.J. and Abruna, H.D. (2001) *Chemical Reviews*, **101**, 1897.

188 Lindsay, S.M. and Ratner, M.A. (2007) *Advanced Materials*, **19**, 23, p. 23.

189 Tai, Y., Shaporenko, A., Grunze, M. and Zharnikov, M. (2005) *The Journal of Physical Chemistry B*, **109**, 19411.

190 Nagy, G. and Walker, A.V. (2006) *The Journal of Physical Chemistry B*, **110**, 12543.

191 Walker, A.V., Tighe, T.B., Cabarcos, O.M., Reinard, M.D., Haynie, B.C., Uppili, S., Winograd, N. and Allara, D.L. (2004) *Journal of the American Chemical Society*, **126**, 3954.

192 Hugelmann, M. and Schindler, W. (2003) *Surface Science*, **541**, L643.

193 Simeone, F.C., Kolb, D.M., Venkatachalam, S. and Jacob, T. (2008) *Surface Science*, **602**, 1401.

194 Simeone, F.C., Kolb, D.M., Venkatachalam, S. and Jacob, T. (2007) *Angewandte Chemie International Edition*, **46**, 8903.

195 Cavalleri, O., Kind, H., Bittner, A.M. and Kern, K. (1998) *Langmuir*, **14**, 7292.

196 Manolova, M., Ivanova, V., Kolb, D.M., Boyen, H.G., Ziemann, P., Buttner, M., Romanyuk, A. and Oelhafen, P. (2005) *Surface Science*, **590**, 146.

197 Manolova, M., Kayser, M., Kolb, D.M., Boyen, H.G., Ziemann, P., Mayer, D. and Wirth, A. (2007) *Electrochimica Acta*, **52**, 2740.

198 Qu, D.Y. and Uosaki, K. (2006) *Chemistry Letters*, **35**, 258.

199 Jennings, G.K. and Laibinis, P.E. (1997) *Journal of the American Chemical Society*, **119**, 5208.

200 Silien, C. and Buck, M. (2008) submitted.

201 Jennings, G.K. and Laibinis, P.E. (1996) *Langmuir*, **12**, 6173.

202 Oyamatsu, D., Kuwabata, S. and Yoneyama, H. (1999) *Journal of Electroanalytical Chemistry*, **473**, 59.

203 Nishizawa, M., Sunagawa, T. and Yoneyama, H. (1997) *Langmuir*, **13**, 5215.

204 Cavalleri, O., Gilbert, S.E. and Kern, K. (1997) *Chemical Physics Letters*, **269**, 479.

205 Sondag-Huethorst, J.A.M. and Fokkink, L.G.J. (1995) *Langmuir*, **11**, 2237.

206 Cavalleri, O., Hirstein, A., Bucher, J.P. and Kern, K. (1996) *Thin Solid Films*, **285**, 392.

207 Eliadis, E.D., Nuzzo, R.G., Gewirth, A.A. and Alkire, R.C. (1997) *Journal of the Electrochemical Society*, **144**, 96.

208 Whelan, C.M., Smyth, M.R. and Barnes, C.J. (1999) *Langmuir*, **15**, 116.

209 Esplandiu, M.J. and Hagenström, H. (2002) *Solid State Ionics*, **150**, 39.

210 Hagenström, H., Schneeweiss, M.A. and Kolb, D.M. (1999) *Langmuir*, **15**, 7802.

211 Hagenström, H., Esplandiu, M.J. and Kolb, D.M. (2001) *Langmuir*, **17**, 839.

212 Epple, M., Bittner, A.M., Kuhnke, A., Kern, K., Zheng, W.Q. and Tadjeddine, A. (2002) *Langmuir*, **18**, 773.

213 Sun, L. and Crooks, R.M. (1991) *Journal of the Electrochemical Society*, **138**, L23.

214 Zamborini, F.P., Campbell, J.K. and Crooks, R.M. (1998) *Langmuir*, **14**, 640.

215 Green, M.P. and Hanson, K.J. (1992) *Journal of Vacuum Science & Technology A*, **10**, 3012.

216 Honbo, H., Sugawara, S. and Itaya, K. (1990) *Analytical Chemistry*, **62**, 2424.

217 Gilbert, S.E., Cavalleri, O. and Kern, K. (1996) *The Journal of Physical Chemistry*, **100**, 12123.

218 Hölzle, M.H., Zwing, V. and Kolb, D.M. (1995) *Electrochimica Acta*, **40**, 1237.

219 Kuwabata, S., Kanemoto, H., Oyamatsu, D. and Yoneyama, H. (1999) *Electrochemistry*, **67**, 1254.

220 Oyamatsu, D., Kanemoto, H., Kuwabata, S. and Yoneyama, H. (2001) *Journal of Electroanalytical Chemistry*, **497**, 97.

221 Shimazu, K., Kawaguchi, T. and Isomura, T. (2002) *Journal of the American Chemical Society*, **124**, 652.

222 Li, S. and Crooks, R.M. (1991) *Journal of the Electrochemical Society*, **138**, L23.

223 Kaltenpoth, G., Völkel, B., Nottbohm, C.T., Gölzhäuser, A. and Buck, M. (2002) *Journal of Vacuum Science & Technology B*, **20**, 2734.

224 Wilhelm, T. and Wittstock, G. (2000) *Mikrochimica Acta*, **133**, 1.

225 Wilhelm, T. and Wittstock, G. (2001) *Electrochimica Acta*, **41**, 275.

226 Yang, G.H., Amro, N.A. and Liu, G.Y. (2003) *Nanofabrication Technologies*, **5220**, 52.

227 Ross, C.B., Sun, L. and Crooks, R.M. (1993) *Langmuir*, **9**, 632.

228 Schoer, J.K., Zamborini, F.P. and Crooks, R.M. (1996) *The Journal of Physical Chemistry*, **100**, 11086.

229 Schoer, J.K. and Crooks, R.M. (1997) *Langmuir*, **13**, 2323.

230 Shen, C. (2008) Self-assembled Monolayers of Thiolates as Templates for Micro/Nano Fabrication, PhD thesis, University of St Andrews, St Andrews, UK.

231 Madueno, R., Raisanen, M.T., Silien, C. and Buck, M. (2008) *Nature*, **454**, 618.

232 Silien, C., Räisänen, M.T. and Buck, M. Angewandte Chemie International Edition, DOI: 10.1002/anie.200806267.

233 Langerock, S., Menard, H., Rowntree, P. and Heerman, L. (2005) *Langmuir*, **21**, 5124.

234 Cavalleri, O., Gilbert, S.E. and Kern, K. (1997) *Surface Science*, **377**, 931.

235 Lim, J.H., Kim, N.H. and Chang, E.G. (2004) *Journal of the Electrochemical Society*, **151**, C455.

236 Seo, K. and Borguet, E. (2006) *Langmuir*, **22**, 1388.

237 Leggett, G.J. (2006) *Chemical Society Reviews*, **35**, 1150.

238 Huang, J. and Hemminger, J.C. (1993) *Journal of the American Chemical Society*, **115**, 3342.

239 Völkel, B., Kaltenpoth, G., Handrea, M., Sahre, M., Nottbohm, C.T., Küller, A., Paul, A., Kautek, W., Eck, W. and Gölzhäuser, A. (2005) *Surface Science*, **597**, 32.

240 Geyer, W., Stadler, V., Eck, W., Zharnikov, M., Gölzhäuser, A. and Grunze, M. (1999) *Applied Physics Letters*, **75**, 2401.

241 Heister, K., Zharnikov, M., Grunze, M., Johansson, L.S.O. and Ulman, A. (2001) *Langmuir*, **17**, 8.

242 Zach, M.P., Ng, K.H. and Penner, R.M. (2000) *Science*, **290**, 2120.

243 Azzaroni, O., Schilardi, P.L. and Salvarezza, R.C. (2003) *Electrochimica Acta*, **48**, 3107.

244 Azzaroni, O., Schilardi, P.L. and Salvarezza, R.C. (2002) *Applied Physics Letters*, **80**, 1061.

245 Fonticelli, M.H., Corthey, G., Benitez, G.A., Salvarezza, R.C., Giovanetti, L.J., Requejo, F.G. and Shon, Y.S. (2007) *The Journal of Physical Chemistry C*, **111**, 9359.

246 Baker, W.S. and Crooks, R.M. (1998) *The Journal of Physical Chemistry B*, **102**, 10041.

247 Kawaguchi, T. and Shimazu, K. (2001) *Chemistry Letters*, **30**, 90.

248 Pesika, N.S., Radisic, A., Stebe, K.J. and Searson, P.C. (2006) *Nano Letters*, **6**, 1023.

249 Nelson, J.B. and Schwartz, D.T. (2007) *Langmuir*, **23**, 9661.

250 O'Brien, B., Stebe, K.J. and Searson, P.C. (2007) *The Journal of Physical Chemistry C*, **111**, 8686.

251 Azzaroni, O., Fonticelli, M.H., Benitez, G., Schilardi, P.L., Gago, R., Caretti, I., Vazquez, L. and Salvarezza, R.C. (2004) *Advanced Materials*, **16**, 405.

252 Zhang, X.G., Li, X.H. and Li, H.L. (2001) *Journal of Colloid and Interface Science*, **234**, 68.

253 Soolaman, D.M. and Yu, H.Z. (2007) *The Journal of Physical Chemistry C*, **111**, 14157.

254 Herzog, G. and Arrigan, D.W.M. (2003) *Electroanalysis*, **15**, 1302.

255 Yang, N.J., Wang, X.X. and Wan, Q.J. (2007) *Electrochimica Acta*, **52**, 4818.

256 Herzog, G. and Arrigan, D.W.M. (2005) *Electroanalysis*, **17**, 1816.

257 Lee, J., Hwang, S., Lee, H. and Kwak, J. (2004) *The Journal of Physical Chemistry B*, **108**, 5372.

258 Robertson, J.W.F., Tiani, D.J. and Pemberton, J.E. (2007) *Langmuir*, **23**, 4651.

259 Arrigan, D.W.M., Iqbal, T. and Pickup, M.J. (2001) *Electroanalysis*, **13**, 751.

260 Arrigan, D.W.M., Le Bihan, L. and Pickup, M.J. (1999) *Analyst*, **124**, 1797.

261 Liu, S.F., Li, X.H., Li, Y.C., Li, Y.F., Li, J.R. and Jiang, L. (2005) *Electrochimica Acta*, **51**, 427.

262 Farndon, E.E., Walsh, F.C. and Campbell, S.A. (1995) *Journal of Applied Electrochemistry*, **25**, 574.

263 Kim, J.J., Kim, S.K. and Kim, Y.S. (2003) *Journal of Electroanalytical Chemistry*, **542**, 61.

264 Moffat, T.P., Wheeler, D. and Josell, D. (2004) *Journal of the Electrochemical Society*, **151**, C262.

265 Jenq, S.N., Wan, C.C., Wang, Y.Y., Li, H.W., Liu, P.T. and Chen, J.H. (2006) *Japanese Journal of Applied Physics Part 2-Letters & Express Letters*, **45**, L1215.

266 Jenq, S.N., Wan, C.C., Wang, Y.Y., Li, H.W., Liu, P.T. and Chen, J.H. (2006) *Electrochemical and Solid State Letters*, **9**, C167.

267 Kang, M. and Gewirth, A.A. (2003) *Journal of the Electrochemical Society*, **150**, C426.

268 Ivanova, V., Baunach, T. and Kolb, D.A. (2005) *Electrochimica Acta*, **50**, 4283.

269 Ivanova, V., Manolova, M. and Kolb, D.M. (2007) *Nanoscience and Technology Parts 1 and 2*, **121–123**, 363.

270 Yang, Y.C., Yau, S.L. and Lee, Y.L. (2006) *Journal of the American Chemical Society*, **128**, 3677.

271 Whelan, C.M., Smyth, M.R. and Barnes, C.J. (1998) *Journal of Electroanalytical Chemistry*, **441**, 109.

272 Hepel, M. and Tewksbury, E. (2004) *Electrochimica Acta*, **49**, 3827.

273 Matsunaga, M., Nakanishi, T., Asahi, T. and Osaka, T. (2007) *Electrochemistry Communications*, **9**, 725.

Index